sciendo

On the thermodynamics of homolytic C—H bond cleavage in linear and branched alkanes: Comparison of DFT and composite G4 and G4(MP2) methods

Dagmar Štellerová, Vladimír Lukeš

Institute of Physical Chemistry and Chemical Physics, Slovak University of Technology in Bratislava, Radlinského 9, SK-812 37 Bratislava, Slovakia
dagmar.stellerova@stuba.sk

Abstract: This work provides a systematic theoretical study on gas-phase bond dissociation enthalpies for homolytic C—H bond cleavage in linear and branched alkanes. Quantum chemical calculations were performed using the density functional theory (DFT) and *ab initio* composite (G4(MP2), G4) methods. In case of DFT calculations, the M06-2X and B3LYP functionals combined with 6-311++G**, aug-cc-pVDZ, aug-cc-pVTZ, and aug-cc-pVQZ basis sets were covered. In linear molecules, the best agreement with experiment was observed for B3LYP/aug-cc-pVQZ. In both composite approaches, as the number of C atoms increases, the BDE values are affected by the systematic error of the method. For example, G4 BDE of terminal —CH3 group of hexane is 422.6 kJ · mol^{-1} while for undecane it is 415.5 kJ · mol^{-1}. On the contrary, the composite methods are in better agreement with experiments compared to the DFT approaches for simple branched hydrocarbons.

Keywords: alkanes, chemical accuracy, DFT, G4(MP2), radical mechanism

Introduction

The bond dissociation enthalpy (BDE) is a measure of a chemical bond's strength; therefore, this quantity does not depend on a reaction path. It can be defined as the standard enthalpy change when X—Y is homolytically cleaved while providing radical fragments X$^{\bullet}$ and Y$^{\bullet}$. Although the enthalpy change is temperature-dependent, it is often evaluated at standard temperature conditions (298.15 K). Generally, BDEs are useful quantities in investigating the thermodynamics of chemical processes (Rimarčík et al., 2011; Bordwell et al., 1994; Denisov and Tumanov, 2005).

Experimentally deriving BDEs for larger molecules is not realistic. These measurements are suitable for simple and rather small model molecules while requiring a great deal of experience. Three commonly applicable techniques can be used to determine BDEs measured in solution or in gas-phase (Berkowitz et al., 1994). In this context, methods of chemical radical kinetics and equilibrium, various calorimetric and electrochemical methods including the acidity / electron affinity cycle, generation of radicals by pyrolysis or photolysis combined with spectrometric determination of energy levels can be mentioned (Blanksby and Ellison, 2003). Nevertheless, bond dissociation enthalpy investigation is still challenging, and it is subject to considerable experimental errors and uncertainties. Accuracy of many BDE experimental values, especially those dating back to before 1970, is within ±4—10 kJ · mol^{-1} (Darwent, 1970). Therefore, these BDEs can be especially unreliable and have been subject to later revisions (Luo, 2007). For example, experimentally determined BDE of C—H bonds for benzene in 1965 was 430.54 kJ · mol^{-1} (Trotman-Dickenson, 1965), while the currently accepted value is 472(2) kJ · mol^{-1} (Ervin and DeTuri, 2002). A similar situation arose for phenol over a period of 20 years, where O—H BDEs ranging from 358.6 to 380.6 kJ · mol^{-1} were reported in literature (Mulder et al., 2005). On the other hand, experimental accuracy of small molecules is very high. For example, experimental BDE for the hydrogen molecule is 435.780 kJ · mol^{-1} (Balakrishnan et al., 1992).

Because the experimental BDE values are highly dependent on the size of the molecule under investigation, as well as on the methodology and experimental technique, theoretical calculations play a very important role in their investigation. Since the thermodynamics of radical reactions is minimally affected by the environment, the calculations in the gas phase offers plausible results. In case of simple aromatic molecules, the description of the thermodynamics of homolytic X—H bond cleavage for X = O, S, N at the DFT level is in sufficient agreement with the experiment (Klein et al., 2006; Barckholtz et al., 1999) using functionals B3LYP and M06-2X (Lee et al., 1988; Becke, 1988; Zhao and Truhlar, 2008). Paradoxically, *ab initio* BDE calculations can result in large deviations from the experiment due to spin contamination of radicals. This problem does not arise only for the CCSD(T) approach (Raghavachari

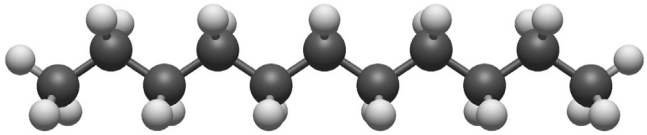

Fig. 1. Optimal *all-trans* M06-2X/6-311++G** geometry of undecane ($\mathbf{C_{11}H_{24}}$) molecule.

et al., 1989), which is very challenging and practically applicable only for small molecules in a large base of atomic orbitals. A certain compromise solution has been introduced by the Gaussian-*n* (G*n*) family of composite approaches (Pople et al., 1989; Curtiss et al., 1990, 1991, 1998, 2007). These approaches combine methods with a high level of theory and a small basis set with methods employing lower levels of theory with larger basis sets. With the development of computer technology, the G4 and G4(MP2) methods have recently gained great popularity in the calculation of thermodynamic quantities of chemically interesting polyatomic molecules (Kováčová, 2024; Rayne and Forest, 2011). This implies a natural need

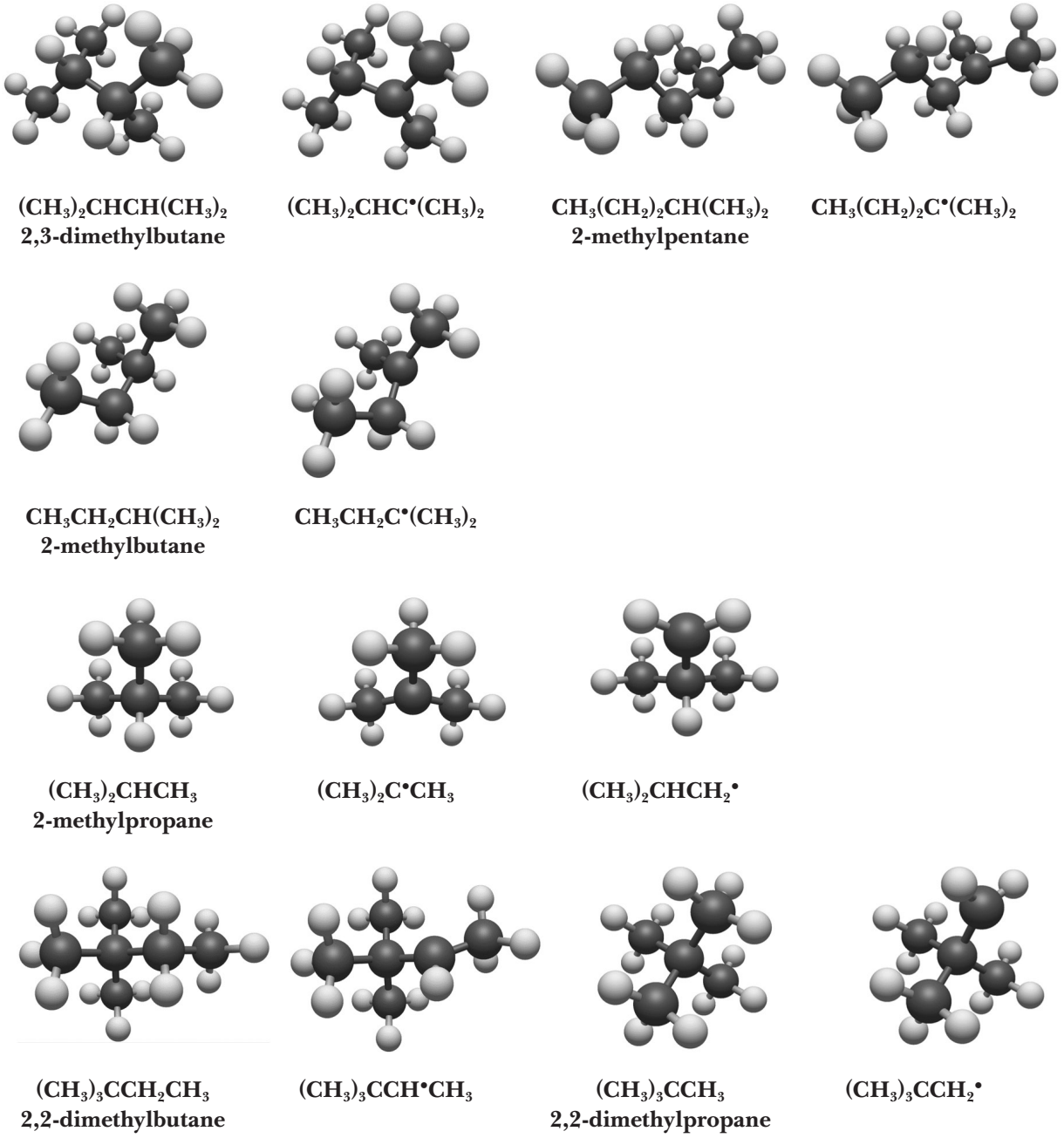

Fig. 2. Optimal M06-2X/6-311++G** geometries of studied branched hydrocarbons and their radical forms.

for a better understanding of the computational reliability of the above approaches with respect to standard DFT approaches.

Since the main purpose of this work is to validate G4 and G4(MP2) methods, systematic computations of linear and simple branched alkanes were performed (see Fig. 1 and Fig. 2). This set of molecules represents an optimal testing system for possible induction effect of methyl groups on thermodynamic hydrogen atom abstraction. Moreover, radicals of these molecules play a key role in oxidation reactions in industrial processes and chemical laboratories and the energetics of these reactions were studied experimentally more than 30 years ago.

Partial aims of this theoretical paper include: (1) to optimize and discuss the gas-phase geometries of molecules; (2) to calculate selected C—H bond dissociation enthalpies by two standardly used hybrid functionals in combination with 6-311++G** basis set of atomic orbitals; (3) to compare 6-311++G** results with calculations of aug-cc-pVNZ (where N = D, T and Q) basis sets; (4) to perform G4 and G4(MP2) calculations of the studied molecules; and (5) to compare the obtained results with available experimental data.

Computational Details

All calculations were performed using default settings of the Gaussian 16 program package (Frisch et al., 2016). Four theoretical approaches, i.e., density functional theory (DFT) 3-paramenter hybrid B3LYP functional, DFT M06-2X hybrid functional, and G4(MP2) and G4 composite *ab-initio* methods, were used to obtain optimal geometries of parent and radical structures. With B3LYP and M06-2X functionals, Pople's triple zeta 6-311++G** (Hariharan and Pople, 1973; Rassolov et al., 1998) and Dunning's (Dunning, 1989) correlation-consistent augmented (aug-cc-pVDZ, aug-cc-pVTZ and aug-cc-pVQZ) basis sets were applied. Since radical formation does not depend on the presence of a solvent (difference $< 5\ kJ \cdot mol^{-1}$), gas-phase optimalization was performed at room temperature (298.15 K). Total gas-phase enthalpy of the hydrogen atom used to calculate BDEs is $-1306\ kJ \cdot mol^{-1}$ (Rimarčík et al., 2010). The optimized structures were confirmed to be real minima by vibrational analysis (no imaginary frequencies). The Avogadro program (Hanwell et al., 2012) was used to design and visualize the studied species.

Results and Discussion

Structures of studied hydrocarbons

Gas-phase calculations were carried out for saturated linear and branched alkanes together with their corresponding radical forms (Fig. 1 and Fig. 2). Within linear hydrocarbons, molecules with the carbon chain of $n = 1$ up to $n = 11$ (see Fig. 1) were studied. Homolytic cleavage was performed at terminal methyl C—H bond of the molecules. For each of them, apart from tetrahedral methane geometry, *all-trans* conformation of dihedral angles has been set. The distance between all neighboring carbons was 1.53 Å, shortened to 1.49 Å for terminal C—C bond in radicals. Bond angles of terminal methyl moiety H—C—H were in range of 107.6 ° to 109.5 ° and 117.6 ° to 120.0 ° for parent and radical conformations, respectively.

As for branched hydrocarbons, 6 small molecules have been selected, namely 2-methylpropane, 2,2-dimethylpropane, 2-methylbutane, 2,2-dimethylbutane, 2,3-dimethylbutane and 2-methylpentane (see Fig. 2). Initial conformation arrangements of branched alkanes were divided from the geometries of linear structures. For the 2-methylpropane and 2,2-dimethylpropane, cleavages of hydrogen from primary carbon have been carried out. Similarly to above mentioned linear structures, the abstraction caused change in H—C—H angles from 107.8 ° to 118.0 ° in 2-methylpropane and 108.0 ° to 118.0 ° in 2,2-dimethylpropane. Geometry of 2,2-dimethylbutane challenged retraction of H atom from secondary carbon. The orientation of C_1—C_2—C_3—C_4 remained planar for both parent and radical conformations. The rest of the branched alkanes went through cleavage of hydrogen from tertiary carbon. The values of dihedral angles defined by H—C—$C^{(\bullet)}$—C atoms slightly titled in parent molecules vary from –4 ° in 2,3-dimethylbutane to 15 ° in 2-methylpropane in their radical forms.

HAT of primary C—H bonds in linear alkanes

In general, quantum-chemical calculations may provide different reaction enthalpies depending on the choice of computational approach, i.e., the type of approximation and the basis set used. To assess the reliability of different theoretical approaches, HAT for homolytic cleavage of C—H terminal methyl groups in linear hydrocarbons was performed. First, the calculations were carried out at the B3LYP/6-311++G** and M06-2X/6-311++G** levels of theory with the results collected in Tab. 1. For both methods, BDE values vary in agreement with the experimental values with the increasing methylene moiety up to butane. In case of higher hydrocarbons (pentane to undecane), the BDE values remain unchanged, with the values of $420.5\ kJ \cdot mol^{-1}$ for B3LYP and $415.0\ kJ \cdot mol^{-1}$ for M06-2X, using the 6-311++G** basis of atomic orbitals. The induction effect along the sigma bonds was present as an explanation. Higher alkanes do

Tab. 1. Experimental (Luo, 2007) and theoretical C—H BDE values of studied hydrocarbons at different levels of theory. Corrected values are in parentheses. All values are in $kJ \cdot mol^{-1}$.

Radical	B3LYP				M06-2X				G4	G4(MP2)	Exp.
	6-311++G**	aug-cc-pVDZ	aug-cc-pVTZ	aug-cc-pVQZ	6-311++G**	aug-cc-pVDZ	aug-cc-pVTZ	aug-cc-pVQZ			
$CH_3^{\bullet}$	437.5 (433.6)	431.7 (433.4)	438.2 (433.6)	439.0 (433.6)	429.1 (434.6)	423.5 (435.0)	430.4 (434.7)	432.2 (435.2)	441.5 (435.4)	443.7 (436.4)	439.3 ±0.4
$C_2H_5^{\bullet}$	418.1 (419.9)	412.8 (419.5)	418.4 (419.9)	419.1 (419.9)	412.8 (419.3)	407.6 (419.2)	413.4 (419.4)	415.1 (419.8)	425.5 (420.9)	427.1 (422.0)	420.5 ±1.3
$C_3H_7^{\bullet}$	421.1 (422.0)	416.1 (421.9)	421.5 (422.0)	422.1 (422.0)	415.6 (422.0)	408.2 (419.8)	416.4 (422.1)	418.2 (422.6)	427.4 (422.6)	428.2 (422.9)	422.2 ±2.1
$C_4H_9^{\bullet}$	420.5 (421.6)	415.6 (421.6)	420.9 (421.6)	421.6 (421.6)	412.5 (419.1)	407.7 (419.2)	413.3 (419.3)	415.0 (419.7)	425.4 (420.8)	425.3 (420.4)	421.3
$C_5H_{11}^{\bullet}$	420.5 (421.6)	415.6 (421.6)	420.9 (421.6)	421.6 (421.6)	415.0 (421.4)	410.1 (421.7)	415.8 (421.5)	417.6 (422.1)	424.1 (419.5)	423.0 (418.4)	419.2
$C_6H_{13}^{\bullet}$	420.5	415.6	420.9	421.6	415.0	410.2	415.8	417.5	422.6	420.6	
$C_7H_{15}^{\bullet}$	420.5	415.6	420.9	421.6	415.0	410.1	415.8	417.6	421.2	418.3	
$C_8H_{17}^{\bullet}$	420.5	415.6	420.9	421.5	415.0	410.2	415.8	417.6	419.8	416.0	
$C_9H_{19}^{\bullet}$	420.5	415.6	420.9	421.6	415.0	410.1	415.8	417.6	418.4	413.6	
$C_{10}H_{21}^{\bullet}$	420.5	415.6	420.9	421.5	415.0	410.2	415.8	417.6	416.9	411.3	
$C_{11}H_2{}^{3}\bullet$	420.5	415.6	420.9	421.5	415.0	410.1	415.8	417.6	415.5	408.9	
$(CH_3)_2CHC^{\bullet}(CH_3)_2$	389.6 (399.7)	386.0 (399.8)	389.3 (399.8)	390.0 (399.8)	391.9 (399.7)	388.3 (400.0)	391.7 (399.7)	393.2 (400.0)	402.5 (399.8)	401.5 (399.7)	399.2 ±13
$CH_3(CH_2)_2C^{\bullet}(CH_3)_2$	386.7 (397.7)	383.0 (397.6)	386.3 (397.7)	387.0 (397.7)	390.0 (397.9)	386.2 (398.0)	389.8 (398.0)	391.3 (398.3)	399.2 (396.8)	398.0 (396.8)	399.3
$CH_3CH_2C^{\bullet}(CH_3)_2$	388.0 (398.6)	384.2 (398.5)	387.5 (398.5)	388.2 (398.5)	391.2 (399.0)	387.4 (399.1)	391.0 (399.1)	392.5 (399.4)	401.7 (399.1)	401.4 (399.7)	400.8
$(CH_3)_2C^{\bullet}CH_3$	391.6 (401.2)	387.7 (401.0)	391.2 (401.1)	391.9 (401.1)	394.0 (401.7)	389.7 (401.4)	393.6 (401.4)	395.0 (401.7)	406.0 (403.0)	406.5 (404.1)	400.4 ±2.9
$(CH_3)_3CCH^{\bullet}CH_3$	405.0 (410.6)	401.1 (410.9)	404.9 (410.5)	405.6 (410.6)	402.8 (410.0)	399.1 (410.8)	403.0 (409.9)	402.1 (408.0)	412.6 (409.1)	411.0 (408.0)	410.2
$(CH_3)_3CCH_2^{\bullet}$	423.2 (423.5)	418.8 (423.9)	423.7 (423.5)	424.3 (423.5)	418.1 (424.3)	413.4 (425.0)	418.8 (424.2)	418.1 (422.5)	427.7 (422.9)	426.7 (421.6)	419.7 ±4.2
$(CH_3)_2CHCH_2^{\bullet}$	420.5 (421.6)	415.5 (421.5)	420.7 (421.5)	421.4 (421.5)	415.8 (422.1)	410.6 (422.1)	416.2 (421.9)	417.9 (422.3)	425.9 (421.2)	425.8 (420.9)	419.2 ±4.2

not affect the terminal C—H BDE value because the induction effect takes place only over short distances and weakens with each additional bond.

To further analyze theoretical approaches, Pople 6-311++G** *split-valence* basis set was compared with Dunning's augmented versions of correlation-consistent polarized basis sets aug-cc-pVNZ. Within the B3LYP functional, uncorrelated values of aug-cc-pVDZ show the lowest BDEs. As the basis set enlarges, the values approach their limits, resulting in aug-cc-pVQZ values which are in excellent agreement with the experiment (see Tab. 1). Assessing the results within the used basis set types, 6-311++G** values are the best fit with aug-cc-pVTZ values (differences up to < 0.7 $kJ \cdot mol^{-1}$). Regarding the M06-2X functional, BDEs within Dunning's basis sets show similar trends as in B3LYP with slightly lower values. For example, BDEs of the smallest methane are 423.5 $kJ \cdot mol^{-1}$ in aug-cc-pVDZ, 430.4 $kJ \cdot mol^{-1}$ in aug-cc-pVTZ, and 432.2 $kJ \cdot mol^{-1}$ in aug-cc-pVQZ. Again, the M06-2X/6-311++G** values can be compared with the M06-2X/aug-cc-pVTZ ones (differences up to < 1.3 $kJ \cdot mol^{-1}$).

For linear hydrocarbons, the newer composite *ab initio* G4 and G4(MP2) methods exhibit different BDEs trends in comparison to the hybrid functionals. For small alkanes, i.e. methane to pentane, G4 and G4(MP2) provide higher BDE values than B3LYP and M06-2X. Furthermore, these calculated values also exceed the experimental ones ranging from 2.2 to 5.2 $kJ \cdot mol^{-1}$ (G4), and from 3.8 to 6.6 $kJ \cdot mol^{-1}$ (G4(MP2)). The G4 / G4(MP2) BDEs of higher alkanes containing 6 to 11 carbons differ in values. For both approaches, as the number of C atoms increases, BDE values of hexane to undecane decline from 422.6 $kJ \cdot mol^{-1}$ to 415.5 $kJ \cdot mol^{-1}$ for G4 and from 420.6 $kJ \cdot mol^{-1}$ to 408.9 $kJ \cdot mol^{-1}$ for G4(MP2). This decreasing trend has no explanation, as only the influence of the nearest —CH_2— groups is described by the induction effect for linear chains of sp3 carbons (McMurry, 2011). It is shown that G4 and G4(MP2) utilize an additive approach to predict thermodynamical parameters of a system. Therefore, it can be stated that DFT hybrid functionals are more reliable in homolytic cleavage of terminal C—H bonds neighboring with a longer linear hydrocarbon chain.

HAT of C—H bonds in simple branched alkanes

In the following section, theoretical C—H BDEs of the six simplest saturated hydrocarbons (see Fig. 2) was calculated by four different computational approaches (see Tab. 1). At the B3LYP/6-311++G** and M06-2X/6-311++G** levels of theory, the lowest BDE was identified for homolytic cleavage of tertiary C—H bonds in the four presented systems within the range of 386.7 $kJ \cdot mol^{-1}$ to 391.6 $kJ \cdot mol^{-1}$ for B3LYP/6-311++G**, and from 383.0 $kJ \cdot mol^{-1}$ to 387.7 $kJ \cdot mol^{-1}$ for M06-2X/6-311++G**. Differences in calculated and experimental values were up to 12.8 $kJ \cdot mol^{-1}$ (B3LYP/6-311++G**) and 9.6 $kJ \cdot mol^{-1}$ (M06-2X/6-311++G**). Slightly higher values of 405.0 $kJ \cdot mol^{-1}$ (B3LYP/6-311++G**) and 402.8 $kJ \cdot mol^{-1}$ (M06-2X/6-311++G**) were predicted for the cleavage of secondary C—H bond in the $\mathbf{(CH_3)_3CCH_2CH_3}$ molecule. Finally, HAT from primary carbon atoms in $\mathbf{(CH_3)_2CHCH_3}$ and $\mathbf{(CH_3)_3CCH_3}$ molecules is thermodynamically least favorable, which was confirmed by experimental data and all further discussed theoretical approaches.

Hybrid functionals combined with the aug-cc-pVNZ basis sets show similar trends as in the above discussed linear alkanes. BDEs approach their limits as the basis set expands. However, a deviation of the predicted and experimental values is up to ±12.6 $kJ \cdot mol^{-1}$ (B3LYP) and ±8.3 $kJ \cdot mol^{-1}$ (M06-2X) even when the largest aug-cc-pVQZ is applied. Furthermore, despite the lower computational complexity, results obtained by the 6-311++G** basis set can be ranked at the aug-cc-pVTZ and aug-cc-pVQZ levels.

In contrast to the hybrid functionals, the obtained BDE results of composite G4 and G4(MP2) show smaller deviations from the experimental data. For example, the predicted values are 427.7 $kJ \cdot mol^{-1}$ (G4) and 426.7 $kJ \cdot mol^{-1}$ (G4(MP2)) for $\mathbf{(CH_3)_3CCH_3}$ with the largest BDE deviations, which differ from the experiment by ±8.0 and ±7.0 $kJ \cdot mol^{-1}$, respectively. These methods have been proved reliable for the studied homolytic cleavage of branched alkanes. Optimization of systems with negligible additive energy contribution, showed lower error compared to that for linear molecules discussed in the previous section.

Comparison of theoretical and experimental results

A disadvantage of quantum-chemical calculations of thermodynamic quantities is that the results may vary depending on the method or the basis of atomic orbitals. Therefore, it is essential to validate the predictive accuracy of the calculations by comparing the theoretical and experimental values for the studied molecules. Tab. 2 shows the dependence parameters obtained for all theoretical treatments following the linear trend. The obtained determination coefficients R^2 are in the range of 0.953 for the M06-2X/aug-cc-pvdz to 0.973 for the G4(MP2) approach. Linear dependencies of the theoretical approaches were used to correlate the calculated BDE values of hydrocarbons.

The slopes and intercepts in Tab. 2 can be used to correct BDEs calculations based on experiment. These values can be directly compared with

Tab. 2. Linear correlation of experimental C—H BDE values of studied hydrocarbons on the calculated ones at different levels of theory.

Level of theory	Basis set	Slope	Intercept ($kJ \cdot mol^{-1}$)	R^2
B3LYP	6-311++G**	0.708	+123.93	0.960
	aug-cc-pVDZ	0.735	+116.15	0.956
	aug-cc-pVTZ	0.692	+130.48	0.960
	aug-cc-pVQZ	0.691	+130.37	0.961
M06-2X	6-311++G**	0.940	+31.31	0.959
	aug-cc-pVDZ	0.994	+14.13	0.953
	aug-cc-pVTZ	0.905	+45.39	0.962
	aug-cc-pVQZ	0.903	+44.83	0.967
G4		0.913	+32.49	0.972
G4(MP2)		0.868	+51.28	0.973

experimental values. The values are presented in parentheses in Tab. 1. As it can be seen, the correlation of linear B3LYP BDEs provided identical values for all four basis sets, varying by a maximum of 0.4 $kJ \cdot mol^{-1}$ identified for the ethane molecule. A similar trend was observed for the M06-2X functional. Unfortunately, in the most corrected BDEs, the values deviated from the experiment further, e.g. the uncorrected value of B3LYP/aug-cc-pVQZ is 439.0 $kJ \cdot mol^{-1}$ while the corrected is 433.6 $kJ \cdot mol^{-1}$. The experiment states the value of 439.3 ±0.4 $kJ \cdot mol^{-1}$. Correction of G4 and G4(MP2) BDE values also did not contribute to better agreement of the results with the experiment.

On the other hand, correction of BDE values for branched hydrocarbons provided the desired result. The hybrid functionals lessened the drifts of the experimental values to the range of –4.2 $kJ \cdot mol^{-1}$ to +2.3 $kJ \cdot mol^{-1}$. Again, these values varied minimally within the basis sets used. Correction of G4 and G4(MP2) BDE values also contributed to better agreement of the results with the experiment, reducing the highest deviations to up to ±3.2 (G4) and ±3.7 $kJ \cdot mol^{-1}$.

Conclusion

Thermodynamics of the C—H bond cleavage of simple linear and branched alkanes has been theoretically investigated. For the studied set of compounds, BDE values were calculated by DFT/B3LYP and DFT/M06-2X functionals followed by composite G4 and G4(MP2) methods. Within the DFT methods, calculations with four basis sets were performed. A comparison of BDEs showed that the reliability of the computational method depends on the type of the investigated system. For linear alkanes, B3LYP predicted values show the best fit with the experiment. Here, comparison of the results predicted by the different basis sets showed that 6-311++G** is in good agreement with the computationally more complex aug-cc-pVTZ and aug-cc-pVQZ approaches. Next, composite methods predicted BDE values of higher linear alkanes (more than five carbons) with the systematic error resulting from the theory of the method. On the other hand, the best compliance with experimental BDE in branched hydrocarbons was predicted by G4 and G4(MP2). These methods are reliable in the investigation of thermodynamic quantities of systems with no long chain of atoms and therefore the additive energy contribution included in the calculation process of the method is negligible. Finally, the predicted values were compared with available experimental data. The obtained linear dependences were used as scaling functions of the calculated BDEs for homolytic cleavage of C—H bonds. Here, correction of BDE values for linear alkanes caused them to underrun the experiment. However, correction of all results for branched alkanes caused a significant adjustment to the experimental data.

Acknowledgement

The work has been supported by the Ministry of Education, Science, Research and Sport of the Slovak Republic (No. VEGA 1/0172/25) and by the Slovak Research and Development Agency (No. APVV-23-0195, APVV-20-0213, APVV-19-0024). We are grateful to the HPC center at the Slovak University of Technology in Bratislava, which is a part of the Slovak Infrastructure of High-Performance Computing (SIVVP project, ITMS code 26230120002, funded by the European region development funds, ERDF) for the computational time and resources made available.

References

Balakrishnan A, Smith V, Stoicheff BP (1992) Phys. Rev. Lett. 68(14): 2149—2152.

Barckholtz C, Barckholtz TA, Hadad CM (1999) J. Am. Chem. Soc. 121(3): 491—500.

Becke AD (1988) Phys. Rev. A 38(6): 3098—3100.

Berkowitz J, Ellison GB, Gutman D (1994) J. Phys. Chem. 98(11): 2744—2765.

Blanksby SJ, Ellison GB (2003) Acc. Chem. Res. 36(4): 255—263.

Bordwell FG, Zhang XM, Satish AV, Cheng JP (1994) J. Am. Chem. Soc. 116(15): 6605—6610.

Curtiss LA, Jones C, Trucks GW, Raghavachari K, Pople JA (1990) J. Chem. Phys. 93(4): 2537—2545.

Curtiss LA, Raghavachari K, Trucks GW, Pople JA (1991) J. Chem. Phys. 94(11): 7221—7230.

Curtiss LA, Raghavachari K, Redfern PC, Rassolov V, Pople JA (1998) J. Chem. Phys. 109(18): 7764—7776.

Curtiss LA, Redfern PC, Raghavachari K (2007) J. Chem. Phys. 126(8): 084108—084112.

De Darwent BB (1970) Bond dissociation energies in simple molecules, NBS Publication.

Dunning TH (1989) J. Chem. Phys. 90(2): 1007—1023.

Ervin KM, DeTuri VF (2002) J. Phys. Chem. A 106(42): 9947—9956.

Denisov ET, Tumanov VE (2005) Russ. Chem. Rev. 74(9): 825.

Frisch MJ, Trucks GW, Schlegel HB, Scuseria GE, Robb MA, Cheeseman JR, Scalmani G, Barone V, Petersson GA, Nakatsuji H, Li X, Caricato M, Marenich AV, Bloino J, Janesko BG, Gomperts R, Mennucci B, Hratchian HP, Ortiz JV, Izmaylov AF, Sonnenberg JL, Williams-Young D, Ding F, Lipparini F, Egidi F, Goings J, Peng B, Petrone A, Henderson T, Ranasinghe D, Zakrzewski VG, Gao J, Rega N, Zheng G, Liang W, Hada M, Ehara M, Toyota K, Fukuda R, Hasegawa J, Ishida M, Nakajima T, Honda Y, Kitao O, Nakai H, Vreven T, Throssell K, Montgomery JA Jr., Peralta JE, Ogliaro F, Bearpark MJ, Heyd JJ, Brothers EN, Kudin KN, Staroverov VN, Keith TA, Kobayashi R, Normand J, Raghavachari K, Rendell AP, Burant JC, Iyengar SS, Tomasi J, Cossi M, Millam JM, Klene M, Adamo C, Cammi R, Ochterski JW, Martin RL, Morokuma K, Farkas O, Foresman JB, Fox DJ (2016) Gaussian 16, Revision B.01, Gaussian, Inc., Wallingford CT.

Hanwell MD, Curtis DE, Lonie DC, Vandermeersch T, Zurek E, Hutchison GR (2012) J. Cheminf. 4: 1—17.

Hariharan PC, Pople JA (1973) Theor. Chim. Acta 28: 213—222.

Klein E, Lukeš V, Cibulková Z, Polovková J (2006) J. Mol. Struct. THEOCHEM 758(2—3): 149—159.

Kováčová A (2024) Acta Chimica Slovaca 17(1): 12—21.

Lee C, Yang W, Parr RG (1988) Phys. Rev. B 37(2): 785—789.

Luo YR (2007) Comprehensive Handbook of Chemical Bond Energies, CRC Press, Boca Raton, New York.

McMurry JE (2011) Organic Chemistry, 8th Edition, Brooks Cole, Pacific Grove CA.

Mulder P, Korth HG, Pratt DA, DiLabio GA, Valgimigli L, Pedulli GF, Ingold KU (2005) J. Phys. Chem. A, 109(11): 2647—2655.

Pople JA, Headgordon M, Fox DJ, Raghavachari K, Curtiss LA (1989) J. Chem. Phys. 90(10): 5622—5629.

Raghavachari K, Trucks G, Pople J, Head-Gordon M (1989) Chem Phys. Lett. 157(6): 479—483.

Rassolov VA, Pople JA, Ratner MA, Windus TL (1998) J. Chem. Phys. 109(4): 1223—1229.

Rayne S, Forest K (2011) PEP 36(5): 410—415.

Rimarčík J, Lukeš V, Klein E, Ilcin M (2010) J. Mol. Struct. 952: 25—30.

Rimarčík J, Lukeš V, Klein E, Rottmannová L (2011) Comput. Theor. Chem. 967(2—3): 273—283.

Trotman-Dickenson AF (1965) Chem. Ind., London 379.

Zhao Y, Truhlar DG (2008) Theor. Chem. Acc. 120: 215—241.

sciendo

Comparison of parametric methods with quantum mechanics based models to estimate Clog *P* values

Dávid Zajaček, Andrej Hlinčík, Lukas Bucinsky, Matej Uhliar

Faculty of Chemical and Food Technology, Slovak University of Technology in Bratislava, Radlinského 9, SK-812 37 Bratislava, Slovakia
david.zajacek@stuba.sk

Abstract: The logarithm of octanol-water partition coefficient (log *P*) is estimated by means of six parametric methods (iLOGP, XLOGP3, WLOGP, MLOGP, SILICOS-IT, OBLogP) and six quantum mechanics (QM) based models. QM models comprise DFT functional choice (B3LYP, M06-X, PBE0, including the xTB parametrization variant), implicit solvent model choice (IEFPCM, SMD, or ALPB), and basis set quality in DFT calculations (6-31G* and 6-311++G**). Several statistics are evaluated to compare Clog *P* estimates to experimentally measured dataset of 36 molecules picked from Meylan and Howard *J. Pharm. Sci.* 84 (1995) 83–92. ChemmineR cluster analysis has been performed to confirm structural diversity of molecules in the employed molecular dataset. XLOGP3 performance is the best among all the methods used, while SMD based DFT models showed a clearly competitive results with the remaining parametric methods irrespective of DFT functional or basis set quality.

Keywords: log *P*, parametric methods, XLOGP3, density functional theory, implicit solvent model, SMD

Introduction

The logarithm of octanol-water partition coefficient (log *P*), also known as the partition coefficient between water and n-octanol phases, is one of the key physicochemical properties accounted for in the process of drug discovery (Arnott and Planey, 2012). The log P coefficient describes the hydrophilic/lipophilic character of a molecule, and is expressed as follows:

$$\log P = \log_{10}\left(\frac{[c]_o}{[c]_w}\right) \tag{1}$$

where $[c]_o$ is equilibrium concentration in n-octanol phase and $[c]_w$ is equilibrium concentration in water phase.

Partition coefficient (log *P*) is an inherent part of pharmacokinetic ADME (absorption, distribution, metabolism, elimination) properties, as well as toxicity (Giaginis et al., 2018), which are crucial for determining correct drug behavior. The study of Hay et al. (Hay et al., 2014) shows the importance of the evaluation of ADME properties in early stage of the drug discovery process to significantly reduce molecules with failures related to inappropriate pharmacokinetic properties during clinical phases. The drug must have suitable water solubility and sufficiently lipophilic character, which is linked to the transport of the drug to and across biological membranes. An optimal log *P* value for a drug is determined by its site of action and method of ingestion.

Several very well-known empirical rules for potential drug candidates have been proposed, including log *P* as their inherent property (Lipinski (Lipinski et al., 2001), Ghose (Ghose et al., 1999), Egan (Egan et al., 2000), Muegge (Muegge et al., 2001)). Lipinski, in 1997, postulated the *rule of five* for orally active drugs, according to which a drug should have a log *P* value of less than 5 (Lipinski et al., 2001). On the other hand, Ghose rules define the acceptable boundary of log *P* between values –0.4 and 5.6 (Ghose et al., 1999). To investigate, whether the potential drug candidate can undergo gastrointestinal absorption or access the brain, the BOILED-Egg model (Daina and Zoete, 2016) was devised. This model was evaluated in respect to correlation between topological polar surface area (TPSA) and log *P* (WLOGP (Wildman and Crippen, 1999)).

Experimental log *P* values are mainly determined using the shake-flask method, i.e. via a separating funnel with water and n-octanol phases (OECD 107 Method, 1995; US EPA, 1996). Also, potentiometric (Avdeef, 1992, 1993) or chromatographic (Donovan and Pescatore, 2002; Kaliszan et al., 2002) methods have been implemented. Unfortunately, these most accurate techniques are inappropriate in terms of time requirements, especially when high throughput screening of millions of molecules is to be performed (Hertzberg and Pope, 2000). Therefore, many *in silico* techniques for log *P* prediction have been devised, with log *P* value that is not experimentally measured but rather determined using computer-aided methods, denoted as Clog *P* (calculated log *P*).

The first group consists of parametric methods working with an assumption that log *P* of a mole-

cule is defined as a summation of increments of individual atoms/fragments forming the molecule, i.e. additive parametric methods. These methods may also include correction factors obtained from regression models. Splitting the molecule to fragments is performed using descriptor-based molecular fragmentation (Jinsong et al., 2024). An atomic based method is used for example in SLOGP (Wildman and Crippen, 1999) or WLOGP (Wildman and Crippen, 1999) approaches, while the fragmental based method is used in KLOGP (Klopman et al., 1994) approach or in studies of Meylan and Howard (Meylan and Howard, 1995, 2000). XLOGP3 (Cheng et al., 2007) approach is an extension of XLOGP (Wang et al., 1997), which is a purely atomic based. XLOGP3 additionally includes a knowledge-based library approach. In this approach, a molecule is compared against a library of known log *P* values (reference molecules), used as a starting point for the XLOGP3 evaluation using the difference between the examined molecule and the reference molecules computed by an additive method (Cheng et al., 2007).

The second group consists of parametric methods based on topology, as exemplified by MLOGP (Moriguchi et al., 1992, 1994). Here, large molecular libraries serve as training sets for multiple regression models, from which mathematical equations for Clog *P* estimation are obtained. These methods highly rely on correctness of log *P* values of molecules present in the input training sets. Occurrence of atoms, fragments, or structural similarities within the molecular libraries is essential. SILICOS-IT (Langenaeker et al., 2010) represents a hybrid approach, which is a combination of fragmental based and topological parametric methods.

The third group of methods is based on physical principles. The log *P* value can be understood as a chemical equilibrium with respect to thermodynamics and is thus directly related to Gibbs free energy of water to n-octanol transfer ($\Delta G_{o/w}$):

$$\mathrm{Clog}\,P = -\frac{\Delta G_{o/w}}{RT\ln(10)} = -\frac{\Delta G_o - \Delta G_w}{RT\ln(10)} \qquad (2)$$

Although the Gibbs energy of transfer ($\Delta G_{o/w}$) can be computed by MC/MD simulations (Jorgensen, 1989; Jorgensen et al., 1990), this approach is very time-consuming. On the other hand, solvation Gibbs free energy in n-octanol (ΔG_o,) and water (ΔG_w) can be obtained relatively easily by quantum mechanics approaches using implicit solvent model. Combining quantum mechanics and Clog *P* estimation is reasonable because log *P* itself is determined by the chemical structure of the molecule, i.e. its electronic structure. This approach was chosen in publications of Michalík and Lukeš (Michalík and Lukeš, 2016) and Nedyalkova et al. (Nedyalkova et al., 2019), where the DFT computational protocol performance was studied showing high correlation in comparison to experimental results. The dataset of Michalík and Lukeš (Michalík and Lukeš, 2016) was comprised of 27 alcohols, while Nedyalkova et al. (Nedyalkova et al., 2019) studied mainly alkanes, alkenes, alcohols, carboxylic acids, and ethers (55 molecules). On the contrary, iLOGP (Daina et al., 2014), as a physics-based parametric model, uses equation (2) indirectly. The evaluation of solvation Gibbs free energies, using Generalized-Born and solvent accessible surface area (GB/SA), serves as parametrization in the three-parameter regression analysis (Daina et al., 2014).

The aforementioned methods as well as methods, which were not discussed, are nicely summarized in the publication by Carrupt et al. (Carrupt et al., 1997). Although various methods for Clog *P* estimation are used, the study of Mannhold et al. (Mannhold et al., 2009) shows that the application of different approaches (with a high extent of diversity) to compute consensus Clog *P* (arithmetic mean) is beneficial when large datasets are studied. Presented work is focused on three main aspects, namely which QM model is able to compete with the accuracy of parametric methods (iLOGP (Daina et al., 2014), XLOGP3 (Cheng et al., 2007), WLOGP (Wildman and Crippen, 1999), MLOGP (Moriguchi et al., 1992, 1994), SILICOS-IT (Langenaeker et al., 2010) and OBLogP (O'Boyle et al., 2011)), dependence of DFT methods' accuracy on the choice of functional/variant, solvent model, and basis set, and finally structural diversity of the employed molecular dataset in the evaluation of Clog *P* and/or their relationship to Clog *P* estimation using cluster analysis.

Computational details

Experimental log *P* values of 36 studied molecules were retrieved from (Meylan and Howard, 1995), and are provided in Table A1. Subsequently, xyz files containing the initial 3D geometries were either drawn with ArgusLab 4.0.1 (Thompson, 2004) or the more complex molecular structures were downloaded from the PubChem database (Kim et al., 2019, 2021) in the sdf format and converted to the xyz format using OpenBabel 2.3.2 (O'Boyle et al., 2011).

Geometry optimization and vibrational analysis of studied molecules were computed by the Gaussian16 program package (Frisch et al., 2016). Calculations of DFT level of theory were performed using three functionals: B3LYP (Becke, 1988, 1993; Lee et al., 1988; Vosko et al., 1980), PBE0 (Adamo and Barone,

1999; Perdew et al., 1996, 1997), and M06-2X (Zhao and Truhlar, 2008). The following basis sets were selected for the presented DFT calculations: 6-31G* (Petersson et al., 1988; Petersson and Al-Laham, 1991; Rassolov et al., 1998, 2001), and 6-311++G** (Clark et al., 1983; Krishnan et al., 1980; McLean and Chandler, 1980). Implicit solvation effects were treated using self-consistent reaction field (SCRF) considering solvation model based on density (SMD) (Marenich et al., 2009) and integral equation formalism variant of polarizable continuum model (IEFPCM) (Miertuš et al., 1981; Miertuš and Tomasi, 1982; Pascual-ahuir et al., 1994). Five combinations of functional, basis set, and solvation models were chosen for the DFT based Clog *P* estimation (Table 1). In addition, as an alternative quantum mechanics method of Clog *P* estimation, the GFN2-xTB method as implemented in the program xTB was used (Bannwarth et al., 2020). GFN2-xTB parametrization (Bannwarth et al., 2019) was applied with strong convergence level threshold for geometry optimization and with the analytical linearized Poisson-Boltzmann model (ALPB) (Ehlert et al., 2021) to include implicit solvent effects. All QM models are summarized in Table 1.

To preserve the integrity of results, each QM model prediction of Clog *P* started from the same initial geometry (for each implicit solvent, water or n-octanol). All vibrational analysis calculations were imaginary frequencies free to ensure that energy minima (local or global) on the potential energy surface of the studied molecules were found. After successful optimization and vibration analysis for water and n-octanol, values of solvation Gibbs free energy were obtained at 298.15 K.

To obtain Clog *P* based on parametric methods, the xyz files were converted to SMILES codes using OpenBabel 2.3.2 (O'Boyle et al., 2011). Five Clog *P* parametric methods, namely iLOGP (Daina et al., 2014), XLOGP3 (Cheng et al., 2007), WLOGP (Wildman and Crippen, 1999), MLOGP (Moriguchi et al., 1992, 1994), and SILICOS-IT (Langenaeker et al., 2010) were evaluated according to the SwissADME website (Daina et al., 2017). Lastly, the OBLogP (O'Boyle et al., 2011) (OpenBabel log *P*) method was estimated using ChemmineR library (Cao et al., 2008) in R. In order to study relationships between the structural similarities of studied molecules and their Clog *P* values, cluster analysis was performed in ChemmineR library (Cao et al., 2008) with c = 0.32 cutoff. The sdf file format was created from SMILES codes (smiles2sdf), which was first transformed into an ap (atomic pair) set (sdf2ap) and then into a generated database of descriptors (apset2descdb), which served as an input for the cluster analysis. Structural formulae of molecules in the dataset as presented in the appendix were depicted using the MarvinSketch (Chemaxon, 2020), see Table A2.

To compare the individual Clog *P* methods with experimental log *P* values, various statistical parameters were evaluated. First of all, linear regression with fixed intercept ($a = 0$) was computed, from which slope b and regression correlation coefficient R were obtained. Then, three common parameters for two datasets comparison were estimated, namely mean absolute error (MAE), mean square error (MSE), and root mean square error (RMSE). Absolute deviations between predicted and experimental values were further evaluated in terms of their median value ($\mathrm{med}(\Delta_{abs})$), and maximum value ($\max(\Delta_{abs})$). In addition, the number of values under the cutoff of 0.5 for the deviation from the experiment ($\#\Delta_{abs} < 0.5$) was monitored.

Results

Parametric methods

Despite the limited size of our dataset of molecules, the XLOGP3 method provided the best results outperforming other methods in all statistical parameters. Only in one single case, the XLOGP3 method provided an absolute deviation from experiment, cutoff of over 0.5. At the same time, only three cases were found where the XLOGP3 Clog *P* deviation from experiment was larger than 0.2.

In other words, there were 29 molecules whose XLOGP3 Clog *P* was determined to an accuracy of two decimal places (Table A3). The success of the method was further emphasized by correla-

Tab. 1. Summary of QM models for Clog *P* estimation.

model	functional/variant	basis set	solv. model
DFT A	B3LYP	6-311++G**	SMD
DFT B	B3LYP	6-31G*	SMD
DFT C	B3LYP	6-311++G**	IEFPCM
DFT D	M06-2X	6-311++G**	SMD
DFT E	PBE0	6-311++G**	SMD
xTB	GFN2-xTB	–	ALPB

tion coefficient R with the value of 0.9978, by a zero med(Δ_{abs}) value, and by very low values of MAE, MSE, and RMSE (Table 2, and Figure 1a). The second top-ranking method (in total as well as among the parametric methods) for our molecular dataset is WLOGP, with fifteen molecules under the 0.5 cutoff of absolute deviation from experimental values (#Δ_{abs} < 0.5). Apart from XLOGP3, it is the only method with MAE, MSE, and RMSE parameters below one. WLOGP also recorded the second lowest max(Δ_{abs}) and second lowest med(Δ_{abs}) (Table 2). MLOGP and SILICOS-IT seem to perform equally well, and it is hard to decide which method outperforms the other. MLOGP provided better results in terms of MAE, MSE, and RMSE, but linear regression parameters (b, R) better described the fit for SILICOS-IT. Maximum of absolute deviations from experiment, max(Δ_{abs}), is also better for SILICOS-IT, as well as med(Δ_{abs}), and #Δ_{abs} < 0.5 (Table 2).

The obtained statistical parameters for the OBLogP method are the second worst. This method recorded the second highest values of MAE, MSE, and RMSE, however, linear regression parameters

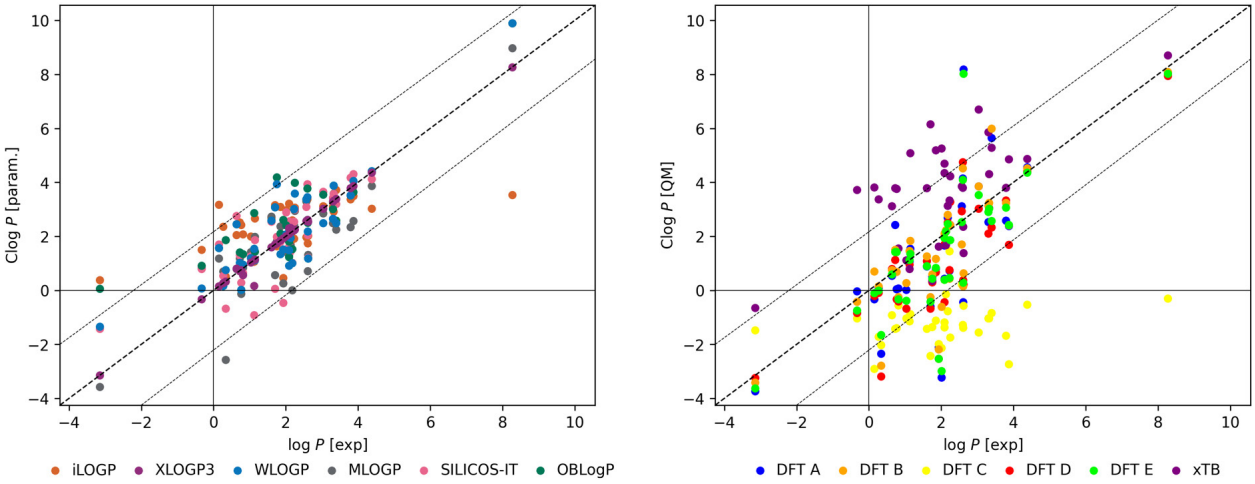

Fig. 1. Clog P vs. experimental log P (a) parametric methods, and (b) QM models.

Tab. 2. Clog P estimation statistics of parametric methods against experimental log P (see Figure 1a).

parameter	iLOGP	XLOGP3	WLOGP	MLOGP	SILICOS-IT	OBLogP
b	0.8117	0.9977	1.0322	0.8950	1.0258	1.0756
R	0.8364	0.9978	0.9459	0.9230	0.9342	0.9301
MAE	1.1056	0.0517	0.7458	0.8011	0.8272	0.8883
MSE	2.2145	0.0299	0.8781	1.0450	1.0720	1.2942
RMSE	1.4881	0.1730	0.9371	1.0222	1.0354	1.1376
med(Δ_{abs})	0.9150	0.0000	0.5800	0.7050	0.6050	0.7150
max(Δ_{abs})	4.74	0.95	2.18	2.90	2.39	3.21
#Δ_{abs} < 0.5	13	35	15	14	15	12

Tab. 3. Clog P estimation statistics of QM models against experimental log P (see Figure 1b).

parameter	DFT A	DFT B	DFT C	DFT D	DFT E	xTB
b	0.8965	0.8691	–0.2953	0.7226	0.8492	1.3272
R	0.7901	0.8558	0.5387	0.7313	0.7985	0.8430
MAE	1.2708	1.0117	3.2708	1.2625	1.1167	1.9736
MSE	3.4377	2.0389	13.1481	3.6929	3.0081	5.7322
RMSE	1.8541	1.4279	3.6260	1.9217	1.7344	2.3942
med(Δ_{abs})	0.7500	0.6900	3.0750	0.7700	0.6800	1.9350
max(Δ_{abs})	5.57	4.11	8.57	7.21	5.41	4.76
#Δ_{abs} < 0.5	12	14	0	16	16	8

fit very well with the experiment. OBLogP also provided the second highest max(Δ_{abs}) and med(Δ_{abs}) values, and the worst #Δ_{abs} < 0.5 value of hits among all parametric methods (Table 2). The last evaluated parametric method, namely iLOGP, is the only parametric method not reaching MAE below one, while providing the worst results in respect to linear regression parameters, MSE, and RMSE parameters, as well as for max(Δ_{abs}), and med(Δ_{abs}).

QM models

Despite QM models cannot fully compete with parametric methods in terms of accuracy of experimental log *P* values estimation, their results are relevant (see Figure 1b, and compare Table 3 and Table 2). Clog *P* values of the DFT B, and DFT E QM models correlate the best with experimental log *P* values. In terms of MAE, MSE, RMSE, and linear regression fit, the most precise results were obtained for the DFT B model, while the DFT E model is more precise with respect to max(Δ_{abs}), med(Δ_{abs}), and #Δ_{abs} < 0.5. The DFT B model recorded the highest coefficient of correlation *R* with the value of 0.8558. Considering the relatively low values of med(Δ_{abs}), i.e. 0.6900 for DFT B, and 0.6800 for DFT E, estimation of molecules with high extend of inaccuracy can be concluded to increase MAE, MSE, and RMSE parameters for these models. Excluding three worst Clog *P* estimations (molecules with the highest absolute deviation from experiment), reached by these models, led to a decrease of RMSE from 1.4279 to 1.0997 for DFT B, and from 1.7344 to 1.0170 for DFT E. In terms of the RMSE parameter, DFT E is the third top-ranked, while DFT B is the fifth top-ranked among all evaluated methods when narrowed datasets for these QM models are considered. Another parameter to compare Clog *P* QM models and parametric methods estimations is the #Δ_{abs} < 0.5 value. Models DFT D, and DFT E outperformed the parametric methods (except for XLOGP3) by considering this parameter, both with sixteen molecules recorded below the 0.5 cutoff. In addition, DFT B model outperformed two parametric methods (iLOGP, OBLogP), and performed equally well with one (MLOGP) with fourteen molecules accounted for. Comparison of DFT A and DFT B models indicates that the use of a smaller basis set, i.e. 6-31G* one, does not lead to deterioration of results, but DFT B performed better in almost all evaluated statistical parameters. The comparison of Clog *P* estimation statistics for the used functionals, i.e. comparison of DFT A, DFT D, and DFT E models [models with the same basis set (6-311++G**) and the same solvation model (SMD)] provided the best PBE0 functional (DFT E). On the other hand, functionals B3LYP (DFT A), and M06-2X (DFT D) performed approximately equally well. Overall, the worst results of Clog *P* estimation were recorded for DFT C, and xTB models. DFT C, as the only model with IEFPCM solvation model used, demonstrated that SMD solvation model leads to considerably better accuracy of experimental log *P* values prediction. The obtained values for DFT C model illustrate that this model predominantly overestimates the Gibbs free energies in water relative to n-octanol (values are lower than experiment, see Figure 1b). On the contrary, values obtained for the xTB model showed predominantly overestimation of Gibbs free energies in n-octanol relative to water (values are higher than experimental ones, see Figure 1b), and this model also showed bad correlation with experimental log *P* (e.g., slope *b* and #Δ_{abs} < 0.5 value).

Comparison of QM models and parametric methods

Column bars in Figure 3 show the success rate of quantum mechanics log *P* estimation, which is closer to the experiment than parametric methods. Each bar in Figure 3 can be maximum 216 in high (minimum is zero), since for each molecule of a given QM model estimation (DFT A, DFT B, DFT C, DFT D, DFT E, and xTB) a comparison was made to all estimations by the employed parametric methods (iLOGP, XLOGP3, WLOGP, MLOGP, SILICOS-IT, OBLogP) in terms of their absolute deviations from experiment. The success rate for each molecule of each quantum mechanics estimation is determined by the color saturation of the region. When a QM model outperforms all six parametric methods for a given molecule, the region is emphasized by striped lines. QM models outperformed by all parametric methods for a given molecule are not present in the corresponding bar in Figure 3. In this performance comparison study, the best results were provided by the DFT E model, in which 94 [43.5 %] cases occurred with this QM model yielding more accurate predictions than the other parametric methods studied. A total of four molecules were found where the DFT E model performed better than all other parametric methods, with three molecules, namely (Z)-4-(azoxycyano) quinoline 1-oxide, 2,8-bis(methylthio)-6-chloropurine, and 2,6-di((S)-*sec*-butyl)phenol, with this model as the best of all methods (QM model and parametric methods combined). The second best QM model in this comparison is DFT B with a success rate of 87 [40.3 %] cases. Better results for this method than for all the other six parametric methods was observed for three molecules. The DFT B model provided best results for one molecule (cocaine) among all twelve methods. Success rates

for DFT D and DFT A models were 84 [38.9 %] cases, and 82 [38.0 %] cases, respectively, with two molecules where the DFT D model outperformed all six parametric methods, while three such molecules were found for the DFT A model. These models did not provide the best overall results for any molecule; however, one molecule (spiroperidol) was calculated with a shared best overall result with DFT D. At the same time, spiroperidol was the only molecule where a QM model (DFT D) predicted the Clog *P* value with a precision to two decimal places (Table A4). The worst results in this comparison study were obtained by the DFT C and xTB methods with success rates in 13 [6.0 %] and 47 [21.8 %] cases, respectively, with no molecules where these methods can compete with all six parametric methods at once. As mentioned above, the XLOGP3 parametric method predicted the Clog *P* value with an accuracy to two decimal places for 29 molecules, which makes it very difficult for QM models to outperform this method. By excluding the XLOGP3 method from this comparison study, an increase of success rate for the DFT E model from 43.5 % to 49.4 %, and for the DFT B model from 40.3 % to 46.1 %, was observed. Bar presentation in Figure 3 includes cases where the absolute deviation from experimental values were high.

Clustering study

The dataset of studied molecules was clustered based on their chemical similarities into five groups. The largest cluster group (7 molecules), named cluster A, consists of molecules whose structure contains four fused rings (three cyclohexanes and one cyclopentane). Two molecules (hydrocortisone 17-valerate, testosterone) have one cyclohexene instead of cyclohexane, while one molecule includes cyclohexa-1,4-diene structure (betamethasone 21-valerate). Cluster B (3 molecules) is formed by two opioids and morphine analogues, namely codeine and naloxone. These molecules contain four fused rings, benzene ring being one of them, and one bridge bicyclic structural element. The third molecule of cluster B, 2-methoxystrychnine, includes one bridge bicyclic structure which is complemented by six fused rings. In cluster C, two molecules with almost identical structure are present. One of them is xanthene-9-carboxylic acid and the second one is thioxanthene-9-carboxylic acid, which contains sulfur instead of an oxygen atom. Both molecules include three fused rings. Cluster D comprises two molecules with 1-(4-fluorophenyl)-4-(piperidin-1-yl)butan-1-one structure. Azaperone includes piperazine instead of piperidine, which is attached to pyridine. On the other hand, spiroperidol includes two spiro rings and a benzene ring. Twenty-two non-clustered molecules were put into cluster E, which shows the high diversity (for clustering with low cutoff value) of the employed studied molecular dataset (Table A1). The high diversity ensures that the considered assessment of the accuracy of Clog *P* estimation is performed for different molecular structures and functional groups.

DFT B and DFT E, which provided the best results in QM model statistics evaluation (Table 3 and Figure 1b), were further analyzed in respect to structural similarities (clustering) performance of Clog *P* estimation (Figure 4). No cluster, except for cluster E, which comprises non-clustered molecules, contains

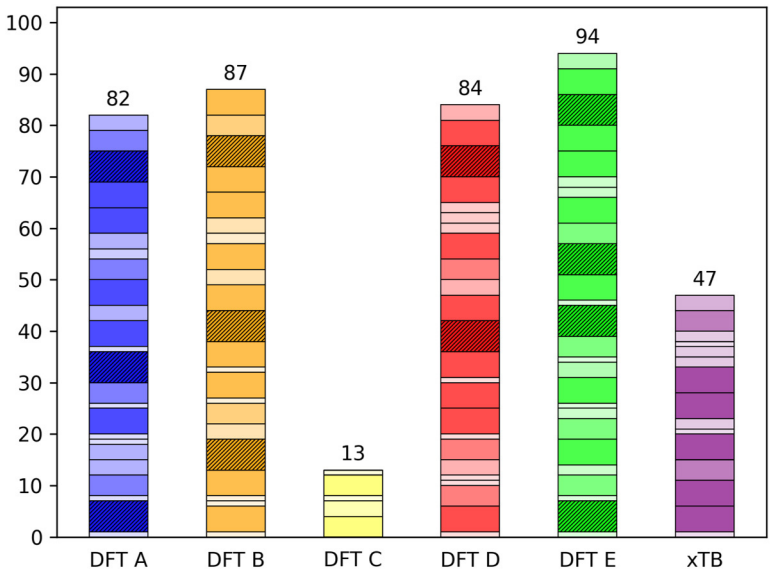

Fig. 3. Performance comparison of counts where QM model provides better prediction of experimental log *P* than parametric methods for all molecules.

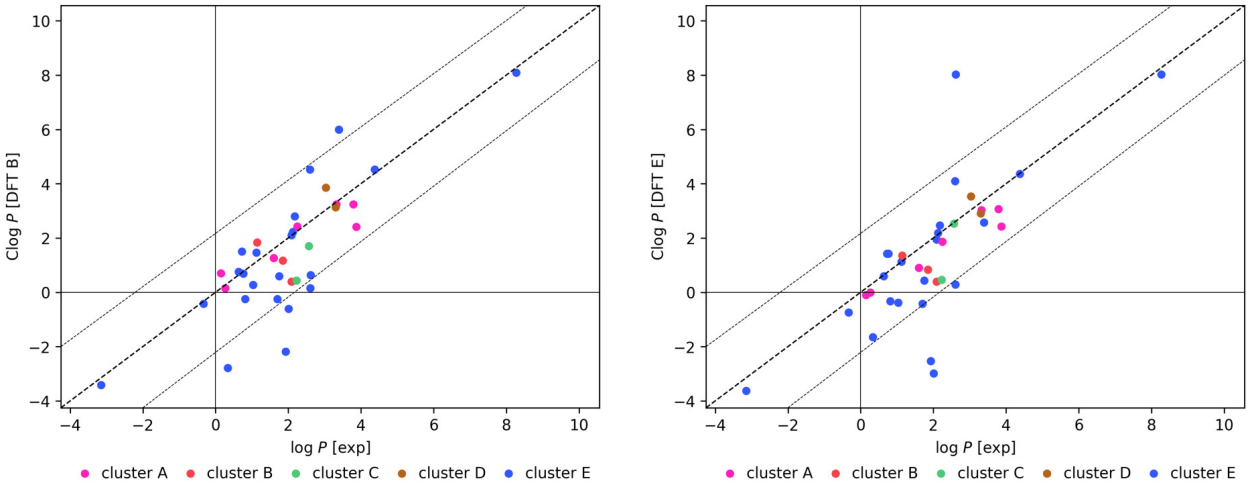

Fig. 4. Clog *P* vs. experimental log *P* from QM models (a) DFT B and (b) DFT E.

molecules with absolute deviation from experiment higher than 2 for both models (Figure 4). RMSE result of the seven molecules of cluster A (Table A5) shows that the DFT B (0.6431) model provided the second best results, while DFT E (0.7046) provided the third best results among all models and methods studied, which means that structures with fused rings are very well described by these QM models. For cluster B, i.e. for molecules containing fused rings and one bridging bicycle element, DFT B, and DFT E models outperformed only the iLOGP method, while no parametric method was outperformed by a QM model in cluster C. For cluster D, the DFT B model showed better statistics than one parametric method (WLOGP) in terms of RMSE, while DFT E model was better than three parametric methods (WLOGP, MLOGP, SILICOS-IT). Considering RMSE distribution across all clusters, structural similarities affect *in silico* Clog *P* determination (Table A5). Prediction for cluster E, i.e. cluster with high structural diversity, was the worst by ten out of all twelve studied methods, except for DFT C and xTB, whose performance across the dataset was not credible.

Conclusions

The comparison of parametric methods and QM methods of experimental log *P* estimation favors the XLOGP3 parametric method as the best performing in all statistical parameters. It is also fair to stress that the remaining parametric methods are in acceptable agreement with experiment. QM methods based on the SMD implicit solvation model, albeit yielding slightly worse statistics, remain competitive to these parametric methods. It is further shown that the IEFPCM model is not well suited for Clog *P* estimation with a significant overestimation of the Gibbs free energy in water relative to n-octanol. On the opposite, the xTB parametrization variant with ALPB solvation model leads to the second least satisfactory performance and tends to overestimate the Gibbs free energy in n-octanol relative to water. Cluster analysis showed that the molecular dataset used is diverse, 22 out of 36 molecules were not clustered at all (single clusters were merged into cluster E), even at the chosen low 0.32 similarity cutoff. The prediction of Clog *P* for A-D clusters led to lower RMSE compared to cluster E for all methods/models, except for DFT C (IEFPCM implicit solvent) and xTB, whose performance across the dataset was not credible.

The main goal of the study was to prove that QM models can predict log *P* with accuracy comparable to parametric methods, which was confirmed especially for DFT B (B3LYP, 6-31G*, SMD) and DFT E (PBE0, 6-311++G**, SMD) models and can be advantageous in the search for Clog *P* in future. When studying large molecular dataset, a beneficial way to estimate Clog P is to average different approaches with a high extend of diversity to compute consensus Clog *P* (Mannhold et al., 2009) with QM methods as a part of the consensus manifold.

Drug candidates based on transition metal complexes with organic ligands are increasingly found in pharmaceutical applications. There are several works, where such compounds were studied as potential therapeutic agents for their anticancer effects (Bertrand and Casini, 2014; Kastl et al., 2012), SARS-CoV-2 main protease inhibition (Karges et al., 2023), or interactions with DNA biomacromolecules (Pages et al., 2015). This raises the question to what extent parametric methods can correctly predict the Clog *P* value of such compounds. Thus, QM models can find a direct application in estima-

tion of Clog *P* of potential drug candidates with a transitional metal.

Acknowledgment
This work was supported by the Slovak Research and Development Agency under the contract nos. APVV-20-0213, APVV-23-0195, and by the Slovak Grant Agency VEGA under contract nos. 1/0175/23 and 1/0172/25. DZ would like to thank Grant STU for the support of young scientists code: 1331 MVP-2025 CEDIZLIE (young scientist STU FCHPT – Zajaček).

References

Adamo C, Barone V (1999) The Journal of Chemical Physics 110: 6158—6170.
Arnott JA, Planey SL (2012) Expert Opinion on Drug Discovery 7: 863—875.
Avdeef A (1992) Quantitative Structure-Activity Relationships 11: 510—517.
Avdeef A (1993) Journal of Pharmaceutical Sciences 82: 183—190.
Bannwarth C, Caldeweyher E, Ehlert S, Hansen A, Pracht P, Seibert J, Spicher S, Grimme S (2020) WIREs Computational Molecular Science 11: e1493.
Bannwarth C, Ehlert S, Grimme S (2019) Journal of Chemical Theory and Computation 15: 1652—1671.
Becke AD (1988) Physical Review A 38: 3098—3100.
Becke AD (1993) The Journal of Chemical Physics 98: 5648—5652.
Bertrand B, Casini A (2014) Dalton Transactions 43: 4209—4219.
Cao Y, Charisi A, Cheng L-C, Jiang T, Girke T (2008) Bioinformatics 24: 1733—1734.
Carrupt P, Testa B, Gaillard P (1997) Computational Approaches to Lipophilicity: Methods and Applications. In Reviews in Computational Chemistry, Volume 11, pp. 241—315.
Cheng T, Zhao Y, Li X, Lin F, Xu Y, Zhang X, Li Y, Wang R, Lai L (2007) Journal of Chemical Information and Modeling 47: 2140—2148.
Clark T, Chandrasekhar J, Spitznagel GW, Von P, Schleyer R (1983) Journal of Computational Chemistry 3: 294—301.
Daina A, Michielin O, Zoete V (2014) Journal of Chemical Information and Modeling 54: 3284—3301.
Daina A, Michielin O, Zoete V (2017) Scientific Reports 7: 42717.
Daina A, Zoete V (2016) ChemMedChem 11: 1117—1121.
Donovan SF, Pescatore MC (2002) Journal of Chromatography A 952: 47—61.
Egan WJ, Merz KM, Baldwin JJ (2000) Journal of Medicinal Chemistry 43: 3867—3877.
Ehlert S, Stahn M, Spicher S, Grimme S (2021) Journal of Chemical Theory and Computation 17: 4250—4261.
Frisch MJ, Trucks GW, Schlegel HB, Scuseria GE, Robb MA, Cheeseman JR, Scalmani G, Barone V, Petersson GA, Nakatsuji H, Li X, Caricato M, Marenich AV, Bloino J, Janesko BG, Gomperts R, Mennucci B, Hratchian HP, Ortiz JV, Izmaylov AF, Sonnenberg JL, Williams-Young D, Ding F, Lipparini F, Egidi F, Goings J, Peng B, Petrone A, Henderson T, Ranasinghe D, Zakrzewski VG, Gao J, Rega N, Zheng G, Liang W, Hada M, Ehara M, Toyota K, Fukuda R, Hasegawa J, Ishida M, Nakajima T, Honda Y, Kitao O, Nakai H, Vreven T, Throssell K, Montgomery JA, Jr. Peralta JE, Ogliaro F, Bearpark MJ, Heyd JJ, Brothers EN, Kudin KN, Staroverov VN, Keith TA, Kobayashi R, Normand J, Raghavachari K, Rendell AP, Burant JC, Iyengar SS, Tomasi J, Cossi M, Millam JM, Klene M, Adamo C, Cammi R, Ochterski JW, Martin RL, Morokuma K, Farkas O, Foresman JB, Fox DJ (2016) Gaussian Inc Wallingford CT 1: Revision B. 01.
Ghose AK, Viswanadhan VN, Wendoloski JJ (1999) Journal of Combinatorial Chemistry 1: 55—68.
Giaginis C, Tsopelas F, Tsantili-Kakoulidou A (2018) The Impact of Lipophilicity in Drug Discovery: Rapid Measurements by Means of Reversed-Phase HPLC. In Rational Drug Design, (Humana New York, NY), pp. 217—228.
Hay M, Thomas DW, Craighead JL, Economides C, Rosenthal J (2014) Nature Biotechnology 32: 40—51.
Hertzberg RP, Pope AJ (2000) Current Opinion in Chemical Biology 4: 445—451.
Jinsong S, Qifeng J, Xing C, Hao Y, Wang L (2024) Communications Chemistry 7: 20.
Jorgensen WL (1989) Accounts of Chemical Research 22: 184—189.
Jorgensen WL, Briggs JM, Contreras MLeonor (1990) The Journal of Physical Chemistry 94: 1683—1686.
Kaliszan R, Haber P, Bączek T, Siluk D, Valko K (2002) Journal of Chromatography A 965: 117—127.
Karges J, Giardini MA, Blacque O, Woodworth B, Siqueira-Neto JL, Cohen SM (2023) Chemical Science 14: 711—720.
Kastl A, Wilbuer A, Merkel AL, Feng L, Di Fazio P, Ocker M, Meggers E (2012) Chemical Communications 48: 1863—1865.
Kim S, Chen J, Cheng T, Gindulyte A, He J, He S, Li Q, Shoemaker BA, Thiessen PA, Yu B, Zaslavsky L, Zhang J, Bolton EE (2019) Nucleic Acids Research 47: D1102—D1109.
Kim S, Chen J, Cheng T, Gindulyte A, He J, He S, Li Q, Shoemaker BA, Thiessen PA, Yu B, Zaslavsky L, Zhang J, Bolton EE (2021) Nucleic Acids Research 49: D1388—D1395.
Klopman G, Li J-Y, Wang S, Dimayuga M (1994) Journal of Chemical Information and Computer Sciences 34: 752—781.
Krishnan R, Binkley JS, Seeger R, Pople JA (1980) The Journal of Chemical Physics 72: 650—654.
Langenaeker W, Gert T, Winter DH (2010) Silicos-it.
Lee C, Yang W, Parr RG (1988) Physical Review B 37: 785—789.
Lipinski CA, Lombardo F, Dominy BW, Feeney PJ (2001) Advanced Drug Delivery Reviews 46: 3—26.
Mannhold R, Poda GI, Ostermann C, Tetko IV (2009) Journal of Pharmaceutical Sciences 98: 861—893.
Marenich AV, Cramer CJ, Truhlar DG (2009) The Journal of Physical Chemistry B 113: 6378—6396.
MarvinSketch was used for drawing displaying and characterizing chemical structures and reactions; Marvin 17.21.0; Chemaxon (2020).
McLean AD, Chandler GS (1980) The Journal of Chemical Physics 72: 5639—5648.

Meylan WM, Howard PH (1995) Journal of Pharmaceutical Sciences 84: 83—92.
Meylan WM, Howard PH (2000) Perspectives in Drug Discovery and Design 19: 67—84.
Michalík M, Lukeš V (2016) Acta Chimica Slovaca 9: 89—94.
Miertuš S, Scrocco E, Tomasi J (1981) Chemical Physics 55: 117—129.
Miertuš S, Tomasi J (1982) Chemical Physics 65: 239—245.
Moriguchi I, Hirono S, Liu Q, Nakagome I, Matsushita Y (1992) Chemical and Pharmaceutical Bulletin 40: 127—130.
Moriguchi I, Hirono S, Nakagome I, Hirano H (1994) Chemical and Pharmaceutical Bulletin 42: 976—978.
Muegge I, Heald SL, Brittelli D (2001) Journal of Medicinal Chemistry 44: 1841—1846.
Nedyalkova MA, Madurga S, Tobiszewski M, Simeonov V (2019) Journal of Chemical Information and Modeling 59: 2257—2263.
O'Boyle NM, Banck M, James CA, Morley C, Vandermeersch T, Hutchison GR (2011) Journal of Cheminformatics 3: 33.
OECD 107 Method (1995) OECD guideline for the testing of chemicals adopted by the Council on 27th July 1995 Partition Coefficient (n-octanol/water): Shake Flask Method.
Pages BJ, Ang DL, Wright EP, Aldrich-Wright JR (2015) Dalton Transactions 44: 3505—3526.
Pascual-ahuir JL, Silla E, Tuñon I (1994) Journal of Computational Chemistry 15: 1127—1138.
Perdew JP, Burke K, Ernzerhof M (1996) Physical Review Letters 77: 3865—3868.
Perdew JP, Burke K, Ernzerhof M (1997) Physical Review Letters 78: 1396—1396.
Petersson GA, Al-Laham MA (1991) The Journal of Chemical Physics 94: 6081—6090.
Petersson GA, Bennett A, Tensfeldt TG, Al-Laham MA, Shirley WA, Mantzaris J (1988) The Journal of Chemical Physics 89: 2193—2218.
Rassolov VA, Pople JA, Ratner MA, Windus TL (1998) The Journal of Chemical Physics 109: 1223—1229.
Rassolov VA, Ratner MA, Pople JA, Redfern PC, Curtiss LA (2001) Journal of Computational Chemistry 22: 976—984.
Thompson MA (2004) Molecular Docking Using ArgusLab, an Efficient Shape-Based Search Algorithm and the a Score Scoring Function (Philadelphia).
US EPA (1996) EPA Product properties test guideline. OPPTS 830.7550 Partition coefficient (n-octanol/H_2O), shake flask method.
Vosko SH, Wilk L, Nusair M (1980) Canadian Journal of Physics 58: 1200—1211.
Wang R, Fu Y, Lai L (1997) Journal of Chemical Information and Computer Sciences 37: 615—621.
Wildman SA, Crippen GM (1999) Journal of Chemical Information and Computer Sciences 39: 868—873.
Zhao Y, Truhlar DG (2008) Theoretical Chemistry Accounts 120: 215—241.

Appendix

Supplementary materials

Tab. A1. Experimental values of log *P* and cluster ID of individual molecules.

ID	name	log *P* [exp]	cluster ID
1	N-(nitrosomethyl)isobutylamine	0.81	E
2	(Z)-4-(azoxycyano)quinoline 1-oxide	1.12	E
3	1-(4-hydroxybutyl)benzotriazole	1.03	E
4	3-(N,N-diethylamino)propylacrylamide	0.72	E
5	(S)-5,7,3'-trihydroxyflavanone	2.61	E
6	2-naphthyl beta-D-glucopyranoside	0.76	E
7	3-ethoxybenzal diethylmalonate	3.39	E
8	cocaine	2.09	E
9	codeine	1.14	B
10	azaperone	3.30	D
11	2-methoxystrychnine	1.85	B
12	gitoxigenin	1.60	A
13	spiroperidol	3.03	D
14	hydrocortisone 17-valerate	3.79	A
15	betamethasone 21-valerate	3.87	A
16	L-glutamine	-3.15	E
17	2,8-bis(methylthio)-6-chloropurine	0.63	E
18	8-(3-nitrophenyl)adenine	1.93	E
19	benzenesulfonyl-L-glutamine	0.33	E
20	decachlorobiphenyl	8.27	E
21	2,6-di((S)-*sec*-butyl)phenol	4.38	E
22	(S)-N-phenyl-3-acetylaminosuccinimide	-0.33	E
23	thioxanthene-9-carboxylic acid	2.57	C
24	xanthene-9-carboxylic acid	2.23	C
25	quinoline-8-sulfonanilide	1.75	E
26	(R)-1-lauryl-4-carboxy-2-pyrrolidone	2.60	E
27	naloxone	2.09	B
28	grayanotoxin III	0.27	A
29	podophyllotoxin	2.01	E
30	glycodeoxycholic acid	2.25	A
31	helveticosol	0.15	A
32	1,1-dichloroethylene	2.13	E
33	methyl salicylate	2.62	E
34	thiodicarb	1.70	E
35	simazine	2.18	E
36	testosterone	3.32	A

Tab. A2. Structural formulae of studied molecules with their related chemical names.

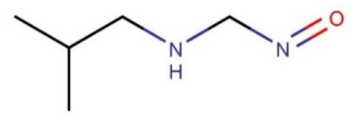 **1#** N-(nitrosomethyl)isobutylamine	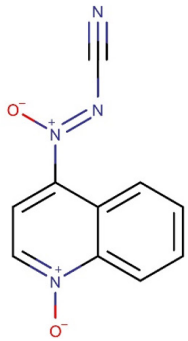 **2#** (Z)-4-(azoxycyano)quinoline 1-oxide
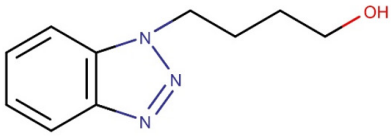 **3#** 1-(4-hydroxybutyl)benzotriazole	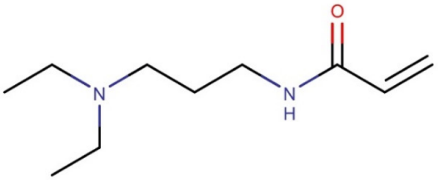 **4#** 3-(N,N-diethylamino)propylacrylamide
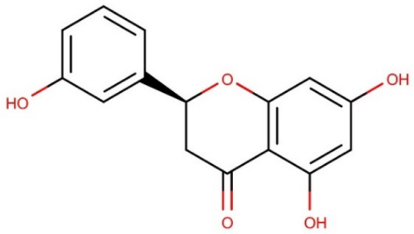 **5#** (S)-5,7,3'-trihydroxyflavanone	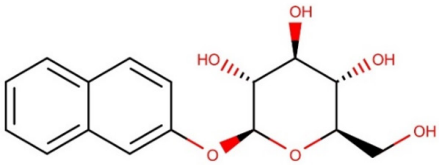 **6#** 2-naphthyl beta-D-glucopyranoside
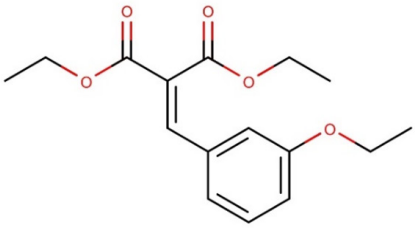 **7#** 3-ethoxybenzal diethylmalonate	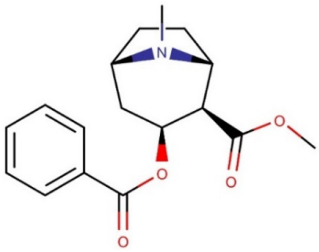 **8#** cocaine
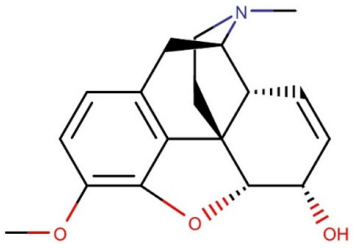 **9#** codeine	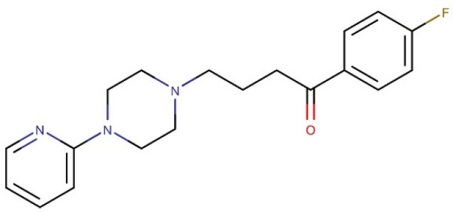 **10#** azaperone
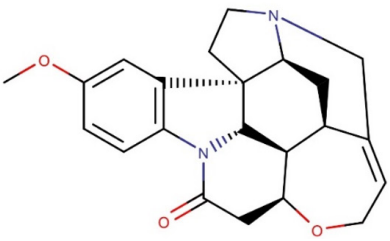 **11#** 2-methoxystrychnine	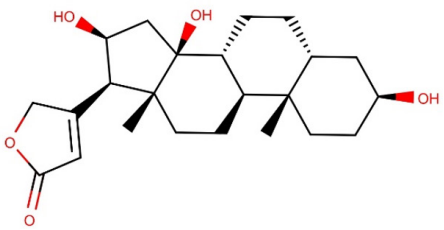 **12#** gitoxigenin

Tab. A2 (continue)**.** Structural formulae of studied molecules with their related chemical names.

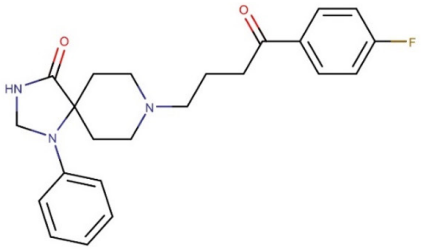 **13#** spiroperidol	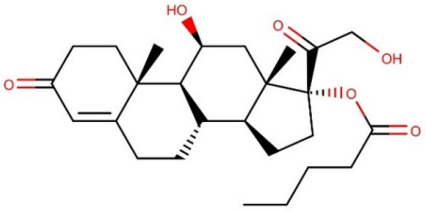 **14#** hydrocortisone 17-valerate
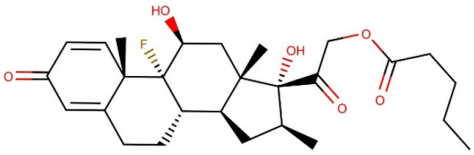 **15#** betamethasone 21-valerate	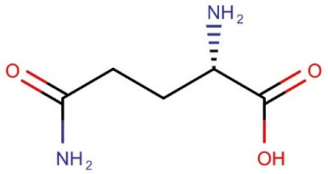 **16#** L-glutamine
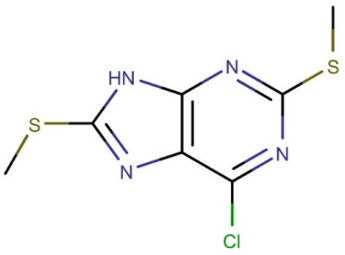 **17#** 2,8-bis(methylthio)-6-chloropurine	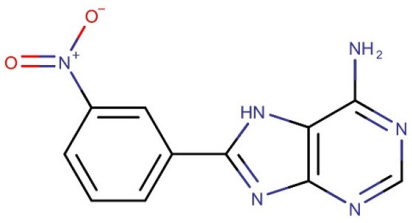 **18#** 8-(3-nitrophenyl)adenine
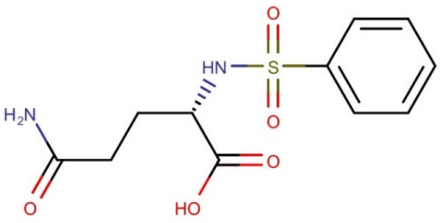 **19#** benzenesulfonyl-L-glutamine	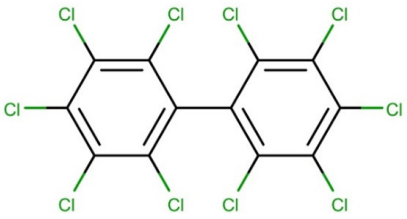 **20#** decachlorobiphenyl
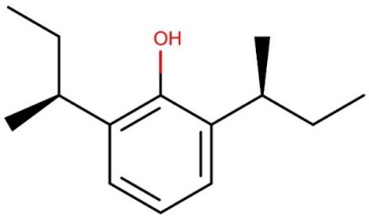 **21#** 2,6-di((S)-*sec*-butyl)phenol	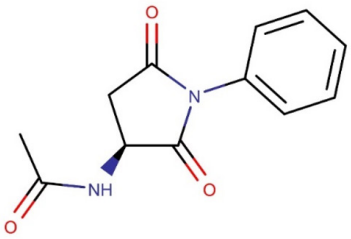 **22#** (S)-N-phenyl-3-acetylaminosuccinimide
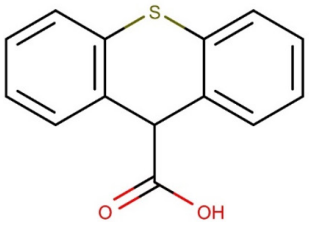 **23#** thioxanthene-9-carboxylic acid	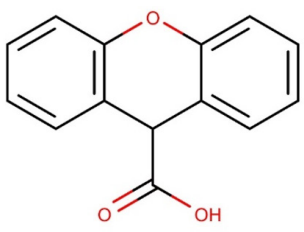 **24#** xanthene-9-carboxylic acid

Tab. A2 (continue)**.** Structural formulae of studied molecules with their related chemical names.

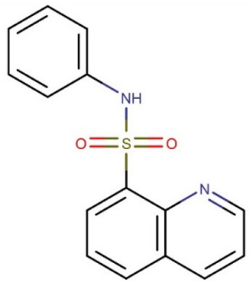 **25#** quinoline-8-sulfonanilide	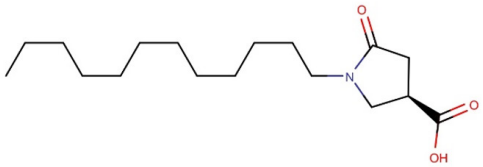 **26#** (R)-1-lauryl-4-carboxy-2-pyrrolidone
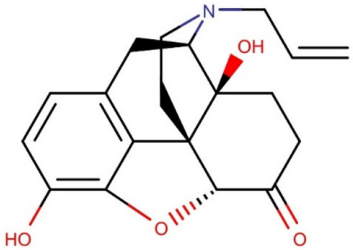 **27#** naloxone	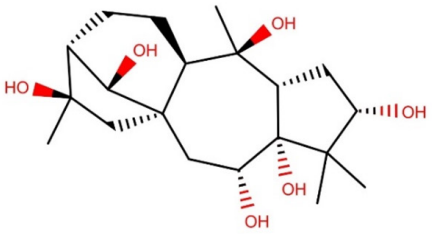 **28#** grayanotoxin III
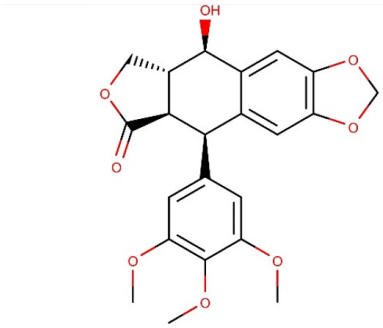 **29#** podophyllotoxin	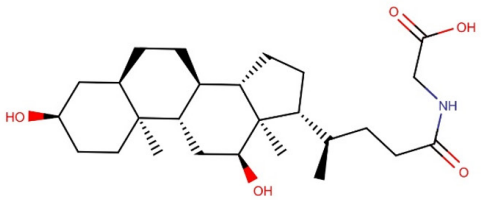 **30#** glycodeoxycholic acid
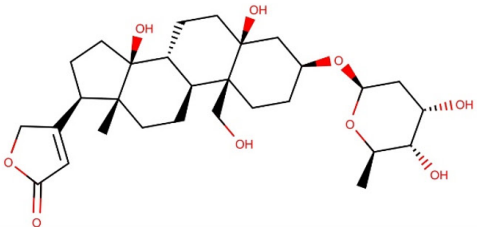 **31#** helveticosol	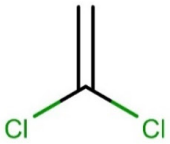 **32#** 1,1-dichloroethylene
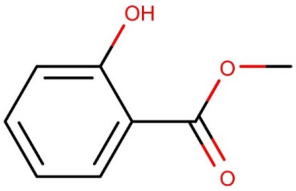 **33#** methyl salicylate	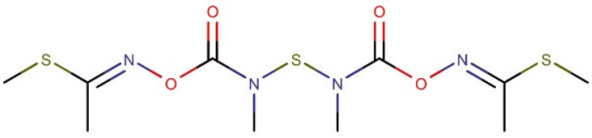 **34#** thiodicarb
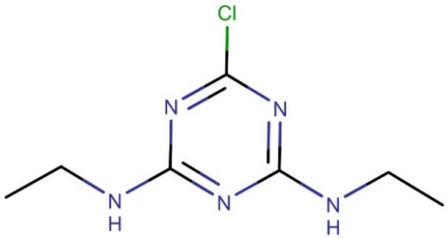 **35#** simazine	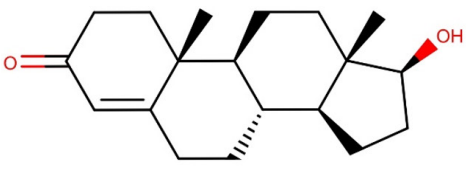 **36#** testosterone

Tab. A3. Clog *P* results from parametric methods.

ID	log *P* [exp]	iLOGP	XLOGP3	WLOGP	MLOGP	SILICOS-IT	OBLogP
1	0.81	2.08	0.57	0.96	0.83	0.65	1.35
2	1.12	1.06	0.17	1.55	1.47	–0.92	2.87
3	1.03	2.00	1.03	1.20	1.42	1.26	1.20
4	0.72	2.52	0.72	1.02	1.19	1.30	1.41
5	2.61	1.74	2.61	2.19	0.71	2.05	2.51
6	0.76	2.43	0.76	0.02	–0.13	0.29	0.02
7	3.39	3.72	3.39	2.49	2.25	3.20	2.59
8	2.09	3.22	2.30	1.49	2.18	1.61	1.81
9	1.14	2.67	1.14	1.12	1.98	1.86	1.44
10	3.30	3.11	3.30	2.66	2.49	3.43	3.01
11	1.85	3.09	1.85	1.34	2.37	1.80	2.10
12	1.60	2.68	1.60	2.58	2.73	2.55	2.58
13	3.03	3.12	3.03	2.49	2.86	3.66	3.55
14	3.79	3.37	3.79	3.52	2.35	4.18	3.52
15	3.87	3.50	3.87	4.06	2.57	4.31	3.64
16	–3.15	0.38	–3.15	–1.34	–3.58	–1.42	0.06
17	0.63	2.05	0.81	2.45	0.80	2.76	2.45
18	1.93	0.46	1.93	1.52	0.26	–0.46	2.61
19	0.33	0.51	0.33	0.76	–2.57	–0.67	1.86
20	8.27	3.53	8.27	9.89	8.98	9.89	9.89
21	4.38	3.03	4.36	4.42	3.87	4.12	4.42
22	–0.33	1.50	–0.33	0.07	0.82	0.80	0.91
23	2.57	1.97	2.57	3.37	3.29	3.10	3.37
24	2.23	1.92	2.23	3.01	2.41	2.54	3.01
25	1.75	1.64	1.75	3.93	1.82	1.99	4.19
26	2.60	3.38	2.60	3.46	2.61	3.93	3.78
27	2.09	1.81	2.09	0.92	1.30	2.56	1.24
28	0.27	2.36	0.27	0.17	0.70	0.54	0.17
29	2.01	2.97	2.01	2.08	1.43	2.90	2.41
30	2.25	3.07	2.25	3.59	2.95	3.00	3.99
31	0.15	3.18	0.15	1.57	1.18	1.70	1.57
32	2.13	1.72	2.32	1.94	1.67	1.44	1.94
33	2.62	2.03	2.55	1.18	1.32	1.21	1.18
34	1.70	3.16	1.70	3.08	0.57	0.06	3.08
35	2.18	2.60	2.18	1.01	0.01	1.02	1.53
36	3.32	2.92	3.32	3.88	3.59	3.58	3.88

Tab. A4. Clog *P* results from QM models.

ID	log *P* [exp]	DFT A	DFT B	DFT C	DFT D	DFT E	xTB
1	0.81	0.08	–0.24	–0.55	–0.41	–0.32	1.56
2	1.12	1.08	1.46	–1.14	0.95	1.13	0.79
3	1.03	0.02	0.27	–1.04	–0.67	–0.38	1.12
4	0.72	2.42	1.51	–1.42	1.13	1.42	3.79
5	2.61	–0.44	0.16	–1.38	0.38	0.29	2.36
6	0.76	0.05	0.69	–1.39	–0.32	1.42	3.76
7	3.39	5.65	5.99	–0.83	2.33	2.57	5.28
8	2.09	1.67	2.10	–1.18	1.71	1.94	4.70
9	1.14	1.55	1.84	–0.87	1.39	1.36	5.08
10	3.30	2.53	3.14	–1.04	2.11	2.91	5.86
11	1.85	0.80	1.17	–1.11	0.68	0.83	5.19
12	1.60	0.89	1.27	–1.42	1.09	0.90	3.79
13	3.03	3.85	3.85	–1.55	3.03	3.54	6.70
14	3.79	2.59	3.24	–1.68	3.33	3.07	3.80
15	3.87	2.38	2.41	–2.73	1.69	2.42	4.86
16	–3.15	–3.73	–3.41	–1.48	–3.24	–3.63	–0.65
17	0.63	0.54	0.75	–0.92	0.79	0.59	3.12
18	1.93	–2.10	–2.18	–1.99	–2.53	–2.53	1.62
19	0.33	–2.34	–2.79	–2.03	–3.18	–1.65	–4.43
20	8.27	8.04	8.09	–0.30	7.95	8.02	8.71
21	4.38	4.57	4.53	–0.53	4.42	4.37	4.87
22	–0.33	–0.03	–0.42	–1.04	–0.83	–0.74	3.72
23	2.57	3.12	1.71	0.22	2.94	2.53	3.86
24	2.23	0.73	0.43	1.45	0.76	0.46	3.34
25	1.75	0.52	0.60	–1.35	0.30	0.44	0.36
26	2.60	4.15	4.53	–1.28	4.75	4.09	3.80
27	2.09	0.43	0.39	–1.37	–0.43	0.40	4.35
28	0.27	0.09	0.15	–1.71	–0.09	0.00	3.37
29	2.01	–3.23	–0.61	–2.13	–5.20	–2.99	5.26
30	2.25	2.43	2.42	–1.74	3.28	1.87	4.23
31	0.15	–0.32	0.70	–2.90	–0.20	–0.10	3.81
32	2.13	2.20	2.22	–0.14	2.18	2.19	1.68
33	2.62	8.19	0.63	–0.57	0.22	8.03	1.38
34	1.70	–0.60	–0.24	–2.42	–0.68	–0.42	6.15
35	2.18	2.70	2.80	–0.77	2.52	2.46	3.13
36	3.32	3.05	3.24	–1.04	3.04	3.03	4.31

Tab. A5. Clog *P* results for individual clusters in terms of RMSE for parametric methods and QM models with respect to experimental log *P*

method	**cluster** A	**cluster B**	**cluster C**	**cluster D**	**cluster E**
iLOGP	1.5053	1.1485	0.4775	0.1487	1.6432
XLOGP3	0.0000	0.0000	0.0000	0.0000	0.2214
WLOGP	0.8623	0.7370	0.7901	0.5921	1.0186
MLOGP	0.9892	0.7303	0.5248	0.5852	1.1268
SILICOS-IT	0.7886	0.4973	0.4342	0.4549	1.2193
OBLogP	0.9602	0.5401	0.7901	0.4210	1.3084
DFT A	0.8038	1.1585	1.1297	0.7954	2.2502
DFT B	0.6431	1.1317	1.4106	0.5908	1.6786
DFT C	4.3219	2.8736	1.7508	4.4616	3.5153
DFT D	0.9721	1.6106	1.0719	0.8415	2.2847
DFT E	0.7046	1.1467	1.2519	0.4540	2.1033
xTB	2.1936	3.2551	1.2034	3.1641	2.3157

sciendo

Temperature-dependent growth kinetics of *Lacticaseibacillus rhamnosus* GG in oat-based milk alternative

Zuzana Matejčeková[1], Tamara Čmiková[2], Pavel Ačai[2], Ľubomír Valík[1]

[1]Department of Nutrition and Food Quality Assessment, Institute of Food Science and Nutrition, Faculty of Chemical and Food Technology, Slovak University of Technology in Bratislava, Radlinského 9, 812 37 Bratislava, Slovakia
[2]Department of Food Technology, Institute of Food Sciences and Nutrition, Faculty of Chemical and Food Technology, Slovak University of Technology in Bratislava, Radlinského 9, 812 37 Bratislava, Slovakia
zuzana.matejcekova@stuba.sk

Abstract: Microbial growth responses of probiotic *Lacticaseibacillus rhamnosus* GG with well-documented health effects were studied in an oat-based milk alternative in the biokinetic temperature range of 8 to 44 °C. The applied Baranyi model (with a fixed parameter value h_0 = 0.407) fitted the growth data well, as shown by the goodness of fit measures (R^2 = 0.995; *RMSE* = 0.153) for the total experimental data set (n = 245). Using the initial inoculations of 2.7 ±0.1 log CFU.ml^{-1}, the maximal population density (MPD) of 8.3 ±0.4 log CFU.ml^{-1} was reached in stationary phase in the temperature range from 12 to 37 °C. Slightly lower MPDs were recorded at higher temperatures, 40 and 44 °C, while an increase in only 1 log was reached at 8 °C. Thus, the MPD 3.7 log CFU.ml^{-1} was only estimated. Based on the experiments, the highest specific growth rate (μ_{max}) of 0.800 h^{-1} and the shortest lag phase (λ) of 0.51 h were observed at 40 °C. The Ratkowsky modified square root model (mSQRT) was used in the secondary modelling for μ_{max} values and the cardinal parameters minimum and maximum temperature were determined: T_{min} = 4.2 °C; T_{max} = 47.8 °C. As drinks of plant origin are produced in large volumes, the production of their fermented varieties is expected to appear in a short time. This is why providing parameters on kinetic behaviour of *L. rhamnosus* GG is essential for industrial process design and further scale up of fermented dairy-free matrice with probiotic potential.

Keywords: dynamic growth modelling, *Lacticaseibacillus rhamnosus* GG; oat beverage; predictive microbiology; probiotics

Introduction

Prevalence of cow's milk allergies, lactose intolerances, and the trend towards plant-based diets requires the food industry to design, supply, and produce novel dairy alternatives. Designing innovative food products emphasising plant production over animal one aligns also with current trends aimed at carbon emissions' reduction. Oat beverages are the most preferred among many milk substitutes (Marchwińska et al., 2023).

Oats are rich in starch, fibre (beta-glucans), antioxidants, vitamins, and healthy fats, with higher protein and lipid content compared to other cereals. The presence of starch in the oat-based formula causes its gel structure. Enzymatic hydrolysis should be performed using α-amylase alone or through a sequential process involving both α- and β-amylase to break down starch into glucose and shorter-chain polysaccharides to ensure the fluidity of the beverage. Oats also contain unsaturated essential fatty acids (oleic and linoleic acid) with a significant impact on nutritional quality. On the contrary, plant-based beverages often do not meet the requirements for traditional dairy products and therefore excessive fortification is needed; commercial oat-based milk alternatives present protein deficiency (≤ 1 g per 100 ml of product). Oats also contain a considerable number of lipases that cause rancidity during processing (Kütt et al., 2023; Masiá et al., 2021). Therefore, fermentation represents a simple and natural way to improve nutritional value, as well as sensory and textural properties. Lactic acid bacteria (LAB) have been used as starter or adjunct cultures in a wide variety of fermented products, including fermented fruits, vegetables, cereal products, dairy products, fermented fish, and meat. One of the LAB's studied is *Lacticaseibacillus rhamnosus* GG (LGG), ATCC 53103, known as *Lactobacillus rhamnosus* before reclassification. Initially, it was isolated from faecal samples of healthy human adults by Sherwood Gorbach and Barry Goldwin, explaining its typical surname letters GG, and was identified as a potential probiotic strain. Numerous clinical trials and human intervention studies have thoroughly examined its beneficial effects. Since then, it has been one of the most extensively investigated probiotic strains used in various commer-

cially available probiotic formulations (Segers and Lebeer, 2014). LGG can produce exopolysaccharides (EPS) in dairy products making it a useful starter culture. This strain has also been investigated in plant-based raw materials, showing EPS production at lower temperatures than the optimal growth temperature in oat-based media and indicating that EPSs are produced after the fermentation process (Masiá et al., 2021). However, commercially available plant-based alternatives are often not fermented, and LAB are added at the final stage of product manufacturing. Furthermore, there is still a knowledge gap regarding the behaviour of traditional milk-derived bacteria in plant-based environments. Currently, we still lack information on strain growth kinetics, or flavour and aroma formation in plant-based fermented drinks (Kütt et al., 2023). To successfully cultivate LAB, the effect of different starter cultures on the fermentation process has to be determined. Although the technologically important parameters like optimal temperature and *pH* for industrially used strains in dairy products are well known, the growth and metabolic behaviour with changing temperature in dairy alternatives are not extensively investigated. Thus, the present study focused on monitoring the growth dynamics of *L. rhamnosus* GG in the biokinetic temperature range of 8 to 44 °C to estimate growth parameters with predictive modelling approaches. The significance of this work lies in comprehensive analysis of the growth dynamics of *L. rhamnosus* GG.

Materials and methodology

Bacterial strain

The strain *Lacticaseibacillus rhamnosus* GG (reclassified from *Lactobacillus rhamnosus* GG since April 2020), registered in the American Type Culture Collection (ATCC) under the number 53103, was used in the experiments and belongs to the collection of the Institute of Food Science and Nutrition (Slovak University of Technology in Bratislava, Slovakia). The strain was stored in polypropylene tubes at –30 °C in Man, Rogosa, and Sharpe (MRS) broth (Biokar Diagnostics, Beauvais, France) containing 25 % (v/v) of glycerol.

Preparation of bacterial suspension

For growth experiments, *L. rhamnosus* GG was first sub-cultured three times for 24 h at 37 ±0.5 °C (5 % CO_2) in MRS broth. Thereafter, the basic suspension for experiments was obtained by overnight incubation at 37 ±0.5 °C (5 % CO_2) in MRS broth. Concentration at the beginning of each experiment was set within the range of 2—3 log CFU · ml^{-1}.

Cultivation conditions and cell counts enumeration

Individual experiments with pure culture of *L. rhamnosus* GG were carried out in 500 ml Erlenmeyer flasks with a volume of 300 ml of pre-tempered commercially available heat-treated oat beverage (containing spring water, 9 % of oats, calcium and vitamin D3) (McCarter a.s., Bratislava, Slovakia). Detailed nutritional composition is outlined in Table 1. A volume of 3 ml of the appropriate dilution of the bacterial culture was added aseptically to a flask and thoroughly mixed. Two parallel static cultivations were carried out at 8, 12, 15, 18, 21, 25, 30, 37, 40 and 44 °C under aerobic conditions. For quantification of *L. rhamnosus* GG, 1 ml samples from each flask were taken at predetermined time intervals and serial ten-fold dilutions were prepared in a solution of 0.85 % NaCl (w/v) and 0.1 % (w/v) peptone (Biolife, Milan, Italy) until the bacterial population reached a stationary phase. Subsequently, 1 ml of certain set dilution was poured by MRS agar (Biokar Diagnostics, Beauvais, France) in duplicate. Agar plates were incubated at 37 °C for 48 h (5 % CO_2). After incubation, the grown lactobacilli colonies were enumerated, and the results were converted into colony-forming units (CFU) per 1 ml of the sample. Sample *pH* was monitored at appropriate time intervals using a WTW 720 pH meter (Inolab, Weilheim, Germany).

Tab. 1. Nutritional composition of oat beverage per 100 ml (McCarter a.s., Bratislava, Slovakia).

Energy value	25 kcal/107 kJ
Fat	< 0.5 g
of which saturated fatty acids	< 0.1 g
Carbohydrates	4.8 g
of which sugars	1.6 g
Proteins	< 0.5 g
Salt	0.07 g
Calcium	112 mg
Vitamin D3	0.75 µg

Mathematical models and evaluation of model performance

The traditional two-step kinetic data analysis approach was applied to describe the microbial growth of *L. rhamnosus* GG in the range of temperatures from 8 to 44 °C. Each growth curve was analysed using the primary predictive model to determine its parameters, and subsequently suitable secondary model was applied to analyse the effect of temperature on maximum specific growth rates and lag times determined from the primary model. The primary model of Baranyi and Roberts (1994), as a system of ordinary differential equations with

initial conditions, was used for the description of *L. rhamnosus* GG microbial growth in modified form:

$$\frac{dx}{dt} = \frac{1}{1+10^{-Q_{10}}} \frac{\mu_{\max}}{\ln 10} \left[1-10^{(x-x_{\max})}\right] \quad (1)$$

$$\frac{dQ_{10}}{dt} = \frac{\mu_{\max}}{\ln 10} \quad (2)$$

$$t = 0,\ x = x_0,\ Q_{10} = Q_{0,10}$$

where $x = \log N$ is the density of the microbial population in log CFU · ml^{-1}, t is the incubation time, Q_{10} is the decimal logarithm of q, 'theoretical critical substance' necessary to allow growth, which is a dimensionless variable that quantifies the actual physiological state of cells, $\mu_{\max}$ is the maximum specific growth rate, $x_{max} = \log N_{max}$ represents the maximum density of microbial population in log CFU · ml^{-1}, $x_0 = \log N_0$ is the initial density of microbial population (log CFU · ml^{-1}), $Q_{0,10}$ is the decimal logarithm of q_0, a measure of the physiological state of inoculum (quantity of the initial 'theoretical critical substance').

Subsequently, it was possible to calculate the values of q_0, h_0, and λ as follows:

$$q_0 = 10^{Q_{0,10}} \quad (3)$$

$$h_0 = \ln\left(1+\frac{1}{q_0}\right) \quad (4)$$

$$\lambda = \frac{h_0}{\mu_{\max}} \quad (5)$$

where h_0 is the dimensionless factor, a different transformation of the initial physiological state of cells q_0, representing suitability indicator of the microorganism population to actual environment, λ is the lag phase duration dependent on q_0 (h_0) as well as on the maximum specific growth rate μ_{max}. Optimised parameters of the Baranyi model in its modified form may be either μ_{max}, $Q_{0,10}$, x_0 and x_{max} or μ_{max}, h_0, x_0 and x_{max}. As the subculture procedures for *L. rhamnosus* GG in the oat beverage were standardised under constant environmental conditions (the same initial physiological state is assumed), thus, according to Baranyi's hypothesis (Baranyi and Roberts, 1994), values q_0 and h_0 should be constant. Therefore, parameters $Q_{0,10} = \log q_0$ or h_0 were fitted first from the individual microbial growth curves and then their average value (q_{av}) was used again as a fixed parameter. This reduces the number of evaluated parameters in the Baranyi model (Eq. (1–2)) to three: μ_{max}, x_0 and x_{max}. Then, the newly obtained kinetic parameters from *L. rhamnosus* GG growth curves, the maximum specific growth rates (μ_{max}), and the lag phase duration (λ) depending on temperature were described with a suitable secondary model compatible with this Baranyi assumption.

One of them can be the extended Ratkowsky square root model (Ratkowsky et al., 1983) used to determine the relationship between μ_{max} and temperatures within the entire biokinetic temperature range, written in its modified form as follows:

$$\mu_{\max} = \left[b_\mu \cdot (T-T_{\min})\left\{1-\exp\left[c_\mu (T-T_{\max})\right]\right\}\right]^2 \quad (6)$$

where the regression coefficient b_μ depends on additional growth conditions and the microorganism present, T is the temperature, T_{min} is the theoretical minimum growth, T_{max} is the maximum growth temperature, and c_μ is the regression coefficient.

The only secondary model for the lag phase (λ) compatible with constant $Q_{0,10} = \log q_{0,av}$ or $h_0 = h_{0,av}$ in the Baranyi model Eq. (1–2) is the following equation describing the link relationship between λ, μ_{max}, and q_0 (Garre et al., 2025):

$$\lambda = \frac{h_{0,av}}{\mu_{\max}} = \frac{\ln\left(1+\frac{1}{q_{0,av}}\right)}{\left[b_\mu \cdot (T-T_{\min})\left\{1-\exp\left[c_\mu (T-T_{\max})\right]\right\}\right]^2} = \frac{\ln\left(1+\frac{1}{q_{0,av}}\right)}{b_\mu^2\left[(T-T_{\min})\left\{1-\exp\left[c_\mu (T-T_{\max})\right]\right\}\right]^2} \quad (7)$$

Then, Eq. (7) can be simplified as follows for the predicted/calculated lag phase.

$$\lambda = \frac{1}{b_\lambda^2\left[(T-T_{\min})\left\{1-\exp\left[c_\mu (T-T_{\max})\right]\right\}\right]^2} \quad (8)$$

where parameter

$$b_\lambda = \sqrt{\frac{b_\mu^2}{\ln\left(1+\frac{1}{q_{0,av}}\right)}} = \sqrt{\frac{b_\mu^2}{h_{0,av}}}$$

or equivalently in form of extended lag square root model:

$$\sqrt{\frac{1}{\lambda}} = b_\lambda\left[(T-T_{\min})\left\{1-\exp\left[c_\mu (T-T_{\max})\right]\right\}\right] \quad (9)$$

Doubling times (t_d) for *L. rhamnosus* GG were calculated using the following equation (Baranyi et al., 1999):

$$t_d = \frac{\ln 2}{\mu} \quad (10)$$

Experimental data of *pH* changes within the temperature range from 12 to 44 °C follow a sigmoidal behaviour and can be mathematically described

by a reparametrised Gompertz-inspired function (Zwietering et al., 1991).

$$pH = pH_0 - \\ -\Delta pH \cdot \exp\left\{-\exp\left[-2.71\left(\frac{k_{pH}}{\Delta pH}\right)\left(lag_{pH} - t\right)+1\right]\right\} \quad (11)$$

where pH_0 is the initial pH value, ΔpH is the asymptotic decrease in pH value (difference of initial pH (pH_0) and final pH value in a stationary phase (pH_{end})), k_{pH} is the maximum pH drop in the exponential phase for the given temperature, lag_{pH} is the lag phase duration in pH.

Goodness-of-fit indices

Statistical 'Goodness-of-fit criteria (indices)' used to evaluate the performance of the applied primary and secondary predictive mathematical models are the sum of squared errors (*SSE*), the determination coefficient (R^2), and the root mean squared error (*RMSE*). They prove the suitability of the model to fit the individual or the entire set of observation points according to Equations (1–9), respectively:

$$SSE = \sum_{i=1}^{n}\left(x_i^{\exp} - x_i^{cal}\right)^2 \quad (12)$$

$$R^2 = 1 - \frac{SSE}{SST} = 1 - \frac{\sum_{i=1}^{n}\left(x_i^{\exp} - x_i^{cal}\right)^2}{\sum_{i=1}^{n}\left(\bar{x}_i^{\exp} - x_i^{\exp}\right)^2} \quad (13)$$

$$RMSE = \sum_{i=1}^{n}\frac{\left(x_i^{\exp} - x_i^{cal}\right)^2}{n} \quad (14)$$

where x_i^{exp} and x_i^{cal} correspond to the given response values observed (experimental) and predicted (calculated), respectively, n is the number of data points, $\bar{x}_i^{\exp}$ is the mean of total experimental values, and *SST* is the total sum of squares. *RMSE*, the measure of residual error (variability), is probably the most informative criterion for testing the goodness of fit of models to data (McKellar and Lu, 2004), and a low *RMSE* value indicates a good fit.

The coefficient of variation (*CV*) was calculated according to Equation (15)

$$CV(\%) = \frac{SD}{\bar{x}} \times 100 \quad (15)$$

where

$$SD = \sqrt{\frac{\sum_{i=1}^{n}\left(x_i - \bar{x}\right)^2}{n-1}}$$

and is the standard deviation in the data set, $\bar{x}$ is the mean value of the initial numbers (x_0 = log N_0) or numbers in stationary phase (x_{max} = log N_{max}) of *L. rhamnosus* GG (Havlicek and Crain, 1988).

The commercial process engineering software Athena Visual Workbench (Stewart & Associates Engineering Software, Madison, WI; www.athenavisual.com) was applied for parameter evaluation of the primary and secondary models as well as for pH values, and Microsoft Excel (Microsoft, Redmond, Washington, USA) was used for the *SSE*, R^2, *RMSE* and *CV*.

Results and discussion

In this work, the growth and acidification capacity of *L. rhamnosus* GG was tested in a pasteurised oat beverage within ten independent cultivation experiments in duplicate trials within the temperature range from 8 to 44 °C. According to the statistical indices *SSE*, *RMSE*, and R^2 in Table 2, the primary model assessed a good fit to the growth curves of *L. rhamnosus* GG with R^2 fluctuating between 0.990 to 0.997 for the given number of experiments. The determination coefficient for the entire data set (n = 245) was equal to 0.995 with the measure of residual error (variability) *RMSE* between 0.030 to 0.224. Permissible deviation of *RMSE* represents an interval from 0.25 to 0.50 and in a more rigorous assessment from 0.1 to 0.15 (Mosel et al., 1995). The *RMSE* value for the total experimental data set (n = 245) equaled 0.153 which is only slightly higher than the more rigorous assessment mentioned above. Martins et al. (2020) and Costa Menezes et al. (2018) also used the Baranyi and Roberts model to describe the kinetics of microbial growth in food products. Additionally, Rosa da Silva et al. (2018) chose the Baranyi and Roberts model which proved to have better statistical indices compared to the modified Gompertz model to describe the growth of *Lactiplantibacillus plantarum*, *Weissella viridescens*, and *Latilactobacillus sakei*. In our oat beverage, *L. rhamnosus* GG growth was characterised by specific growth rates from 0.025 h^{-1} to 0.602 h^{-1} in the range from 8 °C to 44 °C (Tab. 2). Naturally, it was positively determined by temperature increase towards its optimal value. Rosa da Silva et al. (2018) and Li et al. (2013), in their studies, noted the same trend. Figure 1 displays the fitted primary model at observed temperatures. Lag phases and doubling times were reduced with the increasing temperature. Similar patterns were observed by Pelikánová et al. (2011) in *L. paracasei* subsp. *paracasei* in milk. Experimental maximal population densities (MPDs) of *L. rhamnosus* GG in the stationary phase reached levels of 8.3 log CFU · ml^{-1} (*CV* = 4.2 %) from the initial level of 2.7 log CFU · ml^{-1} (*CV* = 3.9 %) except for terminal 8 °C. Except for marginal temperatures 6,

8, and 50 °C, concentrations above 8 log CFU · ml^{-1} in the stationary phase were found with the same strain (LGG) in UHT milk by Valík et al. (2008). In the oat beverage at 8 °C, a slight increase of *L. rhamnosus* GG (μ_{max} = 0.025 h^{-1}) was noted. Liptáková et al. (2007) recorded the same specific growth rate of *L. rhamnosus* VT1 at 8 °C in UHT milk (μ_{max} = 0.025 h^{-1}) while Valík et al. (2008) found a slightly increased μ_{max} of 0.069 h^{-1} for *L. rhamnosus* GG in milk.

Within the cold chain, storage temperature between 4 and 8 °C is strongly recommended. To control the multiplication of LAB associated with spoilage, e.g. in vacuum-packaged meat products, it is necessary to control the storage temperature. Rosa da Silva et al. (2018) recommended to maintain incubation temperatures below 8 °C to reduce the growth of LAB. In our study, further increase in incubation temperature to 12 °C and 15 °C resulted in proliferation of LGG with specific growth rates of 0.038 h^{-1} and 0.069 h^{-1}, represented by the doubling times of 18.2 h and 10.0 h, respectively. Matejčeková et al. (2019) noted almost the same specific growth rates of *L. plantarum* HM1 at 12 °C and 15 °C in lactose-free milk (0.04 h^{-1} and 0.07 h^{-1}, respectively). An increase in temperature resulted in intensive growth across nearly the entire studied temperature range, with the highest calculated specific growth rate at 40 °C (μ_{max} = 0.800 h^{-1}). At this temperature, the shortest time necessary to reach the stationary phase was achieved (approximately 24 h) with the shortest lag phase duration of 0.51 h. *L. acidophilus* NCFM in UHT milk reached by about 3 % higher growth rate (μ_{max} = 0.827 h^{-1}; λ = 1.2 h) at 40 °C (Medveďová et al., 2016). In our study, a slight decrease (25 %) in μ_{max} was observed (t_d = 52 min) at 44 °C. Conversely, Adamberg et al. (2003) noted the highest specific growth rate at 44 °C (μ_{max} = 2.2 h^{-1}; t_d = 18 min) in *Streptococcus thermophilus* St20. Pelikánová et al. (2011) observed the highest specific growth rate at 43 °C (μ_{max} = 0.71 h^{-1}; t_d = 1.8 h) in *L. paracasei* in UHT milk. As a result of growth and multiplication, a decrease in active acidity by about 1.98–2.91 unit was reported. Moreover, a noticeable trend in reduced lag phase duration in *pH* values approaching its optimal value was determined with the increasing temperature (Tab. 3). At 12 °C, the lag phase in *pH* lasted for 248.1 h, whereas at 40 °C it was reduced to 15.6 h. In an oat beverage, final *pH* values ranged from 3.73 to 4.73 in the stationary phase (R^2 fluctuated from 0.961 to 0.997) (Tab. 3). The fastest decrease of *pH* was noted at 44 °C (–0.219 h^{-1}) even though at this temperature μ_{max} decreased by about 25 % compared to 40 °C where the highest specific growth rate was observed (μ_{max} = 0.800 h^{-1}; k_{ph40} = –0.172 h^{-1}). Milk supplemented with 7.5 g · l^{-1} of fructose inoculated with *L. rhamnosus* GG in a study by Østlie et al. (2003) had *pH* of 3.9–4.1 after 24 h at 37 °C. The *pH* values in UHT milk with *L. rhamnosus* GG did not change at temperatures lower than 21 °C, then, at higher temperatures, negligible acid production was noted (Valík et al., 2008). Matejčeková et al. (2016) recorded no significant changes in *pH* values (0.00–0.24 units) during *L. plantarum* HM1 growth in milk.

Kinetic parameters of the primary model (Eq. 1–2), μ_{max} and λ, were described as dependent on temperature with the suitable modified Ratkowsky

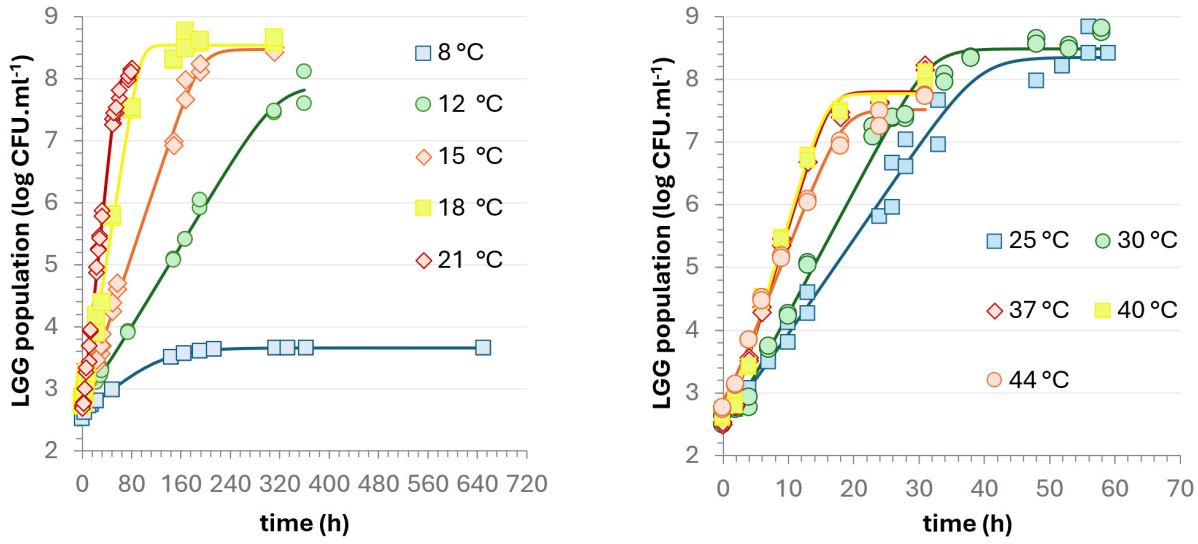

1A 1B

Fig. 1. Primary Baranyi model fitted to the data on *L. rhamnosus* GG at 8, 12, 15, 18, and 21 °C (1A) and 25, 30, 37, 40, and 44 °C (1B). Observed values are depicted using solid markers and the curves represent the prediction lines generated from the primary model.

Tab. 2. Estimated and calculated growth parameters of the Baranyi equation for *L. rhamnosus* GG in oat beverage in the temperature range from 8 to 44 °C with 95 % confidence intervals and goodness-of-fit indices.

T (°C)	μ_{max} (h^{-1})	N_0 (log CFU·ml^{-1})	N_{max} (log CFU·ml^{-1})	λ_1 (h)	*SSE*	R^2	*RMSE*
8	0.025 ±0.002	2.64 ±0.02	3.66 ±0.02	16.43	0.025	0.995	0.030
12	0.038 ±0.001	2.85 ±0.06	7.89 ±0.17	10.71	0.214	0.997	0.094
15	0.069 ±0.002	2.94 ±0.07	8.47 ±0.16	5.92	0.342	0.997	0.115
18	0.144 ±0.007	2.77 ±0.09	8.54 ±0.11	2.83	0.475	0.997	0.135
21	0.224 ±0.008	2.76 ±0.08	8.06 ±0.10	1.82	0.505	0.996	0.122
25	0.348 ±0.023	2.60 ±0.18	8.35 ±0.19	1.17	1.305	0.990	0.224
30	0.449 ±0.026	2.49 ±0.17	8.49 ±0.16	0.91	1.247	0.992	0.211
37	0.785 ±0.080	2.41 ±0.22	7.80 ±0.20	0.52	0.637	0.991	0.194
40	0.800 ±0.064	2.43 ±0.19	7.77 ±0.18	0.51	0.552	0.993	0.175
44	0.602 ±0.048	2.88 ±0.16	7.52 ±0.18	0.68	0.444	0.992	0.157

μ_{max} – specific growth rate, N_0 – initial numbers of *L. rhamnosus* GG, N_{max} – numbers in stationary phase, λ_1 – lag phase duration, *SSE* – sum of squared errors, R^2 – determination coefficient, *RMSE* – root mean squared error. values of λ_1;

$$\lambda = \frac{h_{0,av}}{\mu_{\max}} = \frac{\ln\left(1+\frac{1}{q_{0,av}}\right)}{\mu_{\max}},$$

are calculated through the average value of $q_{0,av} = 0.299$;

$$h_{0,av} = \ln\left(1+\frac{1}{q_{0,av}}\right) = 0.407$$

Tab. 3. **E**xperimental (exp) and calculated (cal) parameters of the Gompertz-inspired function describing *pH* values in oat beverage during the growth of *L. rhamnosus* GG in the range of 12 to 44 °C with 95 % confidence intervals.

T (°C)	pH_0^{exp}	pH_{end}^{exp}	ΔpH^{exp}	pH_0^{cal}	ΔpH^{cal}	k_{pH} (h^{-1})	lag_{pH} (h)	R^2
12	6.71	4.73	1.98	7.03 ±0.16	2.88 ±1.36	–0.027 ±0.005	263.8 ±16.7	0.971
15	6.68	4.07	2.61	6.91 ±0.16	2.85 ±0.48	–0.039 ±0.021	130.8 ±18.9	0.982
18	6.64	3.86	2.78	6.85 ±0.15	2.89 ±0.31	–0.065 ±0.058	78.8 ±11.2	0.992
21	6.68	4.68	2.00	6.83 ±0.12	3.74 ±2.65	–0.079 ±0.022	52.5 ±8.2	0.990
25	6.64	4.47	2.17	6.76 ±0.12	2.93 ±0.98	–0.161 ±0.016	39.9 ±1.8	0.993
30	6.64	3.73	2.91	6.72 ±0.16	2.89 ±0.29	–0.202 ±0.066	26.0 ±2.6	0.996
37	6.67	4.08	2.59	6.74 ±0.16	3.40 ±1.01	–0.245 ±0.015	18.7 ±1.3	0.999
40	6.63	4.08	2.55	6.73 ±0.23	3.22 ±1.19	–0.238 ±0.023	17.9 ±2.0	0.997
44	6.65	4.36	2.29	6.75 ±0.21	3.82 ±1.50	–0.231 ±0.088	20.3 ±3.0	0.997

pH_0^{exp} – experimental initial *pH* value, pH_{end}^{exp} – experimental final *pH* value, ΔpH^{exp} – difference in *pH* values after the incubation period compared to the initial state, pH_0^{cal} – calculated initial *pH* value, ΔpH^{cal} – calculated difference in *pH* values after the incubation period compared to pH_0^{cal}, k_{pH} – rate constant for the decrease of *pH*, lag_{pH} – lag phase duration in *pH*, R^2 – coefficient of determination.

square root secondary model (Ratkowsky et al., 1983; Eq. (6)). Individual points in Figure 2 represent the observed specific growth rate values, while the line depicts the model's predicted specific rates. Parameter estimates and their standard errors with the upper and lower 95 % confidence intervals are listed in Table 4. The model was able to describe the experimental data well, which is not only visible from the graphical presentation (Fig. 2), but is also indicated by low *RMSE* (0.021) and high R^2 values (0.995). Similarly, good performance of the Ratkowsky square root model on the growth of *L. rhamnosus* GG in milk was also shown by Valík et al. (2008). Matejčeková et al. (2019) recorded a good

prediction (R^2 = 0.989) for *L. plantarum* in the three different substrates tested (UHT milk, lactose-free milk, and MRS broth). Furthermore, good prediction by the Ratkowsky model was also reported for *L. paracasei* (R^2 = 0.949) by Pelikánová et al. (2011), *L. plantarum* (R^2 = 0.992), and for *L. sakei* (R^2 = 0.993) by Rosa da Silva et al. (2018). In our experiments in oat beverages, the minimal and maximal temperatures for *L. rhamnosus* GG were estimated as follows: T_{min} = 4.2 °C (theoretical minimum), and T_{max} = 47.8 °C.

The secondary model (Eq. (7)) was applied to describe the temperature dependence of the lag phase duration, compatible with constant $Q_{0,10} = \log q_{0,av}$ or $h_0 = h_{0,av}$ in the Baranyi model Eq. (1–2), expressing the link relationship between λ, μ_{max} and q_0 (Garre et al., 2025). Calculations and predictions of the lag phases are summarised in Table 5. The first λ_1 value for the given temperature was calculated from the Baranyi model, the second and third lag phases were either "purely" predicted (all parameters are fixed as constant) or calculated for the estimated b_λ parameter. Results summarised in Table 5 show that the Baranyi hypothesis on constant value of $\lambda \times \mu_{max}$ is compatible with the temperature interval

Tab. 5. Calculations and predictions of lag phases of *L. rhamnosus* GG in oat beverage for the biokinetic temperature range of 12 to 44 °C.

T (°C)	λ_1 (h)	λ_2 (h)	λ_3 (h)
12	10.71	10.37	10.57
15	5.92	5.41	5.52
18	2.83	3.31	3.38
21	1.82	2.24	2.28
25	1.17	1.46	1.49
30	0.91	0.95	0.97
37	0.52	0.62	0.63
40	0.51	0.58	0.59
44	0.68	0.78	0.80

λ_1 value is calculated from the primary predictive Baranyi model; λ_2 value is predicted by secondary model (Eq. (8)) for

$$b_\lambda = \sqrt{\frac{b_\mu^2}{\ln\left(1+\frac{1}{q_{0,av}}\right)}} = \sqrt{\frac{b_\mu^2}{h_{0,av}}} = 0.0398$$

λ_3 is obtained using secondary model (Eq. (8)) for estimated prameter $b_{\lambda 3}$ = 0.0394 ±0.0012, R^2 = 0.991.

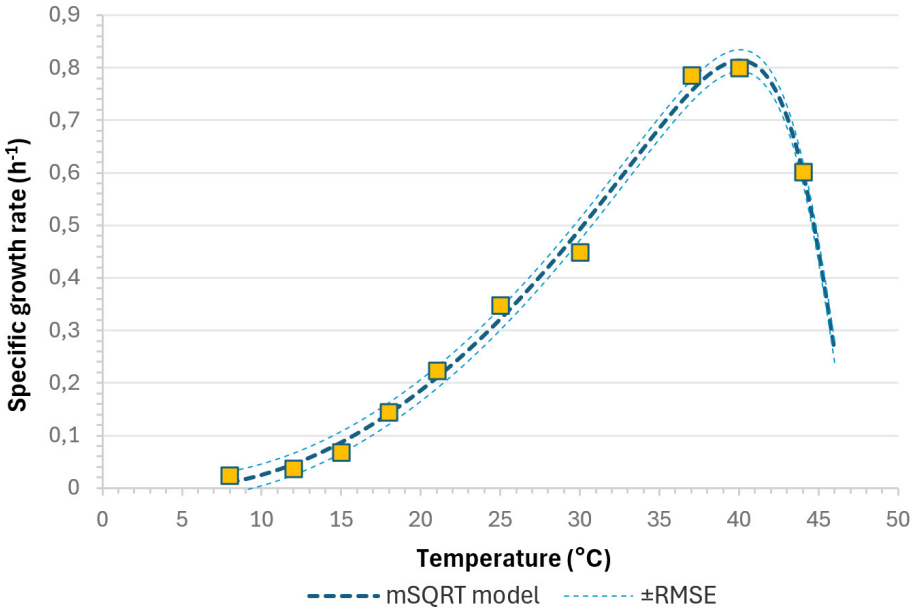

Fig. 2. Experimental data fitting using modified Ratkowsky square root model (mSQRT). Values from primary growth curves are depicted using solid markers and the curve represents the prediction line generated from the mSQRT model.

Tab. 4. Parameters of modified square root model with 95 % confidence intervals.

Parameter	$b_\propto$ ($h^{-1}.°C^{-1}$)	T_{min} (°C)	T_{max} (°C)	$c_\propto$ ($h^{-1}.°C^{-1}$)	R^2	*RMSE*
Value	0.0273 ±0.0049	4.20 ±3.77	47.79 ±2.51	0.330 ±0.260	0.995	0.021

from 12 to 44 °C and R^2 values 0.990 and 0.991 for the predicted ($b_{\lambda 2}$ = 0.0398) and calculated delay phases ($b_{\lambda 3}$ = 0.0394 ±0.0012), respectively.

Conclusion

Lacticaseibacillus rhamnosus GG is commonly used as a probiotic strain in various types of food, mainly in dairy products. The growing need to use alternative sources of plant origin, preference of some groups of consumers, or social pressure to replace dairy products create new challenges for food producers. This also applies to new applications to expand probiotic bacteria carriers in various specific matrices of plant origin. Therefore, the growth characteristics of the probiotic *L. rhamnosus* GG in oat beverages were studied as affected by the incubation temperature. *L. rhamnosus* GG showed good growth properties in the temperature range of 12 °C to 44 °C. Cardinal temperatures were evaluated using the mSQRT model (T_{min} = 4.2 °C; T_{max} = 47.8 °C). Due to the decrease in *pH* to final values ranging from 3.73 to 4.73, *L. rhamnosus* GG may represent a suitable option for the fermentation of alternative milk products based on oats. The results provide essential insights for food manufacturers to consider when formulating and developing fermented plant-based dairy alternatives to select strains with known growth or survival characteristics.

Acknowledgments
The authors gratefully acknowledge financial support from APVV-190031 and VEGA 1/0132/23.

References

Adamberg K, Kask S, Laht TM, Paalme, T (2003) Int J Food Microbiol 85: 171–183.
Baranyi J, Roberts TA (1994) Int J Food Microbiol 23(3–4): 277–294.
Baranyi J, Pin C, Ross T (1999) Int J Food Microbiol 48: 159–166.
Costa Menezes NM, Martins WF, Longhi DA, Falcão de Aragão GM (2018) 139: 113–119.
Garre A, Valdramidis V, Guillén S (2025) Int J Food Microbiol 431: 111078.
Havlicek LL, Crain RD (1988) Practical Statistics for the Physical Sciences. American Chemical Society Washington.
Kütt ML, Orgusaar K, Stulova I, Priidik R, Pismennõi D, Vaikma H, Kallastu A, Zhogoleva A, Morell I, Krišči unaite T (2023) Heliyon 9(5): e15627.
Li MY, Sun XM, Zhao GM, Huang XQ, Zhang JW, Tian W, Zhang QH (2013) J Food Sci 78(4), M600–M604.
Liptáková D, Valík Ľ, Lauková A, Strompfová V (2007) Czech J Food Sci, 25: 272–282.
Marchwińska K, Gwiazdowska, D, Juś K, Gluzińska P, Gwiazdowska, J, Pawlak-Lemańska K (2023) Appl Sci 13(23): 12707.
Martins WF, Longhi DA, Falcão de Aragão GM, Melero B, Rovira J, Diez AM (2020) Int J Food Microbiol 318: 108466.
Masiá C, Geppel A, Jensen PE, Buldo P (2021) Foods 10(3): 573.
Matejčeková Z, Liptáková D, Spodniaková S, Valík Ľ (2016) Acta Chim Slov 9(2): 104–108.
Matejčeková Z, Spodniaková S, Dujmić E, Liptáková D, Valík Ľ (2019) J Food Nutr Res 58(2): 125–134.
McKellar RC, Lu X (2004) Modeling Microbial Responses in Food. Boca Raton: CRC Press.
Medveďová A, Mančušková T, Valík Ľ (2016) Acta Aliment 45(1): 104–111.
Mosel DA, Corry JE, Struik CB, Baird R (1995) West Sussex: John Wiley & Sons, Inc.
Østlie HM, Helland MH, Narvhus JA (2003) Int J Food Microbiol 87: 17–27.
Pelikánová J, Liptáková D, Valík Ľ (2011) Potravinárstvo 5: 187–191.
Ratkowsky DA, Lowry RK, McMeekin TA, Stokes AN, Chandler RE (1983) J Bacteriol 154: 1222–1226.
Rosa da Silva AP, Longhi DA, Dalcanton F, Falcão de Aragão GM (2018) BABT 61: 18160159.
Segers ME, Lebeer S (2014) Microb Cell Fact 13: 1–16.
Valík Ľ, Medveďová A, Liptáková D (2008) J Food Nutr Res 47 (2): 60–67.
Zwietering MH, De Koos JT, Hasenack BE, De Wit JC, Van't Riet K (1991) Appl Environ Microbiol 57(4): 1094–1101.

sciendo

Aflatoxin M_1 in cheese: situation on the Slovak market

Lukáš Kolarič, Emma Vinohradská, Peter Šimko

Slovak University of Technology in Bratislava, Faculty of Chemical and Food Technology, Institute of Food Science and Nutrition, Department of Food Technology, Radlinského 9, 812 37 Bratislava, Slovak Republic
lukas.kolaric@stuba.sk

Abstract: Aflatoxin M_1 (AFM_1), which is a hydroxylated metabolite of aflatoxin B_1, can be irreversibly bound to casein micelles and thus, its higher content is measured in cheese than in the original milk. The present study describes validation of a reliable and rapid method for AFM_1 content determination in cheese applied to 36 kinds of cheese sold in Slovakia during the spring of 2024. The method consisted of three basic steps: extraction of AFM_1 from cheese, purification of extracts using immunoaffinity columns, and determination of AFM_1 content by high performance liquid chromatography with fluorescence detection. Suitability of the method was proved by the limits of detection and quantification equal to 2.0 and 6.0 ng/kg, respectively, which is in accordance with the limits set by European legislation for analytical procedures for AFM_1 determination in milk. Accuracy of the method was determined using a recovery test, spiking cheese with AFM_1, and varied between 87.8 and 100.5 %. Precision was confirmed by low relative standard deviations, 0.3—7.9 %, and Hor-Rat values (0.01—0.32) of the results obtained on different days. Experiments showed the AFM_1 content in all cheese to be below the limit of quantification, which indirectly confirmed the absence of AFM_1 in milk as raw material. However, AFM_1 contamination of milk is expected to increase due to global warming in future; therefore, AFM_1 contamination should be an essential part of current food safety issues.

Keywords: aflatoxin M_1, cheese, detection, food control, high performance liquid chromatography, validation

Introduction

Mycotoxins are secondary metabolites of filamentous fungi found in food and feed. It is estimated that more than 25 % of agricultural production in the world is contaminated with mycotoxins, the concentration of which is higher than the limits of EU or Codex Alimentarius (Eskola et al., 2020). These toxins are produced by the activity of filamentous fungi of the genus *Aspergillus flavus* and *A. parasiticus* during the production of agricultural crops, their storage, and processing into feed or food. One of the most dangerous mycotoxins is aflatoxin B_1 (AFB_1), which is a commonly occurring contaminant in cereal-based foods (Williams et al., 2004). AFB_1 is metabolized in the liver of animals by the hepatic microsomal mixed function oxidase system (cytochrome P450) to a reactive epoxide intermediate, while approximately 0.5 to 5 % is hydroxylated to less harmful aflatoxin M_1 (AFM_1), which is then excreted into milk (Popescu et al., 2022). According to the recent Risk Assessment of the presence of aflatoxins in food published by the European Food Safety Authority (EFSA) (EFSA CONTAM Panel, 2020), chronic dietary exposure to aflatoxins was estimated using a dataset of 209 802 analytical results from 69 166 samples. In adults, the mean lower limit (LB) exposure to AFB_1 ranged from 0.22 to 0.49 ng/kg body weight per day and the mean upper limit exposure (UB) ranged from 1.35 to 3.25 ng/kg body weight per day. The highest estimated exposure to AFM_1 was in infants with the mean exposure of 1.6/2.0 ng/kg (LB/UB) body weight per day. The main contributors to the overall AFM_1 mean exposure were liquid milk and fermented milk products in all age groups. According to the Rapid Alert System for Food and Feed (RASFF), aflatoxins accounted for 20.9 % (10 302) of the total number of notifications from 2002 to 2020 (Bhardwaj et al., 2023). The latest RASFF report from 2022 (2023) showed that mycotoxins were the third most notified category (485 notifications with a 10.5 % increase compared to 2021), with notifications mainly related to the detection of the presence of aflatoxins (413).
The concern about AFM_1 contamination in milk and dairy products is significant mainly due to factors such as high toxicity at low concentrations, association with liver and kidney cancer, and thermal stability to autoclaving, pasteurization, and sterilization. Carcinogenic potency of AFM_1 is lower than that of AFB_1 (about 1 tenth of that of AFB_1). However, AFM_1 is also classified as a group 1 compound carcinogenic to humans by the International Agency for Research on Cancer (IARC) (Sarmast et al., 2021; Stella et al., 2024). Therefore, several organizations and countries limited the maximum tolerable residue level of AFM_1 in milk and dairy products, i.e. 50 ng/kg for raw milk or thermally

treated milk, and 25 ng/kg for infants' foods in European Union (Commission Regulation, 2023), 500 ng/kg for milk in the USA (Popescu et al., 2022), 50 ng/kg for milk, and 250 ng/kg for cheese in Turkey (Vaz et al., 2020), or 100 ng/kg for different types of milk in Iran (Popescu et al., 2022).

Due to the high consumption of milk and dairy products and the health hazards of AFM_1, global occurrence of AFM_1 in these products has emerged as one of the most critical issues in past decades, especially in immunologically vulnerable age groups (Muaz et al., 2022). Recently, many scientific publications have focused on AFM_1 content determination in milk and dairy products. Over the last five years, more than 270 research articles and more than 170 review articles have been recorded in the Web of Science database. The content of AFM_1 in these products significantly varied worldwide (0—3520 ng/kg), whereas the raw and thermal processed milk represents the most studied category. Generally, it can be postulated that variability of AFM_1 content in dairy products is closely related to the geographic location, development level of each country, season, livestock management, and dairy processing systems (Kolarič et al., 2024). The review by Muaz et al. (2022) on AFM_1 occurrence in milk and dairy products in different countries from 2016 to 2020 showed the presence of AFM_1 in more than 50 % tested samples. High number of contaminated samples was noticed mainly in Asian and African countries. None of the studies in Europe indicated mean AFM_1 levels above 50 ng/kg (Muaz et al., 2022). However, several other studies indicated also contaminated milk samples in Europe; Bilandžić et al. (2022), Jajić et al. (2019), and Ferrari et al. (2023) reported 109, 245, and 667 positive raw milk samples in Croatia, Serbia, and Italy, respectively. In our previous study (Kolarič and Šimko, 2023), 25 milk and dairy samples were analyzed for AFM_1 content, and none were positive. Moreover, long periods of high temperatures and long-lasting drought summers in European countries with moderate climate over the last decade led to increased incidence of AFB_1 in dairy cow feed and elevated AFM_1 levels in milk and dairy products (Bilandžić et al., 2022). Regarding the distribution of AFM_1 in milk, it can be associated with different parts of milk, mainly with the milk serum and casein, while its concentration in fat fraction is lower (Muaz et al., 2022). It is also reported that the level of AFM_1 can be approximately 3—5 times higher in cheese than in the original milk due to its high affinity for hydrophilic parts of casein or whey proteins (Khaneghah et al., 2021).

Different analytical techniques have been developed for the determination of AFM_1 concentration in milk and dairy products, such as thin layer chromatography (TLC), high performance liquid chromatography (HPLC), and enzyme-linked immunosorbent assay (ELISA). The first Association of Analytical Communities (AOAC) officially approved method for the detection of AFM_1 levels was TLC; however, it is no longer used due to its high detection limit (above 50 ng/kg) and low accuracy. ELISA methods are easy to operate, but confirmation with other detection techniques might be required. Nowadays, HPLC with fluorescence detection (HPLC-FLD) is the official AOAC method for the determination of AFM_1 in dairy products, including cheese (Michlig et al., 2016; Sarmast et al., 2021). Performance criteria for AFM_1 detection methods, including recommended recovery and reproducibility values, are included in Commission Regulation (EC) No. 401/2006. Before detection of AFM_1 by a proper technique, sample preparation steps usually include pretreatment to remove fat and other impurities, centrifugation and filtration stages, as well as extraction or clean-up of samples. Extraction of AFM_1 from cheese samples may also involve slurry preparation (Vaz et al., 2020). An easy and rapid pretreatment step can be provided by applying immunoaffinity column technology (IAC), which combines the extraction and cleanup stages of the analysis (Kolarič and Šimko, 2023). Other options include the application of conventional solid phase extraction columns (SPE), liquid-liquid extraction (LLE), or one-step multifunctional cleanup columns (MycoSep) (Iqbal et al., 2015).

In our previous study (Kolarič and Šimko, 2023), a reliable and precise HPLC-FLD method using IAC extraction was developed and validated for AFM_1 determination in milk and some dairy products. The percentage of AFM_1 recovery reached up to 90.5 % with the limit of detection (LOD) and limit of quantification (LOQ) of 2 and 7 ng/kg, respectively. However, many recent studies described the binding of AFM_1 to casein proteins (Khaneghah et al., 2021), thus AFM_1 can concentrate in cheese to reach detectable levels in comparison to milk. Therefore, the aim of this study was to develop and validate a method for AFM_1 determination in cheese. For that purpose, soft cheese was made from milk spiked with AFM_1. Finally, the method was used to determine AFM_1 content in 36 kinds of cheese available on Slovak market.

Material and Methods

Chemicals and Samples

AFM_1 analytical standard in acetonitrile with the concentration of 0.5 µg/mL, Celite 545 (particle size of 0.02—0.1 mm), and Phosphate buffered saline

(PBS) were purchased from Sigma-Aldrich (USA). Acetonitrile and methanol were HPLC grade and were obtained from Honeywell International Inc (Germany). Liquid rennet (100 % chymosin) and calcium chloride (saturated solution, 33 %) were purchased from Milchema s.r.o. (Považská Bystrica, Slovakia).

Evaluation of AFM_1 contamination in cheese was performed on 36 kinds of cheese obtained from four Slovak dairy factories or local supermarkets. A complete list is included in Table 1. All cheese was purchased during March and April 2024.

Laboratory production of fresh cheese

The cheese was prepared from 1 L of pasteurized cow milk according to modified procedures published by Elsamani et al. (2014) and Kolarič et al. (2022). First, milk was heated to 35 °C and 2 mL of liquid rennet and calcium chloride solution were added. The mixture was stirred for 10 min and left to coagulate for 2 h. The curd was then cut for whey separation, first into pieces of 2 × 2 cm and after 10 min to smaller pieces. The cheese curd was finally placed into a mold lined with a clean cloth and left to settle in the refrigerator overnight. After that, the cheese was removed from the mold and cut into pieces for analysis. The cheese contaminated with AFM_1 was prepared by the same procedure, however AFM_1 standard solution was added into the milk at the concentration of 0.7 ng/mL prior to further processing.

Determination of AFM_1 content in cheese

Extraction of AFM_1 from different kinds of cheese was performed according to modified procedure by Yoon et al. (2016). A sample of 5 g of cheese was transferred quantitatively to a mortar with Celite 545. The mixture was then homogenized with a pestle and quantitatively transferred to a 100 mL Erlenmayer flask. Then, 25 mL of acetonitrile:water (ACN:H_2O) solution (60:40, v/v) were added and the mixture was stirred for 15 min at 4000 rpm using an orbital shaker. This extract was then centrifuged at 3000 rpm for 10 min. Subsequently, 10 mL of the supernatant were diluted with 30 mL of phosphate buffer solution (PBS, pH 7.4) and the solution was filtered using a filter funnel, while 30 mL of the filtrate was taken and used for immunoaffinity extraction (IAC). The extraction of AFM_1 from the filtrate using an IAC column (Vicam, AFM_1) was performed according to the validated method by Kolarič and Šimko (2023). Moreover, AFM_1 was also extracted from whey obtained during cheese production. The tested sample was transferred to the column with a syringe and passed at the flow rate of 2–3 mL/min in a vacuum manifold. The column was then washed twice with 10 mL of deionized water and AFM_1 was eluted with 1.25 mL of a methanol/acetonitrile solution (3:2, v/v) and 1.25 mL of water. Eluted extracts were injected into an HPLC.

HPLC conditions

The HPLC system (Agilent Technologies 1260 infinity system, Santa Clara, CA, USA) consisted of a vacuum degasser, quarterly pump, autosampler, and a fluorescence detector (FLD). Isocratic elution was carried out at the flow rate of 0.8 mL/min using a mobile phase consisting of water and acetonitrile, 80:20 (v/v). The injection volume was 50 µL. An InfinityLab Poroshell 120 C_{18} column (3 × 100 mm, 2.7 µm particle size) with an InfinityLab Poroshell 120 guard column (3 × 5 mm, 2.7 µm particle size) were used as the stationary phase. An FLD detector was set to excitation wavelength of 360 nm and emission wavelength of 440 nm. Retention time of AFM_1 was 4.5 min. Results were recorded using the OpenLab CDS software, ChemStation Edition for LC, and LC/MS systems (product version A.01.08.108).

Statistical evaluation and method validation

All results were statistically evaluated using Microsoft Excel 365 (version 2012) and expressed as average ±standard deviation or as a percentage. The measurements were repeated at least three times.

Before the determination of AFM_1 content in cheese, the method was validated according to Kolarič and Šimko (2023), where complete *in-house* validation used a certified reference material (ERM-BD284, whole milk powder). In this research, *in-house* validation was performed using laboratory prepared contaminated cheese and spiked commercial cheese (no. 3 in Table 1). The calibration curve was calculated by plotting the FLD signal against the known amount of AFM_1 standards at 0.01, 0.03, 0.05, 0.07, 0.1, 0.3, and 0.5 ng. Subsequently, the linearity was recorded from the correlation coefficient (R^2), while the limit of detection (LOD) and limit of quantification (LOQ) were calculated as 3- and 10-fold the standard deviation divided by the slope of the calibration curve, respectively. Accuracy of the method for AFM_1 content determination in cheese was studied as a recovery test of the extraction of AFM_1: 1. In cheese artificially contaminated with AFM_1 at three concentrations (0.5, 0.7, and 1.0 ng/mL), and 2. In cheese prepared from milk contaminated at concentration of 0.7 ng/mL. Precision of the method was evaluated from repeatability, intermediate precision, and the Horwitz ratio (HorRat). Repeatability was calculated from the relative standard deviation (RSD)

Tab. 1. List of evaluated kinds of cheese.

No.	Name	Source	City and State
1	Bryndza, fat in dry matter 48 %	Local supermarket	Bratislava, Slovakia
2	Cottage cheese natural, fat content 4.2 %	Local supermarket	Bratislava, Slovakia
3	Processed cheese, fat in dry matter 43 %	Local supermarket	Bratislava, Slovakia
4	Processed curd cheese, fat content 26 %	Local supermarket	Bratislava, Slovakia
5	Eidam, fat in dry matter 45 %	Dairy company	Levice, Slovakia
6	Cheese threads unsmoked, fat in dry matter 35 %	Dairy company	Bánovce nad Bebravou, Slovakia
7	Cheese threads, fat in dry matter 25 %	Dairy company	Stankovany, Slovakia
8	Unsmoked cow cheese, fat in dry matter 25 %	Dairy company	Stankovany, Slovakia
9	Semi-soft unripened cow cheese, fat in dry matter 50 %	Dairy company	Bánovce nad Bebravou, Slovakia
10	Semi-hard unripened cow cheese, fat in dry matter 50 %	Dairy company	Bánovce nad Bebravou, Slovakia
11	Cheese with noble mold, production date 25th of January 2024, fat in dry matter 50 %	Dairy company	Levice, Slovakia
12	Cheese with noble mold, production date 15th of February 2024, fat in dry matter 50 %	Dairy company	Levice, Slovakia
13	Cheese with noble mold, production date 27th of February 2024, fat in dry matter 50 %	Dairy company	Levice, Slovakia
14	Cheese with noble mold, production date 4th of March 2024, fat in dry matter 50 %	Dairy company	Levice, Slovakia
15	Cheese with noble mold, production date 27th of March 2024, fat in dry matter 50 %	Dairy company	Levice, Slovakia
16	Cheese with noble mold, production date 20th of February 2024, fat in dry matter 50 %	Dairy company	Levice, Slovakia
17	Cheese with noble mold, production date 11th of March 2024, fat in dry matter 50 %	Dairy company	Levice, Slovakia
18	Cheese with noble mold, production date 4th of April 2024, fat in dry matter 50 %	Dairy company	Levice, Slovakia
19	Cheese with noble mold, production date 20th of February 2024, fat in dry matter 55 %	Dairy company	Levice, Slovakia
20	Cheese with noble mold, production date 14th of March 2024, fat in dry matter 55 %	Dairy company	Levice, Slovakia
21	Cheese with noble mold, production date 9th of April 2024, fat in dry matter 55 %	Dairy company	Levice, Slovakia
22	Mozzarella grated, fat in dry matter 45 %	Local supermarket	Bratislava, Slovakia
23	Eidam unsmoked, fat in dry matter 45 %	Dairy company	Levice, Slovakia
24	Eidam smoked, fat in dry matter 45 %	Dairy company	Levice, Slovakia
25	Cheese balls (fresh cheese with herbs), fat in dry matter 25 %	Dairy company	Stankovany, Slovakia
26	Cheese balls (fresh cheese with garlic), fat in dry matter 25 %	Dairy company	Stankovany, Slovakia
27	Cheese balls (fresh cheese with paprika), fat in dry matter 25 %	Dairy company	Stankovany, Slovakia
28	Cheese balls (fresh cheese with gyros pepper), fat in dry matter 25 %	Dairy company	Stankovany, Slovakia
29	Salami cheese unsmoked, fat in dry matter 45 %	Dairy company	Levice, Slovakia
30	Salami cheese smoked, fat in dry matter 45 %	Dairy company	Levice, Slovakia
31	Brick cheese smoked, lactose free, fat in dry matter 45 %	Dairy company	Levice, Slovakia
32	Cheese for grill, fat in dry matter 45 %	Dairy company	Levice, Slovakia
33	Curd defatted, fat in dry matter 5 %	Dairy company	Bánovce nad Bebravou, Slovakia
34	Curd, fat in dry matter 38 %	Dairy company	Bánovce nad Bebravou, Slovakia
35	Salted cheese unripened, fat in dry matter 46 %	Dairy company	Leštiny, Slovakia
36	Salted cheese ripened, fat in dry matter 46 %	Dairy company	Leštiny, Slovakia

of four replicates of the samples on the same day, and intermediate precision was then recorded from RSD on three different days. The Horwitz ratio (HorRat) was calculated as the ratio of the observed RSD to the corresponding predicted relative standard deviation (PRSDR): PRSDR (%) = 2C(–0.15), where C is the concentration expressed as mass fraction (Horwitz and Albert, 2006).

Results and discussion

Validation of the method for AFM_1 determination in cheese

Results of *in-house* validation of the proposed method are summarized in Table 2. The calibration curve was linear in all concentration ranges from 0.01 to 0.5 ng of AFM_1, while R^2 was calculated to be 1. LOD and LOQ values were also satisfactory, 2.0 and 6.0 ng/kg, respectively. Thus, this method can be used for the determination of AFM_1 even below the maximum tolerable residue level. According to EU regulations, the maximum level of AFM_1 in raw milk, heat-treated milk and milk for milk-based products production is 50 ng/kg, while that for infant formulae and food for special medical purposes for infants and young children is only 25 ng/kg (Commission Regulation, 2023). Regarding cheese, there is no legal limit for maximum level of AFM_1, so it varies depending on the country; however, it is set to 250 ng/kg in most European countries. In Italy, different limits are applied for soft cheeses (250 ng/kg) and hard cheeses (450 ng/kg) (Ismail et al., 2016; Mudannayake et al., 2024). The same LOD for AFM_1 analysis in dairy products was described by Murshed (2020). Higher LOD and LOQ were described by Škrbić et al. (2015), 38.0 and 125.0 ng/kg in white cheese, and 6.0 and 20.0 ng/kg in hard cheese, respectively; however, a different analytical technique (UHPLC-MS/MS) was used. Iha et al. (2011) calculated the LOD and LOQ to 3 ng/kg and 10 ng/kg, respectively, for the HPLC-FLD method of AFM_1 determination in cheese, yogurt, and dairy beverages. Jakšić et al. (2021) compared two analytical methods for the evaluation of AFM_1 in cheese, ELISA and HPLC-FLD, concluding that LOD for ELISA was higher (25 ng/kg) than for HPLC-FLD (10 ng/kg), but still below the reference values of AFM_1 in these products.

Accuracy of the method was studied as a recovery test. First, recovery was calculated as the percentage of AFM_1 extracted from commercial cheese spiked with three different concentrations of AFM_1 (0.5, 0.7, and 1.0 ng/mL). The recovery varied from 87.8 % to 100.5 %, respectively, with RSD in the range from 3.4 % to 4.3 %, respectively. According to Regulation (EU) No. 401/2006 laying down the methods of sampling and analysis for official control of mycotoxin levels in foodstuffs, recovery values in samples with AFM_1 concentration in the range of 0.01—0.05 ng/mL should be 60—120 %, and for samples with AFM_1 concentration above 0.05 ng/mL, in the range of 70—110 %, which agrees with the results of this work. Cattaneo et al. (2011) spiked three soft fresh Italian cheese samples with AFM_1 concentrations of 0.1, 0.25, and 0.5 ng/mL. The mean recoveries varied from 77.3 to 70.8 %. Moreover, their results also showed that the highest recovery value of 95 % was obtained using the enzymatic digestion procedure. Pietri et al. (2016) also used enzyme-assisted extraction of AFM_1 from cheese, noticing that recoveries ranged from 87.1 to 88.5 % when using chloroform extraction, while they reached 95.4 to 96.3 % by applying pepsin extraction. AFM_1 recovery rates from cheese samples published by Yoon et al. (2016), who used the same extraction conditions as in this study, were 83.2, 83.7, and 98.7 % at the spiking levels of 0.1, 0.25, and 0.5 ng/mL of AFM_1, respectively. The acetonitrile/water extraction solution was also applied by Škribić et al. (2015) in the determination of AFM_1 content in white and hard cheese samples with the recovery of the method ranging from 73—111 % for white cheese and from 71—80 % for hard cheese. All these studies, however, calculated the method recovery spiking AFM_1 standard directly to the cheese. Accuracy of the method for AFM_1 content determination in cheese can also be influenced by the association of AFM_1 with milk proteins (especially casein). Thus, the recovery test was also done in the laboratory produced cheese prepared with artificially contaminated milk (0.7 ng/mL of AFM_1), showing that 24.2 % of AFM_1 was released into the whey and the remaining 75.8 % into the cheese curd. Recovery of the proposed method was then calculated from the sum of AFM_1 in cheese curd and whey. In this approach, recovery value was 94.7 % with RSD of 2.6 %. Similar results were published by Iha et al. (2013). In their research, milk samples naturally contaminated with AFM_1 concentrations of 0.1 ng/mL were used to produce soft cheese. The mean recovery of AFM_1 from cheese was 71 % and from whey it was 39 %. Cavallarin et al. (2014) studied the transfer rate of AFM_1 from milk to three ripened traditional Italian cheese products. In the Robiola cheese made from milk contaminated with AFM_1 at 0.01 ng/mL, 30.7 % of AFM_1 was transferred to whey and 68.0 % to curd. But Primosale and Maccagno cheese products showed higher percentage of AFM_1 transferred to whey, 60—82 % of the total amount of AFM_1 present in milk, sug-

gesting that partitioning of AFM_1 between cheese and whey depends on the type of manufacturing. Moreover, transfer of AFM_1 from milk to cheese was found to be significantly related to moisture loss during processing than to the cheese manufacturing procedure.

The last step in *in-house* validation of the proposed method, precision was evaluated from repeatability (obtained RSD values of results in one day) and intermediate precision (obtained RSD values of results in three different days). For this purpose, laboratory prepared cheese from artificially contaminated milk was used. Repeatability varied from 0.3 to 7.9 %, and intermediate precision was calculated to be 5.8 %. Precision of the method should also be approved by the HorRat parameter, which is lower than or equal to 2 (Ribeiro and Brandão, 2017). In this work, HorRat ranged from 0.01 to 0.32, demonstrating excellent precision of this method for AFM_1 determination in cheese. Yoon et al. (2016), who used similar conditions, reached RSD for repeatability and intermediate precision in the range of 9.1—13.1 % and 2.1—12.8 %, respectively. Extraction of AFM_1 from white and hard cheese using an dichloromethane/acetone mixture and UHPLC-MS/MS detection, resulted in RSD of repeatability varying from 7—9 % and 4—10 %, respectively (Škribić et al., 2015). Kamel et al. (2017) compared two analytical techniques, LC with a single quadrupole and tandem MS for the analysis of AFM_1 level in white cheese. Recovery and precision values were 99.3 % and 8.7 % for single quadrupole and 100 % and 6 % for tandem MS, respectively. Peña-Rodas et al. (2020) validated the method for AFM_1 content determination in hard white cheese products and showed HorRat values between 0.92 to 1.04, while no significant differences were observed between the five days of the validation test.

Determination of AFM_1 content in cheese

Cheese as one of the most popular dairy products is manufactured by different technologies, while the primary consumers of cheese are Europe, North America, and Oceania (Khaneghah et al., 2021).

Tab. 2. Validation parameters for AFM_1 determination in cheese by HPLC-FLD method

Method linearity				
Slope	5595.9			
Intercept	5.7684			
Correlation coefficient (R^2)	1.0			
LOD [ng/kg]	2.0			
LOQ [ng/kg]	6.0			
Method recovery[a]				
Laboratory prepared fresh soft cheese	The level of AFM_1 standard added to raw milk [ng/mL]	Determined value [ng/kg]	Recovery [%]	
	0.70	0.50 ±0.02 (cheese curd) 0.16 ±0.01 (cheese whey)	94.7 ±2.5	
Spiked cheese sample [ng/mL]	Determined value [ng/mL]	Recovery [%]		
0	> LOQ	-		
0.50	0.44 ±0.03	87.8 ±3.0		
0.70	0.67 ±0.05	95.6 ±3.6		
1.00	1.01 ±0.04	100.5 ±4.3		
Method precision[b]				
The level of AFM_1 in the laboratory prepared fresh soft cheese [ng/mL]	Repeatability	RSD [%]	Intermediate precision [RSD %]	HorRat
0.50 ±0.02	Day 1	7.9	5.8	0.32
	Day 2	0.3		0.01
	Day 3	3.8		0.15

Values are expressed as mean ±standard deviation, [a]n = 3, [b]n = 4;

AFM_1 — aflatoxin M_1, LOD — limit of detection;

LOQ — limit of quantification, RSD — relative standard deviation.

Contamination of cheese with AFM_1 can thus cause serious health problems, while the prevalence of AFM_1 in cheese may occur due to (Khaneghah et al., 2021):

1. Contamination of feed with AFB_1 eaten by lactating animals (biotransformation of AFB_1 into AFM_1 excreted in milk).
2. Prevalence of AFM_1 in dried milk applied in the formulation of some cheeses.
3. Growing of toxigenic *Aspergillus spp.* on cheese during maturation and consequent synthesis of aflatoxins.

The most important factor affecting the level of AFM_1 in cheese is its prevalence in raw materials, especially milk and powdered milk, due to the direct relationship between AFB_1 content in animal fodder and the level of AFM_1 in milk. The conditions of handling in the supply chain, factory apparatuses, and hygiene must also be considered (Khaneghah et al., 2021). According to the systematic review published by Campagnollo et al. (2016), the rate of cheese contamination with AFM_1 is influenced by many factors, such as cheese type, type of unit operations, renneting temperature, pH of saturated brine, exposure of contaminated milk to light, or by the analytical method used for AFM_1 quantification.

In this study, 36 kinds of cheese obtained from different Slovak dairy factories or local supermarkets were analyzed for the presence of AFM_1. Eighteen samples were delivered from Levice, most of them were cheese with noble mold produced between January and April 2024. Other cheese originated from the regions of Liptov, Orava, or Bánovce nad Bebravou in Slovakia, comprising samples of soft fresh cheeses, curd cheese, or steamed cheese in the form of balls or threads. Experimental results showed negative AFM_1 presence (below LOQ of 6.0 ng/kg) in all samples. In Slovakia, the occurrence of AFM_1 in milk or dairy products is not widespread due to high hygienic control and mild climate conditions. Contamination of cheese with AFM_1 was, however, observed in some other European countries (Table 3). Montagna et al. (2008) analyzed 256 samples of cheese in Southern Italy made from milk of various species (cow, buffalo, goat, sheep, sheep-goat) in different ripening stage (fresh, medium, and long-term ripened cheese), with AFM_1 determined in 16.6 % of the analyzed samples and the highest positive incidence in medium and long-term ripened cheese samples made from sheep-goat milk. The range of AFM_1 in all samples was between 50 to 250 ng/kg. In 2012, Anfossi et al. (2012) published a one-year survey on the AFM_1 levels in cheese purchased on the Italian market. They analyzed a total of 102 samples, which were divided in four categories according to maturation, manufacturing, production season, and milk type. Detectable amount of AFM_1 was noticed in more than 83 % samples, with most of them containing AFM_1 concentrations between 50 and 150 ng/kg. Positive correlation between the milk type and manufacturing conditions of cheese was found, as more contaminated cheese samples were obtained from cows' milk and from artisan production. Škrbić et al. (2015) analyzed 23 white and 10 hard cheese samples purchased from the Serbian supermarkets during May and June 2013. The results revealed that 54 % of cheese samples were positive for AFM_1 contamination, while in 13 % samples, the AFM_1 level was above the limit of 250 ng/kg set by some European countries. They also noticed that the average content of AFM_1 was the highest in hard cheese samples (640 ng/kg) and the lowest in white cheese samples produced in households or small private farms (8 ng/kg). Cheese contamination with AFM1 in Serbia was investigated by Torović et al. (2021) during 2019–2020. Up to 70 % of all evaluated cheese samples were positive for the presence of AFM_1 (65.2 % of soft and 73 % of semi-hard cheese, but with no statistical difference). Moreover, the RASFF database showed one notification about the AFM_1 in cheese spread from Serbia in 2023 with maximum level of 370 ng/kg (RASFF, 2023). Malissiova et al. (2022) tested 25 kinds of feta cheese randomly purchased from Greek markets, with 7 samples positive for AFM_1, however, with very small average value (2.98 ng/kg), no sample exceeded the maximum tolerable limits. Ilievska et al. (2022) studied AFM_1 contamination in dairy products consumed in North Macedonia. The samples were collected between February and December 2013 and contained 36 kinds of brined white cheese and 65 kinds of hard yellow cheese. AFM_1 was detected in 86.1 % of the brined white cheese samples, with most of the samples not exceeding 100 ng/kg. Similar results were noticed for hard cheese samples, with 5 of them with AFM_1 content above 100 ng/kg. In Europe, available literature data on AFM_1 contamination of cheese is scarce (Jakšić et al., 2021). Recently published systematic review on AFM_1 contamination in cheese of six countries in the West Asia region (Mohammadi et al., 2022) showed that more than 50 % of cheese samples from all included countries were contaminated with AFM_1. Highly positive samples exceeding the maximum tolerable level of AFM_1 originated in countries such as Lebanon, Turkey, or Iran, which can be explained by differences in forage hygiene, geographical and climate conditions, economy, and the management systems from farm to table (Mohammadi et al.,

2022). Similar results were observed in a 20-year data review on the occurrence of AFM_1 in dairy products in Mediterranean countries published by Malissiova et al. (2024). The presence of AFM_1 in cheese was reported mainly in Turkey, Egypt, and Libya. Another global systematic review on the prevalence and concentration of AFM_1 in different types of cheese (Khaneghah et al., 2021) concluded that fresh cheese samples contained higher level of AFM_1 compared to other cheese types. Besides that, the prevalence of AFM_1 in cheeses was also influenced by the origin of milk (cheese from cow's milk was more contaminated than that from goat's or sheep's milk) as well as by the moisture content (hard > semi-hard > soft > semi-soft). The presence of AFM_1 in cheese was also recently observed in Sri Lanka, where 40 samples (80 %) out of the 50 analyzed samples were contaminated with AFM_1, while 34 % samples exceeded the overall regulatory levels for AFM_1 set by Codex Alimentarius Commission (500 ng/kg) and 74 % exceeded the level in Europe (Netherlands — 200 ng/kg). The results confirmed previously published observations that hard cheese is more contaminated than soft cheese samples (Mudannayake et al., 2024).

Conclusion

In this study, the HPLC-FLD method using IAC extraction was validated for the determination of AFM_1 content in cheese. It was proved that the proposed method provides accurate, precise, and sensitive results with LOD 2.0 ng/kg, which is below the AFM_1 limit set by the European regulation applicable for milk. Recovery of the method ranged from 87.8 % to 100.5 %, while its precision was confirmed by the HorRat parameter. Thus, it can be concluded that this method has satisfactory parameters for AFM_1 determination in cheese according to Regulation (EU) No. 401/2006. Subsequently, 36 kinds of cheese samples obtained in Slovakia were tested for the presence of AFM_1 with no positive result. However, due to global warming, the growth of toxigenic fungi is expected in countries with moderate climate. Previous results showed the presence of AFM_1 in cheese in other European regions, such as Serbia, Italy, Greece, or Spain. Furthermore, since AFM_1 has high affinity to casein, concentration of this toxin found in cheese was around 3—5 times higher than in the original raw milk. Therefore, the results of this study can serve as a basis for rapid and reliable detection of AFM_1 levels in cheese.

Acknowledgement
The authors would like to thank Ing. Pavol Štefánik from CLIMAX, Ltd. for providing cheese samples from Slovak dairy companies.
This work was supported by the Slovak Research and Development Agency under Contract APVV-22-0102.

Tab. 3. Occurrence of AFM_1 in cheese reported in some countries in 2010.

Country/Region	Cheese type	Positive/Total sample	Detected range of AFM_1 [ng/kg]	Reference
Slovakia	Different kinds of cheese	0/36	–	This study
Serbia	Commercial white cheese samples	10/23	130—550	Škrbić et al. (2015)
	Hard cheese samples	10/10	80—2230	
	White cheese samples produced in households and small private farms	9/21	130—220	
Italy	Different kinds of cheese	85/102	50—250	Anfossi et al. (2012)
Serbia	Different kinds of cheese	42/60	26—591	Torović et al. (2021)
Greece	Feta cheese	7/25	2—4	Malissiova et al. (2022)
Spain	Grated, fresh and semi-dried cheese samples	0/72	–	Cano-Sancho et al. (2010)
North Macedonia	Brined white cheese	31/36	< 11—795	Ilievska et al. (2022)
	Hard yellow cheese	58/65	< 11—366	
Turkey	Ezine cheese	60/120	19—158	Eker et al. (2019)
	Halva cheese	7/120	50—213	
Spain	Manchego cheese	–/82	2—522	Rubio et al. (2011)
Turkey	Different kinds of cheese	217/217	50—595	Yeşil et al. (2019)

References

2022 Annual Report Alert and Cooperation Network. European Commission, 2023, 22 pp.

Anfossi L, Baggiani C, Giovannoli C, D'Arco G, Passini C, Giraudi G (2012) Food Control 25: 125—130.

Bhardwaj K, Meneely JP, Haughey SA, Dean M, Wall P, Zhang G, Baker B, Elliott CT (2023) Food Control 149: 1—18. Article no. 109687.

Bilandžić N, Varga I, Varenina I, Kolanović BS, Luburić ĐB, Đokić M, Sedak M, Cvetnić L, Cvetnić Ž (2022) Foods 11: 1—16. Article no. 1959.

Campagnollo FB, Ganev KC, Khaneghah AM, Portela JB, Cruz AG, Granato D, Corassin CH, Oliveira CAF, Sant'Ana AS (2016) Food Control 68: 310—329.

Cano-Sancho G, Marin S, Ramos AJ, Peris-Vicente J, Sanchis V (2010) Rev. Iberoam. Micol. 27(3): 130—135.

Cattaneo TMP, Marinoni L, Barzaghi S, Cremonesi K, Monti L (2011) J. Chromatogr. A 1218: 4738—4745.

Cavallarin L, Antoniazzi S, Giaccone D, Tabacco E, Borreani G (2014) Food Control 38: 174—177.

Commission Regulation (EC) No 401/2006 of 23 February 2006 laying down the methods of sampling and analysis for the official control of the levels of mycotoxins in foodstuffs. Available on https://eur-lex.europa.eu/legal-content/EN/ALL/?uri=celex %3A32006R0401.

Commission regulation (EU) 2023/915 of 25 April 2023 on maximum levels for certain contaminants in food and repealing Regulation (EC) No 1881/2006. Available on https://eur-lex.europa.eu/eli/reg/2023/915/oj/eng.

EFSA CONTAM Panel (EFSA Panel on Contaminants in the Food Chain), Schrenk D, Bignami M, Bodin L, Chipman JK, del Mazo J, Grasl-Kraupp B, Hogstrand C, Hoogenboom LR, Leblanc JC, Nebbia CS, Nielsen E, Ntzani E, Petersen A, Sand S, Schwerdtle T, Vleminckx C, Marko D, Oswald IP, Piersma A, Routledge M, Schlatter J, Baert K, Gergelova P and Wallace H (2020) EFSA J. 18(3): 6040.

Eker FY, Muratoglu K, Eser AG (2019) Environ. Monit. Assess. 191: 1—8. Article no. 523.

Elsamani MO, Habbani SS, Babiker EE, Ahmed IAM (2014) LWT — Food Sci. Technol. 59: 553—559.

Eskola M, Kos G, Elliott CT, Hajšlová J, Mayar S, Krska R (2020) Crit. Rev. Food Sci. Nutr. 60(16): 2773—2789.

Ferrari L, Rizzi N, Grandi E, Clerici E, Tirloni E, Stella S, Bernardi CEM, Pinotti L (2023) Toxins 15: 1—10. Article no. 168.

Horwitz W, Albert R (2006) J. AOAC Int. 89(4): 1095—1109.

Iha MH, Barbosa CB, Favaro RMD (2011) J. AOAC Int. 94(5): 1513—1518.

Iha MH, Barbosa CB, Okada IA, Trucksess MW (2013) Food Control 29: 1—6.

Ilievska G, Stojanovska-Dimzoska B, Koceva D, Stojković G, Angeleska A, Dimitrieska-Stojković E. (2022) J. Food Qual. Hazards Control 9: 14—22.

Iqbal SZ, Jinap S, Pirouz AA, Faizal ARA (2015) Trends Food Sci. Technol. 46: 110—119.

Ismail A, Akhtar S, Levin RE, Ismail T, Riaz M, Amir M (2016) Crit. Rev. Microbiol. 42(3): 418—427.

Jajić I, Glamočić D, Krstović S, Horvatović PM (2019) J. Hellenic Vet. Med. Soc. 69(4): 1283—1290.

Jakšić S, Baloš MŽ, Popov N, Torović L, Krstović S (2021) Int. J. Dairy Technol. 74(4): 681—688.

Kamel E, Bazalou M, Sdeek FA, Konuk M (2017) Int. J. Food Prop. 20(2): 2294—2304.

Khaneghah AM, Moosavi M, Omar SS, Oliveira CAF, Karimi-Dehkordi M, Fakhri Y, Huseyn E, Nematollahi A, Farahani M, Sant'Ana AS (2021) Food Control 125: 1—8. Article no. 107960.

Kolarič L, Kántorová P, Šimko P (2022) Molecules 27: 1—13. Article no. 2919

Kolarič L, Minarovičová L, Lauková M, Kohajdová Z, Šimko P (2024) Trends Food Sci. Technol. 150: 1—9. Article no. 104603.

Kolarič L, Šimko P (2023) Acta Chim. Slovaca 16: 99—108.

Malissiova E, Soultani G, Tsokana K, Alexandraki M, Manouras A (2022) Clin. Nutr. ESPEN 47: 189—193.

Malissiova E, Tsinopoulou G, Gerovasileiou ES, Meleti E, Soultani G, Koureas M, Maisoglou I, Manouras AA (2024) Dairy 5: 491—514.

Michlig N, Repetti MR, Chiericatti C, García SR, Gaggiotti M, Basílico JC, Beldoménico HR (2016) Chromatographia 79: 1091—1100.

Mohammadi S, Keshavarzi M, Kazemi A, Rahmdel S, Nouri M, Rastegar A, Ghaffarian-Bahraman A (2022) Int. J. Dairy Technol. 75(3): 653—667.

Montagna MT, Napoli C, De Giglio O, Iatta R, Barbuti G (2008) Int. J. Mol. Sci. 9(12): 2614—2621.

Muaz K, Riaz M, de Oliveira CAF, Akhtar S, Ali SW, Nadeem H, Park S, Balasubramanian B (2022) Toxin Rev. 41(2): 588—605.

Mudannayake A, Karunarathne S, Jayasooriya PW, Nanayakkara D, Abesooriya A, Silva S, Fernando R (2024) Heliyon 10: 1—7. Article no. e35155.

Murshed S (2020) J. Food Qual. 2020: 1—8. Article no. 8839060.

Peña-Rodas O, Martinez-Lopez R, Pineda-Rivas M, Hernandez-Rauda R (2020) Toxicol. Rep. 7: 1157—1163.

Pietri A, Fortunati P, Mulazzi A, Bertuzzi T (2016) Food Chem. 192: 235—241.

Popescu RG, Rădulescu AL, Georgescu SE, Dinischiotu A (2022) Toxins 14: 1—15. Article no. 853.

RASFF (2023). Available on: https://webgate.ec.europa.eu/rasff-window/screen/notification/645846.

Ribeiro TMG, Brandão PRG (2017) Tecnol. Metal. Mater. Miner. 14(2): 183—189.

Rubio R, Licón CC, Berruga MI, Molina MP, Molina A (2011) J. Dairy Sci. 94: 2775—2778.

Sarmast E, Fallah AA, Jafari T, Khaneghah AM (2021) LWT — Food Sci. Technol. 148: 1—10. Article no. 111772.

Stella R, Bovo D, Noviello S, Contiero L, Barberio A, Angeletti R, Biancotto G (2024) Food Control 157: 1—7. Article no. 110149.

Škrbić B, Antić I, Živančev J (2015) Food Control 50: 111—117.

Torović L, Popov N, Živkov-Baloš M, Jakšić S (2021) J. Food Compos. Anal. 103: 1—7. Article no. 104122.

Vaz A, Silva ACC, Rodrigues P, Venâncio A (2020) Microorganisms 8: 1—16. Article no. 246.

Williams JH, Phillips TD, Jolly PE, Stiles JK, Jolly CM, Aggarwal D (2004) Am. J. Clin. Nutr. 80: 1106—1122.

Yeşil ÖF, Hatipoğlu A, Yuldiz A, Vural A, Erkan ME (2019) Erzincan University Journal of Science and Technology 12(1): 479—488.

Yoon BR, Hong SY, Cho SM, Lee KR, Kim M, Chung SH (2016) J. Food Nutr. Res. 55: 171—180.

sciendo

A fluorescent dye assay for antibody aggregates and its application in aggregate stability evaluation

Tomáš Molnár, Veronika Rupčíková, Simona Kotuličová, Milan Polakovič

Department of Chemical and Biochemical Engineering, Institute of Chemical and Environmental Engineering, Faculty of Chemical and Food Technology, Slovak University of Technology, Radlinského 9, 812 37 Bratislava, Slovakia
milan.polakovic@stuba.sk

Abstract: Aggregation of proteins naturally occurs during different stages of cultivation and downstream processes and is often associated with quality reduction in the final product. Therefore, determining the presence of aggregates is important. In this study, a fluorescence-based analytical method using the dye Nile red was developed for antibody aggregates quantification. The fluorescence assay demonstrated selectivity and sensitivity towards hydrophobic surfaces of aggregates within reliable quantification range of 0.0165—1.65 g/L. Validation confirmed high reproducibility, with intra-assay and inter-assay coefficients of variation within acceptable limits. The dye was stable in commonly used buffer systems and in the presence of salts. Comparative analysis of SEC and fluorescence methods indicated that fluorescence detection remains sensitive to aggregation beyond SEC's detection threshold. Thermal stability studies revealed that polyclonal antibodies have higher resistance to thermal stress than monoclonal antibodies, which suggests that structural variability plays an important role in thermal stability. Additionally, antibody aggregation was shown to be pH-dependent, with increased aggregation at both low and high pH levels. Polyclonal antibodies were stable at pH 5—6. In more acidic conditions, soluble aggregates were formed, while at neutral and basic pH, aggregation was accompanied by the formation of insoluble particles. The effect of salts on aggregation was variable, with NaCl promoting aggregation at high concentrations, NaSCN facilitating dissociation of aggregates, and Na_2SO_4 inducing precipitation. Guanidine HCl exhibited a stabilizing effect, preventing aggregation over time.

Keywords: monoclonal antibody, polyclonal antibody, fluorescence assay, aggregation, kinetics

Introduction

Protein-based pharmaceuticals represent the fastest growing group of biological therapeutics, with a wide range of important applications (Li et al., 2016). Among these, antibodies, also known as immunoglobulins — essential components of the immune system, play a critical role in identifying and neutralizing pathogens such as bacteria and viruses (Forthal, 2014). Their use in both therapy and diagnostics have expanded dramatically, especially with the development of monoclonal antibodies for treating cancer, autoimmune disorders, and infections (Lu et al., 2020).

A significant challenge in the production, storage, and administration of therapeutic antibodies is their propensity to aggregate (Vazquez-Rey and Lang, 2011). Understanding the mechanisms of antibody aggregation is crucial for developing strategies to mitigate this issue. Aggregation refers to the process in which individual antibody molecules bind together to form larger complexes. This process can be driven by intrinsic factors, such as antibody's primary sequence and structure, as well as extrinsic factors, including formulation conditions and physical stress like agitation and temperature or pH changes (Wang et al., 2010; Arosio et al., 2011; Arosio et al., 2013; Wolfrum et al., 2017).

Antibody aggregation can compromise product safety, efficacy, and shelf-life (Vazquez-Rey and Lang, 2011; Roberts, 2014), which makes accurate detection and quantification of aggregates essential. Several analytical methods are commonly used for this purpose, each with specific limitations. Size-exclusion chromatography (SEC) is widely employed, but its efficiency can be compromised by factors such as trapping of large aggregates on column prefilters (Arosio et al., 2013), dilution-induced aggregate dissociation due to the mobile phase (Carpenter et al., 2010), and pressure-induced aggregation within the system (Wang and Roberts, 2018).

Sedimentation velocity analytical ultracentrifugation (SV-AUC) offers high sensitivity over a wide concentration range but requires precise instrument calibration and operator expertise (Berkowitz, 2006; Arthur et al., 2009). Light obscuration (LO) is limited by its inability to differentiate between protein aggregates, air bubbles, and other particles, and its sensitivity is affected by aggregate size (den Engelsman et al., 2011; Hawe et al., 2020). Nanoparticle tracking analysis (NTA) can detect small particles (below 0.1 μm), but its accuracy is heavily dependent on instrument settings and sample purity (Gross et al., 2016).

An ideal analytical method should minimize interference from sample components, environmental background, and non-specific interactions (Zolls et al., 2012). During protein aggregation, hydrophobic

regions typically buried within the protein become exposed, which makes hydrophobic-binding fluorescent dyes particularly useful as they emit strong fluorescence only upon binding to these exposed surfaces (Demeule et al., 2007; Hawe et al., 2008; Hawe et al., 2009). The selection of an appropriate dye is essential, as fluorescent probes vary in their specificity and selectivity for different aggregate types (Hawe et al., 2008).

In this study, the use of the fluorescent dye Nile red for antibody aggregates quantification was investigated. Key performance parameters assessed included the dye's specificity for antibody aggregates, assay sensitivity, and reproducibility. The results were benchmarked against SEC, a standard technique in aggregate analysis. Additionally, stability studies were performed to examine the effects of pH, salt type, and temperature on antibody aggregation.

Materials and methods

Materials

In this study, polyclonal antibody solution Gammanorm was kindly provided by Octapharma (Vienna, Austria), and monoclonal antibody solution (Adalimumab, Humira, AbbVie, USA) was kindly provided by Sartorius Stedim Biotech (Goettingen, Germany). Black 96-well polystyrene microtiter plates were obtained from Greiner Bio-One (Frickenhausen, Germany). Guanidine hydrochloride and Tris base were purchased from Sigma–Aldrich (St. Louis, USA). Salts and other chemicals used for buffer preparation were obtained from Mikrochem (Pezinok, Slovakia). Aggregates for assay development were prepared by incubating polyclonal antibody solutions of defined concentration at 60 °C for 48 hours using a thermal shaker (Thermal Shake Lite, VWR, USA). Residual content of IgG monomers was verified by SEC, as described below.

Quantification of aggregates using fluorescence dye

Aggregate quantification was carried out in 96-well plates. Calibration curve was prepared by appropriately diluting aggregate samples in 10 mM acetate buffer (pH 5). For each measurement, 55 µL of 20 µM Nile red stock solution was mixed with 1045 µL of the sample. Then, 200 µL of the resulting mixture was transferred to each well and analyzed using a Synergy H1 fluorescence reader (BioTek, USA) with excitation wavelength of 590 nm and emission wavelength of 645 nm.

Size-exclusion chromatography

SEC was employed to determine the concentration of antibody aggregates. The analysis was performed on an Agilent 1100 HPLC system (Palo Alto, CA, USA) equipped with a Biozen 3 µm dSEC-2 column (Phenomenex, Torrance, CA, USA). Detection was carried out using a diode-array detector (DAD) set to the wavelength of 280 nm. The mobile phase consisted of 50 mM phosphate buffer (pH 6.8) supplemented with 300 mM NaCl to minimize non-specific interactions. Flow rate was maintained at 0.6 mL/min, and the injection volume was 10 µL.

Heat-induced antibody aggregation

Thermal stability of monoclonal and polyclonal antibodies was evaluated at elevated temperatures. Monoclonal antibody solutions were incubated at 40 °C, 50 °C, and 60 °C, while polyclonal antibody solutions were incubated at 40 °C, 60 °C, and 70 °C using a thermal shaker (Thermal Shake lite, VWR, USA). Samples were collected at predefined time intervals, and the monomer-to-aggregate ratio in each sample was determined using SEC and the fluorescence-based assay. Each incubation experiment was performed in duplicate. Arithmetic means and standard deviations were calculated and plotted.

Stability study

Stability of polyclonal antibody monomers and aggregates was evaluated across the pH range of 3 to 9. Different buffer systems (20 mM) were used to achieve the desired pH conditions: acetate buffer for pH 3—5, phosphate buffer for pH 6—8, and Tris-HCl buffer for pH 9. Samples were incubated at 4 °C overnight. The effect of different salts was investigated at pH 5 by adjusting the salt concentration to 250, 500, and 1000 mM. The monomer-to-aggregate ratio in each sample was determined using the fluorescence-based assay. Stability of fluorescence dye was verified at all tested conditions. Each incubation experiment was performed in duplicate. Arithmetic means and standard deviations were calculated and plotted.

Results and discussion

A key objective of this study was to establish a fluorescence-based analytical method using the fluorescence dye Nile red, which can complement or potentially replace SEC measurements for aggregate determination. The dye emitted only weak fluorescence in all aqueous buffer systems used. Fluorescence intensity did not change when antibody monomers were added, but it rapidly increased in the presence of aggregates. This confirms the selectivity and sensitivity of the dye for hydrophobic surfaces which are typically exposed

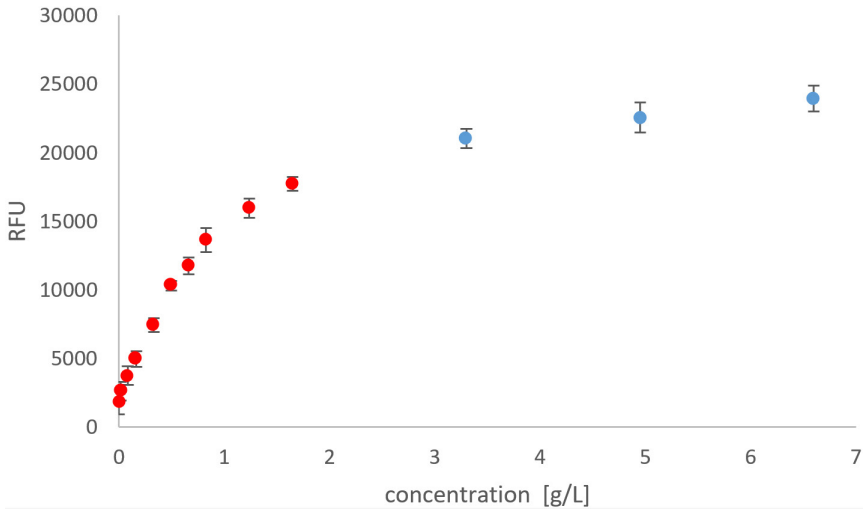

Fig. 1. Calibration curve for antibody aggregates determination using fluorescent dye Nile red, constructed for the concentration range of 0–6.6 g/L. Symbol ● delimits the concentration range for reliable determination of aggregates in unknown samples. These data were fitted with the equation: RFU = 2168 + 18165c – 5372.6c^2, R2 = 0.9977.

Tab. 1. Validation of Nile red fluorescence assay using samples with defined aggregate concentration.

Aggregate concentration [g/L]	Intra-assay CV* [%]				Inter-assay CV [%]	Accuracy [%]
	Day 1	Day 2	Day 3	Day 4		
0.08	3.9	7.5	2.2	7.3	7.4	3.7
0.33	4.2	5.2	4.6	1.7	10	9.3
0.66	6.8	8.4	4.6	6.8	7.6	6.2
1.24	1.9	4.6	2.9	4.1	8.4	8.3

*Four replicates were conducted for each sample.

during protein unfolding and oligomerization (Demeule et al., 2007; Hawe et al., 2009).

A calibration curve was constructed across a wide range of aggregate concentrations (0–6.6 g/L) to assess the relationship between fluorescence intensity and aggregate concentration. The fluorescence signal intensity showed minimal variation at concentrations above 1.65 g/L, suggesting a plateau effect (Fig. 1). Despite the nonlinear nature of the calibration curve, the fluorescence method proved to have sufficient sensitivity to quantify aggregates within the concentration range of 0.0165–1.65 g/L (Fig. 1). To ensure accurate quantification of unknown samples, a quadratic regression model was employed to accommodate deviations from a straight-line model. (Rozet et al., 2011).

Validation of the fluorescence assay demonstrated satisfactory reliability, with intra-assay coefficients of variation (CV) ranging from 1.7 % to 7.3 %, and inter-assay CVs ranging from 7.4 % and 10 % (Table 1). These values fall within the commonly accepted limits for analytical methods, confirming the reproducibility of the technique. Additionally, accuracy of the fluorescence assay ranged from 3.7 % to 9.3 %, indicating its suitability for quantitative determination of aggregates (Tiwari and Tiwari, 2010; Rozet et al., 2011; Sonawane et al., 2014).

Efficiency and accuracy of SEC and the fluorescence assay were compared by analyzing samples collected during heat-induced aggregation of polyclonal antibodies. Two different concentrations (5 g/L and 16.5 g/L) of polyclonal antibodies were thermally stressed to study the effect of concentration on aggregation kinetics. Both assays yielded similar results for samples collected during incubation of up to 48 hours. However, beyond this point, significant divergence was observed. According to SEC analysis, aggregate concentration remained constant whereas the fluorescence assay indicated a continued increase in aggregate levels (Fig. 2).

This discrepancy suggests that SEC may underestimate aggregation beyond a certain threshold, possibly due to limitations in detecting larger oligomers (Arosio et al., 2013), while the fluorescence assay remains sensitive regardless of aggregate size (He et al., 2010). Interestingly, during the first 8 hours, the rate of aggregate formation was faster at higher initial antibody concentration. This behavior is typical in the early phase of aggregation, where the frequency of molecular collisions, driven by

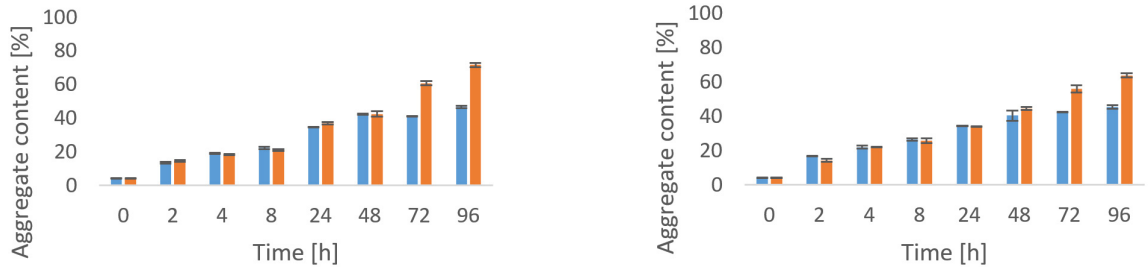

Fig. 2. Comparison of (■) SEC and (■) fluorescence assays for determination of aggregates formed during incubation of polyclonal antibodies at 60 °C, with initial concentrations of (a) 5 g/L and (b) 16.5 g/L. Aggregate content represents the mass fraction of aggregates relative to the total protein content in the solution.

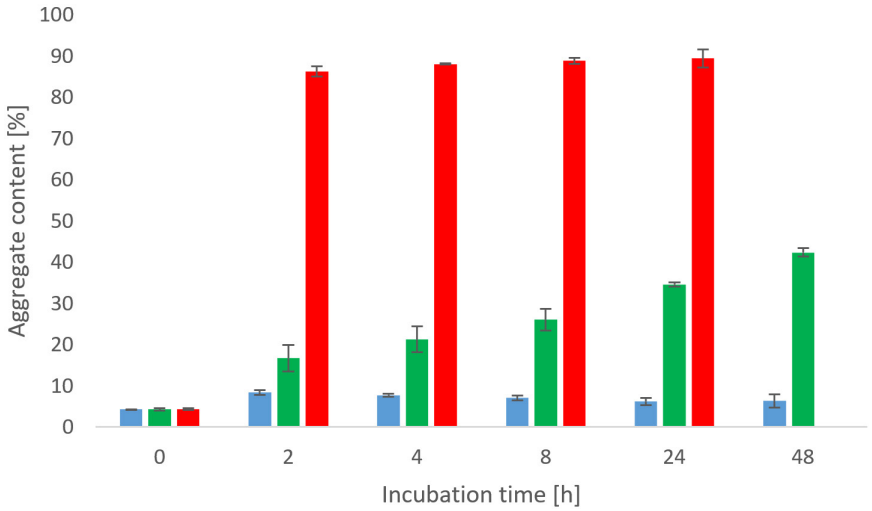

Fig. 3. Aggregation of polyclonal antibodies as a function of incubation time and temperature: ■ 40 °C, ■ 60 °C and ■ 70 °C. Aggregate content as defined in the legend of Fig. 2.

Brownian motion, primarily determines the aggregation rate. However, as aggregation proceeds in an agitated liquid, the process becomes increasingly influenced by convection. It is well established that convection is negatively affected by solution viscosity. Consequently, under convection-controlled conditions, the relative aggregation rate decreases with the increasing protein concentration. This trend is supported by the observation that, between 24 and 48 hours, the relative aggregate content was independent of the initial antibody concentration. Moreover, after 48 hours of incubation, a higher level of aggregates was observed in the sample with lower initial antibody concentration.

To further evaluate the robustness of antibody stability under thermal stress, the stability of monoclonal and polyclonal antibody monomers was examined at elevated temperatures. It should be emphasized that polyclonal antibody preparation initially contained approximately 4 % of antibody aggregates, which could serve as nuclei for the formation of larger aggregates. This should be considered when comparing our results with studies that used pure antibody monomers. Polyclonal antibodies were relatively stable at 40 °C with minimal aggregate formation during the 48-hour incubation period (Fig. 3). However, they responded more sensitively at 60 °C, where the concentration of aggregates gradually increased over the entire period, reaching 42 % after 48 hours. At 70 °C, the proportion of soluble aggregates rapidly increased to over 85 % within the first 2 hours. This value remained stable over time but the total protein concentration in the solution decreased by 80 % due to precipitation (Fig. 3).

In contrast, monoclonal antibodies demonstrated higher sensitivity to thermal stress. The monoclonal antibody preparation initially contained approximately 6 % of aggregates. At 60 °C, nearly all soluble protein content was lost due to precipitation. Even at 50 °C, aggregation was considerable, with 80 % of monomers converting into aggregates within 48 hours. At 40 °C, slower, progressive aggregation was observed, with 14 % of monomers

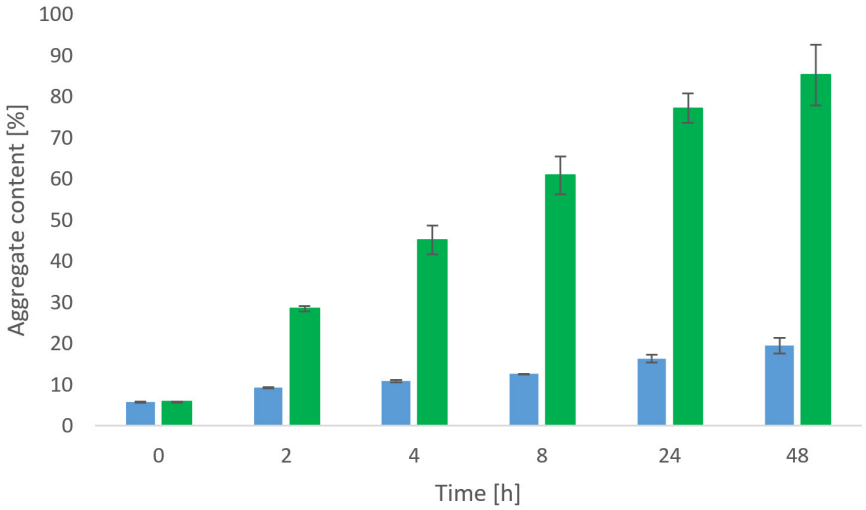

Fig. 4. Aggregation of monoclonal antibodies as a function of incubation time and temperature: ■ 40 °C, ■ 50 °C. Aggregate content as defined in the legend of Fig. 2.

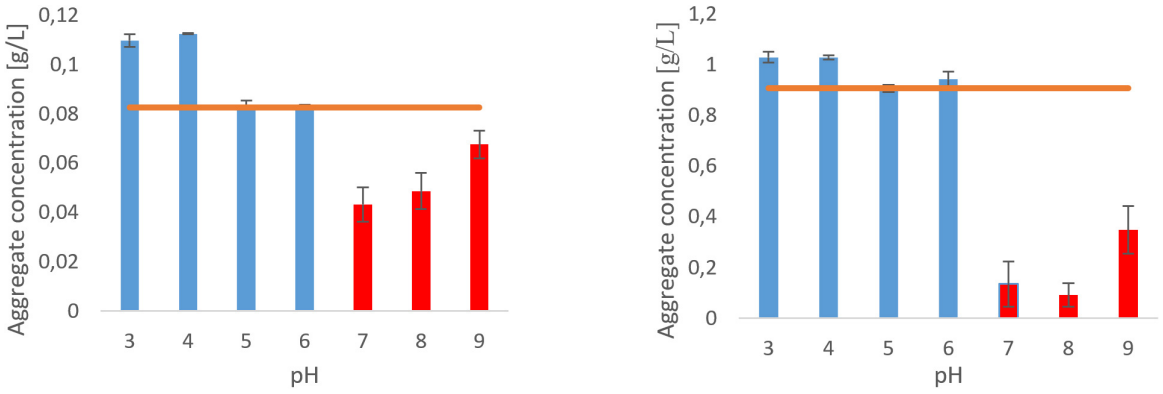

Fig. 5. Effect of pH on the stability of polyclonal antibody solutions: (a) solution predominantly containing monomers and (b) aggregate-enriched solution. (_) Estimated total aggregate concentration, (■) concentration of soluble aggregates, and (■) concentration of aggregates affected by precipitation.

converted into aggregates (Fig. 4). These findings align with previous studies indicating that polyclonal antibodies generally exhibit higher thermal stability than monoclonal antibodies, likely due to their diverse epitope recognition and structural variability (Alexander and Hughes, 1995; Ma et al., 2020).

Effect of pH on the stability of polyclonal antibody solutions was examined. Both samples containing dominantly monomers and those enriched with aggregates remained stable within a narrow pH range (pH 5–6) (Fig. 5), which suggests that the aggregation process is largely pH-dependent rather than being significantly influenced by the initial composition of the solution. At pH below 5, formation of soluble aggregates was observed, likely due to alterations in electrostatic interactions and decreased protein solubility driven by protonation of amino acid residues.

Increased net charge on the antibodies at low pH may disrupt native interactions and promote partial unfolding, leading to non-covalent aggregation (Wu et al., 2023; Meng et al., 2024). Conversely, pH values above 6 suppressed the formation of soluble aggregates but a small amount of insoluble aggregates was formed, indicating a shift in the aggregation mechanism. At higher pH, reduced electrostatic repulsion, increased hydrophobic interactions, and potential exposure of aggregation-prone regions could drive irreversible aggregation and lead to precipitation (Wang et al., 2010; Heads et al., 2019). The results presented in Fig. 5 demonstrate that the degree of precipitation at pH 7–9 increased with the initial aggregate concentration, as indicated by the much steeper relative decrease in soluble aggregates content shown in Fig. 5b compared to Fig. 5a. This suggests that precipitation involves soluble aggregates and does not necessarily affect antibody monomers.

Tab. 2. Influence of different salts on aggregate stability

Salt	Salt concentration	Incubation time	
		2 hours	7 days
NaCl	250	Stable	Dissociation
	500	Stable	Aggregation
	1000	Aggregation	Aggregation
NaSCN	250	Stable	Stable/dissociation
	500	Stable	Stable/dissociation
	1000	Stable	Stable/dissociation
$NaSO_4$	250	Aggregation	Aggregation
	500	Aggregation	Aggregation
	1000	Precipitation	Precipitation
Guanidine HCl	250	Stable	Dissociation
	500	Stable	Dissociation
	1000	Dissociation	Dissociation

Finally, the impact of different salts on aggregates was examined at constant pH (pH 5) during short-term and long-term storage at 4 °C (Tab. 2). The results indicate that NaCl at concentrations up to 500 mM maintained solution stability during short-term storage. However, long-term incubation led to aggregate dissociation at 250 mM and enhanced aggregation at 500 mM. The promotion of aggregation at high NaCl concentrations is consistent with the Hofmeister series, in which chloride ions exert moderate salting-out effects, leading to reduced protein solubility over time (Cai and Hong, 2012).

Furthermore, the observed dissociation of aggregates at 250 mM NaCl suggests a potential re-equilibration of aggregation-prone intermediates, possibly driven by changes in ionic strength and electrostatic interactions (Kang et al., 2021). Interestingly, NaSCN initially induced aggregation, followed by a slight reduction in aggregate levels over time. This behavior aligns with the chaotropic nature of thiocyanate ions, which can disrupt hydrophobic interactions and promote partial unfolding, leading to transient aggregation followed by stabilization as protein molecules reorganize (Baldwin, 1996). The ability of NaSCN to facilitate disaggregation may be attributed to its denaturing effects, which can solubilize preformed aggregates and allow proteins to refold (Maida et al., 2000; Zhou et al., 2008).

Conversely, Na_2SO_4 exhibited a strong aggregation-promoting effect, particularly at the concentration of 1 M, where precipitation was observed. This aligns with the well-documented strong salting-out effects of sulfate ions, enhancing protein-protein interactions by depleting the hydration layer and thereby driving aggregation (Hyde et al., 2017). Guanidine HCl demonstrated a stabilizing effect during short-term storage and significantly reduced aggregation levels during prolonged incubation, especially at 1 M. Guanidine is a well-known denaturant that disrupts non-covalent interactions and can solubilize aggregates by favoring a more unfolded or disaggregated protein state. The decrease in aggregate levels over time suggests a potential refolding mechanism or the prevention of further aggregation through disruption of intermolecular interactions (Baynes et al., 2005; Brummitt et al., 2011).

Conclusions

This study successfully established a fluorescence-based analytical method using dye Nile red to detect and quantify protein aggregates. Validation of the assay confirmed its reproducibility and accuracy. Comparison with SEC during heat-induced aggregation of polyclonal antibodies showed that the fluorescence assay remained sensitive even at high aggregate concentrations, whereas SEC tended to underestimate aggregation degrees beyond a certain threshold. Stability studies revealed significant differences in thermal resistance of polyclonal versus monoclonal antibodies. Additionally, stability was found to be pH-dependent with optimal stability observed between pH 5 and 6. The influence of various salts further underscored the complexity of the aggregation mechanism: high concentrations of NaCl promoted aggregation; NaSCN induced initial aggregation followed by stabilization; Na_2SO_4 caused strong aggregation and precipitation; while Guanidine HCl had stabilizing effect.

Acknowledgements

This work was supported by grants from the Slovak Research and Development Agency (grant numbers:

APVV-20-0312 and APVV-21-0321), the Scientific Grant Agency of the Ministry of Education, Science, Research, and Sports of the Slovak Republic, and the Slovak Academy of Sciences (grant number: VEGA1/0515/22).

References

Alexander AJ, Hughes DE (1995) Anal. Chem. 67(20): 3626–3632.

Arosio P, Rima S, Morbidelli M (2013) Pharm. Res. 30(3): 641–654.

Arosio P, Barolo G, Muller-Spath T, Wu H, Morbidelli M (2011) Pharm. Res. 28(8): 1884–1894.

Arthur KK, Gabrielson JP, Kendrick BS, Stoner MR (2009) J. Pharm. Sci. 98(10): 3522–3539.

Baldwin RL (1996) Biophys. J. 71(4): 2056–2063.

Baynes BM, Wang DI, Trout BL (2005) Biochemistry 44(12): 4919–4925.

Berkowitz SA (2006) AAPS J. 8(3): E590–605.

Brummitt RK, Nesta DP, Chang L, Chase SF, Laue TM, Roberts CJ (2011) J. Pharm. Sci. 100(6): 2087–2103.

Cai W, Hong H (2012) Protein-Protein Interactions: Computational and Experimental Tools Rijeka, Croatia, IntechOpen.

Carpenter JF, Randolph TW, Jiskoot W, Crommelin DJ, Middaugh CR, Winter G (2010) J. Pharm. Sci. 99(5): 2200–2208.

Demeule B, Gurny R, Arvinte T (2007) Int. J. Pharm. 329(1-2): 37–45.

den Engelsman J, Garidel P, Smulders R, Koll H, Smith B, Bassarab S, Seidl A, Hainzl O, Jiskoot W (2011) Pharm. Res. 28(4): 920–933.

Forthal DN (2014) Microbiol. Spectr. 2(4): AID-0019–2014.

Gross J, Sayle S, Karow AR, Bakowsky U, Garidel P (2016) Eur. J. Pharm. Biopharm. 104: 30–41.

Hawe A, Sutter M, Jiskoot W (2008) Pharm. Res. 25(7): 1487–1499.

Hawe A, Kasper JC, Friess W, Jiskoot W (2009) Eur. J. Pharm. Sci. 38(2): 79–87.

Hawe A, Weinbuch D, Zölls S, Reichel A, Carpenter JF (2020). Submicrometer, micrometer and visible particle analysis in biopharmaceutical research and development Amsterdam, Netherlands, Elsevier.

He F, Phan DH, Hogan S, Bailey R, Becker GW, Narhi LO, Razinkov VI (2010) J. Pharm. Sci. 99(6): 2598–2608.

Heads JT, Lamb R, Kelm S, Adams R, Elliott P, Tyson K, Topia S, West S, Nan R, Turner A, Lawson ADG (2019) Protein Eng. Des. Sel. 32(6): 277–288.

Hyde AM, Zultanski SL, Waldman JH, Zhong Y-L, Shevlin M, Peng F (2017) Org. Process Res. Dev. 21(9): 1355–1370.

Kang ZL, Zhang XH, Li X, Song ZJ, Ma HJ, Lu F, Zhu MM, Zhao SM, Wang ZR (2021) J. Food Sci. Technol. 58(6): 2258–2264.

Li W, Prabakaran P, Chen W, Zhu Z, Feng Y, Dimitrov DS (2016) Antibodies (Basel) 5(3).

Lu RM, Hwang YC, Liu IJ, Lee CC, Tsai HZ, Li HJ, Wu HC (2020) J. Biomed. Sci. 27(1): 1.

Ma H, O'Fagain C, O'Kennedy R (2020) Biochimie 177: 213–225.

Maida V, Bennardini F, Bonomi F, Ganadu ML, Iametti S, Mura GM (2000) J. Protein Chem. 19: 311–318.

Meng HK, Pang KT, Wan C, Zheng ZY, Beiying Q, Yang Y, Zhang W, Ho YS, Walsh I, Chia S (2024) Int. J. Biol. Macromol. 282(Pt 2): 136601.

Roberts CJ (2014) Curr. Opin. Biotechnol. 30: 211–217.

Rozet E, Marini RD, Ziemons E, Boulanger B, Hubert P (2011) J. Pharm. Biomed. Anal. 55(4): 848–858.

Sonawane LV, Poul BN, Usnale SV, Waghmare PV, Surwase LH (2014) Pharm. Anal. Acta 5(288): 2.

Tiwari G, Tiwari R (2010) Pharm. Methods 1(1): 25–38.

Vazquez-Rey M, Lang DA (2011) Biotechnol. Bioeng. 108(7): 1494–1508.

Wang W, Roberts CJ (2018) Int. J. Pharm. 550(1-2): 251–268.

Wang W, Nema S, Teagarden D (2010) Int. J. Pharm. 390(2): 89–99.

Wolfrum S, Weichsel U, Siedler M, Weber C, Peukert W (2017) Chem. Ing. Tech. 89(8): 987–994.

Wu Q, Cao C, Wei S, He H, Chen K, Su L, Liu Q, Li S, Lai Y, Li J (2023) Front. Bioeng. Biotechnol. 11: 1257665.

Zhou H-X, Rivas G, Minton AP (2008) Annu. Rev. Biophys. 37(1): 375–397.

Zolls S, Tantipolphan R, Wiggenhorn M, Winter G, Jiskoot W, Friess W, Hawe A (2012) J. Pharm. Sci. 101(3): 914–935.

sciendo

How solid-state fermentation with *A. niger* changes agro-waste of apple, aronia and sea buckthorn to attractive antioxidant compounds

František Kreps, Oliver Jančarik, Mária Greifová

Institute of Food Science and Nutrition, Faculty of Chemical and Food Technology, Slovak University of Technology in Bratislava, Radlinského 9, Bratislava SK-812 37, Slovakia
frantisek.kreps@stuba.sk

Abstract: This work focuses on the influence of solid-state fermentation on the polyphenols and flavonoids conent in fruit pomace of apple, aronia, and sea buckthorn. A comparison was made during a seven-day fermentation of pomace with *A. niger* and with autochthonous microflora, showing that this method has no significance for aronia and sea buckthorn pomace. Autochthonous microflora had a more favorable effect on the content of polyphenols and flavonoids than *A. niger*. However, in the case of apple pomace, the content of total polyphenols increased up to 1425 mg GAE/100 g DW on the seventh day of fermentation with *A. niger*, representing a 7.3-fold increase compared to the initial value of 195 mg GAE/100 g DW. Our results therefore present an attractive way of agro-waste utilization and the subsequent implementation of these isolates in other types of industry.

Keywords: fruit pomace, solid state fermentation, total phenolic content, total flavonoid content, *Aspergillus niger*

Introduction

Waste from fruit and vegetable processing industry has great potential as a source of specific bioactive compounds ranging from proteins to essential fatty acids and polyphenol (Banerjee et al., 2017; Kumar et al., 2017). In Europe, juice production residue ranks as the 5th main contributor to the total yearly food waste (Roda-Serrat et al., 2021). This waste is nowadays used mainly as livestock feed, soil fertilizer, raw material for biofuel production, or it is discarded in landfills. Recovery of bioactive compounds from food processing waste therefore is an attractive opportunity that has received a lot of attention in recent years (Madeddu et al., 2021; Majerska et al., 2019).

Apples are one of the most favorite fruits, mainly due to their delicious taste, high nutritional value, and good storability, depending on the variety. They are also known for their high antioxidant content (Musacchi and Serra, 2018). Chemical composition of apples may vary depending on the variety, production area, harvesting, and storage procedures. In general, an apple contains more than 80 % of water, carbohydrates (fructose, glucose, sucrose), organic acids, vitamins (mainly vitamin C), minerals, and fiber.

Berries, especially black chokeberry (aronia), black elderberry, black currant, blueberry, sea buckthorn, and others are also an excellent source of a wide range of antioxidant substances. The wide range of phytochemicals present in the above-mentioned plants, as well as their different concentration profiles, provide different health benefits in each genus and species (Lavefve et al., 2020). Berries are rich in minerals, vitamins, fiber, and phenolic compounds with high biological activity. High levels of vitamin C, carotenoids, and phenolic compounds in berries give them high antioxidant potential, which is why berries are considered the most important source of antioxidant molecules in human diet.

Antioxidant activity is caused by compounds with protective activity against oxidation. Although these can be found in various fruits, their bioavailability for human organism may be limited as most of these substances are found in conjugated form, where sugar residues are attached to hydroxyl groups. Studies show that these compounds can be released or converted into more active forms by fermentation. They attribute these changes to metabolic activities affecting phenolic acids, flavonoids, tannins, release of antioxidant peptides, changes in vitamin content, and production of exopolysaccharides. For example, filamentous fungi can produce β-glucosidase, which releases polyphenols bound to cell wall structures and increases the extractable content of polyphenols (Verni et al., 2019; Waldbauer et al., 2017).

Fermentation is an important part of food biotechnology. Initially, it was used to preserve food products and prevent diseases. The process has evolved with human civilization to the extent that production and extraction of bioactive compounds is possible (Martins et al., 2011). The two types of fermentation commonly used in the industry are Submerged Fermentation (SmF) and Solid-State

Fermentation (SSF). The principle of SmF consists in a liquid medium as a source of nutrition for microorganisms so that fermentation can take place. SSF is the same process but in the absence or near absence of free water in the medium. The substrate itself is required to contain the necessary moisture for the microorganism to survive and grow (Erskine et al., 2023). SSF is a more suitable candidate for commercial enzyme production compared to SmF due to the higher yield achieved using the same strain. Although not as conventional as SmF, SSF has attracted interest from both the commercial and the scientific worlds in recent years. As it is solid-state fermentation, it has significantly lower water and energy requirements, which in turn reduces bacterial contamination along with sterilization and production costs (Hansen et al., 2015).

Aspergillus niger is a microscopic filamentous fungus growing on organic matter in the presence of oxygen. It is widely distributed in nature and is found in soil, decomposing plant material, or compost. The conditions for its growth include a wide range of pH values, from 1.4 to 9.8 with the optimum between 4—6.5, and temperature range of 6—47 °C with optimal temperature between 24—37 °C. This versatility, together with the water activity of 0.88—0.98 required for optimal growth and sporulation, makes it an industrially attractive organism with simple cultivation. It is used in the food industry, specifically for food enzymes production. *A. niger* fermentation is dependent on substrates containing sucrose, which increases the production costs; however, a cheaper and more sustainable substrate can be used (Passamani et al., 2014; Upton et al., 2017).

The goal of our work was to use agro-waste of apple, aronia, and sea buckthorn processing focusing on fermentation with *A. niger*, which offers efficient transformation of waste into a source of valuable antioxidants that can be further used in the food, pharmaceutical, or cosmetic industry.

Materials and methods

Chemicals

Aronia pomace was prepared from fruits of "Leikora" cultivar, pressed at ecofarm Aronia Agro s.r.o Žiar nad Hronom SR). Sea buckthorn pomace was from "Nero" cultivar berries, obtained from Tvrdošovce agricultural cooperative (poľnohospodárske družstvo Tvrdošovce, SR). Apple pomace was prepared from "Golden Delicious" cultivar, pressed at McCarter, a.s. (Dunajská streda, SR).

Aspergillus niger (CCM 8189) was grown on selective YGC agar (yeast extract glucose chromamphenicol agar) (Biolife, Italia) and Tween 80 (Merck Life Science, SR) was used as surface-active substance to create spore suspension. Composition of the mineral nutrient medium for solid state fermentation was prepared with chemicals from Centralchem (SR) (Sodium nitrate p.a., Potassium dihydrogen phosphate p.a., Potassium chloride p.a., Magnesium sulfate heptahydrate p.a., Copper sulfate pentahydrate p.a.) and Lachema Brno (CR) (Zinc sulfate hydrate p.a., Ferrous sulfate monohydrate p.a.).

Other chemicals used in the analytic methods were purchased from VWR (CR) (HPLC water and HPLC methanol), Centralchem (SR) (Ethanol 96 %, Glacial acetic acid, Folin-Ciocalteu reagent p.a., Sodium carbonate anhydrous p.a.), Merck Life Science (SR) (Gallic acid of analytical purity, Quercetin ≥ 95 %, Eriodictyol ≥ 98 %).

Preparation of spore suspension

A. niger CCM 8189 was borrowed from the Institute of Biochemistry and Microbiology (originally purchased from the Masaryk University in Brno). It was inoculated on selective YGC agar (yeast extract glucose chromamphenicol agar) (Biolife, Italia) and grown at 30 °C for 5—7 days. After incubation, sterile 0.1 % Tween 80 solution was used to loosen the spores from the surface of the agar medium. The spore suspension was poured through sterile gauze into a sterile, flat-bottomed, wide-necked titration flask using a funnel. The number of spores/ml was determined by the cultivation method.

Solid state fermentation (SSF)

In each substrate, the number of colony forming units was first determined by the cultivation method. Their numbers were $9.1 \cdot 10^1$ CFU/g for apple pomace, $9.3 \cdot 10^1$ CFU/g for sea buckthorn pomace, and $9.8 \cdot 10^1$ CFU/g for aronia pomace. The substrate suitable for SSF was prepared according to Gulsunoglu et al. (2020), with 5 g of dried and ground fruit pomace weighted and 25 ml of distilled water added, and enriched with the minerals listed in Table 1. Next, 1 ml of the spore suspension ($4.8 \cdot 10^6$ spores/ml) was added to

Tab. 1. Composition of the mineral medium (Gulsunoglu et al., 2020).

Compound	Content [g/l]
$NaNO_3$	6.00
KH_2PO_4	1.52
KCl	0.50
$MgSO_4 \cdot 7H_2O$	0.50
$ZnSO_4 \cdot H_2O$	0.01
$CuSO_4 \cdot 5H_2O$	0.01
$FeSO_4 \cdot H_2O$	0.01

the Erlenmeyer flasks with the weighed substrate, which was then closed with a stopper. Samples fermented with autochthonous microflora consisted of substrate enriched only with the mineral medium. All Erlenmeyer flasks were incubated for 7 days at 30 °C in aerobic conditions. Samples were taken on the 0^{th}, 3^{rd}, and 7^{th} day always from three parallels.

Sample preparation and extraction

Preparation and extraction of dried fermented samples were carried out as follows: 2 g of each sample were weighed; extraction solvent was prepared by mixing water and food-grade ethanol in a 20:80 ratio (H_2O:EtOH) and 20 ml of the prepared solvent were added to each weighed sample. Extraction was performed in an ultrasound bath for 30 minutes. Once the extraction was complete, the extracts were filtered to remove solids, and the filtrate was evaporated under pressure below 18 mbar at 30 °C until the solvent was removed. The prepared extracts were stored in a freezer at –30 °C.

Determination of total polyphenol content and other reducing compounds

Total content of polyphenols (TPC) and other reducing compounds, including certain amino acids, proteins, and other antioxidants, in fermented fruit pomace was determined using a modified method (Zhu et al., 2023) with gallic acid as the standard and the Folin-Ciocalteu reagent. Concentration of phenolic compounds and other reducing compounds was determined based on the calibration curve prepared by analyzing the individual dilutions of the gallic acid standard with gallic acid concentration ranging from 0,0001 to 1 mg/ml. The prepared concentrations were dosed as 100 µl into test tubes and 500 µl of Folin-Ciocalteu's reagent was added. After 3 minutes, 1500 µl of 20 % sodium carbonate solution was added. Finally, everything was topped with 7900 µl of distilled water. The same preparation was used for the samples, except for them being diluted in the ratio of 10:1. A blank was prepared in two parallels containing distilled water instead of the sample. Finally, the entire rack was wrapped in aluminum foil and the solutions were let to react in the dark for 2 hours at room temperature. After two hours, the samples were vortexed and pipetted (250 µl) onto a 96-well microplate from a BioTek Reader spectrophotometer. Absorbance was measured at the wavelength of 765 nm using the BioTek Reader spectrophotometer. All samples, calibration solutions and blanks were dosed onto the plate in two parallel measurements. TPC values were determined as the equivalent of gallic acid in milligrams per 100 g of dry matter (mg GAE/100 g DW).

Determination of total flavonoid content

Total flavonoid content (TFC) in the samples was determined spectrophotometrically using a solution of aluminum chloride and quercetin as a standard (Kreft, 2002). First, calibration solutions were prepared by gradually diluting a quercetin stock solution to concentrations of 0.001, 0.002, 0.003, 0.01, 0.02, and 0.03 mg/ml. Then, 2 ml of each calibration solution was placed into a test tube and 0.2 ml of a 5 % aluminum chloride solution was added. The fermented samples were diluted in UV ethanol and prepared analogically to the calibration solutions, 2 ml of the sample was pipetted into the test tube and 0.2 ml of a 5 % aluminum chloride solution was added. For the blank, the preparation was identical, only instead of the sample, UV ethanol was used. Each sample was vortexed thoroughly and allowed to react at room temperature for 30 minutes. Then, the samples were pipetted onto the plate of a BioTek Reader spectrophotometer in 250 µl portions for analysis. A parallel sample was also pipetted for each sample, calibration solution and blank. Absorbance was measured at the wavelength of 420 nm. Total flavonoid content (TFC) was evaluated as quercetin equivalent in milligrams per 100 g of dry matter (mg QE/100g DW).

Determination of specific flavonoids

Reversed-phase high-performance liquid chromatography was used to determine eriodictyol and quercetin employing two methods (Gulsunoglu et al., 2020), (Liu et al., 2021) which were modified several times to achieve the best possible separation. Modifications comprised varying both stationary and mobile phases, mobile phase gradient, injection volume, and concentration. Finally, conditions listed in Table 2 were applied.

Tab. 2. Conditions used in specific flavonoids analysis.

Column	SunShell C18, 2.6 µm, 4.6 × 150 mm
Mobile phase	A – water with the addition of 0.1 % acetic acid, B – methanol
pH of phase A	2.8
Gradient for phase B	0 – 15 min 20 – 50 %, 15 – 20 min 50 – 70 %, 20 – 40 min 70 %
Flow rate	1.000 ml/min
Injection	5 µl
Pressure	204 bars
Temperature	30 °C
Detector	MWD
Wavelength	280 nm
Length of analysis	40 minutes

Evaporated extracts were used for the analysis; 10 mg of each extract were weighed and dissolved in 1 ml of HPLC methanol. Subsequently, the sample was filtered through a 0.22 µm microfilter into vials. Content of the given polyphenol in the sample was determined using a calibration curve considering quantitative parameters, specifically the peak area. First, a mixed standard was prepared, knowing the elution times of both standards. In the work, the standard for eriodictyol and quercetin were used. Stock solution was prepared in the ratio of 1:1 and HPLC grade methanol was used as a solvent. Next, calibration solutions were prepared in concentrations of 0.05, 0.04, 0.03, 0.02, 0.01, 0.008, 0.005, and 0.003 mg/ml, and the calibration curve was expressed as the dependence of the peak area on the concentration of the mixed standard. This calibration curve was then used to calculate the concentrations of the specific polyphenols in the fermented samples.

Statistical analysis

All data obtained experimentally were processed by descriptive statistics in the Microsoft Office program – Excel 365. When determining the total content of phenolic compounds and total flavonoid compounds, the values were reported as the average of three individual experiments and the error bars were expressed as confidence interval. When determining the content of specific polyphenols, the values were reported as the average of three measurements ± standard deviations.

Results and discussion

Total polyphenol content (TPC) and other reducing compounds in apple pomace

Effect of apple pomace fermentation on TPC values and other reducing compounds was more significant than that of the below mentioned berries. TPC increased with each passing day (Fig. 1). On day 0, when the substrate was freshly inoculated, the same results were recorded for fermentation with autochthonous microflora and fermentation with *A. niger* (NM). The initial value was 195 mg GAE/100 g DW; Gulsunoglu et al. (2020) stated an initial value of 350 mg GAE/100 g.

The difference between inoculated and non-inoculated substrate was established on the 3rd day when *A. niger* hydrolyzed polyphenols with the help of the produced enzymes, increasing the content of polyphenols to 939 mg GAE/100 g of dry matter, which represents an almost 5-fold increase compared to the initial value. Gulsunoglu et al. (2020) recorded only a 2-fold increase. This difference may be caused by different variety or different content of peels, stalks, cores, and pulp in apple pomace. Also, a different collection strain of *A. niger* was used. Increase of TPC values was also seen in samples fermented with autochthonous microflora. The highest content of phenolic compounds, as expected, was on the 7th day, with 1471 mg GAE/100 g of dry matter, which is 1.5 times more than on the 3rd day. Fermentation with *A. niger* provided a result 4.1 times higher than that with autochthonous

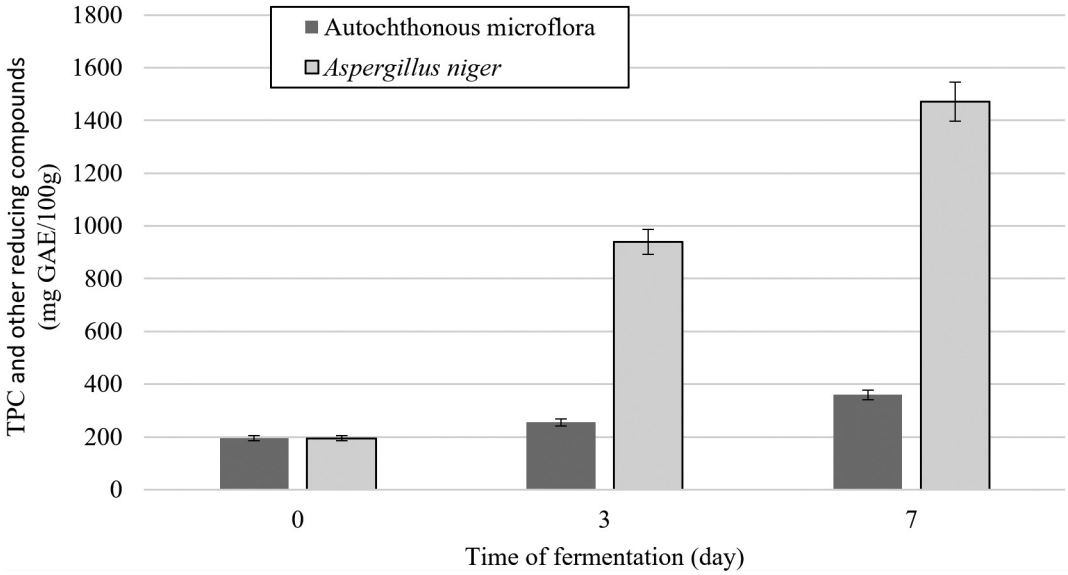

Fig. 1. Total content of polyphenolic (TPC) and other reducing compounds in apple pomace fermented with autochthonous microflora and *A. niger*.

microflora. The results are in agreement with the study by Gulsunoglu et al. (2020), which shows total content of phenolic compounds obtained by fermentation with *A. niger* of 1425 mg GAE/100 g of dry matter with slower onset but a continuous addition of phenolic compounds. The results were thus equal on the 7th day.

Total flavonoids content (TFC) in apple pomace

In non-fermented apple pomace, the total flavonoid content (TFC) typically ranges between 85 to 140 mg QE/100 g DW (Rana et al., 2015; Gulsunoglu et al., 2020). Our baseline 110 mg QE/100 g DW, aligns well with these values, and is similar to 99 mg QE/ 100g DW reported by Rana et al. (2015). Our results for TFC (Fig. 2) correspond well with findings reported in Rana et al., (2015) and Gulsunoglu et al. (2020).

Gulsunoglu et al. (2020) observed a TFC of 382 ±18 mg QE/100 g DW in apple peels fermented with *A. niger*, which is comparable to our value of 360 mg QE/100 g DW on day 7. TFC measured on day 3 of fermentation with *A. niger* (228 mg QE/100 g DW) matched the values reported by Gulsunoglu et al. (2020) well, despite our initial TFC being approximately 20 % lower. Autochthonous microflora showed only a transient increase on day 3 (150 mg QE/100 g DW), followed by a significant decline to values even lower than the initial baseline (100 mg QE/100 g DW). Similarly, the significant decline in TFC observed in the sample fermented with autochthonous microflora on day 7 parallels the degradation patterns described in their work.

The marked TFC increase to 360 mg QE/100 g DW in the *A. niger* fermented sample on day 7 correlates well with our HPLC results, which identified quercetin (20 mg/100 g) and eriodictyol (300 mg/100 g) as the predominant flavonoids present. This suggests that these two compounds are likely the major contributors to the total flavonoid content in fermented apple pomace.

Determination of specific flavonoids in apple pomace

Apple pomace contains several phenolic compounds that occur in free forms or conjugated with sugars, acids, and other biomolecules soluble or insoluble in water (De Araújo et al., 2021). However, after fermentation, there is a change in the phenolic profile of apple pomace and a change in the content. Quercetin occurs in apple pomace in various structures, when various glycosides are bound to it with a glycosidic bond, e.g. quercetin-3-O-glucoside, quercetin-3-O-rhamnoside, and others (Gumul et al., 2021). During fermentation with *A. niger,* enzymes are produced, such as glucosidase, which cleave glycosidic bonds creating new interesting phenolic compounds. Such a compound is eriodictyol, which is mainly found in citrus fruits, but it is formed during the fermentation of apple pomace via the transformation of other flavonoids. This phenomenon has been proven by HPLC analysis (Fig. 3a, b), confirming the presence of eriodictyol in 7-day fermented apple pomace. The obtained data were compared with those of Gulsunoglu et al. (2020) in table no. 3, showing the quercetin content decrease, i.e. consumption, during fermentation. When measuring the content of eriodictyol, responses on the 0th day were not measured. However, some values obtained on the 3rd and 7th day of fermentation with autochthonous microflora were

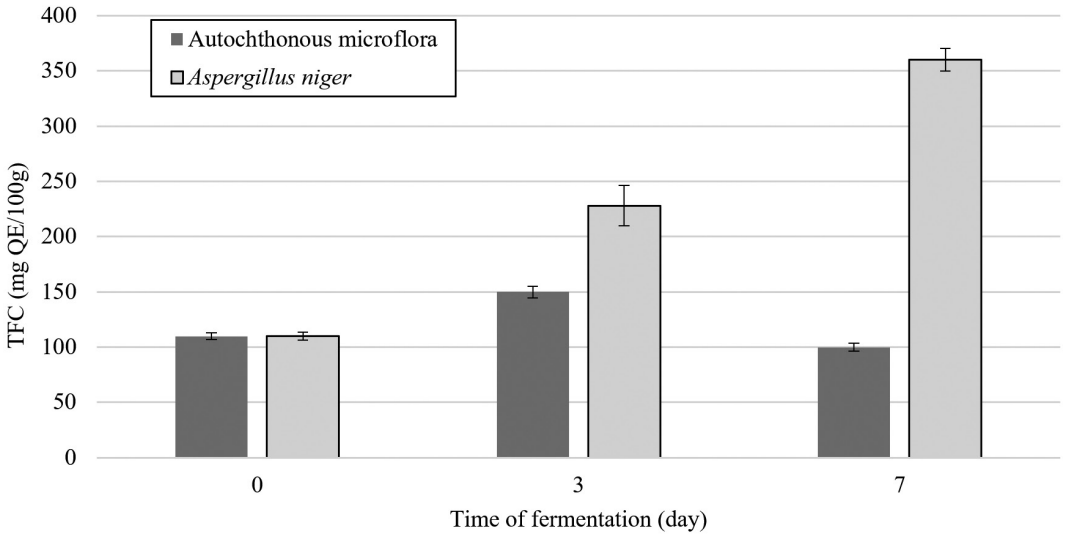

Fig. 2. Total content of flavonoids (TFC) in apple pomace fermented with autochthonous microflora and *A. niger*.

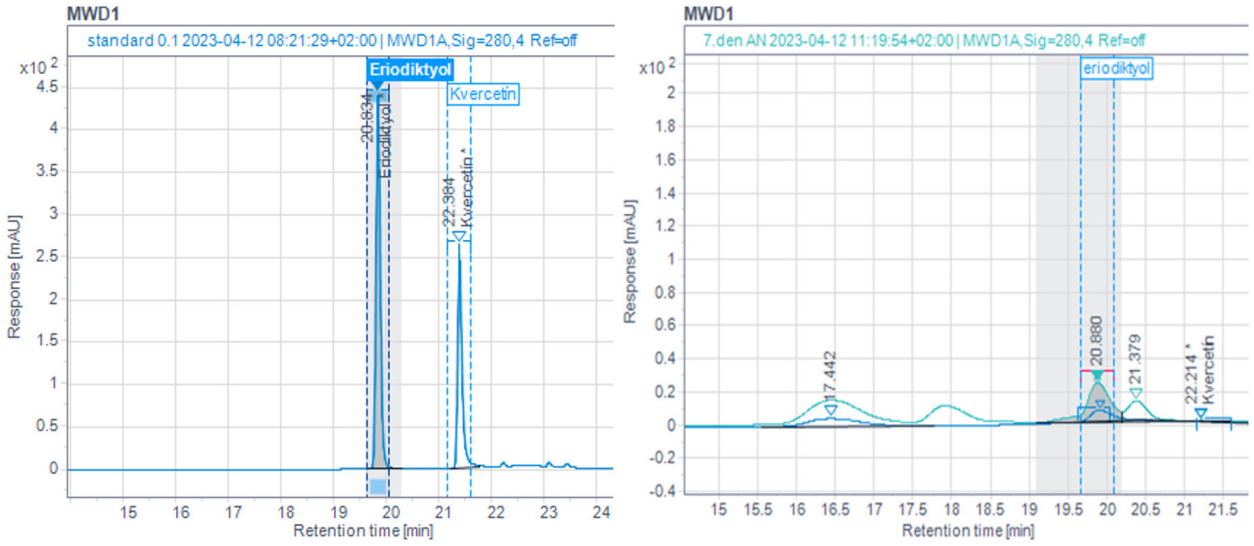

a) b)

Fig. 3. a) — HPLC analysis of 1 mg/ml of eriodictyol and quercetin in a mixture.
b) — Overlap of the standards with a sample of apple pomace fermented for 7 days by *A. niger*.

Tab. 3. Effect of fermentation on the content of quercetin and eriodictyol in fermented and unfermented apple pomace.

		Results (mg/100 g DW)		**Gulsunoglu et al., (2020) (mg/100 g DW)**	
Analytes	Day	Autochthonous microflora	*A. niger* (CCM 8189)	Autochthonous microflora	*A. niger* (ZDM2)
Quercetin	0.	20.0 ±0.3	20.0 ±0.3	19.9 ±0.9	19.9 ±0.9
	3.	17.5 ±0.2	21.5 ±0.3	17.9 ±2.4	22.5 ±0.7
	7.	16.3 ±0.6	20.0 ±1.0	14.2 ±3.6	18.1 ±3.9
Eriodictyol	0.	–	–	–	–
	3.	49.2 ±0.2	203.1 ±7.9	ND	264.1 ±5.0
	7.	54.4 ±0.2	300.0 ±16.4	ND	639.2 ±14.5

not reported in the above publication (Gulsunoglu et al., 2020), probably because eriodictyol standard was not used to seek the peak overlap, which was identified by HPLC-MS/MS and HPLC-PDA.

In apple pomace fermented by *A. niger*, an increase in eriodictyol was observed. However, compared to the given publication, the increase was lower as our results were half of those presented on the 7th day of fermentation. This difference arose from a modification of their procedure, as a different drying method, different collection strain of *A. niger*, different extraction solvent, and different variety of apple pomace were used. Either of the collection strains of *A. niger* used in fermentation and subsequent extraction of phenolic compounds produces ochratoxin A. However, they belong to the 2nd risk group, which means that they can be the cause of human or animal diseases (Varga et al., 2007). The collection strain used in this paper is only suitable for laboratory research purposes, and thus for our model experiment. Our results can serve as a template for the use of the collection strain *A. niger*, used in the food and pharmaceutical industry, for example in the production of citric acid.

Levels of quercetin and eriodictyol measured in fermented apple pomace in this study are consistent with data reported in previous research. Quercetin concentrations in both fermented samples ranged between 20—21.5 mg/100 g DW, aligning closely with findings of Gulsunoglu et al. (2020), who identified quercetin as a dominant flavonoid in apple by-products, showing minimal fluctuation after solid-state fermentation (SSF) with *Aspergillus niger* (ZDM2).

Eriodictyol levels significantly increased during the fermentation process, with the highest concentration (300 mg/100g DW on day 7) recorded in samples fermented with *A. niger*. This value remains below the maximum of 639 mg/100g DW observed by Gulsunoglu et al. (2020) for a different *A. niger* strain (ZDM2).

Nevertheless, our findings support the hypothesis that *A. niger* fermentation promotes enzymatic transformation of phenolic precursors to bioac-

tive flavonoids, with eriodictyol emerging as a key marker of fermentative bioconversion.

Total polyphenol content (TPC) and other reducing compounds in aronia samples

The total content of compounds with redox activity was determined as a TPC value of 1691 mg GAE/100 g DW in aronia pomace on the 0th day of fermentation (Fig. 4). On the 3rd day of fermentation, the values increased rapidly, reaching a value of 7880 mg GAE/100 g DW in the fermentation with autochthonous microflora, which is approximately 4.6-fold the original TPC value. In samples fermented with *A. niger*, the TPC values were 6925 mg GAE/100 g DW on the 3rd day, which is about 4-fold the original value.

Various studies on the fermentation of agro-waste to obtain biologically significant substances monitored changes in the content of polyphenolic compounds during solid state fermentation of fruit pomace. For example, Dulf et al. (2018) observed the effect of solid-state fermentation on aronia pomace using the Folin-Ciocalteu reagent method to determine TPC. Their research showed that TPC and other reducing compounds in SSF processes increase significantly during the growth period. For SSF with *Aspergillus niger*, their content of TPC gradually increased until the 9th day, when the maximum value of 1703.5 mg GAE/100 g DW represented more than 1.7-fold the initial value. In the following days of fermentation, a decrease in TPC was observed. Compared to the study by Dulf et al. (2018), higher levels of TPC and other reducing compounds were measured on each day of aronia pomace fermentation. This fact can be attributed to the different composition of the pomace, i.e. the content of skins, seeds, pulp or stems. The content of antioxidant substances can also be due to the difference in variety, growing conditions, growing place, etc. It is also necessary to consider that a different strain of microflora can cause differences in the results.

On the 7th day of fermentation, the difference between the microflora in the aronia samples was observed. While with the autochthonous microflora the values continued to increase up to the value of 11420 mg GAE/100 g DW, a trend of lower growth of TPC values was observed in the fermentation with *A. niger*. TPC values of the autochthonous microflora on the 7th day of fermentation were 1.5-fold higher compared to those of *A. niger*. The fact that the autochthonous microflora provided better results in increasing polyphenolic compounds during fermentation can be justified by the ability of natural microflora to adapt to the environment, its diversity and a wide range of enzymes, in contrast to the artificially added *A. niger*.

Total flavonoid content (TFC) in aronia samples

The total flavonoid content of aronia samples was 418 mg QE/100 g DW on the 0th day of fermentation (Fig. 5). On the 3rd day of fermentation, their content increased in both microflorae, increasing 2.3-fold, up to 952 mg QE/100 g DW, in samples fermented with autochthonous microflora, and approximately 2-fold, up to 835 mg QE/100 g DW, in samples fermented with *A. niger*. On the 7th day of fermentation, a slight increase was observed in *A. niger* samples, up to 861 mg QE/100 g DW, while in the case of autochthonous microflora,

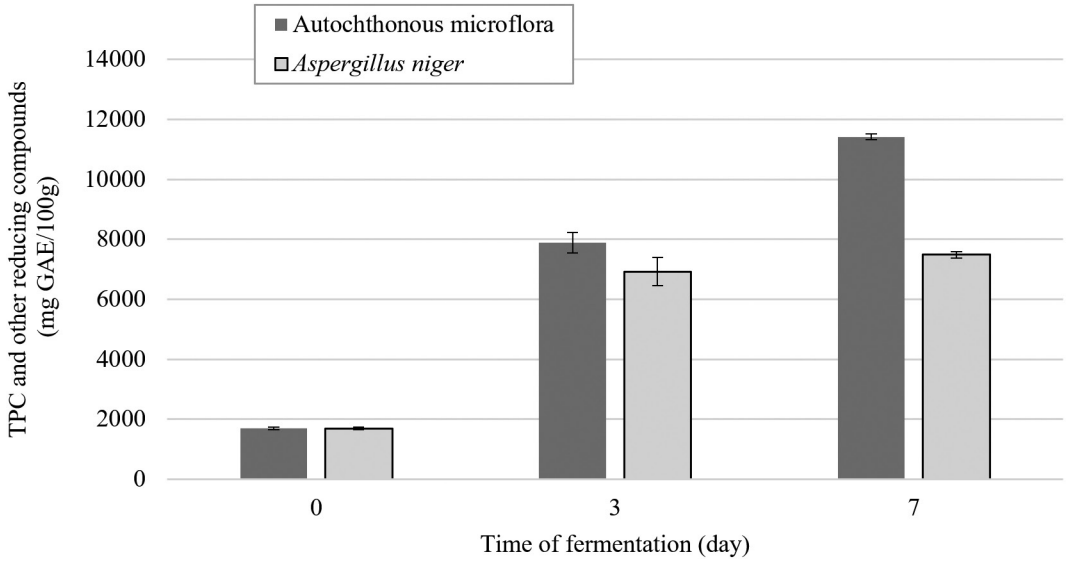

Fig. 4. Total content of polyphenolic (TPC) and other reducing compounds in aronia pomace fermented with autochthonous microflora and *A. niger*.

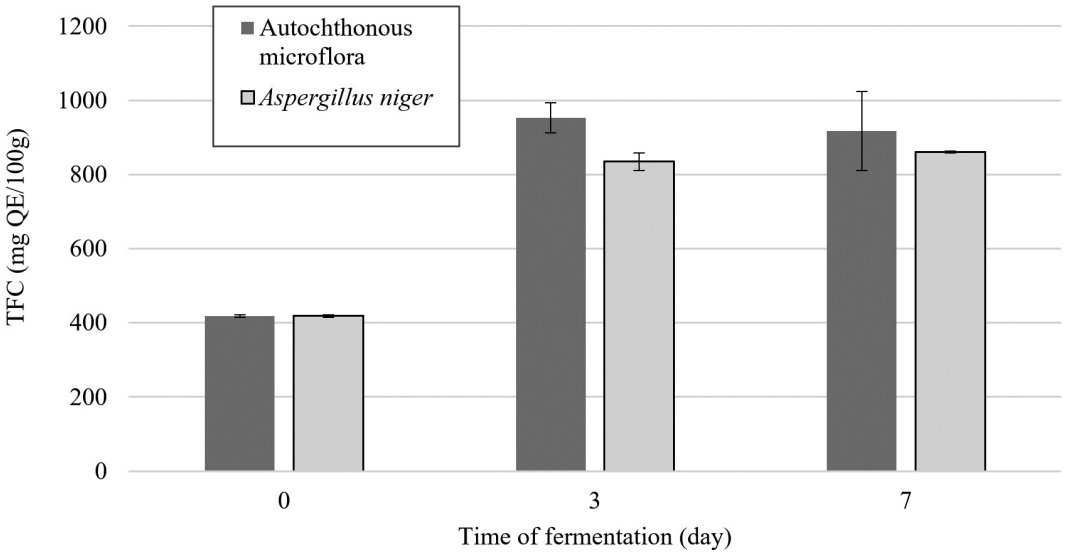

Fig. 5. Total content of flavonoids (TFC) in aronia pomace fermented with autochthonous microflora and *A. niger*.

Tab. 4. Effect of fermentation on the content of quercetin and eriodictyol in fermented and unfermented aronia pomace.

		Results (mg/100 g DW)	
Analytes	Day	Autochthonous microflora	*A. niger* (CCM 8189)
Quercetin	0	226.5 ±3.5	226.5 ±3.5
	3	207.2 ±4.1	239.8 ±5.0
	7	191.4 ±4.6	228.3 ±3.9
Eriodictyol	0	ND	ND
	3	59.4 ±2.6	182.7 ±3.9
	7	66.5 ±2.1	269.4 ±5.5

on average, the values decreased down to 917 mg QE/100 g DW.

Results for aronia samples can be compared with those of Dulf et al. (2018), in which the total amount of flavonoids in fermented aronia pomace showed similar trends as total polyphenols. When *A. niger* was used for solid-state fermentation, the TFC level in their study increased 1.5-fold by day 9 (to 264.00 mg QE/100 g DW) compared to the initial value (176.00 mg QE/100 g DW) followed by a decline during the remaining growth period. The increase in total flavonoid content was greater in SSF with *R. oligosporus*, increasing 1.6-fold by day 6 (to 277.00 mg QE/100 g DW) before gradually decreasing during the remaining fermentation period. This course of fermentation is analogic to our measurements with aronia pomace, where the content of total flavonoids differs numerically, which may be caused by the aspects mentioned above, but their content increases with the course of fermentation. Aronia pomace fermented with *A. niger* showed similar increase in our (2-fold) and in the comparative (1.5-fold) study. An analogic course of the effect of fermentation on TFC (increase in values) was observed also in a study with plum pomace (Dulf et al., 2016). However, again, we can state that the naturally present microflora had a more efficient composition of microorganisms considering that it had a better effect on increasing TFC during the fermentation of aronia pomace. Therefore, it can be stated that there is potential to follow up on our study with fermentation experiments of aronia pomace using other microbiological strains to find the ones more effective in increasing TFC values.

Determination of specific flavonoids in aronia pomace

Quantification of quercetin and eriodictyol in aronia pomace during solid-state fermentation (Tab. 4.) revealed notable dynamics in flavonoid composition. The initial quercetin concentration of 226.5 ±3.5 mg/100 g DW in non-fermented pomace aligns with values reported in literature. Sosnowska et al. (2022) observed total quercetin derivatives ranging from 199.5 to 623.6 mg/100 g DW depending on the ripening stage and cultivar. Our data fall

into the lower–intermediate range, likely reflecting varietal, climatic, and processing differences.

Throughout fermentation, quercetin levels remained relatively stable in samples inoculated with *Aspergillus niger*, with a slight increase by day 3 and stabilization at 228.3 ±3.9 mg/100 g DW on day 7. In contrast, a gradual decrease was observed in samples fermented with autochthonous microflora. This suggests that *A. niger* promotes limited hydrolysis of glycosidic forms into free quercetin without significant degradation.

Eriodictyol, undetectable in unfermented pomace, emerged as a key flavonoid during fermentation. Its concentration increased to 182.7 ±3.9 mg/100 g DW by day 3 and peaked at 269.4 ±5.5 mg/100 g DW on day 7 in *A. niger*-fermented samples, while its values remained significantly lower in the autochthonous treatment. Formation of eriodictyol can be attributed to the enzymatic activity of *A. niger*. These findings are consistent with observations by Dulf et al. (2018), who reported enhanced flavonoid bioavailability after fermenting aronia pomace with *A. niger*.

Total polyphenol content (TPC) and other reducing compounds in sea buckthorn pomace

Using the Folin-Ciocalteu reagent method to determine TPC and other reducing compounds resulted in a value of 1324 mg GAE/100 g DW in sea buckthorn pomace on the 0th day of fermentation (Fig. 6). On the 3rd day, TPC values increased to 1943 mg GAE/100g DW in the autochthonous microflora samples (>1.4-fold) and to 1976 mg GAE/100 g (approximately 1.5-fold) in *A. niger* samples. On the 7th day of fermentation, a slight decrease was observed in both microflora samples, 1773 mg GAE/100 g DW for the autochthonous microflora and 1648 mg GAE/100 g DW for *A. niger* (Fig. 6). A similar experiment was performed by Dulf et al. (2015), where two Sambucus species were fermented with *Aspergillus niger*. On the 3rd day of fermentation, the maximum increase in TPC values was observed, the values decreased and stabilized in the following days. In their study, this fermentation progress was explained by the lack of nutrients, so a limited amount of certain nutrients for optimal growth and enzymatic processes can be assumed also in sea buckthorn samples.

Total flavonoids content (TFC) in sea buckthorn pomace

TFC values in sea buckthorn samples showed different trend to aronia samples (Fig. 7). On the 0th day of fermentation, TFC of 518 mg QE/100 g DW was measured and the content of flavonoids decreased during the fermentation in the presence of both microflorae. On the 3rd day of fermentation, only 0.4-fold of the original flavonoid content was measured in autochthonous microflora samples, while it was 0.6-fold of the initial value, decreased to 307 mg QE/100 g DW, in *A. niger* samples.

The 7th day of fermentation showed even lower values. During the fermentation with autochthonous microflora, TFC values decreased down to 184 mg QE/100 g DW (35.5 % of the initial content of total flavonoids). In samples fermented with *A. niger*, TFC of only 235 mg QE/100 g DW (approximately 45 % of the content from day 0) were determined. A possible explanation is that SSF with *Aspergillus niger* increases the total polyphenol content in sea buckthorn pomace by releasing bound phenolics and transforming flavonoids into simpler phenolics. At the same time, the total flavonoid content probably decreases due to enzymatic degradation,

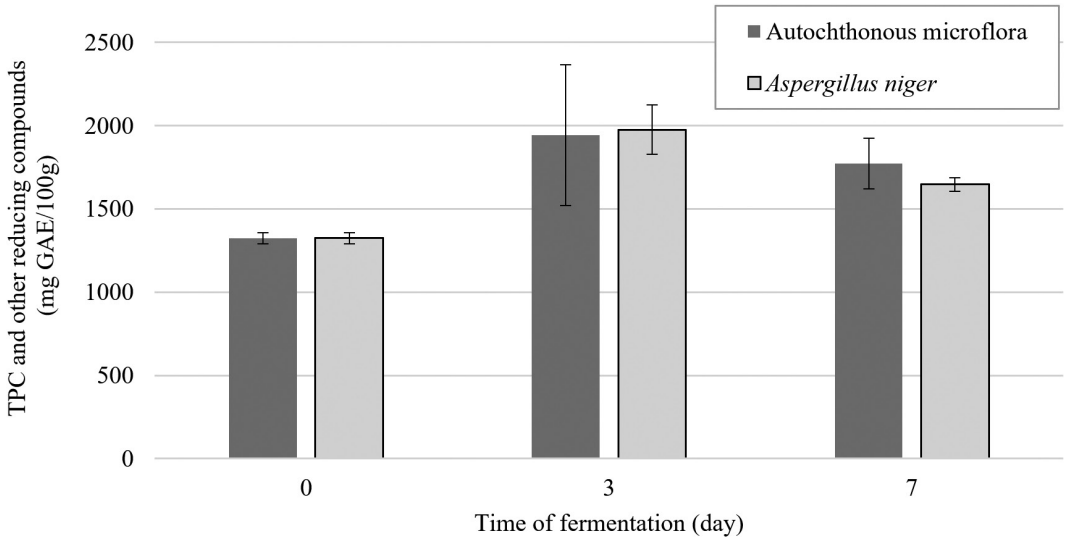

Fig. 6. Total content of polyphenols (TPC) and other reducing compounds in sea buckthorn pomace fermented with autochthonous microflora and *A. niger*.

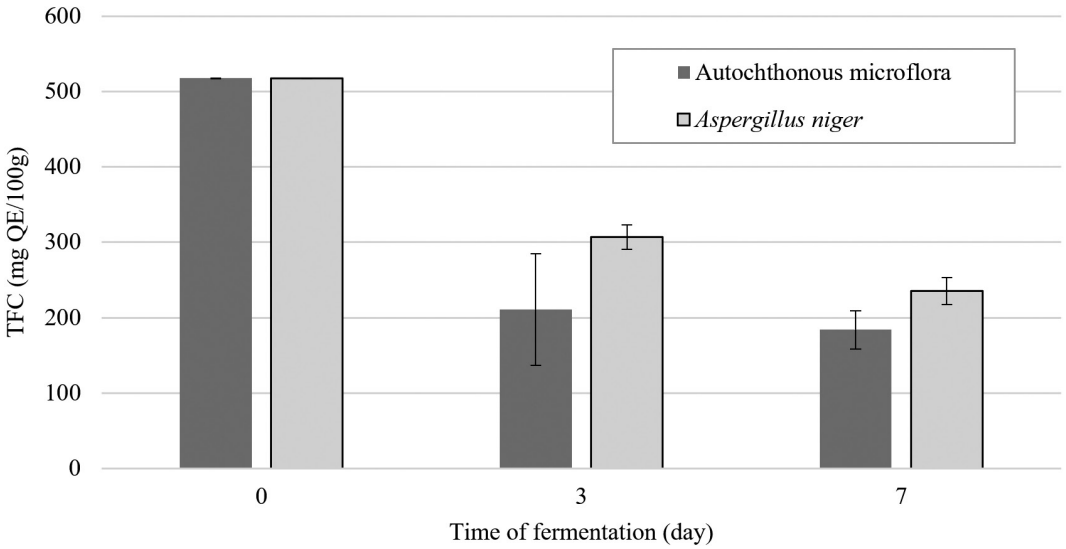

Fig. 7. Total content of flavonoids (TFC) in sea buckthorn pomace fermented with autochthonous microflora and *A. niger*.

Tab. 5. Effect of fermentation on the content of quercetin and eriodictyol in fermented and unfermented sea buckthorn pomace.

		Results (mg/100 g DW)	
Analytes	Day	Autochthonous microflora	*A. niger* (CCM 8189)
Quercetin	0	9.1 ±0.3	9.1 ±0.3
	3	7.6 ±0.4	8.5 ±0.3
	7	7.2 ±0.3	7.9 ±0.2
Eriodictyol	0	ND	ND
	3	27.3 ±1.5	95.6 ±2.3
	7	35.4 ±1.9	146.8 ±3.1

oxidation, or fungal metabolism. There are currently no published studies on the influence of fermentation on the total flavonoid content in sea buckthorn pomace, to compare our results.

Determination of specific flavonoids in sea buckthorn pomace

Initial quercetin content in sea buckthorn pomace was 9.1 ±0.3 mg/100 g DW (Tab. 5), closely matching the values reported by Dienaitė et al. (2020), who found 7.6–9.0 mg/100 g DW in sea buckthorn pomace fractions. Fermentation with either autochthonous microflora or *A. niger* led to a modest reduction in quercetin concentration by day 7. In samples fermented with autochthonous microflora, the quercetin content decreased to 7.2 ±0.3 mg/100 g DW, while in those fermented with *A. niger*, it reached 7.9 ±0.2 mg/100 g DW. This reduction suggests either partial degradation of quercetin or its transformation into secondary metabolites during the fermentation process.

During fermentation, both *A. niger* and autochthonous microflora produce various enzymes, including β-glucosidase, peroxidases, and phenoloxidases, which can hydrolyze glycosidic bonds (e.g., quercetin-3-O-glucoside to aglycone quercetin) and subsequently oxidize or catabolize aglycones. Oxidative enzymes may further convert quercetin into quinone structures or open the flavonoid ring, leading to the formation of phenolic acids or other low-molecular-weight metabolites (Hur et al., 2014).

Eriodictyol was not detectable in the initial material but was observed as early as the 3rd day of fermentation. In samples fermented with *A. niger*, the concentration increased significantly up to 146.8 ±3.1 mg/100 g DW on day 7. A similar, though less pronounced, increase occurred in autochthonous fermentations (35.4 ±1.9 mg/100 g DW). These results confirm the role of fungal fermentation in phenolic profile modification, particularly in matrices such as sea buckthorn, which are naturally rich in glycosylated flavonoids. The observed eriodictyol levels suggest partial enzymatic conversion from precursor compounds during solid-state fermentation.

To date, no peer-reviewed studies have explicitly reported the fermentation of sea buckthorn pomace

with *Aspergillus niger*. Most available publications focus on either the fermentation of sea buckthorn juice or the application of lactic acid bacteria. Although sea buckthorn pomace contains valuable flavonoids, its fermentation with filamentous fungi remains underexplored. The absence of direct studies in this context indicates a promising opportunity for future research into fungal valorization of sea buckthorn by-products.

Conclusions

This study demonstrated that solid-state fermentation (SSF) using *Aspergillus niger* significantly influences the polyphenolic profile of fruit pomace substrates, albeit in a substrate-specific manner. In apple pomace, fermentation with *A. niger* resulted in a 7.3-fold increase in total polyphenol content (TPC) and more than a 3-fold increase in total flavonoid content (TFC), with quercetin and eriodictyol identified as major contributors. These findings support the potential of fungal SSF as an efficient valorization strategy for apple by-products.

In contrast, the effects of fermentation on aronia and sea buckthorn pomace were less pronounced. While both types of pomace showed an increase in TPC during early fermentation stages, the results revealed superior performance of autochthonous microflora compared to *A. niger*, particularly in terms of sustained phenolic enrichment. However, in aronia pomace, *A. niger* induced a significant increase in eriodictyol content, reaching 269.4 mg/100 g DW by day 7, while maintaining quercetin levels. This bioconversion aligns with literature describing fungal enzymatic release and transformation of glycosylated flavonoids.

In sea buckthorn pomace, both TPC and TFC values decreased after day 3 of fermentation despite an increase in eriodictyol concentration, particularly in *A. niger*–fermented samples. This suggests that although fungal fermentation enhances specific bioactive compounds, it may also lead to the degradation of flavonoid structures in substrates with limited nutrient availability.

Overall, the findings underscore the promising potential of SSF with *A. niger* in enhancing the content of bioactive compounds in apple pomace. In case of aronia and sea buckthorn, future studies should investigate optimized fermentation parameters and explore alternative microbial strains to achieve improved flavonoid bioconversion.

Acknowledgements

This publication was supported by the Slovak Scientific Grant Agency VEGA based on contract no. 1/0141/23.

References

Banerjee J, Singh R, Vijayaraghavan R, MacFarlane D, Patti AF, Arora A (2017) Food Chem. 225, 10–22.

De Araújo FF, De Paulo Farias D, Neri-Numa IA, Pastore GM (2021) Food Chem. 338, 127535.

Dienaitė L, Pukalskas A, Pukalskienė M, Venskutonis PR (2020) Antioxidants. 9 (4), 274.

Dulf FV, Vodnar DC, Dulf EH, Diaconeasa Z, Socaciu C (2018) LWT 87, 241–249.

Dulf FV, Vodnar DC, Socaciu C (2016) Food Chem. 209, 27–36.

Erskine E, Ozkan G, Lu B, Capanoglu E (2023) ACS Omega 8, 4543–4553.

Gulsunoglu Z, Purves R, Karbancioglu-Guler F, Kilic-Akyilmaz M (2020) Biocatal. Agric. Biotechnol. 25, 101562.

Gumul D, Ziobro R, Korus J, Kruczek M (2021) Antioxidants 10, 807.

Hansen GH, Lübeck M, Frisvad JC, Lübeck PS, Andersen B (2015) Process Biochem. 50, 1327–1341.

Hur SJ, Lee SY, Kim YC, Choi I, Kim GB (2014) Food Chem. 160, 346–356.

Kreft S (2002) J. Exp. Bot. 53, 1801–1804.

Kumar K, Yadav AN, Kumar V, Vyas P, Dhaliwal HS (2017) Bioresour. Bioprocess. 4, 18.

Lavefve L, Howard LR, Carbonero F (2020) Food Funct. 11, 45–65.

Liu, Lihua, Zhang C, Zhang H, Qu G, Li C, Liu L (2021) Foods 10, 1343.

Madeddu C, Roda-Serrat MC, Christensen KV, El-Houri RB, Errico M (2021) Waste Biomass Valorization 12, 1143–1166.

Majerska J, Michalska A, Figiel A (2019) Trends Food Sci. Technol. 88, 207–219.

Martins S, Mussatto SI, Martínez-Avila G, Montañez-Saenz J, Aguilar CN, Teixeira JA (2011) A review. Biotechnol. Adv. 29, 365–373.

Musacchi S, Serra S (2018) Sci. Hortic. 234, 409–430.

Passamani FRF, Hernandes T, Lopes NA, Bastos SC, Santiago WD, Cardoso MDG, Batist LR (2014) J. Food Prot. 77, 1947–1952.

Rana S, Gupta S, Rana A, Bhushan S (2015) Food Sci. Hum. Wellness. 4, 180–187.

Roda-Serrat MC, Andrade TA, Rindom J, Lund PB, Norddahl B, Errico M (2021) Waste Biomass Valorization 12, 1815–1827.

Sosnowska D, Kajszczak D, Podsędek A (2022) Molecules. 27 (22), 8031.

Upton DJ, McQueen-Mason SJ, Wood AJ (2017) Biotechnol. Biofuels 10, 258.

Varga J, Kocsubé S, Tóth B, Frisvad JC, Perrone G, Susca A, Meijer M, Samson RA (2007) Int. J. Syst. Evol. Microbiol. 57, 1925–1932.

Verni M, Verardo V, Rizzello C (2019) Foods 8, 362.

Waldbauer K, McKinnon R, Kopp B (2017) Planta Med. 83, 994–1010.

Zhu Z, Wang Y, Lin D, Liu G, Cao C, Gong W, Zhou Y, Li N, Chen L, Li Y, Hu Z, Peng Y, Xie C (2023) Ind. Crops Prod. 195, 116422.

STU
FCHPT

Weight loss of coffee cream in polystyrene packaging

Ľubomír Valík[1], Monika Hrušková[1], Pavel Ačai[2], Silvia Mošovská[1]

[1]Department of Nutrition and Food Quality Assessment, Institute of Food Science and Nutrition, Faculty of Chemical and Food Technology, Slovak University of Technology in Bratislava, Radlinského 9, 812 37 Bratislava, Slovakia
[2]Department of Food Technology, Institute of Food Sciences and Nutrition, Faculty of Chemical and Food Technology, Slovak University of Technology in Bratislava, Radlinského 9, 812 37 Bratislava, Slovakia
lubomir.valik@stuba.sk

Abstract: This study aimed to quantify the weight loss of coffee cream (10 % fat) packaged in 10 g and 5 g polystyrene (PS) tubes over 316 days. A total of 13,760 weight measurements were performed across four production batches. Significant linear dependence between the absolute weight of coffee cream and time was observed, with negative slopes of –0.009 g/d and –0.007 g/d, and R^2 values of 0.990 and 0.996 for 10 g and 5 g tubes, respectively. Considering the surface area of the PS tube without its aluminium lid, water vapour transmission rates were calculated as 3.34 ±0.08 g/m²·d for 10 g tubes and 2.56 ±0.07 g/m²·d for 5 g tubes. Time required to decrease the weight of the cream by 10 % was 137.0 ±3.0 days for 10 g fillings and 84.0 ±1.9 days for 5 g fillings. Conversely, a loss of 1 g occurred over 110.7 ±2.4 days and 144 ±3.3 days in 10 g and 5 g tubes, respectively. These findings provide producers with an estimate of the excess amount of coffee cream needed to maintain the declared value in PS packaging material, depending on the intended shelf life.

Keywords: coffee cream, polystyrene packaging material, water vapour transmission, weight loss prediction

Introduction

Coffee cream, a dairy product standardised to 10 % or 12 % fat, is homogenised, treated at ultra-high temperature (UHT, 140 °C for 4–6 seconds), and aseptically packed in small tubes. With a shelf life exceeding four months, maintaining quality, including the declared weight of this commercially sterile product over time, is crucial. While microbiological defects can appear quickly at ambient temperatures and are prevented through incubation tests, nutritional, chemical, and physical changes require longer periods to manifest. Although weight loss does not pose health risks, consumers can perceive it negatively.

Packaging materials play a vital role in protecting dairy products from oxygen, light, moisture, and bacterial contamination, thereby extending shelf life (Deshwal et al., 2020). Each packaging type has unique permeability characteristics. Light transmission can cause off-flavours in dairy products due to photosensitizers like riboflavin, chlorophyll, and porphyrin, leading to lipid oxidation (Deshwal et al., 2020; Böhner et al., 2016).

Currently, small volumes of coffee cream are predominantly packaged in single-use polystyrene (PS) or polypropylene (PP) tubes, which are highly permeable to light and gases (Haji-Saeid et al., 2007; Böhner et al., 2016). These materials are more permeable to molecules of low molecular weight compared to metal or glass packaging (Siracusa, 2012). Böhner et al. (2016) highlighted that PS packaging has the highest surface-to-volume ratio and oxygen admission rate, making it less effective than PP and glass containers. Aluminium foil of thickness of at least 15 microns, commonly used as a closure, provides excellent impermeability (Deshwal et al., 2020).

Various intrinsic and extrinsic factors influence water vapour permeability of packaging materials. Composition of food and ambient environment (humidity, temperature) affect the barrier properties of polymers. Water content in food can lead to polymer swelling, altering the packaging's permeability over time. Higher temperatures enhance gas transport due to increased polymer segment motion (Gajdoš et al., 2001; Siracusa, 2012).

Ensuring the declared weight of food products until the end of their shelf life is crucial for producers. This study aims to provide quantitative data on the weight changes of coffee cream packed in PP containers with aluminium foil. The findings will help determine the necessary excess initial weight to maintain the declared value throughout the product's shelf life.

Materials and methods

Design of the study

The 10 % fat-content coffee cream filled in 10 g and 5 g polystyrene tubes from four productions

were kept in the laboratory at temperatures in the range of 22 °C to 24 °C and at 40–50 % RH for up to 316 days. Almost 14,000 weight measurements of whole tubes were performed with automatically calibrated analytical balances with readability from 1.0 to 0.1 mg. Primary data acquired at each measurement time were processed with Excel (Microsoft 365, Redmond, WA, USA) and @Risk vs. 8.5.1 (Lumivero, Denver, CO, USA) with periodical basic statistic evaluation and fitting of data distribution included. Net weights of the coffee cream were estimated as stochastic differences between the weights of the filled and empty containers with lids (from 160 to 820 and 200 pieces, respectively). The mean values resulting from fitting distributions were used in the regression analysis of the time dependence.

Surfaces in contact with polystyrene material

To calculate the surfaces in contact with the product or the atmosphere above it, the general formula for the area of a truncated cone was used (Fig. 1; Szczepanek, 2024). The real contact surface of polystyrene consists of the base surface (S_B, smaller circle with radius r) and the lateral surface area calculated using the following formulas:

$$S_B = \pi r^2 \quad (1)$$

$$L_S = \pi s(r + R) \quad (2)$$

S_B is the surface of the base, r is the radius of the base of an inverted truncated cone (smaller circle), R is the larger radius of the top circle, and s is the slant height calculated with the formula in which h is the height of the truncated cone:

$$s = \sqrt{((R-r)^2 + h^2)} \quad (3)$$

Thus, the surfaces in contact with the product or the atmosphere above it were calculated as the surface of the base plus the corresponding lateral surface area or the truncated cone lateral surface area corresponding to the volume of the atmosphere, respectively. The following general equation was used to calculate volumes (V) in the truncated cone:

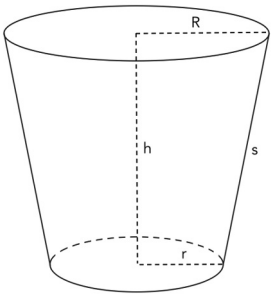

Fig. 1. Dimensional characteristics of a truncated cone.

$$V = \frac{\pi h(r^2 + rR + R^2)}{3} \quad (4).$$

The base, upper circle diameters, and height of 10 tubes were measured with a digital calliper (±0.01 mm). Uniform distributions of these dimensions were used for stochastic calculations of the slant (s), volume (V), and surface (S) of the coffee cream cones, performed using @Risk tools. The dimensions mentioned above were measured for declared weights of 10 g and 5 g tubes filled with 11 g and 6 g of cream (10 % fat), respectively. The average values and calculated surfaces of PS tubes in contact with air or cream, as well as with air and product, are summarised in Table 1.

Water vapour permeability

Water permeation through a polymer material involves four main steps: adsorption on the inner surface of the packaging material, diffusion through the polymer barrier, desorption on the outer surface, and transport of water vapour molecules into the surrounding air (Jing et al., 2021). Adsorption

Tab. 1. Average values of coffee cream tube dimensions and calculated surfaces of air and cream in contact with PS material.

	Height (mm ±SD)	Base radius (r; mm ±SD)	Upper radius (R; mm ±SD)	Slant (s; mm ±SD)	PS surface in contact with cream/air (S; mm^2 ±SD)	Volume (V; cm^3 ±SD)	Weight declared/ filled
Whole tubes	22.4 ±0.2	14.2 ±0.1	15.3 ±0.1	22.9 ±0.3	–	15,3	
Cream space	16.4 ±0.2	14.2 ±0.1	15.2 ±0.1	16.4 ±0.3	2142 ±21	11,1	10 g/11 g
Air space	6.0 ±0.1	14.3 ±0.1	15.3 ±0.1	6.1 ±0.2	566 ±6	4,2	
Whole tubes	23.3 ±0.2	13.6 ±0.2	14.5 ±0.3	23.3 ±0.3	–	15	
Cream space	12.5 ±0.3	13.6 ±0.2	13.8 ±0.1	12.5 ±0.3	1656 ±40	7	5 g/6 g
Air space	10.8 ±0.1	13.8 ±0.2	12.5 ±0.3	10.8 ±0.1	961 ±4	8	

and diffusion of water molecules are influenced by the hydrophilic nature of the polymer surface (adsorption) and the porosity and polarity of the permeable material (diffusion), which are associated with the higher solubility of water molecules. Overall moisture permeation through the packaging material can be described by Fick's law of diffusion. Polystyrene polymer (PS6), used for coffee cream containers, is an amorphous polymer generally more permeable to small molecules such as water and gases. The permeability for water vapour through polystyrene can differ between the liquid contact surface (bottom part of the cone container) and the gas-exposed surface (upper part) due to factors such as swelling, surface interactions, and contamination. Moisture loss from the coffee cream tube through the polystyrene PS6 surface under steady-state conditions was expressed for the total considered transmission permeation surface area with an overall (effective) permeation coefficient, following the Fick's law of diffusion, as:

$$\frac{\Delta m_W}{\Delta t} = \frac{\psi A\left(P_{W_1} - P_{W_2}\right)}{\delta} = \frac{\psi A\left(P_W^{'}\varphi_1 - P_W^{'}\varphi_2\right)}{\delta} \quad (5)$$

where Δm is the weight difference (moisture loss for liquid product by permeation during storage) between two weight measurements of the time coffee cream tube, Δt is the period between two weight measurements, ψ is the coefficient of moisture permeability for the packaging material PS6, A is the considered transmission permeation surface area of the coffee cream tube (truncated cone), p_{W_1} and p_{W_2} are partial water vapour pressures inside the coffee cream tube and outside (environment), respectively (driving force for moisture transmission), p'W is the saturated vapour pressure of water in air at the given temperature, φ_1 and φ_2 are relative humidities of corresponding water vapour inside the coffee cream tube and outside (environment), respectively, δ is the thickness of the wall of the truncated polystyrene PS6 truncated cone.

Water vapour transmission rate (WVTR) can be calculated using the following equation:

$$\mathrm{WVTR} = \frac{\Delta m_W}{\Delta t}\frac{1}{A} \quad (6)$$

where $\Delta m_W/\Delta t$ is the slope of the moisture loss as a function of storage time, $m_W = \mathrm{f}(t)$.

Using Equations (5) and (6), WVTR is obtained as follows:

$$\mathrm{WVTR} = \frac{\psi\left(P_{W_1} - P_{W_2}\right)}{\delta} = \frac{\psi\left(P_W^{'}\varphi_1 - P_W^{'}\varphi_2\right)}{\delta} \quad (7)$$

Finally, the water permeability coefficient through the polystyrene PS6 surface contacting the liquid and gas phase can be calculated from the rearranged equation (7):

$$\psi = \frac{\mathrm{WVTR}\cdot\delta}{\left(p_{W_1} - p_{W_2}\right)} \quad (8)$$

Results and discussion

As expected, net weight of coffee cream gradually decreased during storage. The main driving force of the release of water molecules and their transfer through the polystyrene packaging material is the difference between the relative humidity in the tubes of coffee cream and the outside atmosphere. Since coffee cream has high water activity, the equilibrium relative humidity over the product can be close to 100 %, which creates a driving force of approximately 50 % RH compared to outside storage conditions. The rate of water-vapour transmission is determined by the permeability characteristics of the material. Although water molecules can be released from the cream film, fat globules, and proteins in contact with the polystyrene material, this study only estimated the overall transfer rates of water vapour.

Weight loss trends

Figure 2 shows changes in the individual distributions of the net weights of coffee cream during long storage. The frequency of the data decreased, and the weight values expanded to broader ranges over time, leading to an increase in standard deviation with storage time.

To evaluate the overall trend of weight decrease over time, data from a linear relationship displayed in Figure 3 were analysed using regression analysis. The regression parameters and statistical indices are summarised in Table 2 for coffee creams with declared weight of 10 g and 5 g, initially filled with 11 g and 6 g, respectively. The data show low fit errors and statistically significant linear relationship, with determination coefficients higher than 0.9897.

Slope values for net weight loss express the overall weight loss in g/d. At least two partial processes are involved: saturation of relative humidity over the fluid coffee cream and transmission of water vapour through the packaging material. The volume and surface area of the packaging material over the fluid influence both processes. The study identified a lack of knowledge concerning the transfer of water molecules from the fluid in contact with polystyrene, as represented by the slope values determined. This work provides information on the general kinetics of weight loss and compares the rate in polystyrene packaging filled with different volumes of coffee cream.

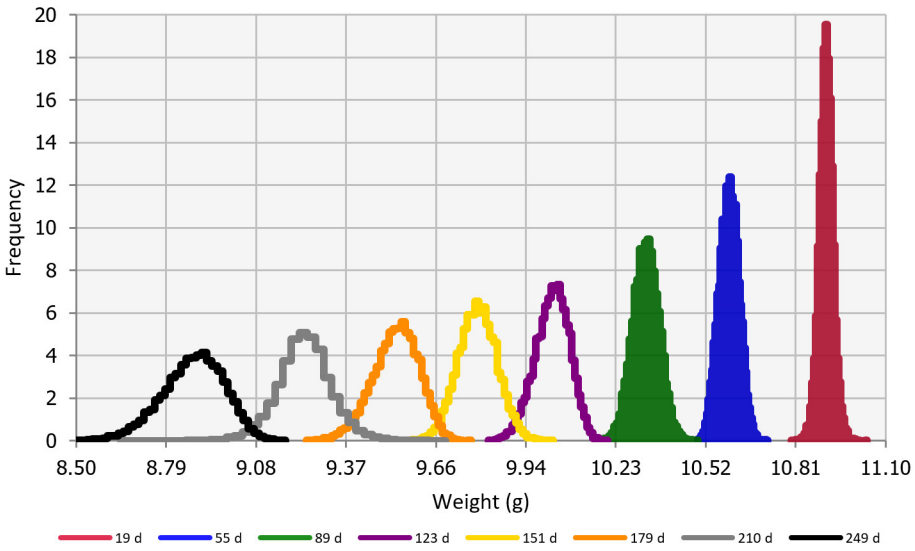

Fig. 2. Distributions of the weight of coffee cream during storage at ambient temperatures (22–24 °C).

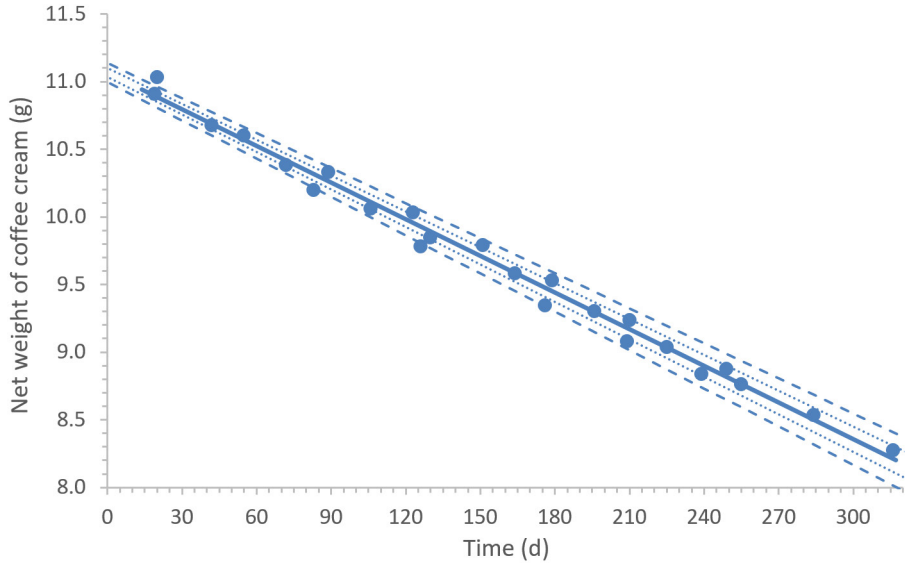

Fig. 3. Average net weights of coffee cream (declared as 10 g but filled to 11 g) in dependence on storage time under ambient laboratory conditions (T/RH: 22–24 °C/40–50 %).

From a practical perspective, the study predicts how much product should be overfilled against the declared weight to maintain it at the end of its shelf life. For example, for an initial filling of approximately 1 g above the declared weight, a 10 g coffee cream is expected to reach the declared weight after 118.1 days on average (95 % CI: 105.6 to 131.7 days). After 6 or 9 months, the net weight decreases to 9.44 g (95 % CI: 9.58 to 9.30 g) or 8.63 g (95 % CI: 8.81 to 8.45 g), respectively. However, all dry matter remains in the tubes.

Vapour transmission rates

Based on the measured dimensions of 10 coffee cream tubes and the geometry of the inverted truncated cone (Eqs. 1–4), the estimated BetaGeneral distributions of the slant height, surface, and volume were represented with the following means and standard deviations: s = 22.39 ±0.25 mm, S = 2703.04 ±29.23 mm², V = 15.26 ±0.23 mm³. Considering the surface of the PS tube without an aluminium lid and the slopes from Table 1, the normally distributed vapour transmission rates were calculated as 3.34 ±0.08 g/m²·d for 10 g tubes and 2.57 ±0.06 g/m²·d for 5 g tubes (Eq. 6). These values are within the range of 0.8–3.9 g/m²·d mentioned by Kjeldsen (1993) and Keller and Kouzes (2017).

Comparison of net weight loss slopes

Comparison of net weight loss slopes for the 5 g and 10 g products (Table 2) revealed that the negative

Tab. 2. Regression parameters and statistical indices of linear regression.

Regression	Parameter	Estimate	SE	*t*-value	*p*-value	n	R^2	RMSE
Net weight loss (10 g)	Intercept (g)	11.0664	0.0339	326.64	4.81×10^{-42}	24	0.9900	0.0779
	Slope (g/d)	-9.03×10^{-3}	1.93×10^{-4}	-46.78	1.61×10^{-23}			
Relative weight loss (10g)	Intercept	1.0030	0.0029	346.76	1.29×10^{-42}		0.9897	0.0067
	Slope	-7.58×10^{-4}	1.65×10^{-5}	-45.99	2.32×10^{-23}			
Net weight loss (5 g)	Intercept (g)	6.0758	0.0245	247.68	4.62×10^{-15}	9	0.9982	0.0386
	Slope (g/d)	-6.94×10^{-3}	1.58×10^{-4}	-44.04	8.13×10^{-10}			
Relative weight loss (5 g)	Intercept	1.0221	0.0043	236.97	3.81×10^{-13}		0.9986	0.0054
	Slope	-1.19×10^{-3}	2.61×10^{-5}	-45.56	7.50×10^{-9}			

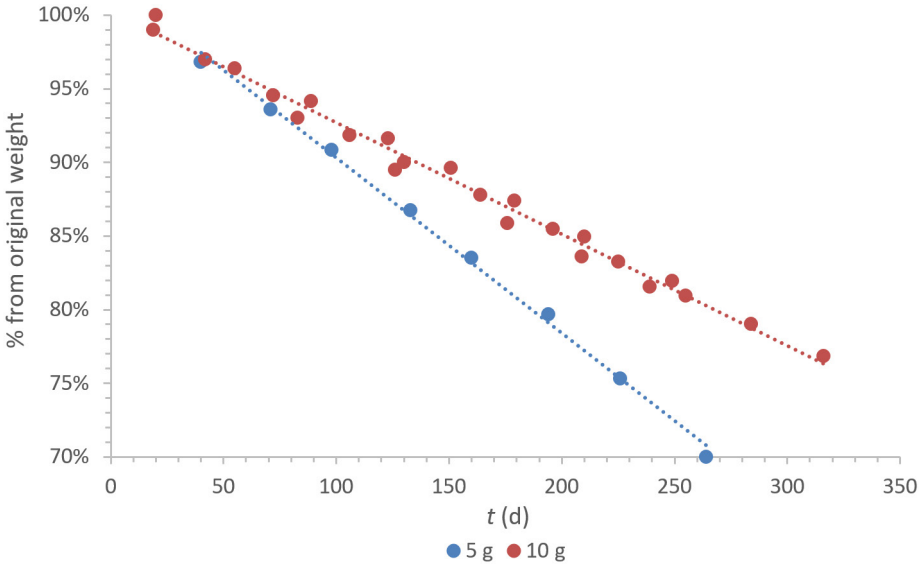

Fig. 4. Relative weight loss of coffee cream in dependence on storage time under ambient laboratory conditions (T/RH: 22—24 °C/40—50 %). Data represent the average percentages related to the initial weight of four productions, three with a declared 10 g weight and one with a declared weight of 5 g.

slope value for 10 g tubes (-9.03×10^{-3} g/d) is lower than that for 5 g tubes (-6.94×10^{-3} g/d). Parameter errors for the 5 g and 10 g products were low, about 2 % of the parameter values. The difference between the storage tests of 10 g and 5 g tubes is in the different volumes of the product and the space over it. A higher volume of fluid coffee cream in 10 g tubes is in contact with a larger surface of the polystyrene material and the outside atmosphere. Conversely, a lower volume of the atmosphere over the product can be better saturated with water vapour from the higher volume of coffee cream, suggesting higher driving force for a longer time. The opposite ratios are in 5 g tubes, with less coffee cream in contact with the packaging material and a larger volume for water vaporisation. These phenomena generally counteract each other, making it difficult to specify their effects within the presented experiment. The relevant output of this work resulted from simple total regression relations (Fig. 3).

Relative Weight Loss

The same data sets, in relative form, were used to express the relationship between the percentage of weight loss from the original weight and storage time (Fig. 4). Despite the lower net weight loss in the 5 g tubes (Table 1), the relative weight loss declined faster with time in the 5 g tubes compared to the 10 g tubes.

Water Permeability Coefficients

For validation purposes, one objective was to calculate the water permeability coefficient of the PS6 polystyrene packaging material (Eq. 8). The transmission of water through the PS tube is different in the liquid phase (coffee cream) and in the atmosphere over the product. Differences may arise from slight swelling of the polymer and surface contamination in contact with the liquid phase. The portion of the PS6 material exposed only to the atmosphere might not undergo the same swelling effect, potentially leading to lower

permeability. Surface contamination in the bottom part of the tube reduces the effective permeability of water. Based on our data and the average thickness of the tube PS material (δ = 0,10 mm), the total permeability coefficients were calculated as 2.3×10^{-12} g·m/(m²·s·Pa) for 10 g tubes and 1.8×10^{-12} g·m/(m²·s·Pa) for 5 g tubes. These coefficients are consistent with typical polystyrene packaging material values in the range of 10^{-12} to 10^{-13} g·m/(m²·s·Pa) (Feng, 2015) at temperatures of 25 °C and 30 °C.

Conclusions

In this study, weight loss of coffee cream packaged in 10 g and 5 g polystyrene tubes over 316 days was quantified. Results show a significant linear relationship between the weight loss and storage time, with higher weight loss rates observed in 10 g tubes compared to 5 g tubes. Primary factors influencing weight loss, include the relative humidity difference between the coffee cream and the surrounding atmosphere, the permeability characteristics of the polystyrene material. The findings provide valuable insights for producers, enabling them to estimate the necessary overfill to maintain the declared weight throughout the product's shelf life. Calculated water WVTR and permeability coefficients are consistent with existing literature, validating the study's methodology and results. On the other hand, environmental factors such as temperature and relative humidity should be carefully considered, as they significantly influence the permeability of polystyrene coffee cream tubes and the transmission of water vapour from the product. Elevated temperatures increase the free volume and molecular mobility within the polystyrene matrix, thereby enhancing its permeability to moisture. Concurrently, higher relative humidity intensifies the partial pressure gradient across the packaging barrier, accelerating moisture transfer. Together, these effects can lead to excessive water loss, potentially compromising the product's texture, flavour, and shelf life if not properly controlled.

Acknowledgments
The authors gratefully acknowledge financial support from VEGA 1/0132/23.

References

Böhner N, Adolf L, Tybussek T, Rieblinger, VM, Langowski HC (2017) Int Dairy J 64: 37—47.
Deshwal GK, Panjagari NR (2020) J Food Sci Technol 57: 2377—2392.
Feng P (2015) Polymer Aging of Plastic Scintillators. Sandia National Laboratories, Albuquerque.
Gajdoš J, Galic K, Kurtanjek Ž, Cikovic N (2000) Polym Test 20: 49—57.
Haji-Saeid M, Sampa MH, Chmielewski AG (2007) Radiat Phys Chem 76: 1535—1541.
Jing Z, Guo Y, Ren M, Zhao X, Shao H, Zhou Y, Shuai M (2021) E-Polym 21: 830—844.
Keller PE, Kouzes R (2017) Water Vapor Permeation in Plastics. Pacific Northwest National Laboratory, Richland.
Kjeldsen P (1993) Water Res 27: 121—131.
Siracusa V (2012) Int J Polym Sci: 302029.
Szczepanek A. Available at: https://www.omnicalculator.com/math/truncated-cone. Accessed: April 5, 2025.

STU
FCHPT

Quantum-chemical studies of triangulo cobalt-hydride clusters with trimethylphosphine and carbonyl ligands

Martin Breza

Department of Physical Chemistry, Faculty of Chemical and Food Technology STU, Radlinskeho 9, SK-81237 Bratislava, Slovakia
martin.breza@stuba.sk

Abstract: Geometry of neutral $[H_n\{Co(\mu_2\text{-}CO)(PMe_3)_2\}_3]$ complexes, n = 0→4, in three lowest spin states was optimized at the B3LYP/6-311G* level of theory with GD3 dispersion correction. The most stable quartet spin state was found for $[\{Co(\mu_2\text{-}CO)(PMe_3)_2\}_3]$ whereas the doublet or triplet spin states are the most stable in the remaining complexes. Hydrogenation of $[\{Co(\mu_2\text{-}CO)(PMe_3)_2\}_3]$ to the complexes with μ_3-H bridges is more advantageous at lower temperatures. Trigonal symmetry is preserved only in $[(\mu_3\text{-}H)\{Co(\mu_2\text{-}CO)(PMe_3)_2\}_3]$. Neutral H_2 units in $[(H_2)\{Co(\mu_2\text{-}CO)(PMe_3)_2\}_3]$, $[(H_2)(\mu_3\text{-}H)\{Co(\mu_2\text{-}CO)(PMe_3)_2\}_3]$, and $[(H_2)_2\{Co(\mu_2\text{-}CO)(PMe_3)_2\}_3]$ are only physisorbed and show vanishing spin density. Spin density is concentrated dominantly at positively charged Co atoms and only the vanishing spin density is located at the negatively charged μ_3-H atoms. There are no Co—Co bonds and the Co_3 triangles are held together only by μ_2-CO and μ_3-H bridges.

Keywords: DFT calculations; electronic structure; geometry optimization; QTAIM.

Introduction

Atomic clusters exhibit unique structural and electronic characteristics which offer significant potential to achieve novel material properties and functions (Tsukamoto, 2024). Unlike nanoparticles, their small size is the source of eccentric physical and chemical properties implied by quantum effects. Their electronic states resemble rather those of molecules than those of bulk materials. The steric and electronic structures of atomic clusters offer potential for achieving novel properties and functions.

A re-established concern in catalysis by low-valent transition metal clusters is implied by their multiple binding sites and unusual bridging coordination (Hogarth et al., 2010; Böhme and Schwarz, 2010). Moreover, they act as electron buffer for catalytic reactions and can have desirable magnetic properties (Nombel et al., 1999; Moberg et al., 2006; Liu et al., 2015; Craig and Murrie, 2015). Metal carbonyl clusters $[Et_4N]_2[Fe_3(CO)_9E]$ (E = S, Se, Te) were investigated as well (Guzman-Jimenez et al., 2003). The first tricobalt clusters $Co_3(CO)_3(CO)_3L_3$, L = PPh_3 or P^nBu_3 were synthesized in 1969 (Pregaglia et al., 1969) and their hydride X-ray structure was later reformulated as $HCo_3(CO)_3(CO)_3(PPh_3)_3$ (Bradamante et al., 1983). Concurrently, an analogous hydrido cluster $HCo_3(CO)_9$ has been synthesized as deduced by mass spectrometry (Facchinetti et al., 1979, 1981).

Klein et al. (1992a) synthesized the X-ray structure of $[H\{Co(\mu_2\text{-}CO)(PMe_3)_2\}_3]$ by photochemical activation and published. Position of the central μ_3-H atom in the trigonal space group R-3c was deduced based on semiempirical INDO calculations. This compound was used as a catalyst in linear trimerization of phenylethyne (Klein et al., 1992b). The synthesis, X-ray structures, and magnetic properties of a whole series of isostructural triangulo cobalt-hydride clusters $[X\{Co(\mu_2\text{-}CO)(PMe_3)_2\}_3]$, X = none, H, and H_3 (see Fig. 1 and Tab. 1) were published as well (Klein et al., 1997; Boča et al., 2000). $[H_3\{Co(\mu_2\text{-}CO)(PMe_3)_2\}_3]$ was obtained from $[H\{Co(\mu_2\text{-}CO)(PMe_3)_2\}_3]$ and H_2 at 20 °C in tetrahydrofuran.

Paramagnetic $[\{Co(\mu_2\text{-}CO)(PMe_3)_2\}_3]$ complex in doublet spin state (Fig. 1) forms dark violet hexagonal crystals sparingly soluble in toluene, benzene, or tetrahydrofuran (Klein et al., 1997; Boča et al., 2000). Mass spectra indicate the presence of more than 10 % of $[H\{Co(\mu_2\text{-}CO)(PMe_3)_2\}_3]$ in solid $[\{Co(\mu_2\text{-}CO)(PMe_3)_2\}_3]$. The effective magnetic moment slowly decreases (from 1.9 μ_B at room temperature) up to 30 K (1.7 μ_B) and then rapidly drops (1.3 μ_B at 4 K). This can be explained by thermally inaccessible quartet spin state and weak antiferromagnetic interactions between neighboring complexes.

Paramagnetic $[H\{Co(\mu_2\text{-}CO)(PMe_3)_2\}_3]$ complex (in triplet ground spin state) forms a continuous range of mixed crystals with $[\{Co(\mu_2\text{-}CO)(PMe_3)_2\}_3]$ and cannot be separated by recrystallization (Klein et al., 1997; Boča et al., 2000). In the presence of protic acids or metal hydrides, $[H\{Co(\mu_2\text{-}CO)(PMe_3)_2\}_3]$ is

readily transformed to $[H_3\{Co(\mu_2\text{-}CO)(PMe_3)_2\}_3]$, which indicates hydride character of the μ_3-H atom. The effective magnetic moment of $[H\{Co(\mu_2\text{-}CO)(PMe_3)_2\}_3]$ decreases from 3.1 μ_B at 300 K to 2.5 μ_B at ca 30 K and then rapidly drops to 1.7 μ_B at 4 K. This is consistent with two unpaired electrons per molecule, antiferromagnetic coupling in a Co_3 unit and ferromagnetic Co—H coupling. The decrease under 30 K is explained by zero-field splitting of the triplet spin state and/or the antiferromagnetic intermolecular interaction. A tendency to reach a singlet spin state is also possible.

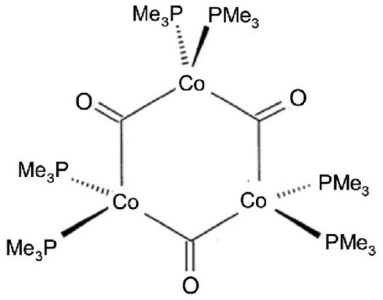

Fig. 1. Schematic structure of $[\{Co(\mu_2\text{-}CO)(PMe_3)_2\}_3]$.

Tab. 1. Interatomic distances (in Å) in X-ray structures of $[H_n\{Co(\mu_2\text{-}CO)(PMe_3)_2\}_3]$ clusters (Klein et al., 1992a; Klein et al., 1997).

n	0	1	3
Co—Co	2.4055(5)	2.421(1)	2.4320(7) 2.4321(7)
Co—H	–	Not detected	1.71(3)
Co—C	1.904(2)	1.921(6) 1.913(10)	1.915(2)
Co—P	2.1929(5)	2.195(2) 2.198(2)	2.202(1)
C—O	1.188(3)	1.172(11)	1.179(4)

$[H_2\{Co(\mu_2\text{-}CO)(PMe_3)_2\}_3]$ was not confirmed by IR spectra (Klein et al., 1997).

Paramagnetic $[H_3\{Co(\mu_2\text{-}CO)(PMe_3)_2\}_3]$ (in triplet ground spin state) can be recrystallized from tetrahydrofuran (Klein et al., 1997; Boča et al., 2000). Mass spectra show successive loss of three H atoms, and IR spectra indicate at least one μ_3-H moiety. However, hydrogenation of cyclopentene or cyclohexene in tetrahydrofuran by this complex failed. The effective magnetic moment of $[H_3\{Co(\mu_2\text{-}CO)(PMe_3)_2\}_3]$ is nearly temperature independent up to 2.6 μ_B at 20 K and then rapidly decreases to 1.59 μ_B at 4 K. The explanation is similar to that for $[H\{Co(\mu_2\text{-}CO)(PMe_3)_2\}_3]$. However, magnetic susceptibility down to 3.8 K confirms antiferromagnetic coupling within the Co_3 ring and Co—H interaction of antiferromagnetic nature.

Semiempirical INDO study (Breza, 1994) of the electronic structure of $^2[\{Co(\mu_2\text{-}CO)(PMe_3)_2\}_3]^0$ and $^3[H\{Co(\mu_2\text{-}CO)(PMe_3)_2\}_3]^0$ in the $[\{Co(\mu_2\text{-}CO)(PMe_3)_2\}_3]^0$ experimental geometry (the left superscript denotes the spin multiplicity while the right superscript denotes the charge of the molecule) indicate positive H charges. Very high electron density is concentrated at the Co_3 ring (negative Co charges). Central μ_3-H atoms are most probably located over the center of the Co_3 triangle (1.2—1.3 Å). Co atoms are held together via carbonyl bridges rather than by direct Co—Co bonding.

The aim of our recent study is a quantum-chemical study of neutral triangulo-$[H_nCo_3(\mu_2\text{-}CO)_3(PMe_3)_6]$ clusters, n = 0→4, in various spin states to explain experimentally observed data. In the first step, structure of the model clusters was optimized. Subsequently, their geometries (especially the positions of added H atoms) and electronic structures were compared. Regarding the size of the clusters under study, standard DFT treatment was used.

Method

Geometry optimization of neutral $[H_n\{Co(\mu_2\text{-}CO)(PMe_3)_2\}_3]$ molecules, n = 0→4, in three lowest spin states was performed using the Gaussian16 software (Frisch et al., 2016) using the B3LYP hybrid functional (Becke, 1993) with GD3 dispersion correction (Grimme et al., 2010). The 6-311G* basis sets from the Gaussian16 library (Frisch et al., 2016) were used for all atoms and the non-methyl hydrogens were augmented with p functions. The optimized structures were tested on the absence of imaginary vibrations to confirm that they correspond to the minima of the adiabatic potential surface. The complexes in singlet spin states (S) were treated using unrestricted formalism within a 'broken symmetry' treatment (BS) and its energy (E_S) was corrected in the relation to the high spin state (HS) as follows:

$$E_S = E_{HS} + (E_{BS} - E_{HS})\frac{< S^2 >_{HS}}{< S^2 >_{HS} - < S^2 >_{BS}} \qquad (1)$$

where E_{HS} and E_{BS} are high-spin (HS) and 'broken symmetry' (BS) energies, respectively, whereas $<S^2>_{HS}$ and $<S^2>_{BS}$ are the corresponding spin-square values (Malrieu and Trinquier, 2012). Quintet spin states were used as the HS ones. Gibbs energy as the sum of DFT energy E and Gibbs energy contribution (G_{contr}) in case of the singlet spin state (G_S) can be approximated as

$$G_S = E_S + G_{contr,BS} \qquad (2)$$

where $G_{contr,BS}$ is Gibbs energy contribution in the BS state (Saito et al., 2009).

Electronic structure of the complexes studied was evaluated in terms of Quantum Theory of Atoms-in-Molecule (QTAIM; Bader 1994). QTAIM topological analysis of electron density is a powerful tool for chemical bonding and structure analysis in molecules and crystals. The first derivative (gradient) of the electron density vanishes at its 'critical points' (CP) such as maxima, minima, and saddle points.

Atom positions are determined by electron density maxima. QTAIM atomic charges are obtained using the electron density integrated over atomic basins.

In equilibrium geometry, a pair of bonded atoms are linked by a line, i.e., a bond path along which the electron density is maximally concentrated (ridges of electron density). The presence of a bond path between two atoms is the necessary (but not sufficient) condition for the presence of a chemical bond. The set of bond paths for a given molecule, the molecular graph, faithfully recovers the network of chemical bonds assigned based on chemical considerations. The saddle point of electron density at the bond path is a bond critical point (BCP).

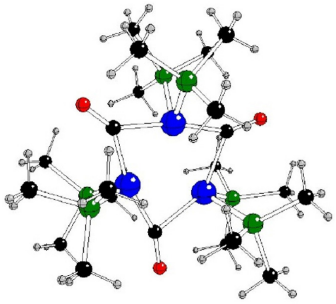

$^{4}[\{Co(\mu_2\text{-}CO)(PMe_3)_2\}_3]^0$
model A

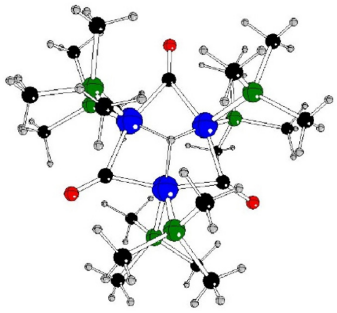

$^{3}[(\mu_3\text{-}H)\{Co(\mu_2\text{-}CO)(PMe_3)_2\}_3]^0$
model B

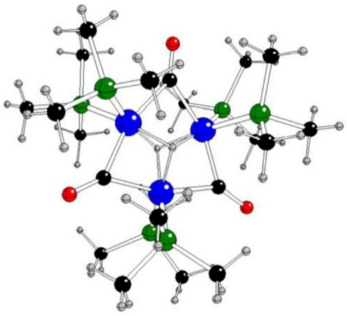

$^{2}[(\mu_3\text{-}H)_2\{(\mu_2\text{-}CO)(PMe_3)_2\}_3]^0$
model C1

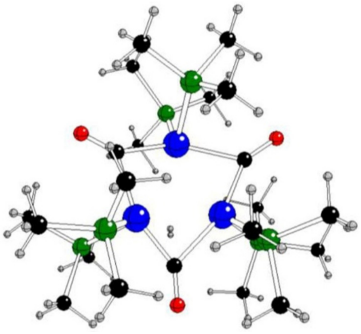

$^{2}[(H_2)\{C_3(\mu_2\text{-}CO)(PMe_3)_2\}_3]^0$
model C2

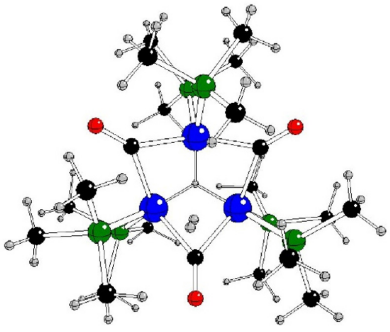

$^{3}[(H_2)(\mu_3\text{-}H)\{Co(\mu_2\text{-}CO)(PMe_3)_2\}_3]^0$
model D

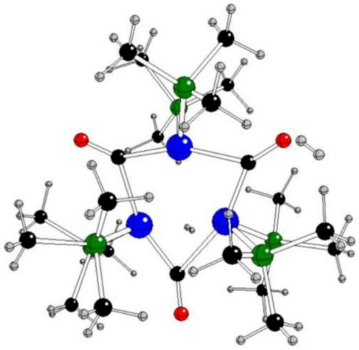

$^{2}[(H_2)_2\{Co(\mu_2\text{-}CO)(PMe_3)_2\}_3]^0$
model E

Fig. 2. Optimized geometries of model systems under study in the most stable spin states (Co – blue, C – black, O – red, P – green, H – gray).

Tab. 2. Absolute DFT energies (E_{DFT}), and Gibbs energies at 298 K (G_{298}), and their relative values related to $^4[\{Co(\mu_2\text{-}CO)(PMe_3)_2\}_3]^0$ (ΔG_{298}), average spin-square values ($<S^2> = S(S+1)$), related spin (S), and relative abundance of individual spin states of the same compound of model systems $[H_n\{Co(\mu_2\text{-}CO)(PMe_3)_2\}_3]$ in various spin states defined by spin multiplicities (M_S). The most stable spin states of individual complexes are denoted in bold.

n	Model	M_S	E_{DFT} [hartree]	G_{298} [hartree]	$<S^2>$	S	ΔG_{298} [kJ/mol]	Relative abundance [%]
0	A	2	–7255.57495	–7254.94365	1.4158	0.7906	7.7	4.3
		4	**–7255.57531**	**–7254.94657**	**3.9475**	**1.5488**	0.0	95.7
		6	–7255.51520	–7254.88980	8.8095	2.5097	149.1	0.0
1	B	1	–7256.18630[a)]	–7255.54623[a)]	1.1239	0.6721	–1603.8[b)]	35.3
		3	**–7256.19928**	**–7255.55797**	**2.1639**	**1.0537**	–1605.3	64.7
		5	–7256.13628	–7255.49964	6.1386	2.0276	–1452.1	0.0
2	C1	**2**	**–7256.77269**	**–7256.12844**	**1.1433**	**0.6804**	–3103.1	100.0
		4	–7256.74928	–7256.10430	3.8154	1.5163	–3039.7	0.0
		6	–7256.70765	–7256.07484	8.9475	2.5327	–2962.4	0.0
	C2	**2**	**–7256.74530**	**–7256.09832**	**1.6532**	**0.8796**	–3024.0	100.0
		4	–7256.73400	–7256.09615	3.9398	1.5469	–3018.3	0.0
		6	–7256.69178	–7256.05110	8.8138	2.5106	–2900.1	0.0
3	D	1	–7257.35707[a)]	–7256.70031[a)]	1.1284	0.6741	–4628.0[b)]	2.6
		3	**–7257.36818**	**–7256.71265**	**2.1743**	**1.0572**	–4637.0	97.4
		5	–7257.31730	–7256.67566	6.1388	2.0276	–4539.9	0.0
4	E	**2**	**–7257.92627**	**–7257.27248**	**1.6506**	**0.8786**	–6106.9	99.9
		4	–7257.92381	–7257.26446	3.9650	1.5530	–6085.9	0.0
		6	–7257.87440	–7257.22477	8.8121	2.5103	–5981.6	0.0

Remarks:

[a)]uncorrected value in the BS state

[b)]corrected value according to Eq. (2).

Tab. 3. Reaction Gibbs energies ($\Delta_r G_T$) of hydrogenation reactions at various temperatures (T).

Reaction	$\Delta_r G_{298}$ [kJ/mol]	$\Delta_r G_{200}$ [kJ/mol]	$\Delta_r G_{100}$ [kJ/mol]
$^4[\{Co(\mu_2\text{-}CO)(PMe_3)_2\}_3]^0 + 0.5\ ^1(H_2)^0 \rightarrow ^3[(\mu_3\text{-}H)\{Co(\mu_2\text{-}CO)(PMe_3)_2\}_3]^0$	–54.9	–64.5	–73.4
$^4[\{Co(\mu_2\text{-}CO)(PMe_3)_2\}_3]^0 + ^1(H_2)^0 \rightarrow ^2[(\mu_3\text{-}H)_2\{Co(\mu_2\text{-}CO)(PMe_3)_2\}_3]^0$	–2.3	–16.3	–29.5
$^4[\{Co(\mu_2\text{-}CO)(PMe_3)_2\}_3]^0 + ^1(H_2)^0 \rightarrow ^2[(H_2)\{Co(\mu_2\text{-}CO)(PMe_3)_2\}_3]^0$	76.8	63.8	51.5
$^4[\{Co(\mu_2\text{-}CO)(PMe_3)_2\}_3]^0 + 1.5\ ^1(H_2)^0 \rightarrow ^3[(H_2)(\mu_3\text{-}H)\{Co(\mu_2\text{-}CO)(PMe_3)_2\}_3]^0$	14.2	–5.3	–23.6
$^4[\{Co(\mu_2\text{-}CO)(PMe_3)_2\}_3]^0 + 2\ ^1(H_2)^0 \rightarrow ^2[(H_2)_2\{Co(\mu_2\text{-}CO)(PMe_3)_2\}_3]^0$	94.8	75.8	54.4

QTAIM bond characteristics are usually evaluated in terms of electron density (ρ), its Laplacian ($\nabla^2\rho$), bond ellipticity (ε), and delocalization indices (DI). The electron density Laplacian ($\nabla^2\rho$) is defined as:

$$\nabla^2\rho = \lambda_1 + \lambda_2 + \lambda_3 \quad (2)$$

and bond ellipticity (ε) is given as:

$$\varepsilon = \frac{\lambda_1}{\lambda_2} - 1 \quad (3)$$

where λ_i are eigenvalues of the Hessian of BCP electron density, $\lambda_1 < \lambda_2 < 0 < \lambda_3$. BCP electron density ($\rho_{BCP}$) is proportional to the bond strength; the value and sign of its BCP Laplacian ($\nabla^2\rho_{BCP}$) describes the relative electron density contribution of bonded atoms to the bond (covalent *vs.* dative bonding); its BCP bond ellipticity (ε_{BCP}) describes its deviation from cylindrical symmetry (such as in ideal single or triple bonds) due to its double-bond character, mechanical strain, and other perturbations.

Electron delocalization index DI(A,B) is the average number of electrons delocalized (shared) between atoms A and B (Keith, 2019). It is used as a bond

Tab. 4. Relevant interatomic distances and bond angles in model systems $[H_n\{Co(\mu_2\text{-}CO)(PMe_3)_2\}_3]$ in the most stable spin states (M_S).

n	0	1	2	2	3	4
Model	A	B	C1	C2	D	E
M_S	4	3	2	2	3	2
Distance [Å]						
Co—Co	2.524 2.489 2.445	2.420(3×)	2.459(2×) 2.381	2.537 2.530 2.568	2.428 2.459 2.430	2.536 2.572 2.529
$Co—C_{C=O}$	1.765, 2.055 1.785, 2.108 1.918, 1.869	1.914(3×) 1.896(3×)	1.912, 1.979 1.890, 1.888 1.981, 1.910	1.814, 2.054 1.818, 2.102 1.802, 2.086	1.893, 1.918 1.909, 1.920 1.904, 1.910	2.116, 1.800 2.078, 1.815 2.045, 1.819
Co—P	2.180, 2.181 2.281, 2.279 2.215, 2.213	2.214(3×) 2.216(3×)	2.229(2×) 2.205(2×) 2.228(2×)	2.239, 2.246 2.210(2×) 2.240, 2.247	2.217, 2.218 2.245, 2.243 2.243, 2.251	2.224(2×) 2.241, 2.238 2.219, 2.241
C—O	1.187 1.184 1.193	1.188(3×)	1.183(2×) 1.186	1.186(2×) 1.184	1.189 1.186 1.188	1.183 1.187 1.189
Angle [deg]						
Co—Co—Co	60.1 58.4 61.5	60.0(3×)	61.0 57.9 61.0	59.4 60.9 59.7	60.8 59.6 59.5	61.0 59.4 59.6
$Co—C_{C=O}—Co$	82.3 79.0 80.4	78.9(3×)	78.9(2×) 77.0	81.6 80.4 82.1	79.1(2×) 79.9	80.3 82.4 81.6
$Co—C_{C=O}—O$	158.0/119.6 129.6/151.3 138.1/141.5	140.4(3×)/ 140.7(3×)	137.3/143.8 143.9/137.2 141.5(2×)	133.8/144.5 133.2/146.4 131.9/146.0	141.4/139.5 140.3/139.8 140.5/140.4	131.8, 147.8 132.0, 145.5 135.1, 143.3
P—Co—P	103.4 102.5 100.4	100.1(3×)	100.7(2×) 103.2	98.1 99.4 98.9	100.1 98.5 96.5	98.8 98.0 99.7

Tab. 5. Distances to Co atoms and heights over the Co_3 plane of the H atom in the central μ_3-bridge, H_{centr}, and in the added H_2 unit, H_{H2}, of the model systems $[H_n\{Co(\mu_2\text{-}CO)(PMe_3)_2\}_3]$ in the most stable spin states, M_S.

n	1	2	2	3	4
Model	B	C1	C2	D	E
M_S	3	2	2	3	2
Distance [Å]					
$Co—H_{centr}$	1.693(3×)	1.747/1.739 1.703(2×) 1.738/1.747	–	1.691 1.682 1.694	–
$Co—H_{H2}$	–	–	2.769/3.468 3.504/4.163 2.970/3.623	3.546/4.219 2.960/3.620 3.027/3.736	2.040/3.695, 5.598/6.084 2.815/3.522, 7.095/7.627 3.623/4.275, 5.866/6.533
$(H—H)_{H2}$	–	–	0.746	0.747	0.746, 0.744
Height [Å]					
$Co_3—H_{centr}$	0.955	1.007/1.008	–	0.932	–
$Co_3—H_{H2}$	–	–	2.550/3.278	2.723/3.447	2.613/3.342, 4.546/5.046

Tab. 6. Charges and spin populations of relevant atoms of the model systems $[H_n\{Co(\mu_2\text{-}CO)(PMe_3)_2\}_3]$ in the most stable spin states, M_S.

n	0	1	2	2	3	4
Model	A	B	C1	C2	D	E
M_S	4	3	2	2	3	2
Charge						
Co	0.27 0.46 0.31	0.39(3×)	0.46(2×) 0.40	0.35 0.31 0.33	0.39 0.40 0.41	0.30 0.34(2×)
$C_{C=O}$	0.59(2×) 0.63	0.63(2×) 0.64	0.66 0.69 0.68	0.64 0.63(2×)	0.64(3×)	0.62 0.64 0.63
O	–1.19(2×) –1.18	–1.19(3×)	–1.18(3×)	–1.18 –1.19(2×)	–1.19(2×) –1.18	–1.19(2×) –1.18
P	1.61, 1.54 1.60, 1.55 1.62, 1.60	1.61(3×) 1.59(3×)	1.59(4×) 1.60(2×)	1.58/1.56 1.58/1.59 1.55/1.57	1.59, 1.56 1.58, 1.59 1.62, 1.59	1.56(3×)/ 1.58(3×)
H_{centr}	–	–0.32	–0.29(2×)	–	–0.32	-
H_{H2}	–	–		0.02, –0.06	0.03, –0.06	0.02, –0.05 0.00, –0.00
Spin						
Co	0.70 1.75 0.93	0.80(3×)	0.81(2×) –0.48	1.07 –0.91 0.99	0.78 0.82 0.84	–0.91 1.00 1.05
$C_{C=O}$	–0.10(2×) –0.09	–0.09(3×)	–0.09 –0.00(2×)	–0.08 0.02 –0.04	–0.09(3×)	0.02 –0.04 –0.08
O	–0.07(2×) –0.03	–0.06(3×)	–0.06 –0.00(2×)	–0.06 0.01 –0.03	–0.06(3×)	0.01 –0.03 –0.05
P	0.01(3×) 0.00(3×)	–0.00(4×) 0.01(2×)	0.01(4×) –0.01/–0.00	0.00(6×)	0.01(3×) –0.03(3×)	0.00(5×) 0.01
H_{centr}	–	–0.03	–0.02(2×)	–	–0.03	–
H_{H2}	–	–	–	0.00, 0.01	–0.00, –0.01	0.00(4×)

index for atoms A and B connected by a bond path. Ring critical points (RCP) are located inside cyclic structures with two positive and one negative eigenvalues of the Hessian of RCP electron density. Local minima of electron density are known as cage critical points (CCP) with three positive eigenvalues of the Hessian of CCP electron density.

QTAIM topological analysis of electron density was performed using the AIMAll software (Keith, 2019). The AIM2000 software (Biegler-König et al., 2001) was used to draw molecular graphs of the studied systems. The MOLDRAW software was used for geometry manipulation and visualization (Ugliengo, 2012).

Results and Discussion

Geometry optimization of neutral triangulo-complexes $[\{Co(\mu_2\text{-}CO)(PMe_3)_2\}_3]$ (model A), $[(\mu_3\text{-}H)\{Co(\mu_2\text{-}CO)(PMe_3)_2\}_3]$ (model B), $[(\mu_3\text{-}H)_2\{(\mu_2\text{-}CO)(PMe_3)_2\}_3]$ (model C1), $[(H_2)\{C_3(\mu_2\text{-}CO)(PMe_3)_2\}_3]$ (model C2), $[(H_2)(\mu_3\text{-}H)\{Co(\mu_2\text{-}CO)(PMe_3)_2\}_3]$ (model D), and $[(H_2)_2\{Co(\mu_2\text{-}CO)(PMe_3)_2\}_3]$ (model E) was performed in three lowest spin states (M_S) starting from X-ray structures of $[H_n\{Co(\mu_2\text{-}CO)(PMe_3)_2\}_3]$ and/or their modifications (Klein et al., 1992a; Klein et al., 1997). Starting positions of H_2 molecules in models C2, D, and E were approximately 1.5/2.5 Å over

Tab 7. Delocalization indices, DI, and electron density at bond critical points, ρ_{BCP}, of the relevant bonds of the model systems $[H_n\{Co(\mu_2\text{-}CO)(PMe_3)_2\}_3]$ in the most stable spin states, M_S.

n	0	1	2	2	3	4
Model	A	B	C1	C2	D	E
Ms	4	3	2	2	3	2
DI						
Co—$C_{C=O}$	0.868/0.764 1.130/0.525 0.506/1.073	0.812(3×) 0.779(3×)	0.773/0.728 0.667/0.807 0.810/0.664	1.040/0.545 0.576/1.029 0.538/1.064	0.785/0.772 0.817/0.804 0.798/0.778	1.033/0.594 0.521/1.068 0.549/1.033
Co—P	0.780/0.792 0.671/0.667 0.740/0.737	0.745(3×)	0.723(2×) 0.753(2×) 0.726/0.722	0.705/0.733 0.762/0.767 0.738/0.713	0.743(2×) 0.719/0.717 0.706/0.714	0.761/0.746 0.710/0.734 0.748/0.722
C—O	1.409 1.428 1.434	1.430(3×)	1.445 1.450(2×)	1.451 1.439(2×)	1.433 1.427 1.442	1.432 1.452 1.442
Co—H_{centr}	–	0.366(3×)	0.325/0.332 0.377(2×) 0.324/0.326		0.366 0.375 0.362	–
$(H—H)_{H2}$	–		–	0.876	0.876	0.881 0.974
ρ_{BCP} [e/Bohr^3]						
Co—$C_{C=O}$	0.155, 0.089 0.076, 0.151 0.115, 0.127	0.116(3×) 0.121(3×)	0.118(2×) 0.102/0.121 0.122/0.102	0.144/0.086 0.144/0.148 0.080(2×)	0.122, 0.116 0.118, 0.115 0.119, 0.117	0.144/0.088 0.076/0.149 0.082/0.144
Co—P	0.096(2×) 0.079(2×) 0.089(2×)	0.089(6×)	0.086(2×) 0.091(2×) 0.086(2×)	0.083(2×) 0.090/0.089 0.083(2×)	0.089, 0.088 0.084, 0.083 0.082, 0.084	0.087(3×) 0.084(3×)
C—O	0.423 0.426 0.417	0.421(3×)	0.423 0.426(2×)	0.425 0.422(2×)	0.421 0.423 0.422	0.421 0.427 0.423
Co—H_{centr}	–	0.084(3×)	0.076(2×) 0.085(2×) 0.077(2×)	–	0.084 0.085 0.083	–
$(H—H)_{H2}$	–	–		0.263	0.264	0.262(2×)

the center of the Co_3 triangle. Energy data of optimized structures are presented in Tab. 2. Relative abundances of individual spin states of the same compound (Table 2) were evaluated using Boltzmann statistics. The most stable structures of the remaining models correspond to doublet or triplet spin states, except for model A (the most stable quartet spin state). Structures in the most stable spin states are presented in Fig. 2.

Reaction Gibbs energies of $[\{Co(\mu_2\text{-}CO)(PMe_3)_2\}_3]$ (model A) hydrogenation at various temperatures are presented in Tab. 3 (based on Tab. A1 data in Appendix). It is evident that hydrogenation to models B, C1, and D containing μ_3-H bridges is energetically more advantageous at low temperatures, whereas formation of C2 and E containing only H_2 units is not favored.

Only $[(\mu_3\text{-}H)\{Co\ (\mu_2\text{-}CO)(PMe_3)_2\}_3]$ (model B) in the triplet spin state exhibits trigonal symmetry (see Tab. 4). The lower symmetry of the remaining model systems can be explained by the Jahn-Teller effect and, to a lesser extent, by the non-symmetric location of the H_2 unit. Co—C_{C-O} bond length alternation can be observed in our systems. It can be concluded that μ_3-H bridges stabilize the Co_3 unit (lower average Co—Co distances; see Tab. A2 in Appendix).

Except for the distances Co—Co and Co—$C_{C=O}$ in $[(\mu_3\text{-}H)\{Co(\mu_2\text{-}CO)(PMe_3)_2\}_3]$ (model B) and Co—H_{centr} in $[(H_2)(\mu_3\text{-}H)\{Co(\mu_2\text{-}CO)(PMe_3)_2\}_3]$ (model D), the calculated interatomic distances

Tab. 8. Laplacians ($\nabla^2\rho_{BCP}$) and ellipticities (ε_{BCP}) at bond critical points of the relevant bonds of model systems $[H_n\{Co(\mu_2\text{-}CO)(PMe_3)_2\}_3]$ in the most stable spin states (M_S).

n	0	1	2	2	3	4
Model	A	B	C1	C2	D	E
M_S	4	3	2	2	3	2
$\nabla^2\rho_{BCP}$ [e/Bohr^5]						
Co—$C_{C=O}$	0.342, 0.484 0.189, 0.199 0.293, 0.442	0.319(3×) 0.310(3×)	0.308(2×) 0.250/0.335 0.336/0.249	0.385/0.232 0.369/0.391 0.204/0.211	0.311, 0.322 0.303, 0.311 0.314, 0.304	0.362/0.237 0.198/0.401 0.215/0.382
Co—P	0.195, 0.189 0.197, 0.185 0.199, 0.200	0.205(3×) 0.208(3×)	0.208/0.206 0.202(2×) 0.207(2×)	0.195/0.207 0.204/0.209 0.206/0.199	0.207, 0.203 0.200(2×) 0.198, 0.202	0.205/0.200 0.196/0.208 0.206(2×)
C—O	0.165 0.178 0.204	0.207(3×)	0.230 0.243(2×)	0.230 0.210(2×)	0.214 0.204 0.225	0.201 0.235 0.212
Co—H_{centr}	–	0.201(3×)	0.164/0.166 0.149(2×) 0.165(2×)	–	0.200 0.206 0.204	–
$(H—H)_{H2}$	–	–	–	–1.056	–1.060	–1.058(2×)
ε_{BCP}						
Co—$C_{C=O}$	0.033, 0.032 0.171, 0.123 0.053, 0.006	0.050(3×) 0.056(3×)	0.062(2×) 0.052/0.037 0.036/0.053	0.024/0.155 0.023/0.009 0.181/0.161	0.046, 0.044 0.059, 0.052 0.050, 0.057	0.010/0.175 0.194/0.017 0.131/0.025
Co—P	0.046, 0.198 0.060, 0.097 0.048, 0.069	0.028(3×) 0.034(3×)	0.019/0.036 0.032(2×) 0.036/0.019	0.116/0.056 0.055/0.024 0.051/0.048	0.062, 0.031 0.031, 0.054 0.036, 0.067	0.043/0.028 0.085/0.055 0.071/0.041
C—O	0.038 0.024(2×)	0.037(3×)	0.042 0.038(2×)	0.031(2×) 0.033	0.037 0.035(2×)	0.033(2×) 0.029
Co—H_{centr}	–	0.003(3×)	0.075/0.065 0.003/0.002 0.065/0.074	–	0.031 0.018 0.033	–
$(H—H)_{H2}$	–	–	–	0.000	0.001	0.000(2×)

are longer than their X-ray counterparts (compare Tabs. 1, 4, 5, and A3 in Appendix). The calculated distances between Co atoms and the added H_2 units are too long for any bonding. The Co—$C_{C=O}$—O angles are more variable than other relevant bond angles in the systems under study.

The relevant parts of the QTAIM molecular graphs (Bader, 1994) of the studied model systems are presented in Figs. A1—A6 in Appendix. There are no Co—Co bond paths, which excludes any Co—Co bonding. The same holds for the bond paths between Co atoms and H_2 units. According to the molecular graphs, Co_3 units are held together exclusively by μ_2-CO and μ_3-H bridges. There are bond paths between the H_2 units and methyl atoms that might not be real bonds.

Positive Co charges increase slightly due to μ_3-H presence. Atomic charges of Co (ca +0.3), carbonyl C (ca +0.6), O (ca –1.2) nd P (ca +1.6) do not depend on the number of H atoms added (Tabs. 6 and A4 in Appendix). The charges of the bridging μ_3-H atoms are negative (ca –0.3) unlike the neutral H_2 units. Spin populations (in Tabs. 6 and A4 in Appendix presented as populations of unpaired α or β electrons) are concentrated dominantly at Co atoms. Spin populations at carbonyl groups (prevailingly β electrons) are more than one order lower. The remaining atoms (including μ_3-H atoms) have only a vanishing spin density.

Bond strengths within QTAIM treatment can be deduced from delocalization indices and BCP electron densities that exhibit similar trends (Tabs. 7 and A5 in Appendix). As mentioned above, there is no Co—Co bonding in our systems. Co—$C_{C=O}$ bonds can be divided into two groups according to the alternating Co—$C_{C=O}$ distances. Their

variations can be ascribed mainly to the symmetry decrease due to Jahn-Teller effect despite the stabilizing effect of the H_{centr}—Co bonds. Co—P and much stronger C—O bonds exhibit significantly lower variations. The H_{centr}—Co bonds are not so weak as expected. The H—H bonding in the H_2 unit corresponds to a single bond and is not bonded to the central Co_3 unit.

Except for H_2 units, BCP Laplacians ($\nabla^2\rho_{BCP}$) are positive (Tabs. 8 and A6 in Appendix), which reflects the polarity of the Co—$C_{C=O}$, Co—P, C—O and Co—H_{centr} bonds. Only some Co—$C_{C=O}$ BCP Laplacians significantly deviate from 0.2 e/Bohr^5. Values of $\nabla^2\rho_{BCP}$ of individual bonds in the A model complex differ from the remaining complexes, but no systematic dependence on the hydrogen content has been observed.

In most cases, BCP ellipticity values are small (Tabs. 8 and A6 in Appendix), indicating vanishing mechanical strain in cyclic structures. The only exceptions are some Co—$C_{C=O}$ bonds in the A, C2, and D complexes and one Co—P bond in the C2 complex.

Conclusions

Our results indicate that the most stable A complex is in the quartet spin state whereas the remaining complexes are most stable in their doublet or triplet spin states. Non-vanishing content of other spin states at room temperature is predicted in the A (doublet) and B (singlet) complexes. Pure DFT functionals usually over-stabilize low-spin (LS) states whereas high-spin (HS) states are strongly favored at the Hartree-Fock theory level (Harvey, 2004; Radon, 2019; Ashley and Jakubikova, 2017). In hybrid DFT functionals, the LS-HS energy difference depends on the exact exchange almost linearly with an optimum at ca 15 %; therefore, the B3LYP hybrid functional with 20 % exact exchange provides ground states very close to the experiment. Hydrogenation of the A complex to complexes with μ_3-H bridges (B, C1, and D models) is more advantageous at lower temperatures; formation of complexes without these bridges (C2 and E models) is improbable even at 100 K. The thermal movement explains why X-ray studies of the complexes at room temperature (Klein et al., 1992a) were not successful in locating added hydrogen atoms.

Unlike X-ray studies (Klein et al., 1992a, 1997), trigonal symmetry is preserved only in the B complex. Deviations from this symmetry are probably caused by the Jahn-Teller effect. Nevertheless, dynamical averaging at high temperatures shows the averaged trigonal structures to oppose the experimentally observed ones.

Spin density is concentrated dominantly at positively charged Co atoms whereas only vanishing spin density is located at the negatively charged μ_3-H atoms. This is in contradiction with the assumption of Boča et al. (Boča et al., 2000) in evaluating magnetic measurements. Neutral H_2 units in C2, D, and E complexes have only vanishing spin density.

Results of QTAIM analysis show missing Co—Co bonds and thus the Co_3 triangles are held together only by μ_2-CO and μ_3-H bridges. Missing bonding between positively charged metal atoms is not exceptional in this type of complexes (see e.g. Breza and Biskupic, 2004a, 2004b; Breza and Manova, 2006; Racioppi et al., 2018; Hamza and Al-Ibadi, 2023). The H_2 units in C2, D, and E complexes are only physisorbed. They are located far from the central part of these complexes and their locations should be variable in real systems. Therefore, they are only hardly observed by X-ray experiments.

Finally, it can be concluded that the X-ray experiments of $[H_n\{Co(\mu_2\text{-}CO)(PMe_3)_2\}_3]$ complexes should be performed at low temperatures and magnetic measurements should be interpreted in terms of the Co—Co interactions only.

Acknowledgement

This research has been supported by the Slovak Scientific Grant Agency VEGA (projects nos. 1/0175/23 and 1/0324/24). The author thanks the HPC center at the Slovak University of Technology in Bratislava, which is a part of the Slovak Infrastructure of High-Performance Computing (SIVVP project ITMS 26230120002, funded by European Region Development Funds) for computational time and resources made available.

References

Ashley DC, Jakubikova E (2017) Coord. Chem. Rev. 337: 97—111.

Bader RFW (1994) Atoms in Molecules. A Quantum Theory. Oxford University Press, Oxford.

Becke AD (1993) J. Chem. Phys. 98: 5648—5652.

Biegler-König F, Schönbohm J, Bayles D (2001) J. Comput. Chem. 22: 545—559.

Boča R, Klein H-F, Schmidt A, Valko M, Linert W (2000) Chem. Phys. Lett. 323: 243—248.

Böhme DK, Schwarz H (2005) Angew. Chem. Int. Ed. 44(16): 2336—2354.

Bradamante P, Pino P, Stefani A, Facchinetti G, Zanazzi PF (1983) J. Organomet. Chem. 251: C47—C49.

Breza M (1994) Polyhedron 13(1): 105—107.

Breza M, Biskupic S (2004a) Coll. Czech. Chem. Commun. 69(11): 2045—2054.

Breza M, Biskupic S (2004b) Coll. Czech. Chem. Commun. 69(11): 2055—2067.

Breza M, Manova A (2006) J. Mol. Struct. (THEOCHEM) 765(1-3): 121—126.

Craig GA, Murrie M (2015) Chem. Soc. Rev. 44(8): 2135—2147.

Facchinetti G, Pucci S, Zanazzi PF, Methong U (1979) Angew. Chem., Int. Ed. Engl. 18: 619—620.
Facchinetti G, Balocchi L, Secco F, Venturini M (1981) Angew. Chem., Int. Ed. Engl. 20: 204—205.
Frisch MJ, Trucks GW, Schlegel HB, Scuseria GE, Robb MA, Cheeseman JR, Scalmani G, Barone V, Petersson GA, Nakatsuji H, Li X, Caricato M, Marenich AV, Bloino J, Janesko BG, Gomperts R, Mennucci B, Hratchian HP, Ortiz JV, Izmaylov AF, Sonnenberg JL, Williams-Young D, Ding F, Lipparini F, Egidi F, Goings J, Peng B, Petrone A, Henderson T, Ranasinghe D, Zakrzewski VG, Gao J, Rega N, Zheng G, Liang W, Hada M, Ehara M, Toyota K, Fukuda R, Hasegawa J, Ishida M, Nakajima T, Honda Y, Kitao O, Nakai H, Vreven T, Throssell K, Montgomery JA Jr, Peralta JE, Ogliaro F, Bearpark MJ, Heyd JJ, Brothers EN, Kudin KN, Staroverov VN, Keith TA, Kobayashi R, Normand J, Raghavachari K, Rendell AP, Burant JC, Iyengar SS, Tomasi J, Cossi M, Millam JM, Klene M, Adamo C, Cammi R, Ochterski JW, Martin RL, Morokuma K, Farkas O, Foresman JB, Fox DJ (2016) Gaussian 16, Rev C01, Gaussian, Inc., Wallingford, CT.
Grimme S, Antony J, Ehrlich S, Krieg H (2010) J. Chem. Phys. 132: 154104
Guzman-Jimenez IY, van Hal JW, Whitmire KH (2003) Organometallics 22(9): 1914—1922.
Hamza NA, Al-Ibadi MAM (2023) Theor. Chem. Accounts 142(11): 00120.
Harvey N (2004) Struct. Bonding 112: 151—183.
Hogarth G, Kabir SE, Nordlander E (2010) Dalton Trans. 39(27): 6153—6174.
Keith TA (2019) AIMAll (Version 19.10.12). TK Gristmill Software, Overland Park, KS, USA (http://aim.tkgristmill.com).
Klein H-F, Mager M, Florke U, Haupt H-J, Breza M, Boca R (1992a) Organometallics 11: 2912—2916.
Klein H-F, Mager M, Isringhausen-Bley S, Florke U, Haupt H-J (1992b) Organometallics 11(10): 3174—3175.
Klein H-F, Mager M, Schmidt A, Huber M, Haase W, Florke U, Haupt H-J, Boca R (1997) Inorg. Chem. 36: 4303—4306.
Liu K, Shi W, Cheng P (2015) Coord. Chem. Rev. 289: 74—122.
Malrieu J-P, Trinquier G (2012) J. Phys. Chem. A 116: 8226—8237.
Moberg V, Homanen P, Selva S, Persson R, Haukka M, Pakkanen TA, Monari M, Nordlander E (2006) Dalton Trans. 279—288.
Nombel P, Lugan N, Donnadieu B, Lavigne G (1999) Organometallics 18(2): 187—196.
Pregaglia GF, Andreetta A, Ferrari GF, Ugo R (1969) J. Chem. Soc. D 590—591.
Racioppi S, Della Pergola R, Colombo V, Sironi A, Macchi P (2018) J. Phys. Chem. 122(22): 5004—5015.
Radon M (2019) Adv. Inorg. Chem. 73: 221—264.
Saito T, Kataoka Y, Nakanishi Y, Matsui T, Kitagawa Y, Kawakami T, Okumura M, Yamaguchi K (2009) Int. J. Quantum Chem. 109: 3649—3658.
Tsukamoto T (2024) Nanoscale 16: 10533.
Ugliengo P (2012) MOLDRAW: A Program to Display and Manipulate Molecular and Crystal Structures, University Torino, Torino. Available online: https://moldraw.software.informer.com (accessed on 9 September 2019).

Appendix

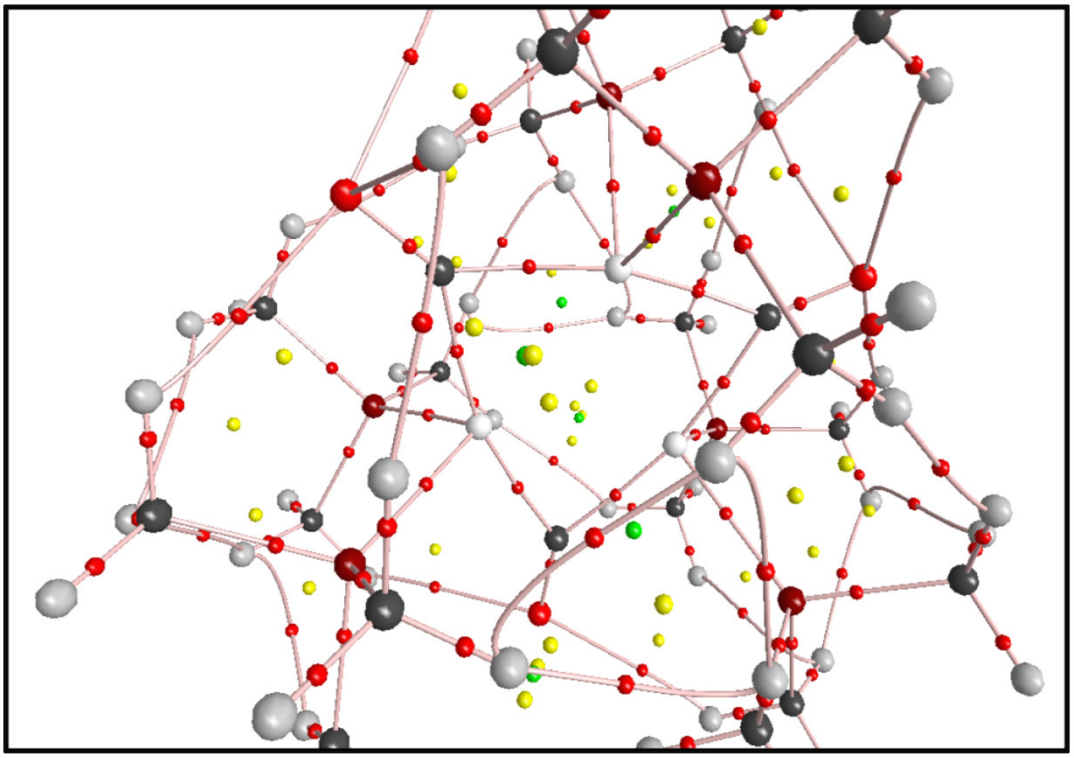

Fig. A1. Relevant parts of molecular graph of $^{4}[\{Co(\mu_2\text{-}CO)(PMe_3)_2\}_3]^0$, model A (Co – light gray, C – black, O – big red, P – dark red, H – dark gray, bond critical points – small red, ring critical points – yellow, cage critical points – green).

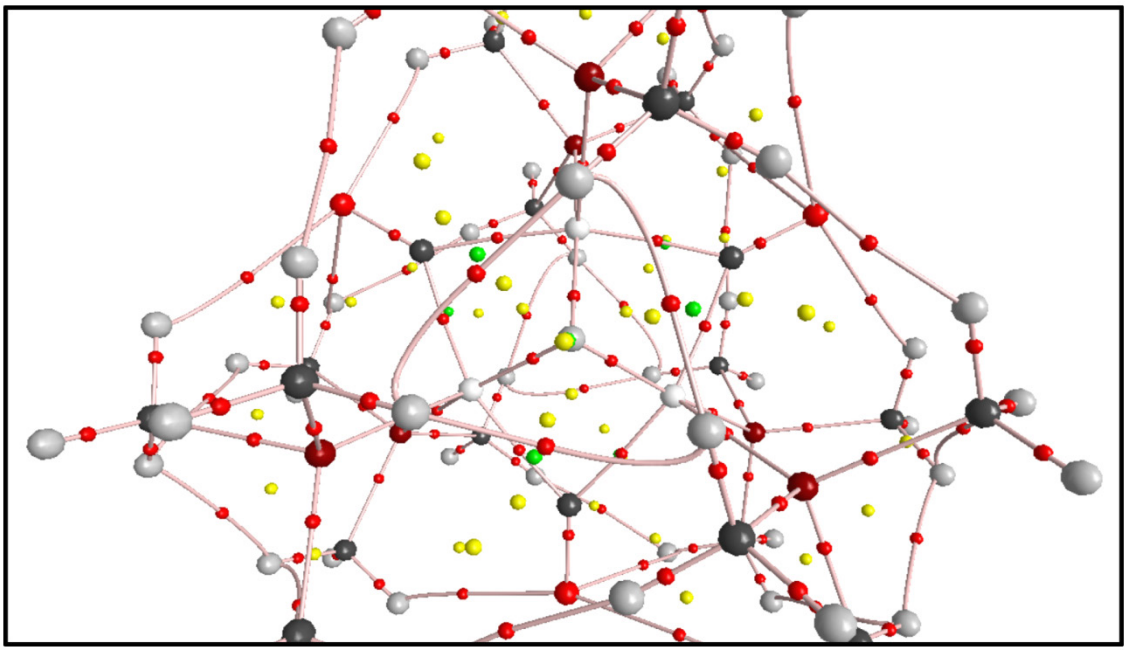

Fig. A2. Relevant parts of molecular graph of $^{3}[(\mu_3\text{-}H)\{Co(\mu_2\text{-}CO)(PMe_3)_2\}_3]^0$, model B (Co – light gray, C – black, O – big red, P – dark red, H – dark gray, bond critical points – small red, ring critical points – yellow, cage critical points – green).

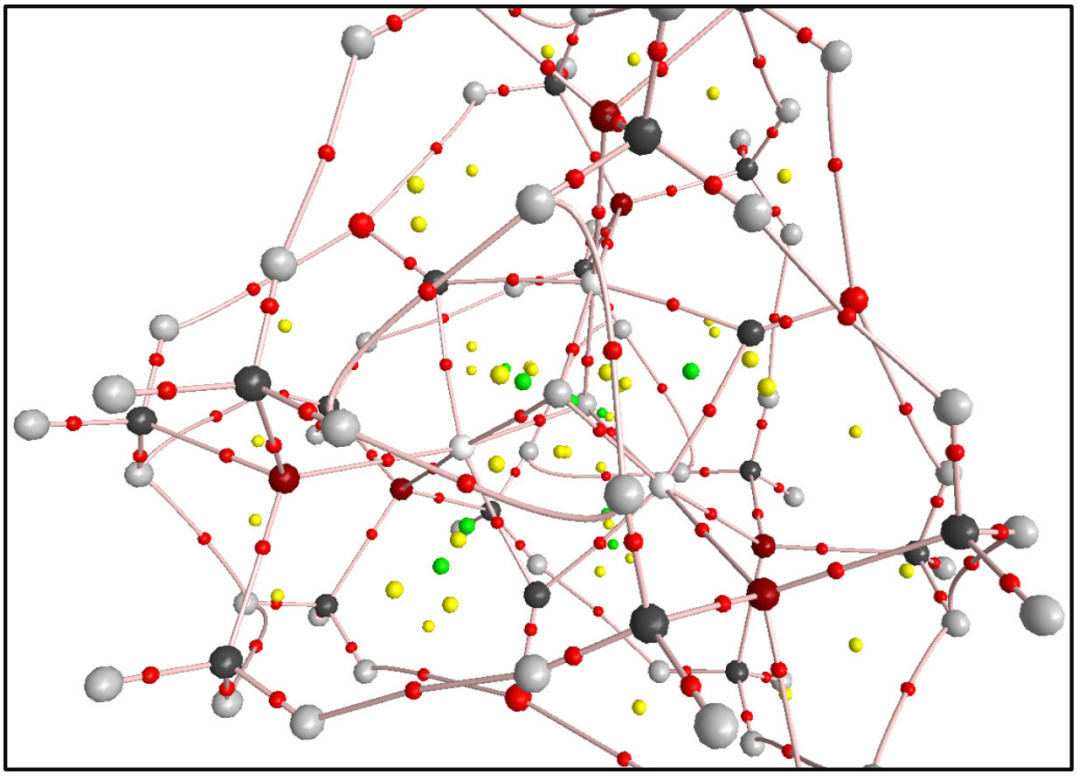

Fig. A3. Relevant parts of molecular graph of $^{2}[(\mu_3\text{-H})_2\{Co(\mu_2\text{-CO})(PMe_3)_2\}_3]^0$, model C1 (Co — light gray, C — black, O — big red, P — dark red, H — dark gray, bond critical points — small red, ring critical points — yellow, cage critical points — green).

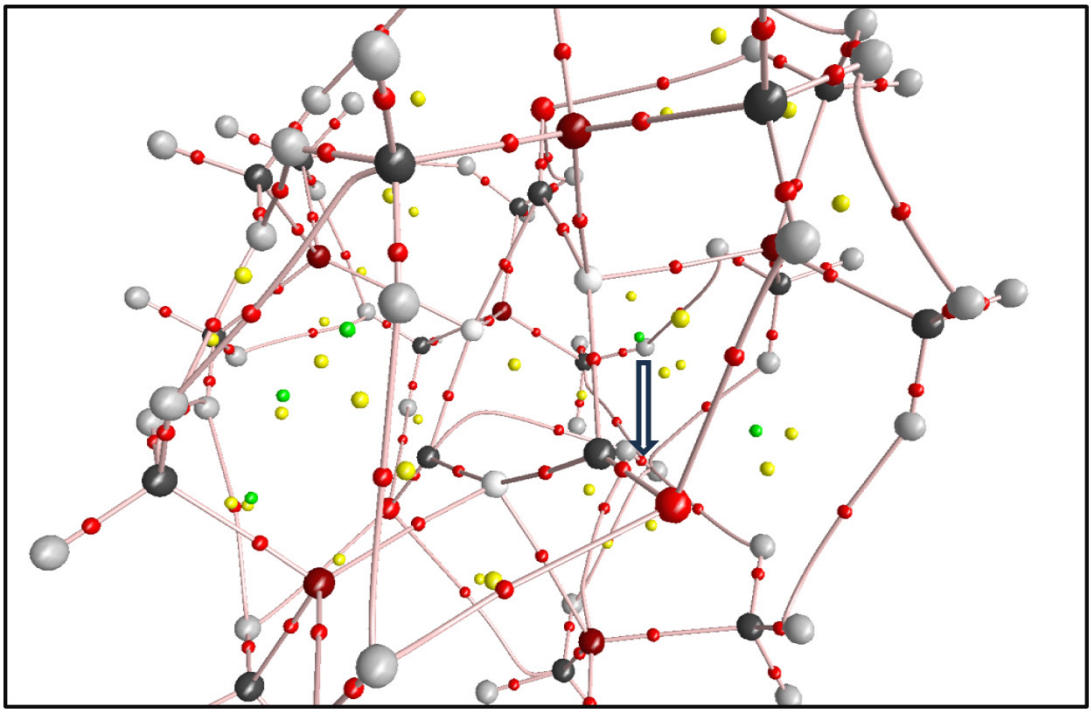

Fig. A4. Relevant parts of molecular graph of $^{2}[H_2\{Co(\mu_2\text{-CO})(PMe_3)_2\}_3]^0$, model C2 (Co — light gray, C — black, O — big red, P — dark red, H — dark gray, bond critical points — small red, ring critical points — yellow, cage critical points — green). Arrow denotes the H_2 molecule.

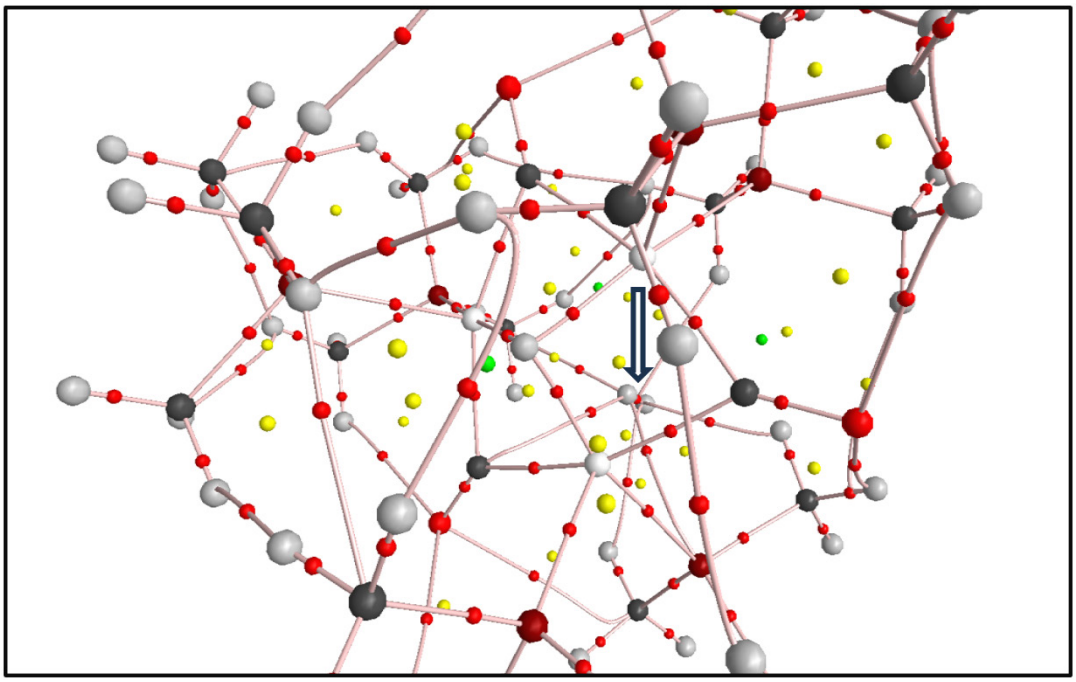

Fig. S5. Relevant parts of molecular graph of $^{3}[(\mu_3\text{-H})H_2\{Co(\mu_2\text{-CO})(PMe_3)_2\}_3]^0$, model D (Co – light gray, C – black, O – big red, P – dark red, H – dark gray, bond critical points – small red, ring critical points – yellow, cage critical points – green). Arrow denotes the H_2 molecule.

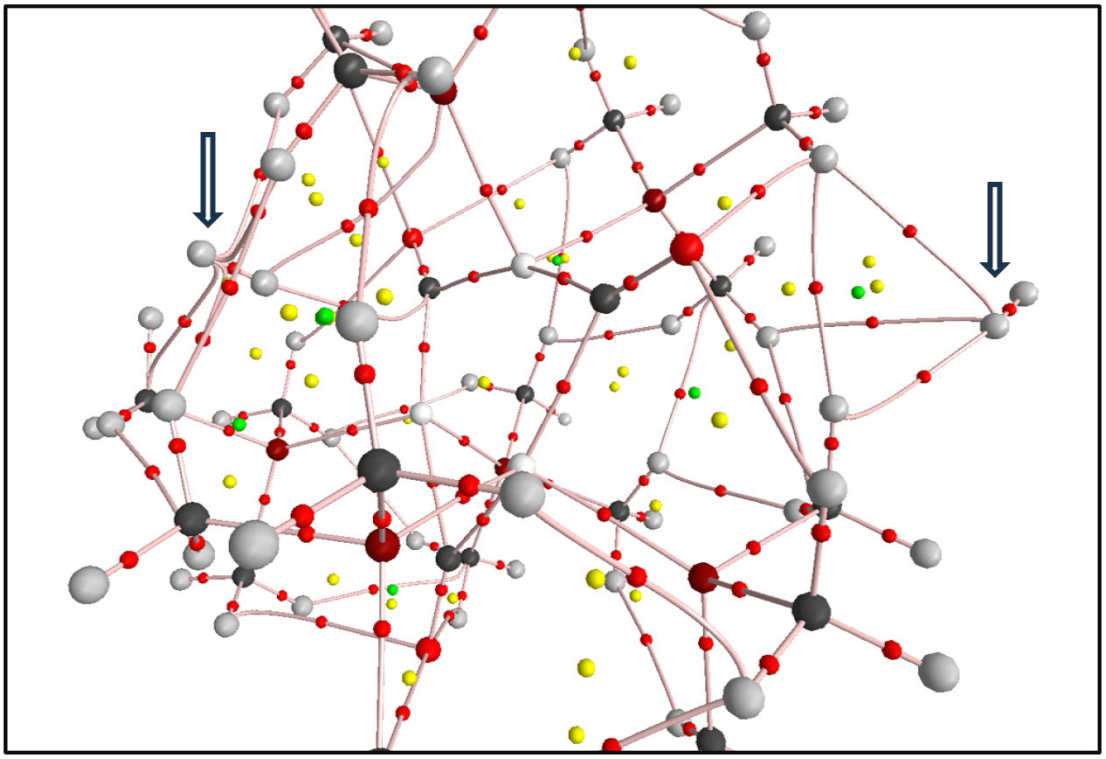

Fig. A6. Relevant parts of molecular graph of $^{2}[(H_2)_2\{Co(\mu_2\text{-CO})(PMe_3)_2\}_3]^0$, model E (Co – light gray, C – black, O – big red, P – dark red, H – dark gray, bond critical points – small red, ring critical points – yellow, cage critical points – green). H_2 molecules are denoted by arrows.

Tab. A1. Gibbs energies (G_T) calculated at various absolute temperatures (T).

Model	Molecule	G_{298} [Hartree]	G_{200} [Hartree]	G_{100} [Hartree]
A	$^4[\{Co(\mu_2\text{-}CO)(PMe_3)_2\}_3]^0$	–7254.94657	–7254.90356	–7254.87262
B	$^3[(\mu_3\text{-}H)\{Co(\mu_2\text{-}CO)(PMe_3)_2\}_3]^0$	–7255.55797	–7255.51631	–7255.48666
C1	$^2[(\mu_3\text{-}H)_2\{Co(\mu_2\text{-}CO)(PMe_3)_2\}_3]^0$	–7256.12844	–7256.08610	–7256.05600
C2	$^2[(H_2)\{Co(\mu_2\text{-}CO)(PMe_3)_2\}_3]^0$	–7256.09832	–7256.05559	–7256.02515
D	$^3[(H_2)(\mu_3\text{-}H)\{Co(\mu_2\text{-}CO)(PMe_3)_2\}_3]^0$	–7256.71265	–7256.67009	–7256.63982
E	$^2[(H_2)_2\{Co(\mu_2\text{-}CO)(PMe_3)_2\}_3]^0$	–7257.27248	–7257.22734	–7257.19619
–	$^1(H_2)^0$	–1.18100	–1.17633	–1.17215

Tab. A2. Averaged relevant interatomic distances and bond angles in model systems $[H_n\{Co(\mu_2\text{-}CO)(PMe_3)_2\}_3]$ in the most stable spin states (M_S).

n	0	1	2	2	3	4
Model	A	B	C1	C2	D	E
M_S	4	3	2	2	3	2
Distance [Å]						
Co—Co	2.486	2.420	2.433	2.545	2.439	2.546
Co—$C_{C=O}$	1.917	1.904	1.927	1.946	1.909	1.946
Co—P	2.225	2.215	2.221	2.232	2.236	2.231
C—O	1.188	1.188	1.184	1.185	1.188	1.186

Tab. A3. Averaged distances to Co atoms and heights over the Co_3 plane of the H atom in the central μ_3-bridge (H_{centr}), and in the added H_2 unit (H_{H2}) of model systems $[H_n\{Co(\mu_2\text{-}CO)(PMe_3)_2\}_3]$ in the most stable spin states (M_S).

n	1	2	2	3	4
Model	B	C1	C2	D	E
M_S	3	2	2	3	2
Distance [Å]					
Co—H_{centr}	1.693	1.730	–	1.689	–
Co—H_{H2}	–	–	3.416	3.518	3.328, 6.467
(H—H)$_{H2}$	–	–	0.746	0.747	0.745
Height [Å]					
Co_3—H_{centr}	0.955	1.007	–	0.932	–
Co_3—H_{H2}	–	–	2.550/3.278	2.723/3.447	2.613/3.342, 4.546/5.046

Tab. A4. Averaged charges and spin populations of relevant atoms of model systems $[H_n\{Co(\mu_2\text{-}CO)(PMe_3)_2\}_3]$ in the most stable spin states (M_S).

n	0	1	2	2	3	4
Model	A	B	C1	C2	D	E
M_S	4	3	2	2	3	2
Charge						
Co	0.35	0.39	0.42	0.33	0.40	0.31
$C_{C=O}$	0.61	0.63	0.67	0.63	0.64	0.63
O	–1.19	–1.19	–1.18	–1.19	–1.19	–1.19
P	1.59	1.60	1.59	1.57	1.59	1.57
H_{centr}	–	–0.32	–0.29	–	–0.32	–
H_{H2}	–	–		–0.04	–0.03	–0.03 0.00
Spin						
Co	1.13	0.80	0.38	0.38	0.81	0.38
$C_{C=O}$	–0.10	–0.09	–0.03	–0.03	–0.09	–0.03
O	–0.06	–0.06	–0.02	–0.03	–0.06	–0.02
P	0.01	–0.00	0.01	0.00	–0.01	0.00
H_{centr}	–	–0.03	–0.02	–	–0.03	–
H_{H2}	–	–	–	0.00	–0.00	0.00

Tab. A5. Averaged delocalization indices (DI), and electron density at bond critical points (ρ_{BCP}), of relevant bonds of model systems $[H_n\{Co(\mu_2\text{-}CO)(PMe_3)_2\}_3]$ in the most stable spin states (M_S).

n	0	1	2	2	3	4
Model	A	B	C1	C2	D	E
M_S	4	3	2	2	3	2
DI						
Co—$C_{C=O}$	0.811	0.796	0.742	0.799	0.792	0.800
Co—P	0.731	0.745	0.733	0.736	0.724	0.737
C—O	1.424	1.430	1.448	1.443	1.434	1.442
Co—H_{centr}	–	0.366	0.344		0.368	–
$(H—H)_{H2}$	–		–	0.876	0.876	0.881 0.974
ρ_{BCP} [e/Bohr^3]						
Co—$C_{C=O}$	0.119	0.119	0.114	0.114	0.118	0.114
Co—P	0.088	0.089	0.088	0.085	0.085	0.085
C—O	0.422	0.421	0.425	0.423	0.422	0.424
Co—H_{centr}	–	0.084	0.079	–	0.084	
Co—H_{H2}	–	–	–		–	
$(H—H)_{H2}$	–	–		0.263	0.264	0.262(2×)

Tab. A6. Averaged Laplacians ($\nabla^2\rho_{BCP}$), and ellipticities (ε_{BCP}) at bond critical points of relevant bonds of model systems $[H_n\{Co(\mu_2\text{-}CO)(PMe_3)_2\}_3]$ in the most stable spin states (M_S).

n	0	1	2	2	3	4
Model	A	B	C1	C2	D	E
M_S	4	3	2	2	3	2
$\nabla^2\rho_{BCP}$ [e/Bohr^5]						
Co—$C_{C=O}$	0.325	0.315	0.298	0.299	0.311	0.299
Co—P	0.194	0.207	0.205	0.203	0.203	0.206
C—O	0.182	0.207	0.234	0.216	0.214	0.216
Co—H_{centr}	–	0.201	0.160	–	0.203	–
$(H—H)_{H2}$	–	–	–	–1.056	–1.060	–1.058
ε_{BCP}						
Co—$C_{C=O}$	0.084	0.053	0.050	0.092	0.051	0.092
Co—P	0.086	0.033	0.029	0.058	0.047	0.054
C—O	0.031	0.037	0.039	0.032	0.036	0.032
Co—H_{centr}	–	0.003	0.047	–	0.027	–
$(H—H)_{H2}$	–	–	–	0.000	0.001	0.000(2×)

STU
FCHPT

Two tetranuclear [Ni(II)/Dy(III)]$_2$ solvatomorphs based on symmetric bicompartmental Schiff base type ligand

Lenka Krešáková, Juraj Černák

Department of Inorganic Chemistry, Faculty of Science, P. J. Šafárik University in Košice, Moyzesova 11, 041 54 Košice, Slovakia
lenka.kresakova@upjs.sk

Abstract: From the system [Ni(*o-van-en*)] — $DyBr_3$, a novel tetranuclear complex [Ni(*o-van-en*)$Dy(H_2O)_2(OH)]_2Br_4 \cdot 6H_2O$ (**1**) was isolated; H_2(*o-van-en*) was synthesized by 2/1 condensation of *o*-vanillin and ethylenediamine. Single crystals (SC) of **1**, upon standing in methanol/isopropanol mother liquor, underwent a SC-SC transformation and yielded a new solvatomorph [Ni(*o-van-en*)$Dy(H_2O)_2(OH)]_2Br_4 \cdot MeOH \cdot$ *i*$PrOH \cdot H_2O$ (**2**). Both complexes, **1** and **2**, were characterized by elemental analysis, infrared spectroscopy, and single crystal X-ray analysis. Crystal structures of both **1** and **2** are ionic. Within the bicompartmental unit {Ni(*o-van-en*)$Dy(H_2O)_2(\mu$-OH)}, the square coordinated Ni(II) atom occupies the smaller cavity (donor set is *cis*-N_2O_2) while the octacoordinated Dy(III) atom (donor set is O_8) is placed in the larger cavity. The two [Ni(*o-van-en*)$Dy(H_2O)_2(\mu$-OH)] units are linked by a pair of μ-OH bridging ligands. The unit cell content is completed by bromide anions and water (**1**) or methanol, isopropanol, and water solvate molecules (**2**).

Keywords: crystal structure analysis, heterometallic complex, Schiff base type ligand, tetranuclear complex

Introduction

In recent years, the well-known multidentate salen-type ligands have been successfully used to stabilize lanthanide ions in various coordination environments (Tsantis et al., 2019). Specifically, polynuclear Schiff base complexes have proven to be notably distinct luminescent complexes (Hardy et al., 2017) as well as single molecule magnets (SMMs) (Chandrasekhar et al., 2013). Attention has been focused on the crystal structures and magnetic properties of Dy(III) complexes. Vignesh et al. (2017) examined the impact of ligand environment around the Dy(III) atom on SMM behavior, as well as the role and significance of the diamagnetic ions, especially their ability to alter the relaxation process. A family of tetranuclear Co(II)/Ln(III) (Ln(III) = Tb, Dy, Ho) complexes belonging to "butterfly complexes" were characterized. Magnetic study of $[Co_2Dy_2(\mu_3\text{-}OH)_2$(*o*-tol)$_4$(mdea)$_2(NO_3)_2]$ (*o*-tol = *o*-toluate, H_2(mdea) = *N*-methyldiethanolamine; KASJAS) (Vignesh et al., 2017) has revealed SMM behavior in the absence of an external field, with U_{eff} of 81.2 cm^{-1}. For previously reported Co_2/Ln_2 butterfly complexes (Langley et al., 2013; Langley et al., 2015), the influence of the Ln(III) coordination sphere modification on the final magnetic properties was studied. A search in the Cambridge Structural Database (CSD) (Groom et al., 2016) revealed 175 hits for *Tr*/Dy complexes (*Tr* refers to a transition metal). Further, a search for structures comprising the *Tr*-O-Dy-$(O)_2$-Dy-O-*Tr* fragment yielded 46 results. These can be divided into six groups considering the presence of the 3*d* atom: **Mn/Dy** (3 hits); **Fe/Dy** (4 hits), **Co/Dy** (8 hits); **Ni/Dy** (6 hits); **Cu/Dy** (3 hits) and **Zn/Dy** (22 hits). Tetranuclear Ni(II)/Dy(III) complexes are summarized in Table 1. Most of the above-mentioned complexes are examples of magnetically active compounds, mostly SMMs. Wu et al. (2017) observed a trend in magnetic interactions when comparing Co_2/Dy_2 complex with an Ni_2/Dy_2 analogue, $[Ni_2Dy_2(Hhms)_2(OAc)_6(MeOH)_2(H_2O)_2] \cdot (NO_3)_2$ (H_2hms = 1-(2-hydroxy-3-methoxybenzylidene)-semicarbazide; VAYNIV) (Tab. 1). The Ni_2/Dy_2 analogue showed longer relaxation time and absence of quantum tunnelling of magnetization at low temperatures; ferromagnetic exchange led to coupling between Ni(II) and Dy(III) atoms (Wu et al., 2017). Using compartmental Schiff base ligand in conjunction with auxiliary ligands, a series of Ni_2/Ln_2 complexes were prepared by Jiang et al. (2017). Tetranuclear structures can be considered as two Ni/Ln dinuclear subunits bridged by two carbonates derived from atmospheric carbon dioxide, i.e. $[(\mu_3\text{-}CO_3)_2${Ni(H*L*2)(EtOH)Dy(OAc)}$_2] \cdot 2$EtOH (H_3L2 = *N*,*N*′-bis(3-methoxysalicylidene)-1,3-diamino-2-propanol); JASTUV01) (Jiang et al., 2017).

Our previous work on dinuclear 3*d*/4*f* complexes (Krešáková et al., 2025; Vráblová et al., 2019) has introduced bottom-up synthesis of these types of complexes based on compartmental multidentate ligands. Preparation of compound **1** in

Tab. 1. List of tetranuclear complexes with $[NiO_2DyO_2DyO_2Ni]$ core upon CSD (version 5.43 update (Nov 2022)) (Groom et al., 2016).

Complex	Refcode	Donor set Ni(II)	Donor set Dy(III)	Reference
$[Ni_2Dy_2(L1)_2(o\text{-van})_2(CO_3)_2(NO_3)_2(MeOH)_2]$	GACQUZ	NO_5	O_9	Upadhyay et al., 2016
$[(\mu_3\text{-}CO_3)_2\{Ni(HL2)(EtOH)Dy(OAc)\}_2]\cdot 2EtOH$	JASTUV01	N_2O_4	O_8	Jiang et al., 2017
$[Ni_2Dy_2(Hhms)_2(OAc)_6(MeOH)_2(H_2O)_2]\cdot(NO_3)_2$	VAYNIV	NO_5	O_9	Wu et al., 2017
$[(\mu_4\text{-}CO_3)_2\{Ni(L3)(H_2O)Dy(NO_3)\}_2]\cdot 2MeCN\cdot 2H_2O$	WIMDED	N_2O_4	O_9	Sakamoto et al., 2013
$[(\mu_4\text{-}CO_3)_2\{Ni(L3)(MeOH)Dy(NO_3)\}_2]$	WIMDUT	N_2O_4	O_9	Sakamoto et al., 2013
$2[(\mu_4\text{-}CO_3)_2\{NiDy(L4)(MeOH)(OAc)\}_2]\cdot 9H_2O\cdot 8MeOH$	XOYLUU	N_2O_4	O_9	Cristovao et al., 2015

Additional text: **H*L1*** = 2-methoxy-6-[(*E*)-phenyliminomethyl] phenol;

H_3*L2* = *N,N´*-bis(3-methoxysalicylidene)-1,3-diamino-2-propanol);

OAc = acetato; **H_2hms** = 1-(2-hydroxy-3-methoxybenzylidene)-semicarbazide;

H_2*L3* = *N,N´*-bis(3-methoxysalicylidene)-1,3-diaminopropane);

H_2*L4* = *N,N´*-bis(5-bromo-3-methoxysalicylidene)propylene-1,3-diamine.

microcrystalline form was performed according to the published approach described previously (Krešáková et al., 2025). As for the crystals' preparation, methanol/isopropanol solvent system in closed vials was chosen with two different types of crystals grown. Herein, a new tetranuclear complex $[Ni(o\text{-}van\text{-}en)Dy(H_2O)_2(OH)]_2Br_4\cdot 6H_2O$ (**1**) and its solvatomorph $[Ni(o\text{-}van\text{-}en)Dy(H_2O)_2(OH)]_2Br_4\cdot MeOH\cdot iPrOH\cdot H_2O$ (**2**) formed via SC-SC transformation are reported.

Material and Methods

Chemicals

Ethylenediamine (≥99.5 %), *o*-vanillin (99 %), $NiCO_3$ (basic hydrate, 46 % as Ni) $DyBr_3\cdot xH_2O$ (p. a.), ethanol (99.8 %), acetone (99.5 %), diethyl ether (99.0 %), isopropanol (99.5 %) were purchased from commercial sources and used as received.

Synthesis of Schiff base ligand H_2(o-van-en)

Ligand H_2(*o-van-en*) was synthesized by a modification of previously reported methods (Andruh, 2015; Vráblová et al., 2019). To the ethanolic solution (50 ml) of *o*-vanillin (0.4542 g, 3 mmol) was added ethylenediamine (0.1 ml, 1.5 mmol). The mixture was refluxed for 5 hours in a boiling flask, and the obtained solution was filtered and left aside to crystallize at room temperature. Dark yellow crystals of the product appeared overnight. The crude product was filtered and washed with a small amount of diethylether. Yield: 90 %.

Anal. [%], calculated for H_2(*o-van-en*), $C_{18}H_{20}N_2O_4$: C, 65.83; H, 6.15; N, 8.53; found: C, 66.05; H, 6.23; N, 8.58.

FT-IR [cm^{-1}]: 3726vw, 2997w, 2931w, 2835w, 2359w, 1630s, 1462s, 1438m, 1408m, 1325w, 1295w, 1244vs, 1189m, 1133m, 1079s, 1049m, 1009m, 987m, 961s, 836s, 791s, 781s, 728s, 620s, 522m, 441m.

^{1}H NMR [ppm]: 3.76s (6H), 3.92s (4H), 6.77—6.80t (2H), 6.99—7.00d (2H), 7.00—7.02d (2H), 8.57s (2H), 13.54s (2H).

^{13}C NMR [ppm]: 55.63 (OCH3), 58.32 (NCH2), 114.68 (ArC4), 117.73 (ArC5), 118.23 (ArC1), 123.09 (ArC6), 147.97 (ArC2—OH), 151.45 (ArC3—OCH3), 167.07 (C═N).

Synthesis of metalloligand [Ni(o-van-en)]·nH_2O (n = 1.17)

The synthesis was carried out according to the procedure described by Vráblová et al. (2019; 2020). Whereby solid H_2(*o-van-en*) (1 g, 3 mmol) and nickel(II) carbonate (0.350 g, 3 mmol) with 8 drops of Et_3N were added to 100 cm^3 of water and heated in an open beaker. After one and half hour brown microcrystalline product of nickel complex was separated by filtration, washed with 2 ml of ethanol and dried in air. Dry product was then used without further purification in the following syntheses of tetranuclear complexes. Yield: 75 %.

Anal. [%], calculated for $[Ni(o\text{-}van\text{-}en)]\cdot nH_2O$ (n = 1.5), $C_{18}H_{21}N_2O_{5.5}Ni$: C, 52.47; H, 5.14; N, 6.80; found: C, 51.91; H, 4.82; N, 6.47.

FT-IR [cm^{-1}]: 3508br, 3064w, 2943w, 2927w, 2829w, 1617s, 1603s, 1544s, 1470s, 1435s, 1401s, 1345s, 1313s, 1225s, 1166m, 1115m, 1092m, 1078m, 1001m, 969m, 865m, 852m, 781w, 733s, 665w, 619m, 564w, 544w, 482m, 430m, 408m.

^{1}H NMR [ppm]: 3.40s (6H), 3.69s (4H), 6.44d (2H), 6.77d (2H), 6.87d (2H), 7.87s (2H).

^{13}C NMR [ppm]: 55.49 (OCH3), 57.98 (NCH2), 113.52 (ArC4), 114.23 (ArC5), 120.25 (ArC1), 124.28 (ArC6), 150.46 (ArC2—OH), 155.37 (ArC3—OCH3), 162.68 (C═N).

Synthesis of [Ni(o-van-en)Dy(H_2O)$_2$(OH)]$_2$$Br_4$·6$H_2O$ (1) and [Ni(o-van-en)Dy(H_2O)$_2$(OH)]$_2$$Br_4$·2MeOH·2iPrOH·2$H_2O$ (2)

Metalloligand [Ni(*o-van-en*)] · *n*H_2O (0.148 g, 0.368 mmol) was dissolved in 15 mL of acetone; then, an acetonic solution (15 mL) of $DyBr_3$ in equimolar amount (0.152 g) was added. The reaction mixture was refluxed for 4 hours. Solid dark brown product of **1** was formed, filtered, and washed well with ethanol. Single crystal form of **1** was prepared by recrystallization using diffusion technique: solid product **1** (0.05 g, 0.03 mmol) was dissolved in methanol (5 mL) and the formed solution was layered with isopropanol (5 mL). After two weeks, brown prisms of **1** appeared in the closed vial system. Part of them was picked up from the mother liqueur and put under inert oil (Fomblin) due to low air stability and was later used for single crystal X-ray data collection. Most of the crystals formed were kept in the mother liquor and after six weeks of standing, these crystals (**2**) were once more checked using single crystal diffractometer; full X-ray data were collected at low temperature immediately after it was picked up from the liquid.

CHN analyses of single crystals were done after short time handling on air:

Anal. [%], calc. for (**1**), $C_{36}H_{58}N_4O_{20}Ni_2Dy_2Br_4$: C, 26.55; H, 3.59; N, 3.44; found: C, 26.42; H, 3.75; N, 3.12.

FT-IR [cm^{-1}] (**1**): 3460vw, 3261br, 2950w, 2850w, 1627s, 1610m, 1561w, 1470s, 1441m, 1410w, 1397w, 1348w, 1334w, 1301s, 1231s, 1170m, 1079s, 1054m, 1041m, 988m, 957m, 866m, 784m, 739s, 691w, 669w, 630w, 604w, 584w, 567w, 541w, 499w, 462m, 441s, 410s.

Anal. [%], calc. for (**2**), $C_{44}H_{74}N_4O_{20}Ni_2Dy_2Br_4$: C, 30.35; H, 4.28; N, 3.22; found: C, 29.66; H, 3.71; N, 3.34.

FT-IR [cm^{-1}] (**2**): 3251br, 2925w, 2848w, 1695vw, 1628s, 1611m, 1561w, 1472s, 1443m, 1403w, 1385w,

Tab. 2. Crystal data and structure refinement for **1** and **2**.

	1	**2**
Empirical formula	$C_{36}H_{58}N_4O_{20}Ni_2Dy_2Br_4$	$C_{44}H_{74}N_4O_{20}Ni_2Dy_2Br_4$
Molecular weight	1628.86	1741.13
Crystal system	Monoclinic	Monoclinic
Space group	$P\,2_1/c$	$P\,2_1/c$
Cell parameters		
a (Å)	10.3469(4)	11.6213(3)
b (Å)	20.4200(6)	21.5497(4)
c (Å)	12.2597(3)	11.8925(2)
α (°)	90	90
β (°)	91.950(3)	96.330(2)
γ (°)	90	90
V (Å^3)	2588.78(14)	2960.15(11)
Z	4	2
D_{calc} (Mg · m^{-3})	2.090	1.953
Abs. coeff. (mm^{-1})	20.254	17.762
Crystal color, form	brown prism	brown prism
Crystal size (mm)	0.232 × 0.149 × 0.092	0.247 × 0.168 × 0.147
T (K)	100(2)	100(2)
Radiation λ (Å)	1.54184	1.54184
θ range (°)	4.208–67.491	3.827–67.494
Index ranges	$-12 \le h \le 12$	$-13 \le h \le 13$
	$-24 \le k \le 24$	$-19 \le k \le 25$
	$-14 \le l \le 14$	$-14 \le l \le 14$
Refl. coll./ indep.	19633 / 4653	21626 / 5326
Goodness-of-fit (F^2)	1.138	1.040
Final R indices	$R1$ = 0.0652,	$R1$ = 0.0722
($I > 2\sigma(I)$)	$wR2$ = 0.1824	$wR2$ = 0.1832
R indices (all data)	$R1$ = 0.0738,	$R1$ = 0.0772
	w$R2$ = 0.1948	$wR2$ = 0.1883
Diff. peak and hole (e · Å^{-3})	–2.81, 3.60	–2.56, 1.98

1334w, 1302s, 1230, 1169m, 1127w, 1110w, 1079s, 1055w, 1023m, 989m, 987w, 955m, 865m, 851w, 818w, 779w, 737s, 689w, 668w, 627w, 605w, 582w, 568w, 541m, 499w, 478w, 462m, 440s, 411s.

Physical measurements

CHN analyses were measured using a CHNOS elemental analyzer Vario MICRO cube instrument (Elementar Analysensysteme GmbH). IR spectra in the 400—4000 cm^{-1} range were recorded on a Nicolet 6700 FT-IR spectrophotometer (Thermo Scientific) using the ATR method. ^{1}H and ^{13}C NMR spectra of H_2(*o-van-en*) ligand were measured in DMSO-d6 solution using a Varian VNMRS 600 spectrometer with an Oxford superconducting magnet (14.09 T, 54 mm bore).

X-ray crystallography

Single crystal X-ray measurements of title complexes **1** and **2** were performed using a Rigaku XtaLAB Synergy S diffractometer equipped with microfocus CuKα radiation and a Hybrid Pixel Array Detector (HyPix-6000HE). An Oxford Cryosystems (Cryostream 800) cooling device was used for data collection at 100 K. CrysAlisPro software was used for data collection, cell refinement, and data reduction (Oxford Diffr., 2022). Data were corrected for absorption effects using empirical absorption correction (spherical harmonics), implemented in the SCALE3 ABSPACK scaling algorithm, and analytical numeric absorption correction using a multifaceted crystal model with CrysAlisPro software (Blessing, 1995). Crystal structures were solved and refined using the SHELXT (Sheldrick, 2015a) and the SHELXL (Sheldrick, 2015b) programs. All non-hydrogen atoms were refined anisotropically. Hydrogen atoms bonded to carbon atoms were placed in calculated positions and refined using a riding model with isotropic thermal parameters tied to their respective parent atoms: $U_{iso}(H) = 1.2\,U_{eq}(C)$ for non-methyl H atoms, and $U_{iso}(H) = 1.5\,U_{eq}(C)$ for methyl groups. Hydrogen atoms bound to oxygen atoms of water and alcoholic molecules were found in the difference map; their isotropic thermal parameters were tied with the parent O atoms ($U_{iso}(H) = 1.5\,U_{eq}(O)$). During refinement, the O—H bond distances were restrained using the DFIX command. In the structure of **2**, the ethylenediamine fragment is disordered over two positions with respective refined site occupation factors 0.50(4)/0.50(4) (C9A, C10A / C9B, C10B). Structural figures were drawn using the Diamond program (Brandenburg and Putz, 2022). Geometric parameters were also calculated using the PLATON program (Spek, 2003). Program Mercury CSD 4.2.0 (Macrae et al., 2020) was used to compare molecular structures. Crystal data and final parameters of the structure refinement are summarized in Table 2, while selected geometric parameters are given in Table 3. Possible hydrogen bonds are gathered in Tables 4 and 5.

Results and discussion

Two new tetranuclear complexes [Ni(*o-van-en*)$Dy(H_2O)_2(OH)]_2Br_4 \cdot 6H_2O$ (**1**) and [Ni(*o-van-en*)$Dy(H_2O)_2(OH)]_2Br_4 \cdot 2MeOH \cdot 2\,iPrOH \cdot 2H_2O$ (**2**) were prepared in a single crystal form from a system consisting of metalloligand [Ni(*o-van-en*)] and $DyBr_3$ using the diffusion method. First, single crystals of **1** formed by recrystallization of the bulk sample while long-time standing of crystals **1** in the mother liquor in the presence of isopropanol led to their transformation to new single crystals **2**. While solvent molecules in complex **1** comprise only water, in complex **2**, methanol and isopropanol also act as solvent molecules alongside water. As the complexes differ in the solvent molecules' content, they can be considered as solvatomorphs (Brittain, 2009). Solvatomorphism is not an uncommon phenomenon, e.g. it was observed in case of $\{[Mn(cyclam)][Fe(CN)_6]\cdot nH_2O\}_n$ (Nowicka, 2017) or $[Cu(ClO_4)_2(LH)_4] \cdot x$(solvent) (*L*H = 5-phenylimidazole) (Loukopoulos et al., 2014), various solvatomorphs of the metalloligand alone have also been studied (Vráblová et al., 2020). Analogous tetranuclear complexes have already been reported, e.g. $[Ni_2Dy_2(L)_2(o\text{-van})_2(CO_3)_2(NO_3)_2(MeOH)_2]$ (H*L* = 2-methoxy-6-[(E)-phenyliminomethyl] phenol; GACQUZ) (Upadhyay et al., 2016), and $[(\mu_4\text{-}CO_3)_2\{Ni(3\text{-}MeOsaltn)(MeOH)Dy(NO_3)\}_2]$ (3-MeOsaltn = *N,N´*-bis(3-methoxy-2-oxybenzylidene)-1,3-propanediaminato; WIMDUT) (Sakamoto et al., 2013) (Table 1). On the other hand, the present two complexes are the first examples in which bromide anions are present as anions.

Complexes **1** and **2** were characterized using IR spectroscopy with typical absorption bands being ν(C═N) vibrations of imine groups from the deprotonated Schiff base ligand (Horák and Papoušek, 1976; Nakamoto, 2009); these were observed at 1627 and 1628 cm^{-1} for **1** and **2**, respectively (Fig. 1). These values are in good agreement with the results reported by Liu et al. (2017) for analogous tetranuclear Ni(II)/Dy(III) complexes as well as for similar dinuclear bromido complexes (Krešáková et al., 2025). Weak but characteristic absorption bands found slightly above 3000 cm^{-1} and slightly below 3000 cm^{-1} were assigned to the $\nu(C_{ar}—H)$ and $\nu(C_{al}—H)$ stretching vibrations, respectively. The broad absorption bands centered at 3261 cm^{-1} (**1**) and 3251 cm^{-1} (**2**) correspond to the ν(O—H)

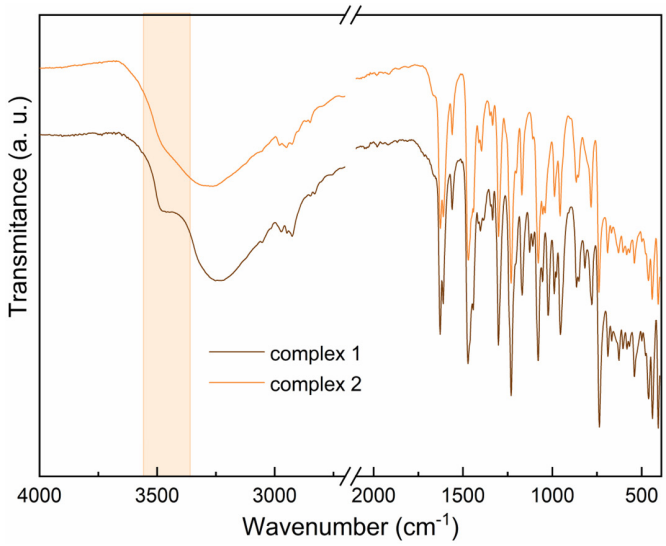

Fig. 1. IR spectra of complexes **1** (brown line) and **2** (orange line).

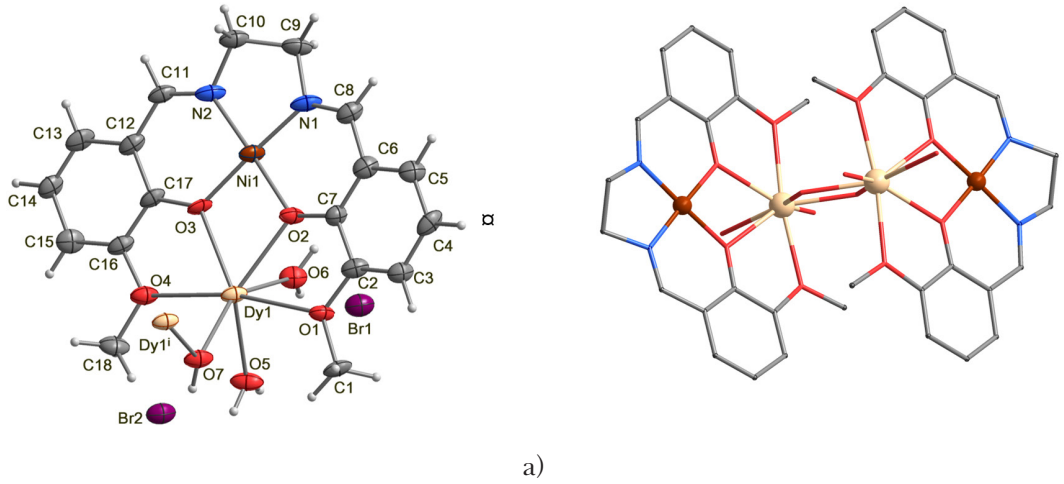

a)

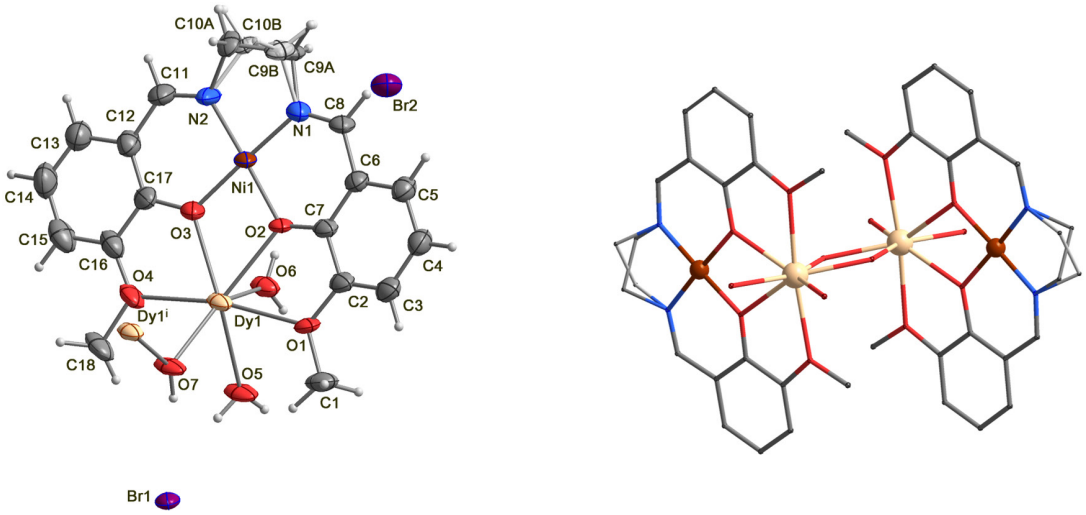

b)

Fig. 2. a), b) left: Asymmetric unit of **1** (a) and **2** (b) with atom numbering scheme. Thermal ellipsoids are drawn at the 50 % probability level (solvate molecules are omitted for clarity).
a), b) right: Tetranuclear Ni_2Dy_2 complex cation in **1** (a) and in **2** (b); Ni(II) atoms are depicted as brown balls, Dy(III) atoms as light orange balls, and nitrogen (blue), oxygen (red), carbon (grey) atoms are drawn in wire model (hydrogen atoms and solvate molecules are omitted for clarity).

vibrations of water (and methanol/isopropanol in **2**) solvate molecules. Another significant sharp absorption band at 1079 cm^{-1} in both spectra was assigned to ν(C—O) valence vibration located on the aromatic ring of the bicompartmental Schiff base ligand.

Crystal structures

Both complexes $[Ni(o\text{-}van\text{-}en)Dy(H_2O)_2(OH)]_2Br_4 \cdot 6H_2O$ (**1**) and $[Ni(o\text{-}van\text{-}en)Dy(H_2O)_2(OH)]_2Br_4 \cdot 2i$PrOH $\cdot$ 2MeOH $\cdot$ $2H_2O$ (**2**) have ionic structure composed of the same centrosymmetric $\{Ni^{II}/Dy^{III}\}_2$ tetranuclear complex cations $[\{Ni(o\text{-}van\text{-}en)Dy(H_2O)_2(OH)\}_2]^{4+}$ and bromide anions; the only compositional difference is in the amount and quality of solvate molecules in **1** and **2** (Fig. 2). While in the structure of **1**, only water solvate molecules are present, in the structure of **2**, molecules of methanol and isopropanol besides water molecules are visible (Fig. 2a, b left). Each fully deprotonated ligand acts as a multidentate linker holding two different metal ions: Ni(II) occupies the cis-N_2O_2 site to fulfill a square configuration, whereas the heavier Dy(III) is held by the O_8 pocket; among these eight oxygen atoms, four are provided by the $(o\text{-}van\text{-}en)^{2-}$ ligand. The Ni(II) and Dy(III) atoms are linked by a pair of monoatomic O-bridges and therefore are in proximity with respective distances Ni···Dy of 3.3888(15) Å in **1** and 3.4152(12) Å in **2**. The two dinuclear units $\{Ni(o\text{-}van\text{-}en)Dy(H_2O)_2\}$ are further linked by a pair of μ-hydroxy bridges between the neighbouring Dy(III) atoms yielding a $\{Dy(\mu\text{-}OH)_2Dy\}$ core and resulting in the formation of the tetranuclear complex cation $[\{Ni(o\text{-}van\text{-}en)Dy(H_2O)_2(\mu\text{-}OH)\}_2]^{4+}$. Within this $\{Dy(\mu\text{-}OH)_2Dy\}$ core, the neighbouring Dy(III) atoms are at distance Dy1···Dy1^i (i: 1 – *x*, 1 – *y*, 1 – *z*) of 3.7195(7) Å in **1** and 3.7310(6) Å in **2** (i: 1 – *x*, 1 – *y*, 2 – *z*). The last two oxygen atoms are from the coordinated aqua ligands (Fig. 2a, b left). The coordination polyhedra of the Dy(III) atom in both **1** and **2**, based on the calculations using the SHAPE program (Llunell et al., 2013), can be described as a trigonal dodecahedron (Fig. 3).

The formation of such tetranuclear complex cations from originally dinuclear ones can be explained by the condensation process (Thompson, 2002; Jiang et al., 2017). A similar tetranuclear cluster $[\{Cu_2L(\mu_{1,1}\text{-}N_3)(ClO_4)\}_2(\mu_{1,3}\text{-}N_3)_2]$ (UZUXOD) (Majumder et al., 2011) is a result of the interlinking of two dicopper(II) units $[Cu_2L(\mu_{1,1}\text{-}N_3)(ClO_4)]^+$ by two end-to-end bridging azide anions. H*L* is a compartmental ligand which is the 1/2 condensation product of 2,6-diformyl-4-ethylphenol and 2-(2-aminoethyl)pyridine (Majumder et al., 2011).

A search in CSD (Groom et al., 2016) showed only six structures based on $\{NiO_2DyO_2DyO_2Ni\}$ core reported up to now (see Table 1). Structures of **1** and **2** show dimeric tetranuclear complex cations $[\{Ni(o\text{-}van\text{-}en)Dy(H_2O)_2(OH)\}_2]^{4+}$ containing the basic fragment $[NiO_2DyO_2DyO_2Ni]$ with a linear arrangement of Ni···Dy···Dy···Ni central atoms. It is noteworthy that Ni(II) atoms are diamagnetic. Similar atomic environments of Dy(III) atoms were found in another polynuclear complex $[Ni_2(L)DyCl(OH)(MeO)(MeOH)_3]_2Cl_2(ClO_4)_2 \cdot MeOH$ (HOBQUM; H_2L=*N,N´*-bis(3-methoxysalicylidene) diethylenetriamine) (Zhao et al., 2014); except that the octa-coordination of Dy(III) is also present with the double OH bridge. Analogous tetranuclear complex $[(\mu_3\text{-}CO_3)_2\{Ni(HL)(EtOH)Dy(CH_3COO)\}_2] \cdot 2EtOH$ (JASTUV01; H_3L = H_3L = *N,N´*-bis(3-methoxysalicylidene)-1,3-diamino-2-propanol) (Jiang et al., 2017) was found; Dy(III) central atom is octa-coordinated with distorted triangular dodecahedral geometry.

Dy1 and Dy1^i (i: 1 – *x*, 1 – *y*, 1 – *z* (**1**); i: 1 – *x*, 1 – *y*, 2 – *z* (**2**)) are doubly bridged by O atoms of hydroxy groups to form a Dy_2O_2 rhombus with angles of 112.2(3)° (**1**) (112.8(2)° (**2**)) and 67.8(3)° (**1**) (67.2(2)° (**2**)) for Dy—O—Dy and O—Dy—O, respectively. Ni—O and Ni—N bond lengths

a) b)

Fig. 3. Coordination polyhedra of Dy(III) atoms in **1** (a) (symmetry code: **i:** 1 – *x*, 1 – *y*, 1 – *z*); and in **2** (b) (symmetry code: **i:** 1 – *x*, 1 – *y*, 2 – *z*).

cover ranges of 1.828(8)–1.851(1) Å for structure **1** and 1.826(6)–1.860(5) Å for structure **2**. These values are in good agreement with analogous Ni(II)/Ln(III) complexes (Krešáková et al., 2025; Vráblová et al. 2019). On the contrary, Dy—O distances are in the range of 2.210(6)–2.500(6) Å for **1** and 2.249(5)–2.492(7) Å for **2** (see Tab. 3). Similar Dy—O values were observed also in related complexes (Wu et al., 2017).

The presence of both coordinated and solvated water molecules in both **1** and **2**, along with additional solvate molecules of methanol and isopropanol found in sample **2**, leads to distinct supramolecular structures of **1** and **2**. A list of potential hydrogen bonds of O—H···O type and possible weak hydrogen bonding interactions of O—H···Br type is provided in Tabs. 4 and 5, respectively. It is important to highlight that one hydrogen atom (H92) from the solvate water molecule (O9) in compound **1** does not engage in the hydrogen bonding network (Fig. 4). The IR spectrum of **1** shows a medium absorption band at 3460 cm^{-1}, which can be attributed to O—H stretching vibrations likely originating from water molecules not involved in extensive hydrogen bonding (see Fig. 1, highlighted area). However, in both spectra, shoulders are centered around 3300 cm^{-1}, which can be explained by OH stretching vibrations of the binding OH groups (Ferraro et al., 1965). Thus, the more pronounced shape of the shoulder in the spectrum of **1** can be ascribed to the water molecule.

Stacking π-π intermolecular interactions of the aromatic rings of the compartmental Schiff base-type ligand also contribute to the stability of the supramolecular structure. Distances of centroids *Cg*1···*Cg*1^{iii} (iii: 1 – *x*, 1 – *y*, – *z* (**1**); iii: *x*, *y*, 1 + *z* (**2**)) are 3.6181(1) for **1** and 3.5322(1) Å for **2**. Consequently, within the structure of both **1** and **2**, a topologically chain-like arrangement of closely positioned dimeric units of tetranuclear complexes running along the *c*-axis is formed (Figs. 4, 5). Unit chains are connected through hydrogen bonding systems, which leads to the formation of a final three-dimensional crystal structure.

Tab. 3. Selected bond lengths and angles [Å, °] for **1** and **2**.

	1	**2**		**1**	**2**
Ni1—N1	1.829(8)	1.826(6)	Dy1—O4	2.500(6)	2.492(7)
Ni1—N2	1.840(8)	1.830(6)	Dy1—O5	2.398(6)	2.415(5)
Ni1—O2	1.851(6)	1.860(5)	Dy1—O6	2.406(6)	2.342(5)
Ni1—O3	1.848(6)	1.845(5)	Dy1—O7	2.210(6)	2.231(5)
Dy1—O1	2.454(6)	2.487(5)	Dy1—O7^{i}	2.271(6)	2.249(5)
Dy1—O2	2.347(6)	2.362(5)	Dy1—O7—Dy1^{i}	112.2(3)	112.8(2)
Dy1—O3	2.362(5)	2.360(5)	O7—Dy1—O7^{i}	67.8(3)	67.2(2)

Symmetry codes: **i:** 1 – *x*, 1 – *y*, 1 – *z* (**1**); **i:** 1 – *x*, 1 – *y*, 2 – *z* (**2**).

Tab. 4. Potential hydrogen bonding interactions in **1** [Å, °].

D—H···A	***d*(D—H)**	***d*(H···A)**	***d*(D···A)**	**<(DHA)**	
O5—H51···O8	0.84(2)	1.92(3)	2.759(9)	173(12)	
O5—H52···Br2^{ii}	0.84(2)	2.44(4)	3.287(6)	163(11)	
O6—H61···O9	0.841(10)	1.93(3)	2.748(10)	165(10)	
O6—H62···Br1	0.840(10)	2.49	3.243(6)	150(8)	
O7—H7···Br2^{ii}	0.84	2.63	3.370(6)	147.9	
O8—H81···Br1	0.840(10)	2.48(3)	3.313(7)	169(11)	
O8—H82···Br2	0.840(10)	2.43(3)	3.252(7)	166(9)	
O9—H91···O10^{vi}	0.840(10)	2.00(4)	2.807(10)	162(13)	
O10—H101···Br1^{iii}	0.840(10)	2.74(11)	3.355(8)	132(12)	
O10^{iii}—H102^{iii}···O8^{v}	0.841(10)	2.12(4)	2.950(10)	167(14)	
π-π	***Cg*···*Cg***	**α**	**β**	**γ**	**Slippage**
*Cg*1···*Cg*1^{iii}	3.6181(1)	0	23.4	23.4	1.435

Symmetry codes: **i:** 1 – *x*, 1 – *y*, 1 – *z*; **ii:** *x*, 3/2 – *y*, 1/2 + *z*; **iii:** 1 – *x*, 1 – *y*, –*z*; **iv:** *x*, *y*, –1 + *z*; **v:** *x*, 3/2 – *y*, –1/2 + *z*; **vi:** –1 + *x*, *y*, *z*. Centroid *Cg*1 is the center of gravity of a six-membered ring C12-C17.

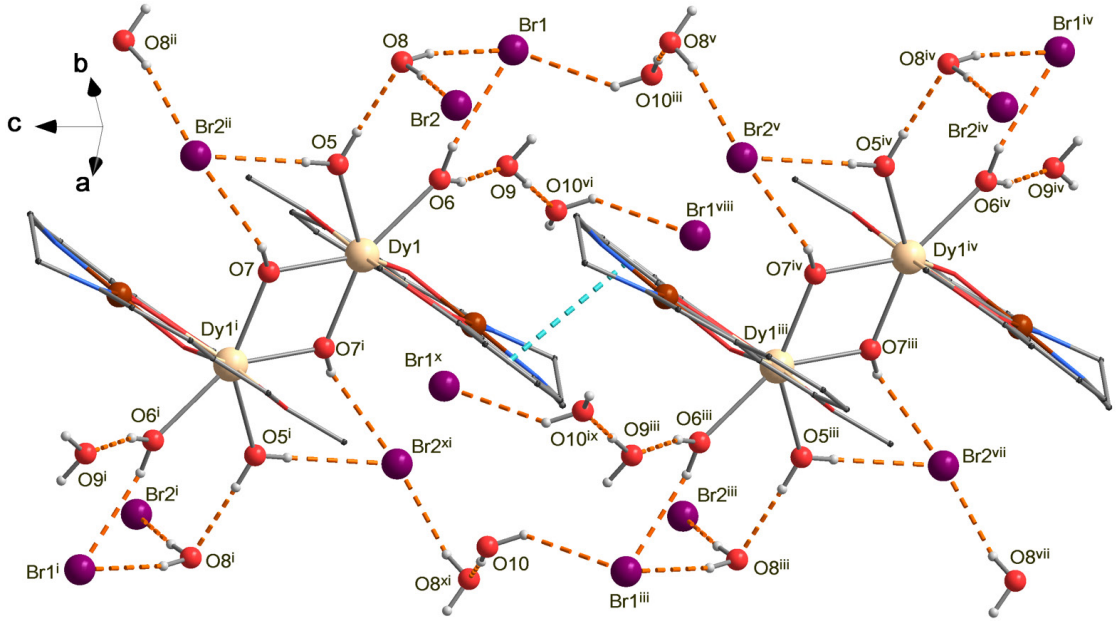

Fig. 4. View of potential hydrogen bonding system in **1** indicating chain-like arrangement of dimers of the Ni_2Dy_2 units. All atoms non-relevant for the hydrogen bonding system are omitted for clarity. Potential hydrogen bonding interactions are drawn as orange dashed lines and π-π interactions are shown as blue dashed lines.

Symmetry codes: **i:** 1 – *x*, 1 – *y*, 1 – *z*; **ii:** *x*, 3/2 – *y*, 1/2 + *z*; **iii:** 1 – *x*, 1 – *y*, –*z*; **iv:** *x*, *y*, –1 + *z*; **v:** *x*, 3/2 – *y*, –1/2 + *z*; **vi:** –1 + *x*, *y*, *z*; **vii:** 1 – *x*, –1/2 + *y*, –1/2 – *z*; **viii:** –x, 1 – *y*, –*z*; **ix:** 2 – *x*, 1 – *y*, –*z*; **x:** 1 + *x*, *y*, *z*; **xi:** 1 –*x*, –1/2 + *y*, 1/2 – *z*.

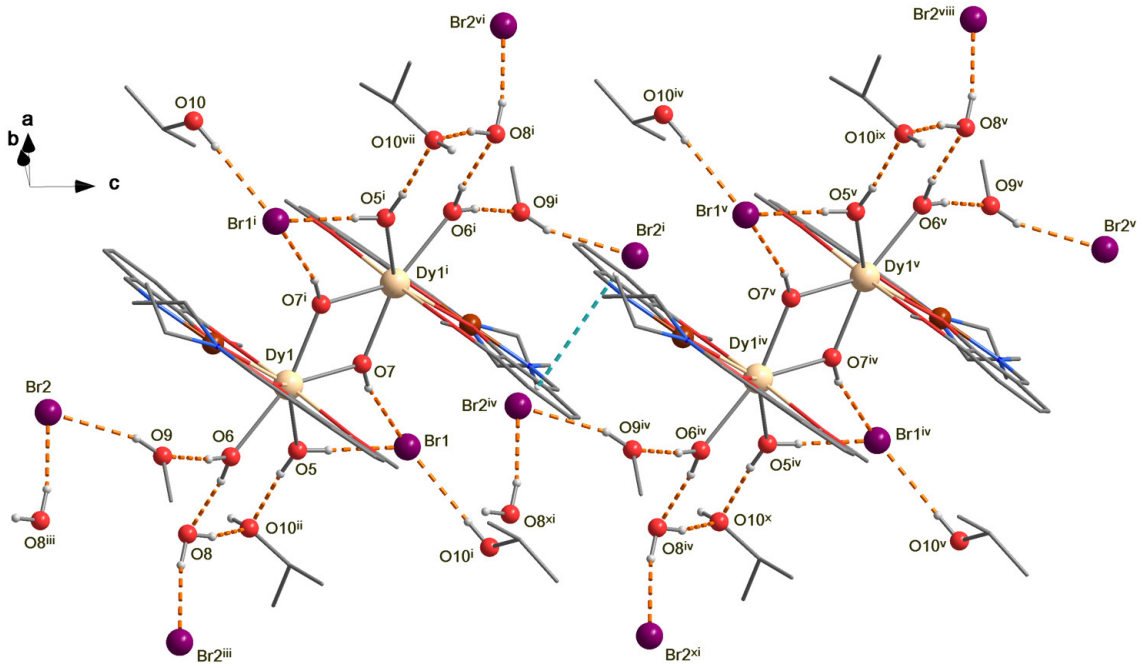

Fig. 5. View of potential hydrogen bonding system in **2** indicating chain-like arrangement of dimers of the Ni_2Dy_2 units. All atoms non-relevant for the hydrogen bonding system are omitted for clarity. Potential hydrogen bonding interactions are drawn as orange dashed lines and π-π interactions are shown as blue dashed lines.

Symmetry codes: **i:** 1 – *x*, 1 – *y*, 2 – *z*; **ii:** 1 – *x*, 1/2 + *y*, 3/2 – *z*; **iii:** *x*, *y*, 1 + *z*; **iv:** –*x*, 1 – *y*, 1 – *z*; **v:** 1 – *x*, 1 – *y*, 3 + *z*; **vi:** 1 + *x*, *y*, 1 + *z*; **vii:** *x*, 3/2 – *y*, 1/2 + *z*; **viii:** 1 + x, *y*, 2 + *z*; **ix:** *x*, 3/2 – *y*, 3/2 + *z*; **x:** 1 – *x*, –1/2 + *y*, 5/2 – *z*; **xi:** –*x*, –1 – *y*, 2 – *z*.

Tab. 5. Potential hydrogen bonding interactions in **2** [Å, °].

D—H···A	***d*(D—H)**	***d*(H···A)**	***d*(D···A)**	**<(DHA)**
O5—H51···Br1	0.85(2)	2.42(3)	3.259(6)	173(12)
O5—H52···O10^{ii}	0.84(2)	1.94(3)	2.771(8)	170(9)
O6—H61···O8	0.84(2)	1.82(3)	2.658(8)	173(9)
O6—H62···O9	0.85(2)	1.83(2)	2.678(8)	175(12)
O7—H7···Br1	0.84	2.54	3.358(5)	166.4
O8—H81···Br2^{iv}	0.84(2)	2.41(4)	3.233(7)	166(13)
O8—H82···O10^{ii}	0.84(2)	2.02(6)	2.778(9)	150(12)
O9—H91···Br2	0.84	2.40	3.209(7)	163.1
O10—H101···Br1^{i}	0.84	2.42	3.262(6)	177.8

π-π	***Cg*···*Cg***	**α**	**β**	**γ**	**Slippage**
*Cg*1···*Cg*1^{iii}	3.5322(1)	0	9.1	9.1	0.560

Symmetry codes: **i:** 1 – *x*, 1 – *y*, 2 – *z*; **ii:** 1 – *x*, 1/2 + *y*, 3/2 – *z*; **iii:** *x*, *y*, 1 + *z*; **iv:** –*x*, 1 – *y*, 1 – *z*. Centroid *Cg*1 is the center of gravity of a six-membered ring C2-C7.

Conclusion

Two novel tetranuclear 3*d*/4*f* complexes were prepared and spectroscopically and structurally characterized. Both complexes, **1** and **2**, exhibit ionic structures built up of bromide anions and tetranuclear $[\{Ni(o\text{-}van\text{-}en)Dy(H_2O)_2(OH)\}_2]^{4+}$ complex cations. In addition, **1** and **2** contain water and methanol/isopropanol/water solvate molecules, respectively, i.e. these complexes are solvatomorphs. The complex cation contains a $[NiO_2DyO_2DyO_2Ni]$ core with Ni-Dy-Dy-Ni linear arrangement of central atoms. The rich system of hydrogen bonding interactions was elucidated based on the presence of various solvent molecules using crystal structure determination.

Acknowledgement

This work was supported by Grant 09I03-03-V04-00176 (project name: Hybrid materials formed of layered aluminosilicates and molecular magnets – HERCULES) financed by the EU/NextGenerationEU/ program "Recovery and Resilience Plan, part of Investment 3: Excellent Science". We would like to thank Dr. Miroslava Litecká from the Department of Materials Chemistry at the Czech Academy of Sciences for gathering X-ray single crystal data.

Appendix A. Supplementary data

Crystallographic data for compounds 1 and 2 are deposited in the Cambridge Crystallographic Data Centre, CCDC no. 2464566 and 2464568, respectively. These data can be obtained free of charge via http://www.ccdc.cam.ac.uk/conts/retrieving.html, or from the Cambridge Crystallographic Data Centre, 12 Union Road, Cambridge CB2 1EZ, UK; fax: (+44) 1223-336-033; or e-mail: deposit@ccdc.cam.ac.uk.

References

Andruh M (2015) Dalton Trans. 44: 16633–16653.

Blessing RH (1995) Acta Cryst. B51: 816–823.

Brandenburg K, Putz H (2022) Program DIAMOND (version 4.6.8) Crystal Impact GbR., Bonn, Germany.

Brittain HG (2009) Polymorphism in Pharmaceutical Solids, 2nd Ed., Informa Healthcare USA, Inc.

CrysAlisPRO (version 1.0.43) (2022) Rigaku Oxford Diffraction, Yarnton, UK.

Cristovao B, Miroslaw B, Klak J, Rams M (2015) Polyhedron 86: 697–704.

Ferraro JR, Walker WR (1965) Inorg. Chem. 4(10): 1382–1386.

Groom CR, Bruno IJ, Lightfoot MP, Ward SC (2016) The Cambridge Structural Database, Acta Crystallogr. B 72: 171–179.

Hardy EE, Wyss KM, Gorden JD, Ariyarathna IR, Miliordos E, Gorden AEV (2017) Chem. Commun. 53: 11984–11987.

Horák M, Papoušek D (1976) Infračervená spektra a struktura molekul. Academia, Praha. ISBN 509-21-857.

Chandrasekhar V, Hossain S, Das S, Sutter J-P (2013) Inorg. Chem. 52: 6346–6353.

Jiang L, Liu Y, Liu X, Tian J, Yan S (2017) Dalton Trans. 46: 12558–12573.

Krešáková L, Litecká M, Oyarzabal I, Titiš J, Červeňáková M, Hillard EA, Robert J, Černák J (2024) New J. Chem. 48: 17750–17760.

Krešáková L, Miño A, Kuchár J, Smolko R, Černák J (2025) J. Coord. Chem. 78: 1930–1948.

Langley SK, Chilton NF, Moubaraki B, Murray K (2013) Chem. Commun. 49: 6965–6967.

Langley SK, Le C, Ungur L, Moubaraki B, Abrahams BF, Chibotaru LF, Murray KS (2015) Inorg Chem. 54: 3631–3642.

Liu Y-A, Wang C-Y, Zhang M, Song X-Q (2017) Polyhedron 122: 278–286.

Llunell M, Casanova D, Cirera J, Alemany P, Alvarez S (2013) SHAPE Program for the Stereochemical Analysis of Molecular Fragments by Means of

Continuous Shape Measures and Associated Tools, Version 2.1 (2013). Universitat de Barcelona, Barcelona, Spain.
Loukopoulos E, Papatriantafyllopoulou C, Moushi E, Kitos AA, Tasiopoulos AJ, Perlepes SP, Nastopoulos V (2024) Acta Crystallogr. B Struct. Sci. Cryst. Eng. Mater. 80: 347–359.
Macrae CF, Sovago I, Cottrell SJ, Galek PTA, McCabe P, Pidcock E, Platings M, Shields GP, Stevens JS, Towler M, Wood PA (2020) J. Appl. Cryst. 53: 226–235.
Majumder S, Sarkar S, Sasmal S, Sanudo EC, Mohanta S (2011) Inorg. Chem. 50: 7540–7554.
Nakamoto K (2009) Infrared and Raman Spectra of Inorganic and Coordination Compound, 6th Edition, J. Wiley & Sons, New York.
Nowicka B, Heczko M, Rams M, Reczyński M, Gaweł B, Nitek W, Sieklucka B (2017) Eur. J. Inorg. Chem. 1: 99–106.
Sheldrick GM (2015a) Acta Crystallogr. A 71: 3–8.
Sheldrick GM (2015b) Acta Crystallogr. C 71: 3–8.
Sakamoto S, Fujinami T, Nishi K, Matsumoto N, Mochida N, Ishida T, Sunatsuki Y, Re N (2013) Inorg. Chem. 52: 7218–7229.
Spackman PR, Turner MJ, McKinnon JJ, Wolff SK, Grimwood DJ, Jayatilaka D, Spackman MA (2021) J. Appl. Cryst. 54: 1006–1011.
Thompson LK (2002) Coord. Chem. Rev. 233-234: 193–206.
Tsantis ST, Lagou-Rekka A, Konadaris KF, Raptopoulou CP, Bekiari V, Psycharis V, Perlepes SP (2019) Dalton Trans. 48: 15668–15678.
Upadhyay A, Das C, Langley SK, Murray KS, Srivastava AK, Shanmugam M (2016) Dalton Trans. 45: 3616–3626.
Vignesh KR, Langley SK, Murray KS, Rajaraman G (2017) Inorg. Chem. 56: 2518–2532.
Vráblová A, Tomás M, Falvello LR, Dlháň Ľ, Titiš J, Černák J, Boča R (2019) Dalton Trans. 48: 13943–13952.
Vráblová A, Tomás M, Titiš J, Černák J, Falvello LR (2020) Inorg. Chim. Acta 512: 119874.
Wu H, Li M, Zhang S, Ke H, Zhang Y, Zhuang G, Wang W, Wei Q, Xie G, Chen S (2017) Inorg. Chem. 56: 11387–11397.
Zhao L, Wu J, Ke H, Tang J (2014) Inorg. Chem. 53: 3519–3525.

STU
FCHPT

Reaction mode of catalytic styrene oxidation using a bis-semicarbazide hexaazamacrocyclic Cu complex

Martin Breza

Department of Physical Chemistry, Faculty of Chemical and Food Technology STU, Radlinskeho 9, SK-81237 Bratislava, Slovakia
martin.breza@stuba.sk

Abstract: Catalytic styrene Ph—CH═CH_2 oxidation is assumed to be a simple reaction procedure; however, its details require further systematic research. Using quantum-chemical treatment, relevant intermediates have been investigated in various charge and spin states of alternative reaction pathways of styrene oxidation by hydroperoxyl using the $[CuL]^-$ catalyst, where H_2L = *trans*-2,9-dibutyl-7,14-dimethyl-5,12-di(4-methoxyphenyl)-1,2,4,8,9,11-hexaazacyclotetradeca-7,14-diene-3,10-dione. Within reaction pathway A, the neutral hydroperoxyl radical is bonded to Cu to form $^2[CuL(OOH)]^-$. Subsequent addition of neutral styrene results in the formation of $^2\{[CuL(OH)](Ph—CH_2—CHO)\}^-$. Reaction pathway B starts with the initial non-radical formation of the π-complex $^1[CuL(Ph—CH═CH_2)]^-$ which is problematic due to its endothermic character. Subsequent addition of a hydroperoxyl radical leads to $^2\{CuL[Ph—CH(OOH)—CH_2]\}^-$ and its oxidation leads to the separation of Ph—CH(OOH)—CH_2. The exothermic reaction path A is preferred over the endothermic reaction path B.

Keywords: B3LYP hybrid functional; broken symmetry treatment; Cu oxidation state; electronic structure; geometry optimization

Introduction

Catalytic oxidation of styrene is an environmentally friendly path of benzaldehyde production, which is an important intermediate in the production of many fine compounds and commodity chemicals (Andrade et al., 2021). Various catalysts differ in the conversion and selectivity of benzaldehyde, styrene epoxide, phenylacetaldehyde, 1-phenylethane-1,2-diol, benzoic acid, phenylacetaldehyde, and other oxidation products. The development of sustainable and effective catalytic systems for benzaldehyde production using green oxidants, such as hydrogen peroxide, is highly significant. For rational design of efficient catalysts, the corresponding reaction mechanisms must be known. Redox-active ligands can contribute by storing and providing electrons, modifying the Lewis acidity of the metal and assisting the formation/breaking of substrate bonding.

Catalytic styrene oxidation is assumed to be a simple reaction procedure, but its details require further systematic research as they are crucial for the development of new catalytic systems. Despite intense studies on the catalyzed oxidation of alkenes with hydrogen peroxide, no generally accepted mechanism of these reactions is known.

The Wacker process (Keith and Henry, 2009) is industrial homogeneous catalytic oxidation of ethylene to acetaldehyde in the presence of $PdCl_2$ and $CuCl_2$ and it is considered to be well understood. Its mechanism is based on active intermediate $[PdCl_2(C_2H_4)(H_2O)]$ with ethylene π-bonded to Pd(II) central atom.

However, other catalytic studies using the 1st row transition metal complexes with multidentate ligands suppose that intermediate M—O—O—H (M is the metal center) is formed and the O—O bond is activated to enable the alkene's reaction (Zhou et al., 2010; Lashanizadegan et al., 2017; Lashanizadegan et al., 2021; Lashanizadegan et al., 2022; Yang and Sarazen, 2022; Wu et al., 2023; Abuhafez et al., 2024; Vala et al., 2024; Razmara et al., 2025; Saveh et al., 2025). Most of these studies are restricted to quantum-chemical modeling of the catalyst (Lashanizadegan et al., 2017; Lashanizadegan et al., 2021; Lashanizadegan et al., 2022; Yang and Sarazen, 2022; Vala et al., 2024; Razmara et al., 2025; Saveh et al., 2025) or its complex with hydroperoxyl (Yang and Sarazen, 2022). The reaction pathway for styrene epoxidation with H_2O_2 using the 8-hydroxylquinolinmanganese(III) complex $[Mn^{III}Q_2Cl]$ in water was modeled as follows (Zhou et al., 2010):

$$[Mn^{III}Q_2Cl] + HOOH \rightarrow [Mn^{III}Q_2Cl(HOOH)] \quad (1)$$

$$[Mn^{III}Q_2Cl(HOOH)] \rightarrow [Mn^{IV}Q_2Cl(OH)]^+ + OH^- \quad (2)$$

$$[Mn^{III}Q_2Cl(HOOH)] + Ph—CH═CH_2 \rightarrow \rightarrow Ph—CHOCH_2 + [Mn^{III}Q_2Cl] + OH^- + H^+ \quad (3)$$

$$[Mn^{IV}Q_2Cl(OH)]^+ + Ph—CH═CH_2 \rightarrow \rightarrow Ph—CHOCH_2 + [Mn^{III}Q_2Cl] + H^+ \quad (4)$$

Another reaction pathway for the oxidation of sty-

rene with O_2 using a cobalt(III)-tetraphenyl catalyst [$HCo^{III}(TPP)$] was modeled without any solvent as follows (Abuhafez et al., 2024):

$$[HCo^{III}(TPP)] + Ph—CH{=}CH_2 \rightarrow \rightarrow [Co^{II}(TPP)]^{\bullet} + (Ph—CH—CH_3)^{\bullet} \quad (5)$$

$$[Co^{II}(TPP)]^{\bullet} + (Ph—CH—CH_3)^{\bullet} + O_2 \rightarrow \rightarrow [Co^{III}(TPP)—O—O—CHPh—CH_3] \quad (6)$$

$$[Co^{III}(TPP)—O—O—CHPh—CH_3] \rightarrow \rightarrow [Co^{III}(OH)(TPP)] + Ph—CO—CH_3 \quad (7)$$

Subsequently, the catalyst was regenerated using Et_3SiH.

In our previous study (Dobrov et al., 2020), the CuL complex (Fig. 1) with *trans*-2,9-dibutyl-7,14-dimethyl-5,12-di(4-methoxyphenyl)-1,2,4,8,9,11-hexaazacyclotetradeca-7,14-diene-3,10-dione (H_2L), a 14-membered bis-semicarbazide hexaazamacrocycle, was synthesized and characterized by analytical and spectroscopic techniques (IR, UV–vis, ^1H and ^{13}C NMR, ESI mass spectrometry, single-crystal X-ray diffraction, and spectroelectrochemistry). This complex selectively catalyzes microwave-assisted oxidation of neat styrene to benzaldehyde using hydrogen peroxide (30 % aqueous solution) as the oxidizing agent under low microwave irradiation (25 W) and in the absence of any added solvent. Under optimized conditions (40 min of irradiation at 80 °C), the catalytic system provided benzaldehyde yields of up to 81 % (turnover frequency up to 2.4×10^3 h^{-1}) as the only product. The CuL catalyst can be very simply separated by cooling to room temperature.

In Dobrov et al. (2020), a free radical mechanism for catalytic oxidation of styrene was proposed initiated by Cu-assisted formation of hydroxyl or hydroperoxyl radicals.

Now, two alternative mechanisms of styrene oxidation by hydrogen peroxide using CuL catalysis are investigated by quantum-chemical treatment. Our study is restricted to the structure, energy, and electron structure of relevant intermediates within these reaction pathways:

i) Reaction pathway A starts with the formation of $[CuL(OOH)]^q$ complex followed by styrene addition.
ii) Reaction pathway B starts with the formation of π-complex $[CuL(Ph—CH{=}CH_2)]^q$ and subsequent addition of hydroperoxyl.

The reaction pathways in literature (Zhou et al., 2010; Abuhafez et al., 2024) are related to changes in the oxidation states of the transition metal atom (Mn(III)/Mn(IV), Co(III)/Co(II), see Eqs. (1)–(7)) and the spin states of reaction intermediates are not considered. Therefore, in our reaction model systems, all intermediates are studied in various charge q and spin states to account for the non-innocent character of ligand L^{2-} and possible Cu(II)/Cu(I) equilibria. DFT calculations in Dobrov et al. (2020) are restricted to the CuL complex in various oxidation and spin states only. Possible reaction paths of catalytic styrene oxidation were not investigated by means of theoretical chemistry. In our recent study, this omission is addressed. The main aim of our preliminary DFT study was to propose which of the catalytic reaction pathways (A or B) is more probable and to identify the charge and spin states of their relevant reaction intermediates. Obtained results should enable proposing a realistic reaction pathway, which can be later studied in more detail.

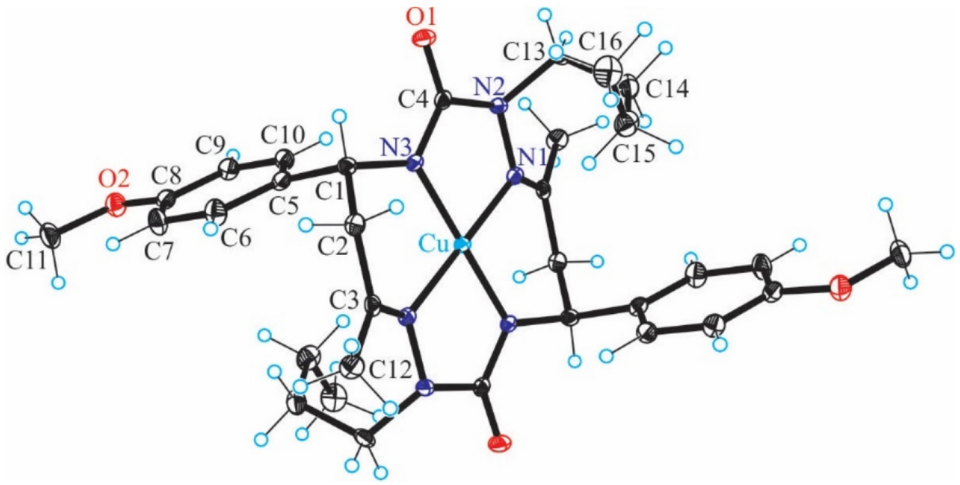

Fig. 1. X-ray structure of CuL with atom-labeling scheme and thermal ellipsoids drawn at 50 % probability level (Dobrov et al., 2020).

Methods

Geometry optimization of the systems under study was performed using B3LYP hybrid functional (Becke, 1993) and 6-311+G* basis sets from the Gaussian library (Frisch et al., 2016) in analogy with our previous study (Dobrov et al., 2020). Optimized structures were tested for the absence of imaginary vibrations using vibrational analysis. Singlet spin states in Cu complexes were treated using unrestricted formalism and their energies related to triplet spin states were corrected as follows ('broken symmetry' treatment, BS) (Malrieu and Trinquier, 2012)

$$E_S - E_T = \frac{\left\langle S^2 \right\rangle_T (E_{BS} - E_T)}{\left\langle S^2 \right\rangle_T - \left\langle S^2 \right\rangle_{BS}} \quad (8)$$

where E_S, E_T, and E_{BS} are singlet, triplet, and 'broken symmetry' (unrestricted singlet) energies, respectively. $\langle S^2 \rangle_T$ and $\langle S^2 \rangle_{BS}$ are triplet and 'broken symmetry' values of spin squares, respectively. Atomic charges, spin populations, and overlap weighted bond orders were evaluated in terms of natural population analysis (Foster and Weinhold, 1980; Reed et al., 1988; Carpenter and Weinhold, 1988). All quantum-chemical calculations were performed using the Gaussian16 software (Frisch et al., 2016). The MOLDRAW software was used for geometry manipulation and visualization (Ugliengo, 2012).

Results

Reaction pathway A

Energy parameters of DFT optimized styrene, hydroperoxyl, $[CuL]^q$ and relevant reaction intermediates in various charge and spin states are presented in Tabs. 1 and A1–A3 of Appendix.

Geometry of $[CuL]^q$ was optimized starting from its X-ray structure (Dobrov et al., 2020) as well as with added hydroperoxyl (starting from the Cu—O distance of ca 2.2 Å) in various charge and spin states (spin multiplicity is denoted as the left superscript where necessary). After geometry optimization, the original square-planar $[CuL]^q$ complex changed its coordination to square-pyramidal only in case of anionic doublet $^2[CuL(OOH)]^-$ (Tabs. A2 and A3 in Appendix, Figs. 2–3, and A1–A2 in Appendix) while its neutral analogues contain the neutral hydroperoxyl radical $(O—O_H—H_O)^0$ (see atomic charges in Tab. 2, spin populations in Tab. 3, and bond orders in Tab. 4) attached by hydrogen bonding $H_O \cdots N3$ (N3 has the highest negative charge and spin population among nitrogen atoms, see Tabs. 2 and 3) without any Cu—O bonds (see Tab. 4, Fig. A2, and Tabs. A2–A3 in Appendix).

Anionic complexes $^1[CuL]^-$ and $^2[CuL(OOH)]^-$ are more stable than their neutral analogues (Tabs. 1 and A1 in Appendix). It can be deduced that they are related by the following exothermic reaction

$$^1[CuL]^- + {}^2(OOH)^0 \rightarrow {}^2[CuL(OOH)]^- \quad (9)$$

as indicated by the reaction Gibbs energy, $\Delta_r G_{298}$ = –56.37 kJ/mol under normal conditions (Tab. A1 in Appendix).

Spin population in $^2[CuL(OOH)]^-$ is located mainly at Cu, unlike the spinless $^1[CuL]^-$ anion. Consequently, spin transfer from neutral hydroperoxyl radical to central Cu atom can be concluded in reaction (9) connected with weakening of the $O—O_H$ bond (Tabs. 3 and 4).

Subsequent addition of neutral styrene to the hydroperoxyl group in $^2[CuL(OOH)]^-$ (due to sterical reasons, C_β must be close to O, and C_α close to OH) causes hydrogen and oxygen transfers resulting in $^2\{[CuL(OH)](Ph—CH_2—CHO)\}^-$ where $Ph—CH_2—CH═O$ is only weakly bonded to $[CuL(OH)]^-$ (Fig. 4, Tabs. 4 and A2–A3 in Appendix). Here, the O atom originally bonded to Cu is shifted to C_β simultaneously with H transfer from C_β to C_α and Cu is bonded to O_H of hydroperoxyl. It is interesting that a removal of one electron results in analogous neutral complexes (Fig. A3, Tabs. A2–A3 in Appendix) with significantly higher energies (Tabs. 1 and A1 in Appendix). Consequently, $C_\alpha—C_\beta$ bonds are weakened and double $C_\beta═O$ bonds are formed (Tab. 4). The strength of Cu—O bond is comparable with that of Cu—N1/N3 (Tab. 4) and the Cu coordination is square-pyramidal (unlike the square-planar $[CuL]^q$, see Tabs. A2–A3 in Appendix). Non-vanishing spin populations in compounds within this reaction pathway can be at Cu, N1, N3 and hydro(pero)xyl oxygen atoms (Tab. 3). Cu in $^1[CuL]^-$ has a less positive charge and no spin population, which implies the oxidation state of Cu(I) (Tab. 2). More positive Cu charges and nonzero spin populations in other compounds of this reaction pathway correspond to the oxidation state Cu(II).

The most probable styrene oxidation step can be described by the exothermic reaction

$$^2[CuL(OOH)]^- + Ph—CH═CH_2 \rightarrow \\ \rightarrow {}^2\{[CuL(OH)](Ph—CH_2—CHO)\}^- \quad (10)$$

as indicated by the reaction Gibbs energy, $\Delta_r G_{298}$ = –266.67 kJ/mol under normal conditions (Tab. A1 in Appendix).

Tab. 1. Relative DFT energies, ΔE_{DFT}, and Gibbs energies at 298 K, ΔG_{298}, of compounds under study with charges q and spin multiplicities M_s. Energy values are related to the most stable systems (in bold) of the same composition.

	q	M_s	ΔE_{DFT} [kJ/mol]	ΔG_{298} [kJ/mol]
$(OOH)^q$	0	2	94.99	97.20
	–1	**1**	**0.00**	**0.00**
	–1	3	67.03	53.90
Reaction path A				
$[CuL]^q$	0	2	127.26	148.50
	–1	**1**	**0.00**	**0.00**
	–1	3	90.95	97.98
	+1	1	748.24	776.49
	+1	3	778.22	799.62
$[CuL(OOH)]^q$	0	1	224.48	232.30
	0	3	224.43	226.92
	–1	**2**	**0.00**	**0.00**
$\{[CuL(OH)](Ph—CH_2—CHO)\}^q$	0	1	322.18	341.47
	0	3	323.41	333.39
	–1	**2**	**0.00**	**0.00**
Reaction path B				
$[CuL(Ph—CH=CH_2)]^q$	**–1**	**1**	**0.00**	**0.00**
	–1	3	37.81	20.01
	0	2	85.46	74.80
$\{CuL[Ph—CH(OOH)—CH_2]\}^q$	0	1	184.97	182.87
	0	3	197.46	188.30
	–1	**2**	**0.00**	**0.00**

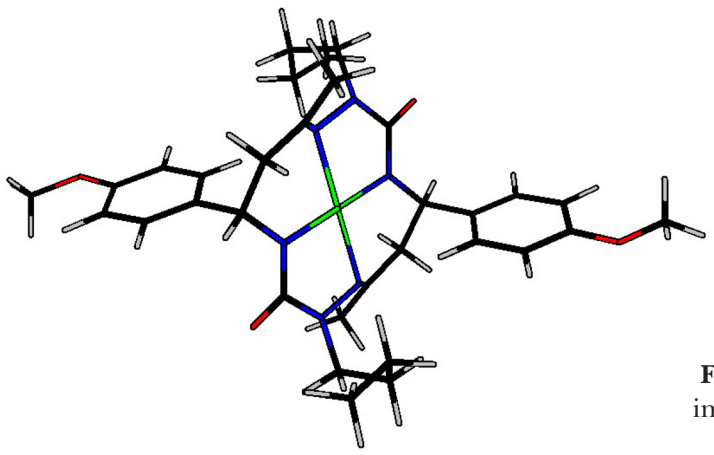

Fig. 2. DFT optimized structure of $[CuL]^-$ in singlet spin state (Cu — green, C — black, N — blue, O — red, H — gray).

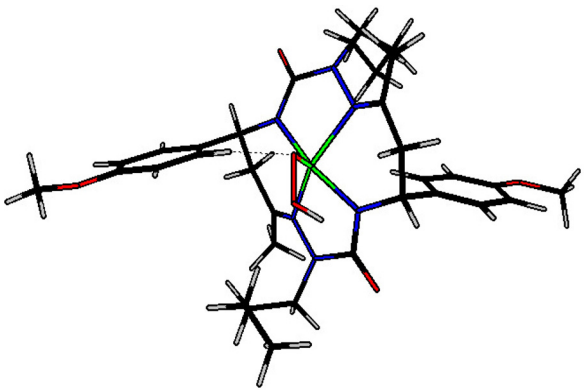

Fig. 3. DFT optimized structure of $[CuL(O—O_H—H_O)]^-$ in doublet spin state (Cu — green, C — black, N — blue, O — red, H — gray).

Tab. 2. Natural charges of C_α, C_β, O, O_H, and H_O atoms in (O—O_H—H_O) and (Ph—C_αH═$C_\beta H_2$) units, and Cu and N atoms in the complexes under study with charges q and spin multiplicities M_s. Data related to systems included in reaction paths A and B are in bold.

	q	M_s	C_α	C_β	O	O_H	H_O
$(OOH)^q$	**0**	**2**	**–**	**–**	**–0.145**	**–0.305**	**0.450**
	–1	1	–	–	–0.767	–0.630	0.396
	–1	3	–	–	–0.511	–0.890	0.401
Ph—CH═CH_2	**0**	**1**	**–0.191**	**–0.346**	**–**	**–**	**–**
Reaction path A							
$[CuL(OOH)]^q$	0	1	–	–	–0.167	–0.317	0.484
	0	3	–	–	–0.167	–0.317	0.484
	–1	**2**	**–**	**–**	**–0.614**	**–0.514**	**0.437**
$\{[CuL(OH)](Ph—CH_2—CHO)\}^q$	0	1	–0.488	0.446	–0.566	–0.925	0.433
	0	3	–0.488	0.448	–0.561	–0.856	0.437
	–1	**2**	**–0.491**	**0.436**	**–0.584**	**–1.188**	**0.424**
Reaction path B							
$[CuL(Ph—CH═CH_2)]^q$	**–1**	**1**	**–0.277**	**–0.472**	**–**	**–**	**–**
	–1	3	–0.240	–0.452	–	–	–
	0	2	–0.192	–0.356	–	–	–
$\{CuL[Ph—CH(OOH)—CH_2]\}^q$	0	1	0.019	–0.251	–0.327	–0.452	0.461
	0	3	0.012	–0.228	–0.319	–0.452	0.457
	–1	**2**	**0.081**	**–0.785**	**–0.347**	**–0.454**	**0.440**
H_2L	0	1	–	–0.357(2×)		–0.680(2×)	–0.383(2×)
Reaction path A							
$[CuL]^q$	0	2	0.927	–0.339(2×)		–0.787(2×)	–0.363(2×)
	–1	**1**	**0.603**	**–0.356(2×)**		**–0.784(2×)**	**–0.404(2×)**
	–1	3	0.853	–0.334		–0.748	–0.373
				–0.504		–0.781	–0.366
$[CuL(OOH)]^q$	0	1	0.925	–0.348(2×)		–0.859	–0.350
						–0.793	–0.355
	0	3	0.925	–0.348(2×)		–0.859	–0.350
						–0.793	–0.355
	–1	**2**	**0.903**	**–0.315**		**–0.777**	**–0.369(2×)**
				–0.332		**–0.750**	
$\{[CuL(OH)](Ph—CH_2—CHO)\}^q$	0	1	0.923	–0.296		–0.651	–0.350
				–0.303		–0.677	–0.347
	0	3	0.955	–0.295		–0.670	–0.337
				–0.307		–0.722	–0.348
	–1	**2**	**0.956**	**–0.312**		**–0.751**	**–0.376**
				–0.317		**–0.743**	**–0.356**
Reaction path B							
$[CuL(Ph—CH═CH_2)]^q$	**–1**	**1**	**0.670**	**–0.326**		**–0.785**	**–0.411**
				–0.270		**–0.782**	**–0.356**
	–1	3	0.885	–0.377		–0.774	–0.372(2×)
				–0.396		–0.781	
	0	2	0.928	–0.340		–0.787	–0.362(2×)
				–0.342		–0.783	
$\{CuL[Ph—CH(OOH)—CH_2]\}^q$	0	1	0.931	–0.340		–0.787	–0.363
				–0.342		–0.784	–0.363
	0	3	0.926	–0.341		–0.787	–0.362
				–0.341		–0.780	–0.363
	–1	**2**	**0.848**	**–0.310(2×)**		**–0.778**	**–0.390**
						–0.759	**–0.351**

Tab. 3. Natural spin populations at C_α, C_β, O, O_H, and H_O atoms in (O—O_H—H_O) and (Ph—C_αH=$C_\beta H_2$) units, and Cu and N atoms in the complexes under study with charges q and spin multiplicities M_s. Data related to systems included in reaction paths A and B are in bold.

	q	M_s	C_α	C_β	O	O_H	H_O
$(OOH)^q$	**0**	**2**	**–**	**–**	**0.742**	**0.268**	**–0.010**
	–1	1	–	–	0.000	0.000	0.000
	–1	3	–	–	1.479	0.535	–0.014
Ph—CH=CH_2	**0**	**1**	**0.000**	**0.000**	**0.000**	**0.000**	**0.000**
Reaction path A							
$[CuL(OOH)]^q$	0	1	–	–	0.701	0.310	–0.008
	0	3	–	–	0.702	0.309	–0.008
	–1	**2**	**–**	**–**	**0.097**	**0.007**	**0.001**
$\{[CuL(OH)](Ph—CH_2—CHO)\}^q$	0	1	–0.002	–0.004	–0.005	–0.343	0.008
	0	3	0.002	0.004	0.005	0.435	–0.011
	–1	**2**	**0.000**	**0.000**	**0.000**	**0.035**	**–0.001**
Reaction path B							
$[CuL(Ph—CH=CH_2)]^q$	**–1**	**1**	**0.000**	**0.000**	**–**	**–**	**–**
	–1	3	0.042	0.174	–	–	–
	0	2	0.000	0.000	–	–	–
$\{CuL[Ph—CH(OOH)—CH_2]\}^q$	0	1	0.035	–0.998	–0.021	–0.006	0.000
	0	3	–0.029	0.982	0.065	0.000	0.000
	–1	**2**	**–0.001**	**0.254**	**0.022**	**–0.001**	**0.000**
Reaction path B							
$[CuL]^q$	0	2	0.526	0.115(2×)		0.111(2×)	0.006(2×)
	–1	**1**	**0.000**	**0.000(2×)**		**0.000(2×)**	**0.000(2×)**
	–1	3	0.590	0.090		0.098	0.001
				0.345		0.115	0.006
$[CuL(OOH)]^q$	0	1	–0.532	–0.110(2×)		–0.111	–0.011
						–0.116	–0.006
	0	3	0.525	0.110(2×)		0.110	0.011
						0.116	0.006
	–1	2	0.575	0.054		0.106(2×)	0.002
				0.047			0.004
$\{[CuL(OH)](Ph—CH_2—CHO)\}^q$	0	1	0.197	0.104(2×)		–0.061	0.008
						0.022	0.003
	0	3	0.673	0.138(2×)		0.296	0.050
						0.186	0.008
	–1	**2**	**0.610**	**0.059**		**0.109**	**0.000**
				0.065		**0.106**	**0.002**
Reaction path C							
$[CuL(Ph—CH=CH_2)]^q$	–1	1	0.000	0.000		0.000	0.000
	–1	3	0.571	0.153		0.111	0.000
				0.166		0.108	0.002
	0	2	0.526	0.115(2×)		0.112	0.006(2×)
						0.110	
$\{CuL[Ph—CH(OOH)—CH_2]\}^q$	0	1	0.527	0.115(2×)		0.112	0.007(2×)
						0.109	
	0	3	0.527	0.115(2×)		0.111(2×)	0.007(2×)
	–1	2	0.507	0.000		0.083	–0.001
				0.023		0.087	0.002

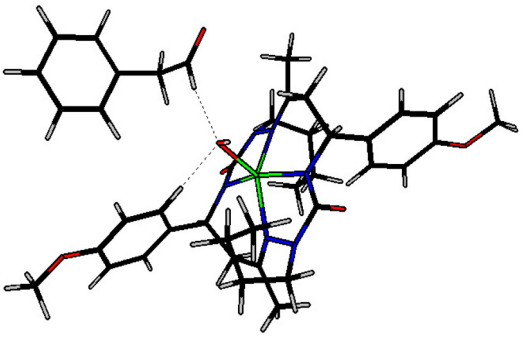

Fig. 4. DFT optimized structure of $\{[CuL(O_H—H_O)](Ph—C_\alpha H_2—C_\beta HO)\}^-$ in doublet spin state (Cu – green, C – black, N – blue, O – red, H – gray).

Reaction pathway B

Structures of $[CuL(Ph—CH=CH_2)]^q$ were optimized starting from $[CuL]^q$ with added neutral styrene in form of a π-complex with Cu—$C_{\alpha/\beta}$ distances of ca 2.4 Å. Only the optimized structure of $^1[CuL(Ph—CH=CH_2)]^-$ preserved the original form of a π-complex where the Cu—$C_{\alpha/\beta}$ bond lengths are comparable with the Cu—N1/N3 ones and the square-planar Cu coordination lost its planarity (Fig. 5, Tabs. A2–A3 in Appendix). Its $^2[CuL(Ph—CH=CH_2)]^0$ and $^3[CuL(Ph—CH=CH_2)]^-$ analogues with separated square-planar $[CuL]^q$ and neutral Ph—CH=CH_2 components are energetically higher (Tabs. 1 and A1–A3, and Fig. A4 in Appendix).

The lower charge and absence of spin at Cu in $^1[CuL(Ph—CH=CH_2)]^-$ indicates the formal oxidation state of Cu(I) unlike the Cu(II) one in $[CuL]^q$, $^2[CuL(Ph—CH=CH_2)]^0$, and $^3[CuL(Ph—CH=CH_2)]^-$ (Tabs. 2–3). The Cu—N1/N3 bonds in $^1[CuL(Ph—CH=CH_2)]^-$ are weaker than in $[CuL]^q$ and they are comparable with the Cu—$C_{\alpha/\beta}$ ones (Tab. 4). The C_α=C_β bond strength is equal to that of free styrene (Tab. 4).

According to our results, the only stable π-complex can be obtained by the non-radical endothermic reaction

$$^1[CuL]^- + Ph—CH=CH_2 \rightarrow \rightarrow {}^1[CuL(Ph—CH=CH_2)]^- \quad (11)$$

as indicated by the reaction Gibbs energy, Δ_rG_{298} = +91.95 kJ/mol under normal conditions (Tab. A1 in Appendix).

An addition of the hydroperoxyl radical to $^1[CuL(Ph—CH=CH_2)]^-$ leads to $^2\{CuL[Ph—CH(OOH)—CH_2]\}^-$ with a split Cu—C_α bond and hydroperoxyl bonding to the C_α site (Fig. 6, Tabs. A2–A3 in Appendix). Subsequently, the spin density is shifted from hydroperoxyl to Cu with a higher positive charge corresponding to the real oxidation state instead of Cu(I) in $^1[CuL(Ph—CH=CH_2)]^-$ (Tabs. 2 and 3). The Cu—N1/N3 bonds are weaker than the Cu—C_β one in $^1[CuL(Ph—CH=CH_2)]^-$ (Tab. 4).

Electron removal from $^1[CuL(Ph—CH=CH_2)]^-$ should correspond to the formal oxidation state Cu(II) but it causes the Ph—CH(OOH)—CH_2 split from the $[CuL]^0$ unit (Tabs. A2–A3 and Fig. A5 in Appendix) with higher energies (Tabs. 1 and A1 in Appendix). Based on charges and spin populations (Tabs. 2 and 3), real Cu(II) oxidation state is preserved in neutral $[CuL(Ph—CH=CH_2)]^0$ complexes and the spin density is shifted from hydroperoxyl to N1 and N3 atoms.

Our results show that the most advantageous hydroperoxyl addition to the above mentioned π-complex can be described by the following endothermic reaction

$$^1[CuL(Ph\text{-}CH=CH_2)]^- + {}^2(OOH)^0 \rightarrow \rightarrow {}^2\{CuL[Ph\text{-}CH(OOH)\text{-}CH_2]\}^- \quad (12)$$

as indicated by the reaction Gibbs energy, Δ_rG_{298} = 35.92 kJ/mol under normal conditions (Tab. A1 in Appendix).

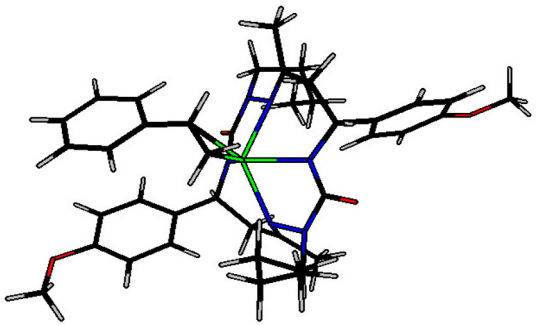

Fig. 5. DFT optimized structure of $[CuL(Ph—C_\alpha H=C_\beta H_2)]^-$ in singlet spin state (Cu – green, C – black, N – blue, O – red, H – gray).

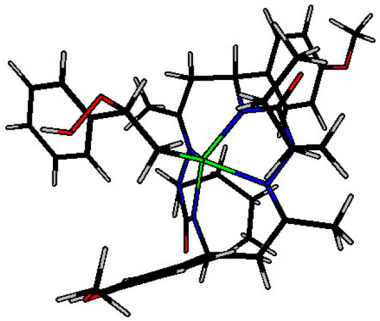

Fig. 6. DFT optimized structure of $\{CuL[Ph—C_\alpha H(O—O_H—H_O)—C_\beta H_2]\}^-$ in doublet spin state (Cu – green, C – black, N – blue, O – red, H – gray).

Tab. 4. Overlap weighted bond orders between C_α, C_β, O, O_H, and H_O atoms in (O—O_H—H_O) and (Ph—C_αH═$C_\beta H_2$) units, and Cu and N atoms in the complexes under study with charges q and spin multiplicities M_s. Data related to systems included in reaction pathways A and B are in bold.

	q	M_s	C_α—C_β	C_α—O	C_α—O_H	C_β—O	C_β—O_H	O—O_H
$(OOH)^q$	**0**	**2**	**–**	**–**	**–**	**–**	**–**	**0.679**
	–1	1	–	–	–	–	–	0.417
	–1	3	–	–	–	–	–	0.090
Ph—CH═CH_2	**0**	**1**	**1.380**	**–**	**–**	**–**	**–**	**–**
Reaction path A								
$[CuL(OOH)]^q$	0	1	–	–	–	–	–	0.720
	0	3	–	–	–	–	–	0.719
	–1	**2**	**–**	**–**	**–**	**–**		**0.505**
$\{[CuL(OH)](Ph—CH_2—CHO)\}^q$	0	1	0.868	–0.027	0.000	1.292	–0.012	0.001
	0	3	0.869	–0.026	0.000	1.294	–0.007	0.001
	–1	**2**	**0.855**	**–0.027**	**0.001**	**1.282**	**–0.017**	**0.001**
Reaction path B								
$[CuL(Ph—CH═CH_2)]^q$	**–1**	**1**	**1.279**	**–**	**–**	**–**	**–**	**–**
	–1	3	1.279	–	–	–	–	–
	0	2	1.379	–	–	–	–	–
$\{CuL[Ph—CH(OOH)—CH_2]\}^q$	0	1	0.949	0.722	–0.025	–0.025	0.000	0.530
	0	3	0.958	0.690	–0.024	–0.019	–0.001	0.529
	–1	**2**	**0.975**	**0.668**	**–0.027**	**–0.043**	**–0.005**	**0.524**
Reaction path A								
$[CuL]^q$	0	2	0.260(2×)		0.339(2×)		–	–
	–1	**1**	**0.188(2×)**		**0.298(2×)**		**–**	**–**
	–1	3	0.272		0.338		–	–
			0.357		0.346			
$[CuL(OOH)]^q$	0	1	0.232		0.311		0.069	–
			0.230		0.305		0.015	
	0	3	0.232		0.310		0.070	–
			0.230		0.305		0.015	
	–1	**2**	**0.238**		**0.305**		**0.302**	**–**
			0.215		**0.313**		**0.023**	
$\{[CuL(OH)](Ph—CH_2—CHO)\}^q$	0	1	0.293		0.384		0.000	0.000(2×)
			0.297		0.391		0.333	
	0	3	0.287		0.362		0.000	0.000(2×)
			0.295		0.386		0.333	
	–1	**2**	**0.241**		**0.308**		**–0.001**	**0.004**
			0.233		**0.310**		**0.309**	**0.009**
Reaction path B								
$[CuL(Ph—CH═CH_2)]^q$	**–1**	**1**	**0.172**		**0.220**		**–**	**0.195**
			0.132		**0.240**			**0.240**
	–1	3	0.287		0.332(2×)		–	–0.001
			0.294					0.007
	0	2	0.259(2×)		0.338(2×)		–	0.001(2×)
$\{CuL[Ph—CH(OOH)—CH_2]\}^q$	0	1	0.258(2×)		0.337		0.000(2×)	0.000(2×)
					0.333			
	0	3	0.258		0.337		0.000(2×)	0.000(2×)
			0.260		0.339			
	–1	**2**	**0.161**		**0.277**		**0.010**	**0.052**
			0.178		**0.262**		**0.003**	**0.324**

Discussion

Using quantum-chemical treatment, relevant intermediates in various charge and spin states were investigated for three reaction pathways of styrene oxidation by hydroperoxyl. The alternative reaction pathways A and B are based on the $[CuL]^q$ catalyst (Fig. 1), most probably its anionic form in the singlet spin state corresponding to the formal oxidation state of Cu(I). In the reaction pathway A, the neutral hydroperoxyl radical is bonded to Cu to form $^2[CuL(OOH)]^-$ (Fig. 3), which is unstable in other charge and spin states. Spin density is shifted to Cu, which corresponds to the real oxidation state of Cu(II). Subsequent addition of neutral styrene results in $^2\{[CuL(OH)](Ph—CH_2—CHO)\}^-$ formation after significant O and H atoms rearrangement; here, only weakly bonded $^2[CuL(OH)]^-$ and $Ph—CH_2—CH═O$ units are present. This reaction pathway seems to be realistic, but the Cu—OH split must be solved (probably by reaction with hydroperoxyl as in Lashanizadegan et al. (2017; 2021)) as well as the formation of benzaldehyde (by interaction with hydroperoxyl (Lashanizadegan et al., 2021) or with $^2[CuL(OH)]^-$ (Zhou et al., 2010; Yang and Sarazen, 2022).

Reaction pathway B starts with the initial non-radical formation of the π-complex $^1[CuL(Ph—CH═CH_2)]^-$ (Fig. 5) in Cu(I) oxidation state (Eq. 11); this reaction is problematic because of its endothermic character. However, its analogues in other charge and spin states do not allow for such π-complex formation. Subsequent addition of a hydroperoxyl radical leads to $^2\{CuL[Ph—CH(OOH)—CH_2]\}^-$ (Fig. 6) with $Cu—C_\beta$ bonding. Its oxidation leads to $Ph—CH(OOH)—CH_2$ separation.

Conclusions

Our DFT study compared two possible reaction pathways of styrene oxidation by hydrogen peroxide under CuL catalysis, where H_2L = *trans*-2,9-dibutyl-7,14-dimethyl-5,12-di(4-methoxyphenyl)-1,2,4,8,9,11-hexaazacyclotetradeca-7,14-diene-3,10-dione. Despite the restriction to the main reaction intermediates, our results indicate that the reaction starts more probably by the formation of $^2[CuL(OOH)]^-$ (reaction pathway A). The alternative reaction pathway B starting with $^1[CuL(Ph—CH═CH_2)]^-$ is afflicted by the endothermic character of this π-complex formation. Possible charge and spin states of the relevant reaction intermediates were also identified. Results of quantum-chemical calculations in vacuum indicate that the exothermic reaction path A (Δ_rG_{298} = –323.04 kJ/mol), which contains two exothermic reaction steps (see Eqs. (9) and (10)), is preferred over the endothermic reaction path B (Δ_rG_{298} = 127.87 kJ/mol), which contains two endothermic reaction steps (see Eqs. (11) and (12)). Future studies should provide additional details on the realistic reaction mechanism, including solvent effects.

Acknowledgement

Slovak Grant Agency VEGA (contract No. 1/0175/23) is acknowledged for financial support. The author thanks the HPC center at the Slovak University of Technology in Bratislava, which is a part of the Slovak Infrastructure of High-Performance Computing (SIVVP project ITMS 26230120002, funded by European Region Development Funds) for the computational time and resources made available.

References

Abuhafez N, Ehlers AW, de Bruin B, Gramage-Doria R (2024) Angew. Chem. Int. Ed. 63: e202316825.

Andrade MA, Martins LMDRS (2021) Molecules 26: 1680 and the references cited in.

Becke AD (1993) J. Chem. Phys. 98: 5648–5652.

Carpenter JE, Weinhold F (1988) J. Mol. Struct. (THEOCHEM) 169: 41–62.

Dobrov A, Fesenko A, Yankov A, Stepanenko I, Darvasiova D, Breza M, Rapta P, Martins LMDRS, Pombeiro AJL, Shutalev A, Arion VB (2020) Inorg. Chem. 59: 10650–10664.

Foster JP, Weinhold, F (1980) J. Am. Chem. Soc. 102: 7211–7218.

Frisch MJ, Trucks GW, Schlegel HB, Scuseria GE, Robb MA, Cheeseman JR, Scalmani G, Barone V, Petersson GA, Nakatsuji H, Li X, Caricato M, Marenich AV, Bloino J, Janesko BG, Gomperts R, Mennucci B, Hratchian HP, Ortiz JV, Izmaylov AF, Sonnenberg JL, Williams-Young D, Ding F, Lipparini F, Egidi F, Goings J, Peng B, Petrone A, Henderson T, Ranasinghe D, Zakrzewski VG, Gao J, Rega N, Zheng G, Liang W, Hada M, Ehara M, Toyota K, Fukuda R, Hasegawa J, Ishida M, Nakajima T, Honda Y, Kitao O, Nakai H, Vreven T, Throssell K, Montgomery JA Jr, Peralta JE, Ogliaro F, Bearpark MJ, Heyd JJ, Brothers EN, Kudin KN, Staroverov VN, Keith TA, Kobayashi R, Normand J, Raghavachari K, Rendell AP, Burant JC, Iyengar SS, Tomasi J, Cossi M, Millam JM, Klene M, Adamo C, Cammi R, Ochterski JW, Martin RL, Morokuma K, Farkas O, Foresman JB, Fox DJ (2016) Gaussian 16, Rev C01, Gaussian, Inc., Wallingford, CT.

Keith JA, Henry PM (2009) Angew. Chem. Int. Ed. 48: 9038–9049.

Lashanizadegan M, Alavijeh RK, Anafcheh M (2017) J. Mol. Struct. 1146: 450–457.

Lashanizadegan M, Ashari HA, Sarkheil M, Anafcheh M, Jahangiry S (2021) Polyhedron 200: 115148.

Lashanizadegan M, Habibi N, Mirzazadeh H, Ghiasi M (2022) React. Kinet., Mechan. Catal. 135: 3223–3242.

Malrieu J-P, Trinquier G (2012) J. Phys. Chem. A 116: 8226–8237.

Razmara Z, Necas M, Karimi P (2025) J. Mol. Struct. 1330: 141440.
Reed AE, Curtiss LA, Weinhold F (1988) Chem. Rev. 88: 899–926.
Sayeh K, Louroubi A, Abdallah N, Fkhar L, Aflak N, Bahsis L, Hasnaoui A, Ali MA, El Firdoussi L (2025) React. Kinet., Mechan. Catal. 138: 911–927.
Ugliengo P (2012) MOLDRAW: A Program to Display and Manipulate Molecular and Crystal Structures, University Torino, Torino. Available online: https://moldraw.software.informer.com (accessed on 9 September 2019).
Vala G, Jadeja RN, Patel A, Choquesillo-Lazarte D (2024) Inorg. Chim. Acta 563: 121925.
Wu Y, Kang J, Gao W, Bi M, Yang D, Ji R, Meng Q, Ma C (2023) J. Comput. Chem. 44: 1917–1927.
Yang RA, Sarazen ML (2022) ACS Catal. 12: 14476–14491.
Zhou Sh, Chen X, Qia Ch (2010) Chem. Phys. Let. 488: 44–49.

Appendix

Tab. A1. DFT energies, E_{DFT}, and Gibbs energies at 298 K, G_{298}, of compounds under study with charges q, spin multiplicities M_s, and spin squares $<S^2>$. Most stable systems are in bold.

	q	M_s	$<S^2>$	E_{DFT} [hartree]	G_{298} [hartree]
H_2L	0	1	0.000	–1876.93425	–1876.26433
Ph—CH═CH_2	0	1	0.000	–309.71674	–309.61529
$(OOH)^q$	0	2	0.754	–150.95195	–150.96003
	–1	1	0.000	**–150.98813**	**–150.99705**
	–1	3	2.014	–150.96260	–150.97652
Reaction path A:					
$[CuL]^q$	0	2	0.754	–3516.26778	–3515.61885
	–1	1	0.000	**–3516.31625**	**–3515.67541**
	–1	3	2.007	–3516.28161	–3515.63809
	+1	1	0.000	–3516.03126	–3515.37966
	+1	3	2.011	–3516.01984	–3515.37085
$[CuL(OOH)]^q$	0	1	1.008	–3667.23105	–3666.56946
				–3667.23104[a)]	–3666.56843[a)]
	0	3	2.008	–3667.23106	–3666.57048
	–1	2	0.754	**–3667.31654**	**–3666.65691**
$\{[CuL(OH)](Ph—CH_2—CHO)\}^q$	0	1	0.554	–3977.02647	–3976.24456
				–3977.02660[a)]	–3976.24371[a)]
	0	3	2.011	–3977.02613	–3976.24679
	–1	2	0.753	**–3977.14931**	**–3976.37377**
Reaction path B:					
$[CuL(Ph—CH═CH_2)]^q$	–1	1	0.000	**–3826.02113**	**–3825.25568**
	–1	3	2.006	–3826.00673	–3825.24806
	0	2	0.754	–3825.98858	–3825.22719
$\{CuL[Ph—CH(OOH)—CH_2]\}^q$	0	1	1.008	–3976.93793	–3976.15870
				–3976.94032[a)]	–3976.15974[a)]
	0	3	2.008	–3976.93556	–3976.15767
	–1	2	0.754	**–3977.01077**	**–3976.22939**

[a)]Corrected according to Eq. (8)

Tab. A2. Selected bond lengths (in Å) between relevant atoms in compounds under study with charges q and spin multiplicities M_s (see Fig. 1 and Tab. 2 for atom notation). Data related to systems included in reaction pathways A and B are in bold.

	q	M_s	C_α—C_β	C_α—O	C_α—O_H	C_β—O	C_β—O_H	O—O_H	N3···H_O
$(OOH)^q$	0	2	–	–	–	–	–	1.326	–
	–1	**1**	**–**	**–**	**–**	**–**	**–**	**1.519**	**–**
	–1	3	–	–	–	–	–	2.222	–
Ph—CH=CH_2	0	1	1.337	–	–	–	–	–	–
Reaction path A									
$[CuL(OOH)]^q$	0	1	–	–	–	–	–	1.326	1.795
	0	3	–	–	–	–	–	1.326	1.794
	–1	**2**	**–**	**–**	**–**	**–**	**–**	**1.473**	**2.298**
$\{[CuL(OH)](Ph—CH_2—CHO)\}^q$	0	1	1.519	2.411	4.376	1.212	3.236	3.750	5.123
	0	3	1.519	2.412	4.418	1.211	3.271	3.770	2.568
	–1	**2**	**1.527**	**2.406**	**3.943**	**1.216**	**3.127**	**3.944**	**2.998**
Reaction path B									
$[CuL(Ph—CH=CH_2)]^q$	**–1**	**1**	**1.373**	**–**	**–**	**–**	**–**	**–**	**–**
	–1	3	1.359	–	–	–	–	–	–
	0	2	1.338	–	–	–	–	–	–
$\{CuL[Ph—CH(OOH)—CH_2]\}^q$	0	1	1.486	1.457	2.375	2.435	2.849	1.449	8.104
	0	3	1.484	1.474	2.384	2.443	2.884	1.447	8.733
	–1	**2**	**1.496**	**1.491**	**2.410**	**2.513**	**2.985**	**1.450**	**6.490**

Tab. A2. (cont.)

	q	M_s	Cu—N1	Cu—N3	Cu—O/O_H	Cu—$C_{\alpha/\beta}$
Reaction path A						
[CuL] (exp.)	0	–	1.962(2) (2×)	1.867(2) (2×)	–	–
$[CuL]^q$	0	2	2.002(2×)	1.892(2×)	–	–
	–1	**1**	**2.135(2×)**	**1.905(2×)**	**–**	**–**
	–1	3	2.021	1.921	–	–
			1.934	1.908		
$[CuL(OOH)]^q$	0	1	2.018	1.912	3.285	–
			2.016	1.886	3.506	
	0	3	2.017(2×)	1.913	3.277	–
				1.886	3.503	
	–1	**2**	**2.095**	**1.948**	**2.049**	**–**
			2.140	**1.941**	**2.914**	
$\{[CuL(OH)](Ph—CH_2—CHO)\}^q$	0	1	2.046	1.872	5.064	5.881
			2.023	1.885	2.039	4.755
	0	3	2.051	1.928	4.946	5.745
			2.031	1.907	1.992	4.633
	–1	**2**	**2.106**	**1.957**	**5.118**	**4.964**
			2.090	**1.961**	**2.064**	**4.398**
Reaction path B						
$[CuL(Ph—CH═CH_2)]^q$	**–1**	**1**	**2.282**	**2.164**	**–**	**2.212**
			2.448	**2.035**		**2.114**
	–1	3	1.980	1.905	–	6.715
			1.969	1.908		6.200
	0	2	2.002	1.891		6.513
			2.001	1.893		7.013
$\{CuL[Ph—CH(OOH)—CH_2]\}^q$	0	1	2.000	1.891	8.398	8.642
			2.001	1.894	7.060	8.561
	0	3	2.006	1.891(2×)	7.748	6.808
			2.003		7.253	5.843
	–1	**2**	**2.106**	**1.957**	**5.118**	**4.964**
			2.090	**1.961**	**2.064**	**4.398**

Tab. A3. Selected bond angles (in degrees) in compounds under study with charges q and spin multiplicities M_s (see Fig. 1 and Table 2 for atom notation). Data related to systems included in reaction pathways A and B are in bold.

	q	M_s	N1—Cu—N1'	N3—Cu—N3'	N1—Cu—N3	N3—Cu—N1' N1—Cu—N3'
Reaction path A						
$[CuL]^q$ (exp.)			180.0	180.0	82.83(7) (2×)	97.17(7) (2×)
$[CuL]^q$	0	2	180.0	180.0	82.2(2×)	97.8(2×)
	–1	**1**	**180.0**	**180.0**	**81.4(2×)**	**98.6(2×)**
	–1	3	176.8	177.0	81.3	95.8
					83.2	99.7
$[CuL(OOH)]^q$	0	1	169.3	177.0	82.7	97.3
					82.4	98.2
	0	3	169.3	177.0	82.8	98.1
					82.3	97.3
	–1	**2**	**139.7**	**159.4**	**79.4**	**94.5**
					79.1	**92.7**
$\{[CuL(OH)](Ph—CH_2—CHO)\}^q$	0	1	156.1	165.7	81.2	95.6
					95.7	95.7
	0	3	158.9	158.6	79.8	95.7
					81.5	95.1
	–1	**2**	**142.1**	**155.6**	**78.3**	**92.8**
					79.6	**93.4**
Reaction path B						
$[CuL(Ph—CH=CH_2)]^q$	**–1**	**1**	**124.9**	**123.7**	**70.8**	**79.6**
					71.0	**88.2**
	–1	3	179.9	179.6	82.4(2×)	97.7
						97.5
	0	2	179.4	179.9	82.2(2×)	97.7(2×)
$\{CuL[Ph—CH(OOH)—CH_2]\}^q$	0	1	179.5	179.9	82.3	97.8(2×)
					82.1	
	0	3	178.3	179.8	82.3(2×)	97.5
						97.9
	–1	**2**	**142.1**	**155.6**	**78.3**	**92.8**
					79.6	**93.4**

Tab. A3. (cont.)

	q	M_s	N1—Cu—O	N3—Cu—O	N1—Cu—$C_{\alpha/\beta}$	N3—Cu—$C_{\alpha/\beta}$
Reaction path A						
$[CuL]^q$ (exp.)			–	–	–	–
$[CuL]^q$	0	2	–	–	–	–
	–1	**1**	**–**	**–**	**–**	**–**
	–1	3	–	–	–	–
$[CuL(OOH)]^q$	0	1	106.0	74.2	–	–
			95.4	52.8		
	0	3	106.1	74.4	–	–
			95.6	52.8		
	–1	**2**	**128.3**	**96.4**	**–**	**–**
			105.3	**79.0**		
$\{[CuL(OH)](Ph—CH_2—CHO)\}^q$	0	1	145.9	93.0	133.1	113.6
			105.8	90.6	137.2	102.9
	0	3	145.2	96.0	132.3	117.6
			101.5	90.4	101.5	106.4
	–1	**2**	**162.7**	**104.3**	**145.2**	**131.8**
			117.6	**100.7**	**154.1**	**114.7**
Reaction path B						
$[CuL(Ph—CH═CH_2)]^q$	**–1**	**1**	**–**	**–**	**143.0**	**119.3**
					110.7	**96.7**
	–1	3	–	–	118.9	49.9
					110.9	51.8
	0	2	–	–	116.3	144.6
					111.2	137.5
$\{CuL[Ph—CH(OOH)—CH_2]\}^q$	0	1	101.1	134.1	109.1	138.8
			100.1	130.1	117.6	131.9
	0	3	107.3	110.5	115.0	106.1
			99.9	117.5	108.6	97.7
	–1	**2**	**162.7**	**104.3**	**145.2**	**131.8**
			117.6	**100.7**	**117.6**	**114.7**

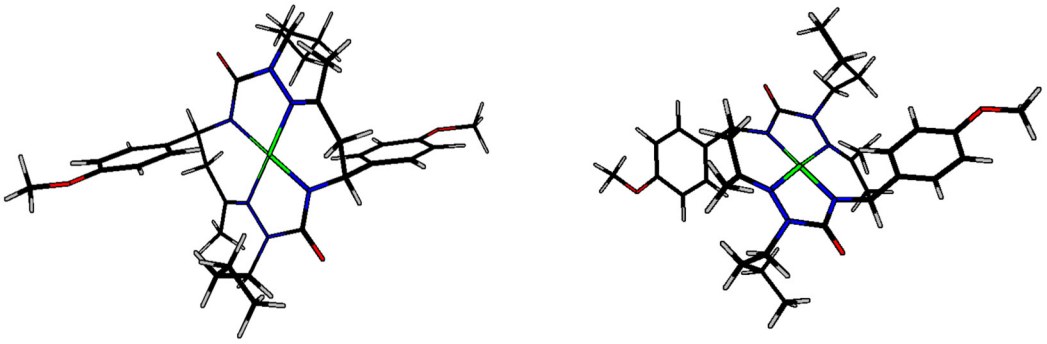

q = 0 M_s = 2 q = –1 M_s = 3

Fig. A1. DFT optimized structure of $[CuL]^q$ in various spin states (Cu — green, C — black, N — blue, O — red, H — gray).

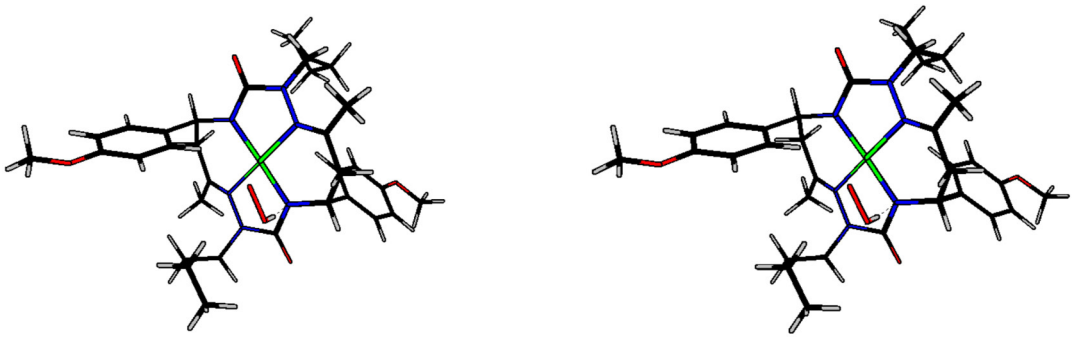

q = 0 M_s = 1 q = 0 M_s = 3

Fig. A2. DFT optimized structure of $[CuL(O—O_H—H_O)]^0$ in singlet and triplet spin states (Cu — green, C — black, N — blue, O — red, H — gray).

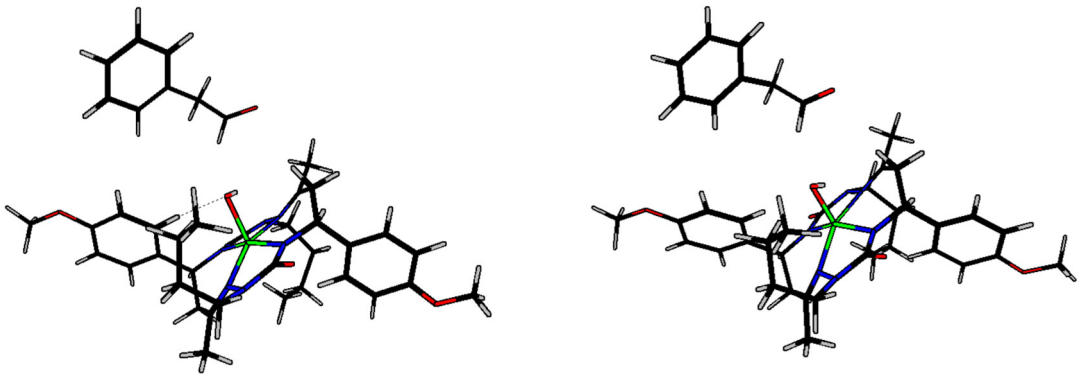

q = 0 M_s = 1 q = 0 M_s = 3

Fig. A3. DFT optimized structure of $\{[CuL(O_H—H_O)](Ph—C_\alpha H_2—C_\beta HO)\}^0$ in singlet and triplet spin states (Cu — green, C — black, N — blue, O — red, H — gray).

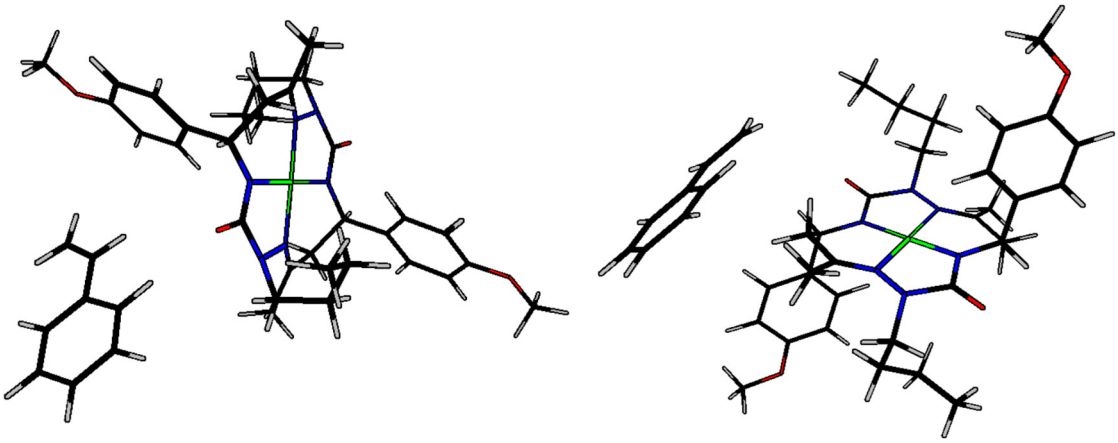

q = 0 M_s = 2 q = –1 M_s = 3

Fig. A4. DFT optimized structure of $[CuL(Ph—C_{\alpha}H═C_{\beta}H_2)]^q$ in various spin states (Cu – green, C – black, N – blue, O – red, H – gray).

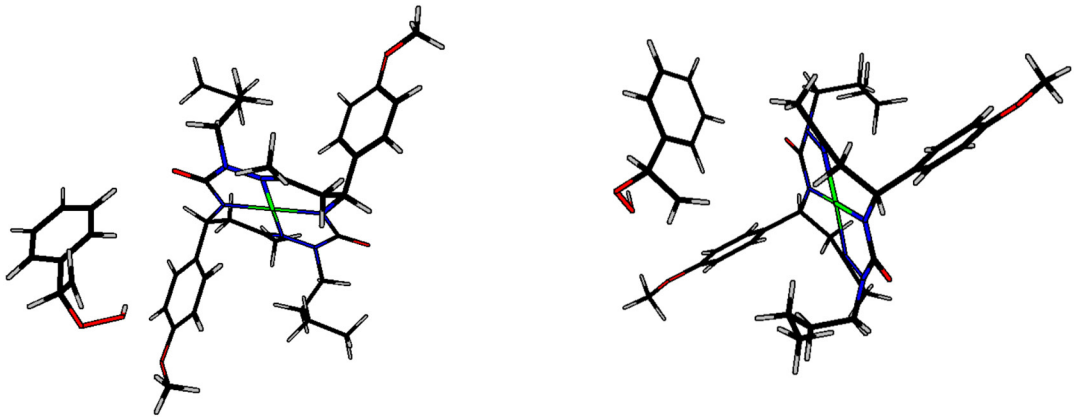

q = 0 M_s = 1 q = 0 M_s = 3

Fig. A5. DFT optimized structure of $\{CuL[Ph—C_{\alpha}H(O—O_H—H_O)—C_{\beta}H_2]\}^0$ in singlet and triplet spin states (Cu –green, C – black, N – blue, O – red, H – gray).